



Tahir

**A new paradigm on the pulsed laser ablation
of transition metal targets in water: synthesis of
carbon sp-sp² hybridized nanomaterial by CO₂/C
reduction**

Tese de Doutorado

Thesis presented to the Programa de Pós-Graduação em Física of
PUC-Rio, in partial fulfillment of the requirements for the degree of
Doutor em Ciências-Física.

Advisor: Prof. Tommaso Del Rosso

Rio de Janeiro

June 2020



Tahir

**A new paradigm on the pulsed laser ablation
of transition metal targets in water: synthesis of
carbon sp-sp² hybridized nanomaterial by CO₂/C
reduction**

Thesis presented to the Programa de Pós-Graduação em Física of PUC-Rio in partial fulfillment of the requirements for the degree of Doutor em Ciências-Física. Approved by the Examination Committee:

Prof. Tommaso Del Rosso

Advisor

Departamento de Física - PUC-Rio

Prof. Marco Cremona

Departamento de Física - PUC-Rio

Prof. Ricardo Queiroz Aucelio

Departamento de Química - PUC-Rio

Prof. Walter Mendes de Azevedo

UFPE

Prof. Gino Mariotto

UNIVR

Rio de Janeiro, June 26th, 2020

All right reserved. Total or partial reproduction of this is forbidden without the authorization of the university, the author, and the advisor.

Tahir

The author is graduated from the University of Malakand KPK, Pakistan. He obtained his Master's degree in Physics at the University of Peshawar KPK, Pakistan. He did a two-year Master of Philosophy (M. Phil) in Physics at Quaid-i-Azam University Islamabad, Pakistan.

Bibliographic data

Tahir

A new paradigm on the pulsed laser ablation of transition metal targets in water: synthesis of carbon sp-sp² hybridized nanomaterial by CO₂/C reduction / Tahir; advisor: Tommaso Del Rosso. Rio de Janeiro: PUC- Rio, Departamento de Física, 2020.

v., 301 f: il. color. ; 30cm

Tese (doutorado) - Pontifícia Universidade Católica do Rio de Janeiro, Departamento de Física.

Inclui bibliográficas

1. Física – Teses. 2. Ablação por Laser Pulsado (PLA). 3. Nanopartículas de Fe₃O₄ (Fe₃O₄NP). 4. Nanopartículas de Metais Nobres (AuNP, AgNP). 5. Pontos Quânticos de Carbono (CQDs). 6. Nanocristais Carbinoides, Tecnologias de Emissão Negativa (NET).
I. Tommaso Del Rosso. II. Pontifícia Universidade Católica do Rio de Janeiro. Departamento de Física. III. Título.

Acknowledgments

Undertaking the Ph.D in Physics has been a truly life-changing experience for me, and it would not have been possible without the support and guidance that I received from many people.

First of all, I am deeply thankful to my supervisor Prof. Tommaso Del Rosso, who is an incredibly smart, good, and very kind person. He compelled me to do high-quality research and appreciated me in each moment. It is his trust and motivation from beginning that enabled me to focus on my research.

I would like to appreciate all the generous help from Prof. Marco Cremona, Prof. Ricardo Queiroz Aucélio, and Prof. Sonia R. W. Louro, for the permission to work in their laboratories, and for giving valuable suggestions and guidelines in each moment.

I want to thank Prof. Jefferson Ferraz and Dr. Carlos A. T. Toloza for their precious help and valuable collaboration. And I wish to thanks all the colleagues which collaborated at the research and discussion of the presented research: Dr. Quaid Zaman, Joao Giesbrecht, Dr. Harold Jose Camargo Avila, Lucas, Vaniceus and Dr. Arthur Rodrigues Jardim Barreto.

I would also like to thanks, Baber Azam, Syed Abrar Sayyaf, Shah Nawaz Khan Sherazi, Rifaqat Ali, Syed Adnan Raza, Syed Hamza Safeer, Asmat, Saba Gul, Dr. Raj Wali Khan, Rafi, Khalil, Shahryar and Abdullah Jan, for their nice friendship, motivation and company during my Ph.D.

Yet most importantly, my family and friends gave me the happiness, courage, and a perspective that always encouraged me. I dedicate this thesis to all family members.

This Study was financed in part by the Coordenação de Aperfeiçoamento de Pessoal de Nível Superior - Brasil (CAPES) - Finance Code 001. Also, I wish to acknowledge the CNPq and FAPERJ for their financial support.

Abstract

Tahir; Tommaso Del Rosso (Advisor), **A new paradigm on the pulsed laser ablation of transition metal targets in water: synthesis of carbon sp-sp² hybridized nanomaterial by CO₂/**

C reduction, Rio de Janeiro, 2020. Ph.D. Tese de doutorado - Departamento de Física, Pontifícia Universidade Católica do Rio de Janeiro.

The principal result of this thesis is the discovery of the formation of different organic materials during the pulsed laser ablation (PLA) process of transition metal targets in deionized water, either in molecular or carbon nanostructured form. This result introduces a new paradigm in the PLA process: the realization of a nano synthesis by the atomization of the gaseous species dissolved in the liquid environment. CO₂ reduction is attributed to the catalytic properties of transition metal-oxide interfaces. All the transition metals used (Au, Ag, Fe) show the formation of molecular organic materials and sp² hybridized luminescent carbon quantum dots (CQDs), characterized by a quantum-yield of about 50%, the highest value reported today for carbon nanoparticles synthesized by PLA. The noble metals, uniquely, allow the simultaneous synthesis of sp-sp² hybridized carbynoid material, such as gold nanoparticle decorated carbynoid nanowires (Cy@Au NWs) and carbynoid nanocrystals supported by silver nanoparticles (Cy@Ag NCs). In the special case of gold, we obtain also the formation of spherical metal nanoparticles, in part encapsulated by a shell of carbynoid material (Au@Cy NPs), where the optical properties may be tuned by the initial CO₂ concentration in the liquid sample. The research introduces new concepts in the synthesis of colloidal solution of metal and carbon nanoparticles starting from a clean system without added chemical reagents, and in the control of the corresponding stability, dimension, hybridization, and optical properties. The synthesized nanomaterials have demonstrated functionality in different types of health and environmental applications: amplification of photodynamic activity of photosensitizers, detection of toxic metal ions with environmental interest, and gene therapy in endothelial cells.

Keywords

Pulsed Laser Ablation (PLA), Fe₃O₄ Nanoparticles (Fe₃O₄NP), Noble Metal Nanoparticles (AuNP, AgNP), Carbon Quantum Dots (CQDs), Carbynoid Nanocrystals, Negative Emission Technologies (NET).

Resumo

Tahir; Tommaso Del Rosso. **Um novo paradigma na ablação por laser pulsado de metais de transição em água: síntese de nanomateriais de carbono com hibridização sp-sp² através de redução CO₂/C**, Rio de Janeiro, 2020. p. Tese de Doutorado - Departamento de Física, Pontifícia Universidade Católica do Rio de Janeiro

O resultado principal desta tese é a descoberta da formação de diferentes materiais orgânicos durante o processo de ablação por laser pulsado (PLA) de alvos de metais de transição em água deionizada, seja em forma molecular que em forma de material nanoestruturado de carbono. Este resultado introduz um novo paradigma no processo de PLA: a realização de uma nanosíntese através da atomização das espécies gasosas dissolvida no ambiente líquido. A redução de CO₂ é atribuída as propriedades catalíticas das interfaces metal-óxidos. Todos os metais utilizados (Au, Ag, Fe) apresentaram a formação de material orgânico molecular e de pontos quânticos de carbono (CQDs) luminescentes com hibridização sp², caracterizados por uma eficiência quântica de cerca 50%, o maior valor reportado até agora para nanopartículas de carbono sintetizadas por PLA. Os metais nobres, por sua vez, permitem a síntese simultânea de nanomaterial carbinoide com hibridização sp-sp², como nanofios carbinoide decorados por nanopartículas de ouro (Cy@Au NWs) e nanocristais carbinoide suportados por nanopartículas de prata (Cy@Ag NCs). No caso especial do ouro, obtemos também a formação de nanopartículas esféricas encapsuladas por uma casca de material carbinoide (Au@Cy NPs), onde as propriedades óticas podem ser controladas através da concentração inicial de CO₂ da amostra líquida. A pesquisa introduz novos conceitos na síntese de soluções coloidais de nanopartículas de metal e de carbono partindo de um sistema limpo sem adição de reagentes químicos, e no controle da correspondente estabilidade, dimensão, hibridização e propriedades óticas. Os nanomateriais sintetizados demonstraram funcionalidade em diferentes tipos de aplicações relacionadas a saúde e meio ambiente: amplificação da atividade fotodinâmica de fotossintetizantes, detecção de íons metálicos tóxicos com interesse ambiental, e terapia genica em células endoteliais.

Palavres - chave

Ablação por Laser Pulsado (PLA), Nanopartículas de Fe_3O_4 ($\text{Fe}_3\text{O}_4\text{NP}$), Nanopartículas de Metais Nobres (AuNP, AgNP), Pontos Quânticos de Carbono (CQDs), Nanocristais Carbinoides, Tecnologias de Emissão Negativa (NET).

Table of contents

1 Introduction	1
1.1. The state of art and achieved advances	1
1.2. Objectives	4
1.3. Infrastructure and contributions	7
1.4. Thesis organization	8
2 Theory and recent literature	12
2.1. Negative emission technologies	12
2.1.1. Introduction	12
2.1.2.1. Gold (Au)	18
2.1.2.2. Silver	18
2.1.2.3. Iron	19
2.3.1. Raman spectroscopy	54
2.4.1. Hybridization states of carbon in nanomaterials	60
2.4.2. Raman of Carbon Nanomaterials	65
3 Instrumentations and experimental methods	77
3.1. Materials and cleaning processes	77
3.1.1. Materials	77
3.1.2. Cleaning of targets	78
3.1.3. Cleaning of glassware	79
3.1.4. Preparation of the aqueous solution of NaOH	79
3.2. Synthesis of the colloidal solution of nanomaterial by PLA	81
3.2.1. Experimental setup for PLA in liquid	81
3.2.2. Calculation of laser spot size and fluence	84
3.2.3. Effect of the water column over the target	86

3.2.4. Procedure for the measurement of F_{ω} and $F_{2\omega}$ during simultaneous ablation by fundamental and second harmonic frequencies	88
3.3. Analytical characterization of the nanomaterials	91
3.3.1. UV-visible spectroscopy	91
3.3.2. Inductively Coupled Mass spectroscopy (ICP-MS) analysis	92
3.3.3. Total Carbon Analysis (TC)	92
3.3.4. Dynamic light scattering (DLS) and ζ -potential	95
3.4. Chemical characterization of the nanomaterial	95
3.4.1. Raman spectroscopy	95
3.4.2. Infrared spectroscopy	97
3.4.3. X-ray photo-electron Spectroscopy (XPS)	98
3.5. Morphological and structural characterization of the nanomaterial: transmission electronic microscopy	98
3.5.1. Used TEM apparatus	99
3.5.2. Preparation of samples	99
3.6. Carbon/metal separation methods	101
3.6.1. Magnetization	103
3.6.2. Amalgamation	104
3.6.3. Precipitation by dialysis and centrifugation	105
3.6.4. Precipitation by salt	105
3.6.5. Heating	107
3.6.6. Electromagnetic induction	108
3.6.7. Conclusions on the separation methods	109
3.7. Photoluminescence spectroscopy	110
3.8. Magnetic characterization	112
4 .	
Results of Au derived nanomaterial	114
4.1. UV-Vis stability Investigation of Au derived nanomaterial	114
4.2. Characterization of the Au derived nanomaterial (dimension, λ_{spr} , charge, total carbon)	118

4.3. Characterization of carbon nanomaterial derived from Au target	125
4.3.1. SERS measurements on Au derived nanomaterial	125
4.3.2. TEM Measurements	127
4.3.3. CQDs	128
4.3.4. Cy@Au NWs	130
4.4. Surface Composition of the CQDs Obtained by CO ₂ /C with Au Target	134
4.5. PL of The CQDs obtained by CO ₂ /C with Au target	136
4.5.1. Steady-state PL	136
4.5.2. Time-Resolved PL (TRPL)	139
4.6. Application of the Au derived nanomaterial	143
4.6.1. Interaction of The Au derived nanomaterial with the copolymer pluronic-F127: stability in media with high Ionic force	143
4.6.2. Effect of the agglomerated Au@Cy/PF127 NCs On the photodynamic activity of Ce6 photosensitizer	145
4.6.3. Citotoxicity of the Au derived nanomaterial	147
4.6.4. Gene therapy with Au derived nanomaterial	148
4.6.5. Optical Sensing of methylmercury in Water by CQDs	152
4.7. Conclusions	153
5 Ag Derived Nanomaterial	157
5.1. UV-Vis stability investigation of Ag derived nanomaterial	158
5.2. Analytical characterization of the Ag derived nanomaterial (dimension, λ_{spr} , charge, total carbon, HRTEM)	159
5.3. Characterization of carbon nanomaterial colloid derived from Ag target	163
5.3.1. SERS measurements on Ag derived nanomaterial	163
5.3.2.1 CQDs	165
5.3.2.2 Cy@Ag Nanocrystals	165
5.4. PL of the CQDs obtained by CO ₂ /C with Ag target	166
5.1. Conclusions	167

6 Fe Derived Nanomaterial	170
6.1. Separation of the different constituents present in Fe derived nanomaterial	170
6.2. Stability and analytical characterization of the Fe derived nanomaterial (dimension, charge, ζ -potential, magnetization)	173
6.2.1. Fe Derived nanomaterial synthesized by PLA with simultaneous ω and 2ω pulses	173
6.2.2. Fe derived nanomaterial synthesized with pulses at single-frequency laser (ω , or 2ω)	179
6.3. Raman, FTIR, and XPS of iron oxide-based nanoparticles and carbon nanomaterial derived from Fe target	182
6.3.1. Raman spectroscopy of Fe derived nanomaterial	182
6.3.2. Magnetite to hematite conversion by laser irradiation in Raman spectroscopy	184
6.3.3. FTIR and XPS analysis on the Fe derived nanomaterial	185
6.4. PL of the CQDs obtained by CO ₂ /C with Fe target	188
6.5. Conclusion	189
7 Our hypothesis on the CO ₂ /C reduction induced by PLA in water	194
7.1. Evidence of the catalytic activity of the NPs synthesized by PLA of transition metal target in the water	194
7.2. Our hypothesis on PLA induced CO ₂ /C reduction in water	199
7.3. The consistency of the proposed model with the experimental results	203
8 Conclusions and perspectives	205
8.1. Conclusions	205
8.1.1. Experimental evidence of CO ₂ /C reduction induced by PLA of transition metal target in water	205
8.1.2. Physical-chemical process associated to the observed CO ₂ /C reduction	207
8.1.3. Control of the dimensions and optical properties of the synthesized nanomaterials	208
8.1.4. Application of the synthesized nanomaterials	211

8.2. Future work and perspectives	212
8.2.1. Future experimental work	212
8.2.2. Perspectives	213
9 Production	217
9.1. List of publications	217
9.2. Conferences	218
Appendix	220
A.1	
Calculation of the dielectric function of small NPs	220
Declaration of ranges, constants and <i>LogNormal</i> function	220
Dielectric function of bound electrons	221
Particle properties	222
Show the graphs	223
Plot results	223
A.2	
Dynamic Light Scattering (DLS) and ζ -potential	224
A.3	
Transmission Electronic Microscopy	225
10 Bibliography	228

List of Figures

- Figure 1.1 Icons used for representation of synthesized nano materials throughout the dissertation. 6
- Figure 1.2 Schematic diagram of the main and peripheral objectives of the research as described in the lines above. 6
- Figure 2.1 (a,b) Renewable energy sources, c) energy transport, d) energy harvesting, e) low-consumption lighting, f) electric vehicles, g) hydrogen production, h) CO₂ conversion to fuels, and i) CO₂ harvesting [47]. 13
- Figure 2.2 Schematic diagram of the most common oxidation states of Fe (a), Ag(b), and Au(c), and the corresponding electronic configuration of the last two orbitals. 16
- Figure 2.3 Creation of a hole-electron pair in metallic semiconductors, further used in redox processes. The bandgap may be excited by different routes: optically, electrically, or thermally. 21
- Figure 2.4 Schemes showing the photo-induced self-stabilizing process of the Ag/Ag₂O interfaces. a) The photogenerated electrons are taken by Ag⁺ ions of the oxide. b) The photogenerated electrons are taken from metallic silver and passed to molecular oxygen, formed in the first part of the process (a). The symbols h and e⁻ represent the photogenerated holes and electrons, respectively. CB and VB indicate the conduction and valence band, respectively [111]. 22
- Figure 2.5 Temporal evolution of electron and lattice temperature of gold vs ablation depth. Thermal equilibrium between electron and lattice occurs approximately after 5 ps [169]. 29
- Figure 2.6 Theoretical ablation depth in a target of gold vs laser fluence F of the laser pulses. The red and blue lines are associated to the temperature-dependent and the temperature-independent electron-phonon coupling [169]. 30
- Figure 2.7 Schematic diagram representing the different stages in the process of formation of NPs by PLA in liquid (adapted from [7]). 31
- Figure 2.8 Summary of the different kind of surface composition of MeNPs in colloidal dispersion obtained from PLA of Au, Ag, and Fe targets in water and different organic solvent) [6]. 33

Figure 2.9 a) Shadowgraphs of the persistent microbubbles created by PLA of different metal targets after 100 ms from the arriving of the laser pulse [32]. b) H₂, O₂, and N₂ gas fraction in the permanent bubbles, depending on different metal targets [32]. c) Concentration of H₂O₂ produced during PLA in the water of different metal targets [32]. d) Intensity of the acoustic waves produced during PLA depending on AuNPs concentration [33], e) Gas production rate during PLA depending on AuNPs concentration [33]. 34

Figure 2.10 Schematic division of the PLA environment into different regions by the composition and state of the atoms. The picture shows the possible carbon nanostructures synthesized throughout our research, as defined in Section 1. 36

Figure 2.11 Scheme of the principal interactions between colloidal nanoparticles. a) vdW dipolar repulsive interaction. b) Steric repulsion, induced after functionalization of the particles with macromolecules or polymers. c) Electro-static repulsion, due to the net charge considering the EDL, consisting of the Stern and diffuse layer. d) Contribution of the EDL potential (green curve), repulsive vdW potential (red curve) and steric repulsion (dotted cyan curve) to the overall X-DLVO potential (blue dashed curve) in the function of the interparticle distance d . Adapted from [186]. 39

Figure 2.12 (a) Schematic diagram of collective oscillation of free electrons in MeNPs, arising from interaction with the incident EM planar wave. (b) The direction of the induced electric field (E_{rest}) and incident electric field (E_{in}). 41

Figure 2.13 Schematic diagram of a spherical NPs of radius a , under the excitation a uniform static electric field polarized along the Z axis. In QSA we are considering $a \ll \lambda$. 42

Figure 2.14 Schematic diagram used to explain the measurement of the extinction spectra of the NPs illuminated by plane EM radiation. 46

Figure 2.15 (a), TEM image of the Au@Cy NPs synthesized by PLA with NaOH concentration of 2 mM. In the inset is reported the experimental statistical size distribution of NPs. (b) Experimental extinction spectra of the synthesized NCs (black line with open circles), and Mie's theoretical fit (dashed grey line) obtained using the statistical distribution reported in (a) [20]. 48

Figure 2.16. Normalized theoretical extinction spectra of AuNPs with a) $r < 10$ nm, b) $r > 10$ nm [210]. 51

Figure 2.17 Experimental extinction spectra of a colloidal dispersion of AgNPs of different dimensions, synthesized by PLA. a) A1, A2, and A3 samples have an average size of 20, 19, and 15 nm, respectively [81]. b) A3, A4, A5 samples have an average size of 15, 12 and 10 nm, respectively [81]. 53

- Figure 2.18 Energy level diagram representing the Raman response of a material. (b) Typical Raman spectrum showing the higher and weaker intensity peaks for Rayleigh, Stokes, and Anti-Stokes scattering respectively. 55
- Figure 2.19 Complete electronic energy diagram of a molecule, comprising of both the excited electronic and molecular states. In the case of Raman spectroscopy, ω_{laser} is the frequency of the laser excitation, and ω_s is the frequency of the non-elastically scattered radiation after the activation of the Raman mode at frequency ω . For each kind of spectroscopy is reported the corresponding value of the optical cross-section in cm^2 [221] 57
- Figure 2.20 Principle of SERS spectroscopy. The N molecules of interest are placed in proximity (within a few nm) with a noble metal nanostructure. The incoming and scattered intensity are amplified by the factor $G_{\text{SERS}} = A\omega_s^2 \cdot A\omega_L^2$. 59
- Figure 2.21 Diagram representing the concept of orbital hybridization in carbon atoms, with the formation of simple hydrocarbons (methane- sp^3 , ethylene- sp^2 , acetylene- sp). 61
- Figure 2.22 Schematic diagram of different kind of carbon nanostructures based on their hybridization [41]. 62
- Figure 2.23 Different kinds of luminescent carbon nanomaterials [234]. 62
- Figure 2.24 Schematic diagram of possible CAWs: a) polyene structure, b) cumulene structure. 63
- Figure 2.25 Theoretical structure of the finite length CyNCs [253]. a) Lateral view. b) Top view. c) HRTEM, and d) SEM image of an isolated CyNC decorated by AuNPs, synthesized by PLA of a gold target in alcohol. 65
- Figure 2.26 a) Experimental Raman spectra of GQD synthesized by electrochemical method. D band and G band are observed at 1350 and 1590 cm^{-1} , respectively [259]; b) Theoretical Raman spectra of different types of carbon nanomaterials[41], c) DFT computed theoretical Raman peaks for hydrogen capped polyynes (continuous lines) of different lengths, and comparison with the experimental spectrum (red points) [255]. The polyynes have been synthesized by the arc discharge method. 66
- Figure 2.27 a) Discrete energies states of a particle in a one-dimensional infinite potential well or box, where E_n stands for the total energy of a particle and $V(x)$ represents the potential energy; b) Transformation of E_g as we pass from bulk semiconductor to SQDs of different dimension; b) and c) scheme of excitation and emission of luminescence in SQDs, adapted from [262, 263]. 68
- Figure 2.28 Schematic diagram of different PL mechanisms in NPs [234]. 68

- Figure 2.29 Representation of the mixed sp^2 - sp^3 carbon NPs, responsible for the PL of type III. Adapted from [235]. 70
- Figure 2.30 Scheme representing the principle of work of the photo-dynamic activity. Adapted from [136]. 73
- Figure 2.31 Schematic diagram of the different stages of PDT [302]. 74
- Figure 2.32 Schematic and specific example of gene therapy by the use of ultra-small AuNPs, adapted from [137]. The AuNPs functionalized with the TFO are able to block the DNA transcription of selected pro-oncologic genes. 76
-
- Figure 3.1 PLD system installed in the *NanoLaserLab* of the Department of Physics of PUC-Rio, where it is possible to perform simultaneously PLA in both vacuum and liquid environment. 82
- Figure 3.2 a) Configuration used for PLA at one single frequency ω or 2ω ; b) Scheme showing the PLA by simultaneous irradiation of pulses at both ω and 2ω frequencies; c) Photo of the PLA set-up corresponding to the configuration represented in a); d) Photo highlighting the last upgrade of the PLA system, with the mechanical moving base of *Zaber* and a sealed glass container, used to perform PLA in controlled CO_2 partial pressure. 83
- Figure 3.3 a) Schematic diagram representing the effect of water on the laser focusing position. b) Scheme used for the calculus of the laser spot size and fluence F on the target. 85
- Figure 3.4. Dependence of F (a), and ϕT (b) on the lens/target distance d , for different heights of the water column over the target: $l_\beta = 0$ cm (black square), $l_\beta = 0.5$ cm (grey circle) and $l_\beta = 1.0$ cm (grey circle)). The values of F are relative to a pulse energy of 2mJ. 87
- Figure 3.5 PLA experimental set-up (PLA- S_1 and PLA- S_2) used for the determination of the energies (E_ω , $E_{2\omega}$) and fluence (F_ω , $F_{2\omega}$) associated to the ω and 2ω frequency laser pulses during the experiments. a) PLA system emitting simultaneously ω and 2ω pulses indicated as PLA- S_1 . DM($\omega, 2\omega$) represents a high power dichroic mirror, transmitting only laser pulses at one of the two frequencies (ω in this case), and reflecting the other one (2ω in this case). b) PLA system with a low divergence angle of the laser pulses, indicated as PLA- S_2 . M is a high power mirror. LT_1 and LT_2 represent the lens-to-target distances in the two experimental set-ups. In both cases, the PLA systems are used for the synthesis of gold nanoparticles in water enriched with NaOH 2 m mol/L, indicated as AuNPs. 91
- Figure 3.6 Dependence of a) TC, b) IC and TOC on the concentration of NaOH in the water solution. 94
- Figure 3.7 Appearance of the samples for SERS and Raman spectroscopy. Drops of MeNPs are deposited and dried on a gold thin film. 97

- Figure 3.8 Emission spectra of the CQDs (red line) overlapped with the extinction spectra of the Au (black line), Ag (grey line), and Fe (green line) derived nanomaterials. 102
- Figure 3.9. TEM image of the fresh Au derived nanomaterial (a,b), and the material after separation (c,d). 103
- Figure 3.10 Photo of a colloidal dispersion of Fe derived nanomaterial before and after the separation by magnetization. The NPs were synthesized by fundamental frequency (ω) laser pulses. 104
- Figure 3.11 Au derived nanomaterial synthesized in 0.06 and 2.0 mmol/L NaOH solution a) before heating, b) after evaporation induced by heating, and c) after filtering and centrifugation. 107
- Figure 3.12 Photos representing the grounding technique for the Au derived nanomaterial. a) Experimental set-up; b) Temporal evolution of the color of the Au derived nanomaterial during the grounding. 109
- Figure 3.13 Photo of the spectrofluorometer model QM1 of PTI (Canada) used for STPL in the Department of Physics of PUC-Rio. The opening of each slits was set at 4 nm, as indicated. The slits S_1 and S_2 are used to modulate the intensity of incoming excitation light, while S_3 and S_4 are the slits to control the intensity of emitting light. 110
- Figure 3.14. Reading system of the scanning magnetic microscope [322]. 112
- Figure 4.1 Temporal evolution of the UV-Vis extinction spectra of the Au derived nanomaterial synthesized at $F = 1.3 \text{ J/cm}^2$ and different values of C_{NaOH} , ranging from 0,02 mmol/L to 20,0 mmol/L. The figure highlighted, is relative to the condition of best stability, with almost no aggregation after more than 90 days. 115
- Figure 4.2 Photos showing the color aspect of the colloids of Au derived nanomaterials with passage of time, synthesized at different values of C_{NaOH} . 116
- Figure 4.3 Temporal evolution of the UV-Vis extinction spectra of the Au derived nanomaterial synthesized at $C_{\text{NaOH}} = 2,0 \text{ mmol/L}$ and different values of F . The smaller fluence of $F = 0.3 \text{ J/cm}^2$ correspond to the threshold PLA value for Au target [169]. 117
- Figure 4.4 Optical extinction value of the Au derived nanomaterial at λ_{LSPR} , synthesized in a time $t_{\text{PLA}} = 45 \text{ min}$ using different values of F . 117

- Figure 4.5) TEM images of the Au derived nanomaterial synthesized at $F = 1.3 \text{ J/cm}^2$ and in a) $C_{\text{NaOH}} = 0.02 \text{ mmol/L}$, c) $C_{\text{NaOH}} = 2.00 \text{ mmol/L}$ and e) $C_{\text{NaOH}} = 8.00 \text{ mmol/L}$. The electron acceleration voltage was 80 keV. The inset represents the experimental statistical size (radius) distribution. The UV-Vis extinction spectra of the corresponding colloidal dispersion are represented in (b), (d) and (f). The grey dotted lines represent the Mie fit obtained in the multipolar approximation using the experimental size distribution shown in (a), (c) and (e). 119
- Figure 4.6 the UV-Vis extinction spectra of the colloidal dispersion of Au derived nanomaterial synthesized at different values of C_{NaOH} (a) and F (b). In the figure are highlighted the optical extinction around 440 nm and the spectral blue-shift. 120
- Figure 4.7 Color aspect of the Au derived nanomaterial depending on the experimental conditions (C_{NaOH} , F), where the direction of the arrow corresponds to increasing values in C_{NaOH} or F . 120
- Figure 4.8 UV-Vis extinction spectra of the Au derived nanomaterial synthesized at the laser pulse frequencies ω and 2ω , in the same experimental condition ($F = 1.3 \text{ J/cm}^2$, $C_{\text{NaOH}} = 2.00 \text{ mmol/L}$). 121
- Figure 4.9. 2D color map representing the intensity of the agglomeration band at the wavelength of 800 nm observed in the experimental UV-Vis spectra of AuNPs pre-synthesized at the fundamental frequency ω . Both the sodium dodecyl sulfate (SDS) concentration (used as a surfactant and stabilizing agent), and the fluence of the pulses at the 2ω frequency, used to make a post-irradiation with 12,000 laser shots, have a clear effect on the optical and morphological properties of the final NPs. Adapted from [331]. 122
- Figure 4.10. Dependence of the central position of the LSPR band (λ_{LSPR}) on (a) TC_0 (i.e. C_{NaOH}), and the fluence F (b). 125
- Figure 4.11 SERS spectra of Au derived nanomaterial in powder synthesized at 2ω with different values of C_{NaOH} . As a comparison, we also report the SERS spectra of the samples obtained by the use of laser pulses at the frequency ω (blue curve), for $C_{\text{NaOH}} = 2.00 \text{ mmol/L}$. The excitation wavelength in the SERS measurements was 638 nm. 126
- Figure 4.12 (a,b) HRTEM of Au@Cy NPs synthesized at $C_{\text{NaOH}} = 0.06 \text{ mmol/L}$. (c) A few agglomerated NPs, synthesized at $C_{\text{NaOH}} = 2.00 \text{ mmol/L}$. The electron acceleration voltage was 80 keV. 128
- Figure 4.13 TEM images of the CQDs derived by CO_2/C with Au target, synthesized at $TC_0 = 3.5 \text{ ppm}$ (a), and 18.0 ppm (b). In the inset are shown the statistical size distribution of the nanomaterial and the corresponding EDX spectra. c,d) Sparse bigger carbon nanoparticles, both in circular and carbon-onion structure. The electron acceleration voltage was kept at 80 keV. 129

Figure 4.14 a) TEM and STEM (b,c) images of the Cy@AuNWs derived by CO₂/C with Au target, synthesized at TC₀ = 18.0 ppm and F = 1.3 J/cm². The inset in (c) shows the corresponding EDX spectra. (d) Statistical log-normal distribution of the longitudinal (L) and lateral (W) linear dimensions of the Cy@AuNWs. e) TEM image of Cy@AuNWs before the separation process, demonstrating the existence of carbynoid structures bigger than the filter pores. 131

Figure 4.15 (a)-(d) HRTEM images of the Cy@AuNWs derived by CO₂/C with Au target, synthesized at TC₀ = 18.0 ppm and F = 1.3 J/cm². The images were taken at an acceleration voltage of 80 kV. e) Bright-field (BF) TEM image of an isolated Cy@AuNWs and f) the corresponding SAED pattern. 132

Figure 4.16 a) HRTEM image of an Au@Cy NP taken at an acceleration voltage of 300 kV. There is no trace of sp hybridization in the carbon shell of the NCs. (b,c) Change of the interplanar distance along the c-axis of the Cy@AuNWs during the irradiation at the electron acceleration voltage of 200 kV. 133

Figure 4.17 Amorphous carbon NWs observed after performing the separation process with a filter of 0.4 μm. The acceleration voltage of 200 kV provoked the real time degradation of the carbon nanostructures. 134

Figure 4.18 FTIR (a) and C1s XPS (b) spectra of the dialyzed CQDs derived from Au target by CO₂/C. 135

Figure 4.19 Schematic representation of all the chemical groups detected on the surface of the carbon nanoparticle: (a) epoxide, (b) hydroxyl, (c) carbonyl, (d) carboxylic acid, (f) all the groups. 136

Figure 4.20 a) Extinction (orange continuous line), excitation (cyan dotted line), and photoluminescence emission spectra (black lines) of the CQDs derived from Au target, synthesized at different values of TC₀: 3.5 ppm (dotted), 18.0 ppm, and 25.3 ppm. b) PL spectra (normalized to the ablation time) of the Au derived CQDs synthesized by the laser pulse ω and 2ω laser pulses. c) Dependence of the PL spectra on the excitation wavelength. The PL spectra were excited at the wavelengths of 300 nm (black line), 315 nm (grey line), and 330 nm (light gray line). d) Dependence of the PL spectra on the value of F used during the PLA of the Au target by F = 60 J/cm² (gray line) and F = 2.6 J/cm² (black line), where the laser pulse spot size on target was constant. The dotted grey line represents the PL curve normalized to the ablation time. 137

Figure 4.21 a) Monitoring of the residual Au concentration by UV-Vis extinction spectroscopy. b) Effect on the PL of the residual gold concentration. 139

Figure 4.22 PL decay curves of CQDs derived from Au target by CO₂/C in water. a) Excitation at 304 nm. b) Excitation at 335 nm. 139

- Figure 4.23 PL decay curves of CQDs derived from Au target by CO₂/C in water. (a) Excitation at 304 nm at λ_{\max} . (b) Excitation at 335 nm at λ_{\max} . The fitting exponentials and the obtained parameters are reported. 140
- Figure 4.24 QY determination. Integrated PL area (at the FWHM) in function of the sample absorbance, for CQDs obtained from CO₂/C reduction by Au and Rhodamine. 142
- Figure 4.25 (a) ζ -potential and LSPR wavelength, (b) hydrodynamic diameter and polydispersity index (PI) of the Au@Cy/PF127 NCs in the function of the concentration of the copolymer. (c) UV-extinction spectra of Au@Cy/PF127 NCs in a 0.15 M NaCl water solution with different concentrations of PF127. (d) Extinction spectra of pellets and supernatant after centrifugation of the colloidal dispersion of NCs with copolymer at the reference concentration of 0.3 mg/ml. 144
- Figure 4.26 TEM image of the Au@Cy/PF127 NCs at the reference concentration of PF127. a) Before centrifugation. b) After centrifugation. 145
- Figure 4.27 a) Extinction spectra of the agg-NCs. The dashed line represents the central wavelength of the optical source used in photodynamic activity measurements. The inset is the HRTEM image of a single agg-NC. b) HRTEM image of the agg-NCs. 146
- Figure 4.28 Absorbance decay of DPBF (A_0-A) at 418 nm normalized to [Ce6] as a function of time. The concentration of the NCs both in the normal (NC) and agglomerated state (agg-NC) was about 25 ppm. The concentration of Ce6 was about 1 $\mu\text{mol/L}$. 147
- Figure 4.29- a) Viability histograms relative to the cellular uptake of the Au derived nanomaterial by cheratinocytes (NCTC), human metastatic melanoma (A375-M6), dermal microvascular endothelial (HMVEC), Endothelial progenitor cells (ECFCs). b) Optical images representing the uptake of the Au derived nanomaterial by A375-M6 melanoma cells after 24 hours (bottom panel). The concentration of gold was 10 $\mu\text{g/ml}$. 148
- Figure 4.30 Images acquired with optical microscope for Endothelial cell (ECs) loaded with the Au derived material at different metal concentrations (5 ppm, 10 ppm). The internalized metal loads into the ECs are identifiable as the dark areas inside the cells. 149
- Figure 4.31 TEM images of the ECs loaded with the Au derived nanomaterial at different metal concentrations (5 ppm, 10 ppm). 149
- Figure 4.32 Optical images of the ECs after 24 hours of treatment by the Au derived nanomaterial. The first image on the left, represents the vehicle (control). In the down-series, the histograms with the number of nodes, meshes and master junction for all the cases. 150

- Figure 4.33 Images of matrigel plug removed from nude mice after 5 days. Without the nanomaterial (center image), with the Au derived nanomaterial (right image). 151
- Figure 4.34 PL emission spectra of Au derived CQDs after dialysis in different concentration of MeHg. The inset represents the linear change in the wavelength ($\Delta\lambda$) corresponding to the maximum PL emission, depending on the concentration of MeHg. 153
- Figure 4.35 Schematic diagram representing the different 'phase' regions present in the PLA environment, together with all the materials synthesized during CO₂/C reduction by the use of Au target. M =Metal; L=Liquid; G=Gas. The reaction takes place in the interface between the plasma plume and the liquid environment. 156
- Figure 5.1 Temporal evolution of the UV-Vis extinction spectra of the Ag derived nanomaterial synthesized at $F = 1.3 \text{ J/cm}^2$ and different values of C_{NaOH} , ranging from 0,02 mmol/L to 2,0 mmol/L.. The inset in each figure represents the corresponding normalized extinction spectra. 158
- Figure 5.2 TEM images of Ag derived nanomaterials synthesized in a) 0.02 mmol/L and b) 2.00 mmol/L, c) 8.00 mmol/L. The inset in each figure shows their corresponding statistical size distribution with Lognormal fit, average size $\langle r \rangle$, and standard deviation. 160
- Figure 5.3 Normalized extinction spectra of Ag derived nanomaterials synthesized in $C_{\text{NaOH}} = 0.02 \text{ mmol/L}$ (black line) and $C_{\text{NaOH}} = 2.0 \text{ mmol/L}$ (gray line). The grey dotted line represents the Mie fit obtained in the dipolar approximation using the lognormal fit of experimental size distribution shown in Figure 5.3 (b). 162
- Figure 5.4 SERS response of nanomaterials in solid form synthesized by PLA of Au (black curve) and Ag (grey curve) targets with $C_{\text{NaOH}} = 2.00 \text{ mmol/L}$. The excitation wavelength was 638 nm. 163
- Figure 5.5 a)-b) HRTEM images of the nanomaterial derived from Ag target after the separation procedure. In b), the inset represents the EDS spectra confirming the presence of silver. c) UV-Vis spectra of the Ag derived nanomaterial after the separation process, confirming the presence of a significant concentration of the metal. 164
- Figure 5.6 a) TEM image of small spherical CQDs obtained by CO₂/C process from Ag target. The inset shows the LogNormal fit of the statistical distribution with standard deviation $\langle \delta \rangle$ and average radius $\langle r \rangle$. b) Carbon onion nanoparticles. 165
- Figure 5.7 a,b) HRTEM image of the rare Cy@Ag NCs. The inset shows the corresponding EDX spectra, together with the FFT pattern. 166

- Figure 5.8 Comparison of the PL spectra of CQD obtained by CO₂/C reduction with Ag (grey curve) and Au (black curve) targets. TC₀ was 18 ppm for both the samples. The PL intensity of the CQDs/Ag has been multiplied by a factor 3. 167
- Figure 5.9 Schematic diagram representing the different 'phase' regions present in the PLA environment, together with all the materials synthesized during CO₂/C reduction by the use of Ag target. 169
- Figure 6.1 a-d) Different steps of the separation process used to identify and isolate the different species in the sample. e) The different species present in the Fe derived nanomaterial. An interrogation point has been placed aside the symbol of the molecular organic material since its presence has still to be detected. 172
- Figure 6.2 Photos of Fe derived nanomaterial synthesized by laser pulses with both ω and 2ω frequency, at $F_{\omega + 2\omega} = 0.9 \text{ J/cm}^2$ (left side), and $F_{\omega + 2\omega} = 3.2 \text{ J/cm}^2$ (right side). (a,b) Fresh nanomaterial. (c,d) After 4 days of magnetization. 174
- Figure 6.3 Temporal evolution of the UV-Vis extinction spectra of the Fe derived nanomaterial synthesized at $F_{\omega + 2\omega} = 0.9 \text{ J/cm}^2$. a) Fresh nanomaterial; b) (FeNPs)^{pr} obtained after 4 days of magnetization. 174
- Figure 6.4 UV-Vis extinction of (FeNP)^{pr}, (FeNP)^{sp}, and transparent CNM obtained by PLA with laser fluence $F_{\omega + 2\omega} = 3.2 \text{ J/cm}^2$. 175
- Figure 6.5 ζ -potential of the CNM obtained after separation (negative), and of the fresh and 4 days aged Fe derived nanomaterial before separation (positive). The colors dark and light grey are used for the representation of samples synthesized at $F_{\omega, 2\omega} = 3.2 \text{ J/cm}^2$ and $F_{\omega, 2\omega} = 0.9 \text{ J/cm}^2$, respectively. 176
- Figure 6.6 TEM images of the (FeNPs)^{pr} synthesized by a) $F_{\omega + 2\omega} = 0.9 \text{ J/cm}^2$ and b) $F_{\omega + 2\omega} = 3.2 \text{ J/cm}^2$. c) TEM image of (FeNPs)^{sp} synthesized by $F_{\omega + 2\omega} = 3.2 \text{ J/cm}^2$. The inset in each figure shows the statistical size distribution with LogNormal fit, and the average diameter (ϕ) and standard deviation (σ). 177
- Figure 6.7 Magnetization curves of (FeNPs)^{pr} synthesized at different laser fluence by simultaneous irradiation with ω and 2ω frequency laser pulses. 178
- Figure 6.8 Extinction spectra of Fe derived nanomaterial synthesized by pulses with a single frequency (ω or 2ω), and pulses with both frequencies ($\omega + 2\omega$). The total ablation time was 120 minutes. 179
- Figure 6.9 Photos of the Fe derived nanomaterial before and after the magnetization along 4 days. A comparison has been made considering the synthesis using single frequency (ω or 2ω) or dual frequency (ω and 2ω) laser pulses. (a,d) $F_{\omega + 2\omega} = 3.2 \text{ J/cm}^2$; (b,e) $F_{\omega} = 2.3 \text{ J/cm}^2$; (c,f) $F_{2\omega} = 2.3 \text{ J/cm}^2$. 180

Figure 6.10 TEM images of the of : a) (FeNPs)^{pr} synthesized by $F_{\omega} = 2.3 \text{ J/cm}^2$; b) (FeNPs)^{pr} synthesized by $F_{2\omega} = 3.2 \text{ J/cm}^2$; c) (FeNPs)^{sp} synthesized by $F_{\omega} = 3.2 \text{ J/cm}^2$. The inset in each figure shows the statistical size distribution with LogNormal fit, the average diameter (ϕ) and standard deviation (σ). 182

Figure 6.11 Typical Raman spectra of the colloidal dispersion of Fe derived nanomaterial a) before separation; b) after separation, on the corresponding (FeNPs)^{pr} and (FeNPs)^{sp}. The measurements of the panel a) are relative to three different regions of the samples, indicated as I, II, and III. 183

Figure 6.12 Raman spectra of (FeNPs)^{pr} synthesized by $F_{\omega + 2\omega} = 0.9 \text{ J/cm}^2$, and excited by a laser irradiance of 10^{-2} kW/mm^2 (blue line), 10^{-1} kW/mm^2 (red line) and 1 kW/mm^2 (green line). The right side photos, show the measurement regions before and after the irradiation. The Raman spectra were excited at the wavelength of 638 nm. 185

Figure 6.13 a) FTIR spectra of fresh Fe derived nanomaterial, (FeNPs)^{sp}, and CNM synthesized by 2ω laser pulses. b) Comparison between the FTIR spectra of the CQDs/Au (gray) and the CNM obtained by PLA of iron (black). 186

Figure 6.14 XPS survey spectra of (FeNPs)^{pr} and (FeNPs)^{sp} synthesized by dual frequency laser pulses ($\omega + 2\omega$). 187

Figure 6.15 XPS spectrum in the a) Fe2p and b) O1s regions of both (FeNPs)^{pr} and (FeNPs)^{sp} synthesized by dual frequency laser pulses ($\omega + 2\omega$). 187

Figure 6.16 a) PL, excitation (black curves) and extinction (orange curve) spectra of the CQDs/Fe in the UV region. The CQDs were synthesized at $F_{\omega, 2\omega} = 3.2 \text{ J/cm}^2$, and separated by magnetization. PL and excitation spectra of the CQDs/Fe, synthesized at laser pulse frequency ω b) or 2ω c), and separated by heating. 189

Figure 6.17 Schematic diagram representing the different 'phase' regions present in the PLA environment, together with all the materials synthesized during CO_2/C reduction by the use of Fe target. An interrogation point has been placed aside the symbol of the molecular organic material since its presence has still to be detected. 192

Figure 7.1 Details of the SERS spectra of the Au and Ag derived nanomaterial in powder form. All the Raman modes indicated in the figure are common to both the spectra. The measurements have been performed at the excitation wavelength of 638 nm, in low irradiation conditions (10^{-2} kW/mm^2). 195

Figure 7.2 Radical polymerization mechanism of formic acid on the noble metal nanoparticle surface forming metal-carbynoid complexes. 197

Figure 7.3 HRTEM images showing multiple oxidations states in the Au (a) and Ag (b) derived samples. The dotted orange lines are only used to help the interpretation of the figure. The interplanar distances of 0.19 nm and 0.14 nm observed in (a), are relative to the planes (620) and (220) of Au₂O₃ and Au, respectively[408–410]. In (b) are observed the interplanar distances of 0.20 nm, 0.24 nm, 0.27 nm and 0.29 nm, associated to the planes (200) and (111) of Ag [81, 411], (100) of Ag₂O [412], and (110) of AgO [81].

199

Figure 7.4 Scheme of the simultaneous physical-chemical processes involved in the CO₂/C reduction by PLA of TMe targets. a) One-step OWS. b) One-step CO₂RR. c) Two-step CO₂RR.

200

Figure 7.5 a) UV-Vis extinction spectra of the Au derived nanomaterial synthesized at C_{NaOH} = 2.00 mM, and different relative velocity (0 μm/s, 300 μm/s, 3000 μ/s) between the Au target and the spot of the laser pulse. b) PL of the Au derived CQDs, depending on the relative velocity (0 μm/s, 300 μm/s) between the Au target and the spot of the laser pulses during the PLA process.

202

Figure 8.1 Diagram representing the main scientific areas where the discovery of the PLA induced CO₂/C reduction by metal-oxide semiconductors may open unexpected perspectives

216

List of Tables

Table 2.1 Atomic number, electronic configuration, and most common oxidation states of Au, Ag, and Fe.	16
Table 2.2 Oxidation states of NPs synthesized by PLA of Au, Ag, and Fe targets in the water.	17
Table 2.3 Value of the bandgap in different types of iron-based oxides, as measured by Giannakis, Stefanos. <i>et. al.</i> [109].	21
Table 3.1 Concentration of NaOH in the aqueous NaOH mother solution used in the present investigation to prepare the final PLA environment; Volume (V_{NaOH}) of stock solution added to 50 ml of UPD water; Experimental and theoretical pH.	80
Table 3.2 Size φ_T and fluence F of the laser pulse for l_β of, 0.0 cm, 0.5 cm, and 1.1 cm, considering different values of the lens/target distance d . The values of F are relative to a pulse energy of 2mJ.	87
Table 3.3 Energy per pulse and fluence, and ablation time used for the PLA of the different transition metal target in water.	88
Table 3.4 Examples of organic and inorganic compounds [314, 315].	93
Table 3.5 Preparation technique and TEM grids used for the different samples analyzed in the present research.	101
Table 3.6 ICP-MS measurement before and after separation with magnet	104
Table 3.7 Concentration of gold and mercury before and after the separation by amalgamation, as measured by IC-PMS.	104
Table 3.8 Gold concentration before and after the separation by dialysis and centrifugation.	105
Table 3.9 ICP-MS measurement of the Au derived nanomaterial before and after precipitation by salt.	106
Table 3.10 TC of Au derived CQDs after different number of dialysis processes.	106
Table 3.11 Metal Au concentration before and after separation.	107
Table 3.12 ICP-MS measurements on Au derived nanomaterial before and after separation by grounding.	108

Table 4.1 Complete analytical characterization of the samples synthesized at	124
Table 4.2 Concentration of gold (C_{Au}) in the solution after separation of CQDS from Au-derived nanomaterial	138
Table 4.3 Decay parameters as a function of the emission wavelength for the best fit (i.e. the double exponential).	141
Table 5.1. Complete analytical characterization of the Ag derived nanomaterial synthesized at $F = 1.3 \text{ J/cm}^2$, for different values of C_{NaOH} .	161
Table 6.1 Complete analytical characterization of the different species present in the Fe derived nanomaterial, synthesized at $F_{\omega+2\omega} = 0.9 \text{ J/cm}^2$ and $F_{\omega+2\omega} = 3.2 \text{ J/cm}^2$. The iron concentration of the sample in ppm is indicated as C_{Fe} .	178
Table 7.1 Vibrational assignment of the molecular vibrations detected in the SERS spectra of Au and Ag based nanomaterial in powder form. The references for the frequency of the Raman modes on AgNPs are taken from [397]. The symbols used for the assignment of the Raman mode are: ν_s (symmetric stretching), ν_{as} (antisymmetric stretching), ω (wagging), and ρ (rocking).	196

List of Abbreviations

Ag	Silver
AgNPs	Ag nanoparticles
Au	gold
Au@cy NPs	Au@carbynoid nanoparticles
BLA	bond length alternation
CAWs	Carbon atomic wires
CB	conduction band
Ce6	Chlorin e6
CFNDs	carbon-based florescent nanodots
C _{NaOH}	NaOH concentration
CNM	carbon nanomaterial
CQDs	carbon quantum dots
Cy@Au NWs	carbynoid nanowires decorated by Au
CyAg NC	carbynoid nanocrystal stabilized by Ag
DOG	drop on the grid
E _{PLA}	Laser energy per pulse
EDS	Energy Dispersed X-ray Spectroscopy
F	the fluence of the pulse of laser
Fe	Iron
(FeNPr) ^{pr}	Precipitator iron oxide NPs after 4 days with magnet
(FeNPr) ^{sp}	Supernatant iron oxide NPs after 4 days with magnet
Fe ₂ O ₃ NPs	hematite nanoparticle
Fe ₃ O ₄ NPs	magnetite nanoparticles
FWHM	full-width half maxima
GQDs	Graphene Quantum Dots
GOD	the grid on the drop
HPLC	High-Performance Liquid Chromatography
HRTEM	High-Resolution TEM
IC	Inorganic carbon
ICP-MS	Inductively Coupled Plasma Mass Spectroscopy
IEC	Ion chromatography (or ion-exchange chromatography)
L	Lens
l _β	height of water above the target
LSPR	localized surface Plasmon resonance
MeNPs	metal nanoparticles
NCs	nanocomposite
NPs	nanoparticles
PF27	Pluronic F27
PL	photoluminescence
PLA	Pulse laser ablation
QY	quantum yield
R	reflector
SQD	semiconductor quantum dots
STEM	scanning transmission electron microscopy
T	target
t _{PLA}	laser irradiation time

TC	total carbon
TIC	total inorganic carbon
TOC	total organic carbon
UPD	ultra-pure deionized
UNFCCC	united nations framework convention on climate change
VB	valance band
ω	first harmonic laser
2ω	second harmonic laser
λ_{LSPR}	localized surface plasmon resonance wavelength
λ_{PLA}	laser pulse wavelength
φ_T	diameter of the laser spot on target
ϕ	diameter of nanoparticle

*“Education is the most powerful weapon which you
can use to change the world”*

Nelson Mandela

1 Introduction

1.1. The state of art and achieved advances

Pulse laser ablation (PLA) in liquids has been used for the production of nanoparticle (NPs) colloids, and PLA at the solid and liquid interface was first reported in 1987 by Patel *et. al.*, where they generated a metastable form of iron oxide from pure iron target [1]. Later on, the synthesis of colloidal dispersions of gold nanoparticles (AuNPs) via PLA in water was first reported in 2001 [2]. These characteristics depend on different parameters associated with the laser pulse, such as fluence, wavelength, ablated target material, the used solvent, and dissolved solutes in solution [3–6]. The aforementioned parameters guide the characteristics of the ablation product by a wide variety of metals and oxides, and it is quite common to introduce surfactant in solution and or stabilizing agents that promote the stability of colloidal solutions over time [2, 7, 8]. Studies on the control of the physical and chemical properties of NPs obtained without ligands in water, or water containing simple salts and/or hydroxides, are rare, for example in the case of silver (Ag) and gold [9–11]. For most of the metals studied during the research (Au, Ag, Fe), the stability of the relative colloidal product in water is dictated by the level of oxidation of the metallic nuclei and, in the case of gold, also by an excess of free localized electrons adsorbed in the metal core, produced in the plasma plume along the PLA process [5].

From the conceptual point of view, the PLA in the liquid is considered by some authors as a green synthesis technique [6, 12, 13], compatible with at least 6 of the 12 rules of green chemistry [6, 8] (i.e Atom Economy, Less Hazardous Chemical Synthesis, Designing Safer Chemicals, Safer Solvents, and Auxiliaries, Reduced Derivatives, Inherently safer chemistry for an accident). In PLA in liquid, the atoms of a small number of reagents introduced into the ablation environment (target, solvent, solutes) combine in the form of suspended nanostructures in

solution [8, 12]. The technique is essentially considered hybrid: a blend of a top-down approach, which makes available atoms, clusters, and fragments of the ablation target material, and bottom-up, where these units come together in the form of nanoparticles [12]. In the process, solvent molecules must also be considered, which can undergo chemical reactions at high temperature, and in some circumstances contribute to the synthesis of organic material in solution [6, 14–16], or the creation of a shell of dielectric material around the metallic nanoparticle [16]. Anyway, in each case, the elemental composition of the core of the NP is always the mirror of the elemental composition of the solid target that was ablated during the PLA process [16–18].

The main result of the present thesis is related to the discovery of different types of organic material synthesized during the PLA process of transition metal targets in deionized water. These organic materials exist either in molecular form or in the form of carbon nanostructured materials colloids, and introducing a new paradigm in the process of PLA of metal in liquid: the realization of a nano synthesis by reduction of the gaseous species dissolved in the liquid environment.

All the transition metals ablated during the thesis (Au, Ag, Fe) showed the formation of molecular organic material and luminescent CQDs [19], with sp^2 hybridization. Noble metal targets allow the formation of different structures with unique properties. In this case, the formation of spherical gold nanoparticles encapsulated by a shell of carbynoid material with mixed $sp-sp^2$ hybridization (Au@Cy NPs) [20], and nanowires of carbynoid material supported by gold nanoparticles (Cy@Au NWs) are observed [19]. Also in the case of silver is possible to observe the formation of carbynoid nanocrystals with irregular shape supported by AgNPs (Cy@AgNCs).

While in the case of all metal (Au, Ag, Fe, etc) target the presence of luminescence CQDs is detected only by increasing the CO_2 content in the water environment by the addition of NaOH, for Fe targets, the synthesis of carbon-based material is detected also in the ultra-pure deionized (UPD) water. The latter observation put in evidence the central role of the facility to oxidize the metal target in the production rate of the organic material and CQDs during PLA.

Nevertheless, metal-oxides and semiconductor surfaces are well known to act as electrochemical interface devices and are often used as functional materials for the production of sustainable bioenergy with carbon capture and storage (BECCS) [21]. Among the BECCS, the electrochemical reduction of CO₂ to gases or fuels is mostly demonstrated by the use of electrochemical ($E = e\Delta V$) cells in low potential regimes, although also thermochemical ($E = kT$) [22–24] and photochemical cells ($E = h\nu$) [25–31] have been demonstrated by the use of different nanostructured interfaces. The activation energy for those redox processes is in a few orders of eV, which can be furnished during PLA by both optical path (via direct incoming laser pulse) or thermal paths. In fact, the redox processes involving water dissociation and production of hydrogen and oxygen reactive species during PLA of metal targets in water, have been recently demonstrated by the group of Prof. Stephan Barcikowski at the Faculty of Chemistry of the University of Duisburg-Essen (Germany) [32, 33].

The reduction of CO₂ to solid carbon (CO₂/C) is now considered the most precious route for permanent storage solution [34]. In fact, reduction of CO₂ to volatile species, although considered value-added chemicals useful for energy-related industrial processes, is not a definite route, since unwanted release in the environment still represents a negative issue from the ecological point of view. Room temperature reduction of CO₂ to solid carbonaceous species has been recently demonstrated by Esrafilzadeh [35] by the use of liquid metal electrodes containing Ce⁽⁰⁾ and Ce⁽³⁺⁾ interfaces, with an activation potential as low as ~ 0.3 V Vs CO₂/C. Although depending on the applied potential, the electro-catalytic process involved in the unique CO₂/C conversion process is described by a chemical loop (CL) in which cerium is continuously oxidized and further reduced to metallic species, in a process involving both electrons and OH⁻ species.

The PLA of transition metal target performed in this research revealed to be a suitable framework in which a similar process might be accompanied with the parallel formation of MeNPs colloidal dispersion. The general behavior of the observed CO₂/C reduction, which is not dependent on the nature of the ablated metal target (Au, Ag, Fe), let us suppose that common property and phenomena might be responsible for the chemical reduction. As detailed in the *Conclusion* section, both redox processes involving different oxides of the transition metals, or

their semiconductor behavior with an optically excitable *energy band-gap*, may be considered responsible for the formation of the carbonaceous material.

Here we have to point out that, in our case, for the first time that CO₂ is not converted to ordinary carbonaceous material, but functional carbon nanomaterial with unique and outstanding photo-luminescent properties, such as low full width half maximum (FWHM) emission band, and the highest quantum yield (QY) (~50%) reported until now for CQDs synthesized by one-step PLA process, that was limited to values between 1% and 12 % in the literature [36, 37]. Moreover, parallel catalytic processes to CO₂/C conversion leads to the synthesis of unique metal-carbon based nanocomposites being, instead of an unwanted process, an opportunity for the control of their physical and optical properties.

In fact, as a valuable point, we also noticed that the control on the synthesis of carbon-based material is accompanied by the parallel control on the size of the metal NPs produced from the target, principally in the case of Au and Fe targets. This is particularly interesting in the case of ultra-small NPs ($R_{NP} < 2.5$ nm), which can act as a nano-biological machine, due to their capacity to enter in the nucleus of human cells and provoke inhibition or enhancement in the expression of different genes [38]. This was the case for the ultra-small Au@Cy NPs synthesized along with our research, which revealed to have the unique and outstanding property to enhance (both *in vitro* and *in vivo* studies) the angiogenic process (angiogenesis is the biological process involved in the formation of new blood vessels) of human endothelial cells, with huge potential in applications such as blood vessels recovery or alternative therapies for visceral obesity in metabolic syndrome associated with type 2 diabetes [38].

1.2. Objectives

The main objective of this dissertation is the understanding of the chemical-physical process observed in 2016 in the *NanoLaserLab* of the Department of Physics of PUC Rio during the PLA process of a gold target in water containing different hydroxides [39]. After drying the as-synthesized material, a sharp peak near 2120 cm⁻¹ was observed in the SERS spectra of the dried AuNPs colloid and

attributed to the presence of gold-carbonyl and other oxocarbons linked to the gold core of the NPs [39, 40].

The spectral coincidence between the Raman vibrations of gold-carbonyl (Au-CO) [39] and carbon atomic wires (CAWs) [41], both centered around 2120 cm^{-1} , was the trigger and the motivation of the investigations led during my Ph.D. research. In fact, as explained in details in Section 4, using particular experimental condition in both the PLA synthesis and physical characterization of the nanomaterials, it was possible to detect the presence of both CO adsorbed on the nanoparticles (Surface Enhanced Raman spectroscopy), and of sp-sp² hybridized carbonyl nanowires supported by AuNPs (High-Resolution Transmission electron Microscopy) [41]. This represents clear evidence that different catalytic reactions involving CO₂ happen during PLA of specific transition metal targets, from the “classical” reduction to CO to the intriguing reduction to solid carbon species.

Therefore, the main objective of this thesis is the deep investigation of the physical-chemical process responsible for the synthesis of the different organic materials generated during PLA of transition metal targets in UPD water. This high challenging objective is accompanied by peripheral objectives (or sub-objectives), some of which are related to the use of all the transition metals, and others relative to the particular transition metal used during PLA.

A common peripheral objective is to understand the effect that experimental (laser pulse fluence F_{PLA} , laser pulse wavelength λ_{PLA} , irradiation time t_{PLA}) and sample (transition metal target, the concentration of NaOH in the water solution C_{NaOH}) parameters have on the stability and dimensions of the relative colloidal dispersion of nanoparticles.

A second common objective is the use of all transition metals, is the study of the efficiency in the production and separation of the luminescent carbon nanomaterials, and their spectroscopic (composition, quantum yield (QY)) [42] and morphological (size, shape) characterization [43].

The last peripheral objective is the use of the Au@CyNCs and QCDs in applications related to health and environment control, such as the amplification of photodynamic activity of photosensitizers [20], gene therapy in human cells [44, 45], and chemical sensing of toxic metal ions in water [46].

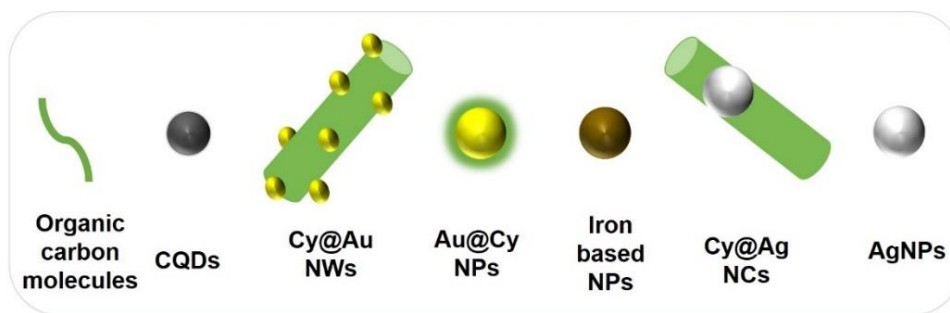


Figure 1.1 Icons used for representation of synthesized nano materials throughout the dissertation.

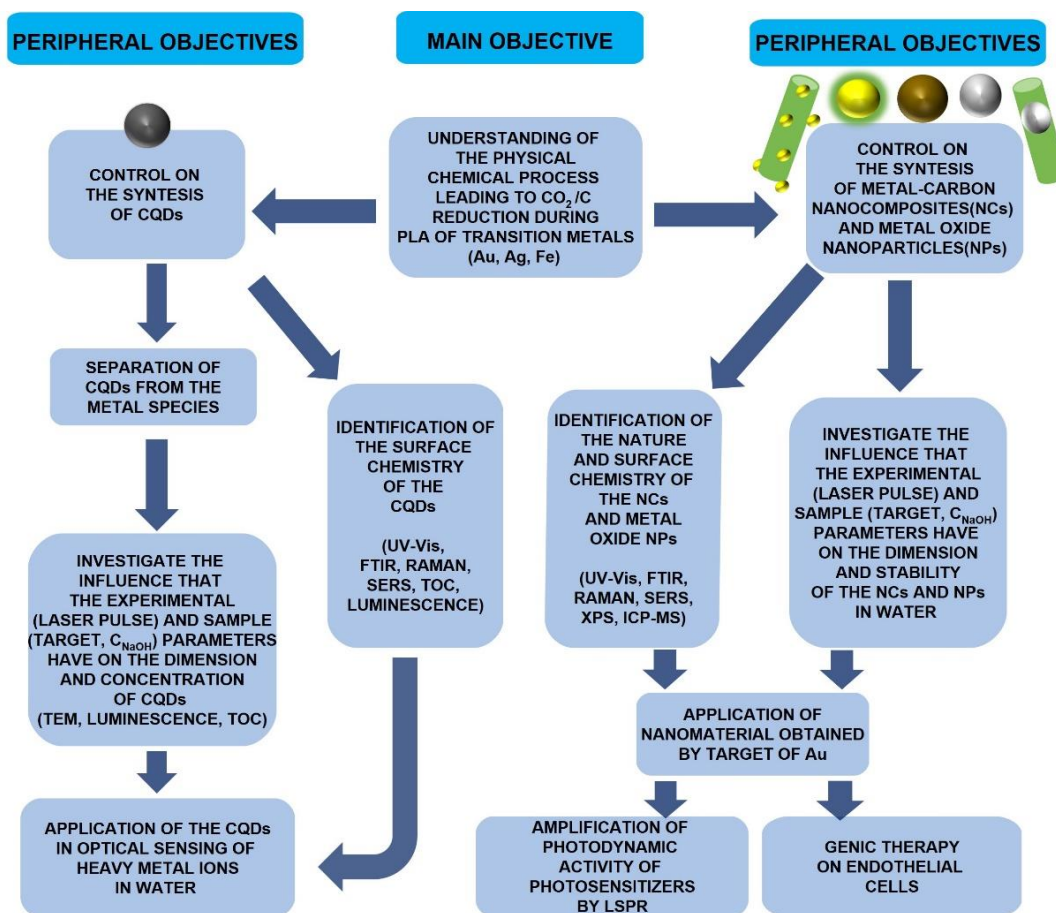


Figure 1.2 Schematic diagram of the main and peripheral objectives of the research as described in the lines above.

In Figure 1.1 we show the icons chosen to represent along with the dissertation the different synthesized organic and inorganic materials, namely organic molecules, carbon quantum dots (CQDs), carbon nanowires decorated

by AuNPs (Cy@Au NWs), carbynoid encapsulated gold nanoparticles (Au@Cy NPs), iron-based NPs and AgNPs colloids.

1.3. Infrastructure and contributions

The presented research is highly interdisciplinary and made use of multiple experimental techniques, involving the collaboration among the scientists active in different research areas such as physics, chemistry, and biology. Although most of the experimental research has been developed in the Department of Physics and Chemistry of the Pontifical Catholic University of Rio de Janeiro, are different the collaboration established along the past 4 years with both national and international scientific partners, which were fundamentals for the effective completion of the thesis.

The principal activity, consisting in the synthesis of functional NPs by PLA process, has been developed in the *NanoLaserLab* of the Department of Physics of PUC-Rio, under the responsibility of Prof. Tommaso Del Rosso, although the simultaneous irradiation by multiple wavelength pulses has been performed in the Laboratorio de Optoelectronica Organica e Molecular (LOEM) of the same Department. UV-Vis, Fourier Transform Infrared (FTIR) spectroscopy, and photoluminescence (PL) spectroscopy have been performed in the *Optical Spectroscopy Multiuser Laboratory* of the same Department, while chemical analytics techniques such as inductively coupled plasma mass spectrometry (ICP-MS), total carbon (TC), and PL based optical sensing measurements have been performed in collaboration with Prof. Ricardo Queiroz Aucelio, from the *Department of Chemistry of PUC-Rio*. The QY of the CQDs has been evaluated in the *Laboratory of Fluorescence of the Department of Informatics of the University of Verona (Italy)*, by the group of Prof. Nicola Daldosso.

Fundamental tools in the presented research, Raman and surface-enhanced Raman spectroscopies (SERS), have been performed both in the *Analytical Central of the Department of Chemistry of PUC-Rio* and by international collaborators, such as the Prof. Gino Mariotto of the *Department of Informatics of the University of*

Verona (Italy), and Prof. Carlo Spartaco Casari, responsible of the *NanoLab in the Department of Energetic of the Polytechnic University of Milano (Italy)*.

Of fundamental importance for the interpretation of the results of the PLA synthesis process, has been the use of Electron Transmission Microscopy (TEM). The latter has been performed in both low- and high-resolution modes in different *Brazilian and international research centers*. Specifically, in Brazil, we used our collaboration with Prof. André Rossi and Dr. Yordy Licea Fonseca of the *Brazilian Center of Research in Physics of Rio de Janeiro (CBPF)*, Dr.ssa Sandra Landi, Prof. Geronimo Perez and Dr. Braulio S Archanjo from the *National Institute of Metrology, Standardization and Industrial Quality of Rio de Janeiro (INMETRO)*, and Prof. Francis Leonard Deepak, from the *International Iberian Nanotechnology Laboratory (INL, Braga, Portugal)*.

The potential application of the Au@Cy NPs in the amplification of the angiogenesis process in human endothelial cells and mice has been performed with the Italian permission of the ethical committee at the *Department of Biomedical, Experimental, and Clinical Sciences of the University of the Studies of Florence (Italy)*, under the supervision of Prof.ssa Gabriella Fibbi and Dr.ssa Anna Laurenzana.

The discussion on the origin of the reduction of CO₂ to solid carbon has been developed in collaboration with the group of Prof. Walter Azevedo, from the *Department of Fundamental Chemistry of the Federal University of Pernambuco (UFPE, Recife, Brazil)*.

1.4. Thesis organization

In Chapter 2 we report a brief and comprehensive theoretical background useful for the interpretation of the different experimental results of the thesis, and the technological context in which they represent an added value contribution.

Indeed, we start the second chapter (Section 2.1) introducing the concept of negative emission technologies (NET), and how nanomaterials represent nowadays a key element for the production of sustainable bioenergy with carbon capture and

storage (BECCS) [47]. We concentrate our attention on the description of the possible metal oxides of the transition metals used in the research, and a brief survey on their use in electro/photocatalytic reduction of CO₂.

The brief technological introduction is followed by fundamentals on the synthesis of NPs by PLA in liquid (Section 2.2.1), and the description of the forces driving their stability as colloidal suspension (Section 2.2.2). This is followed by the description of metal nanoparticles (AuNPs, AgNPs), concentrating on the concept of the Localized Surface Plasmon Resonance (LSPR) [48, 49], the theory of Mie [50], and the theoretical approach used to calculate both NPs and metal concentration (Section 2.2.3). The effect of the size and composition of noble MeNPs on the optical extinction spectra will be discussed in section 2.2.4.

Since the chemical nature of the synthesized material has been determined primarily by spectroscopic techniques, the Sections 2.3.1, 2.3.2, and 2.3.3 are dedicated to the introduction to IR, Raman, and SERS spectroscopy with MeNPs respectively.

Section 2.4 is dedicated to carbon nanomaterial. We introduce the concept of *sp*, *sp*², and *sp*³ hybridization in carbon materials, where particular attention is given to the definition of carbon atomic wires (CAWs) [41], carbynoid material [51], and carbon quantum dots (CQDs). The section ends with a description of the Raman collective modes in carbon nanomaterials, with a definition of the *D* and *G* band of *sp*² structures [52, 53], and of the BLA mode of the *sp* hybridized CAWs [41].

Section 2.4.3 is dedicated to the theory of carbon quantum dots (CQDs), describing their particular luminescent behavior, and the significance of their characteristic parameters such as full width half maximum (FWHM) and QYs [37].

In the last theoretical sections 2.5.1 and 2.5.2 we finally describe the basic concepts of photodynamic activity of photosensitizers and genic therapy in cells, respectively.

Chapter 3 This chapter is dedicated to the description of the material, instrumentation, and experimental methods used in the thesis. We start by describing the materials we used in our experimental work and the process of cleaning used for the targets and vessels (Section 3.1). In Section 3.2 we describe the different experimental set-up and laser sources used to perform PLA in liquid, together with the optical model used to determine the pulse laser fluence *F*. We

continue describing in Section 3.3 all the instruments dedicated to the analytical characterization of the synthesized organic material, namely: UV-Vis spectroscopy, inductively coupled plasma mass spectrometry (ICP-MS), high-performance liquid chromatography (HPLC) and total carbon (TOC), dynamic light scattering (DLS) and Z-potential. Section 3.4 is described as the equipment used to study the chemical composition and nature of the samples, such as FTIR, Raman, SERS, and X-ray photoelectron spectroscopy (XPS). Section 3.5 is dedicated to the imaging of the nanomaterial using Transmission Electron Microscopy (TEM) in different configurations, such as high resolution (HRTEM) and scanning (STEM) modes, together with the study of the elemental composition by energy dispersive x-ray analysis (EDX). We will describe in detail in Section 3.6 about the multiple separation techniques used for the separation of the carbon nanomaterial from the metal species. Section 3.7 is finally dedicated to the description of steady-state and time-resolved fluorimeters, and the methods used to measure the QY of the CQDs.

It is worth noting that in each section related to the different experimental techniques, we will also describe the methods used for the preparation of the samples to be analyzed.

Chapters 4, 5, and 6 report the experimental results obtained during the PLA of Ag, Au, and Fe targets, respectively.

All the chapters start with the description of the influence that the laser pulse parameters F_{PLA} and λ_{PLA} , and the NaOH concentration c_{NaOH} , have on the stability (UV-Vis spectroscopy) and dimensions (TEM analysis) of the relative colloidal dispersion of nanoparticles. We follow with the FTIR, Raman, SERS (when applicable), and XPS (when applicable) spectra of the as-synthesized nanomaterials (before separation), in order to determinate their chemical composition and the surface functional groups. The surface characterization has been extended to the species obtained after separation, of which CQDs are common products, obtained from PLA of all the transition metal targets. We show the TEM (including HRTEM and STEM) images of the CQDs obtained from the different materials with their corresponding EDX spectra, and evaluate their luminescence properties.

Chapter 4, relative to Au targets, deserves particular attention. In fact, here in we also show the TEM (including HRTEM and STEM) images of the Cy@Au

NWs, for which we report for the first time, to the best of our knowledge, a statistical distribution of sizes. For the case of CQDs obtained from Au, we also include the investigation of their QY, and the spectral dependent lifetime, obtained by time-resolved luminescence spectroscopy. We conclude the fifth chapter showing three main applications in which we tested the synthesized nanomaterial:

- the use of CQDs as sensors for different heavy metal ions in water (Cd^{2+} , Pb^{2+} , Hg^{2+} , CH_3Hg^+);
- the use of the agglomerated Au@Cy NPs in the amplification of photodynamic activity, and
- the use of the as-synthesized mix of Au@Cy NPs and CQDs in genic therapy for endothelial cells.

In **Chapter 7** we compare the experimental results obtained in the production of carbon based nanomaterial by the ablation of the different transition metal target in water, and we propose our hypothesis on the origin of the CO_2/C reduction process.

In **Chapter 8** I will analyze the obtained results based on the list of objectives reported in the previous section. We conclude with remarks on the future direction of the research, necessary to complete some missing quantitative values, and confirm our hypothesis on the processes leading to CO_2/C reduction as described in **Chapter 7**.

Chapter 9 includes a list of the published articles, and the national and international conferences attended during my Ph.D. studies.

In the final **Chapter 10**, a comprehensive bibliography is cited to support the conclusions of the research activity performed in the thesis.

2 Theory and recent literature

2.1. Negative emission technologies

2.1.1. Introduction

It passed 100 years since the first scientific article correlating the increase in soil temperature with CO₂ emission [54], and since the industrial revolution until now, the concentration of CO₂ went from 278 ppm to values above 400 ppm [47]. In order to decrease the impact of CO₂ emissions on global warming and environmental instability, it is highly accepted by scientific and political circles communities, the need to drastically reduce the emission of CO₂ into the atmosphere, with the objective of adhering to the guidelines decided during the agreement in the United Nations Framework Convention on Climate Change (UNFCCC), held in Paris in December 2015 [55]. The agreement deals with greenhouse-gas-emissions (GHGs) [47] mitigation, intending to reduce and maintain the increasing of the temperature below 2 °C above the value before the industrial revolution [56]. The key-point to reach such a goal is the development of proper negative emission technologies (NET), which should in principle consider all the steps involved in the production and consumption of energy, from energy harvesting with renewable energies, to electrical distribution and particular application of the energy, as schematically represented in Figure 2.1 [47].

Nanomaterials play today a crucial role in all the applications described in Figure 2.1 [21, 47, 57, 58]. Particularly interesting is the production of sustainable bioenergy with carbon capture and storage (BECCS) [21], as reported in Figure 2.1 (h-i).

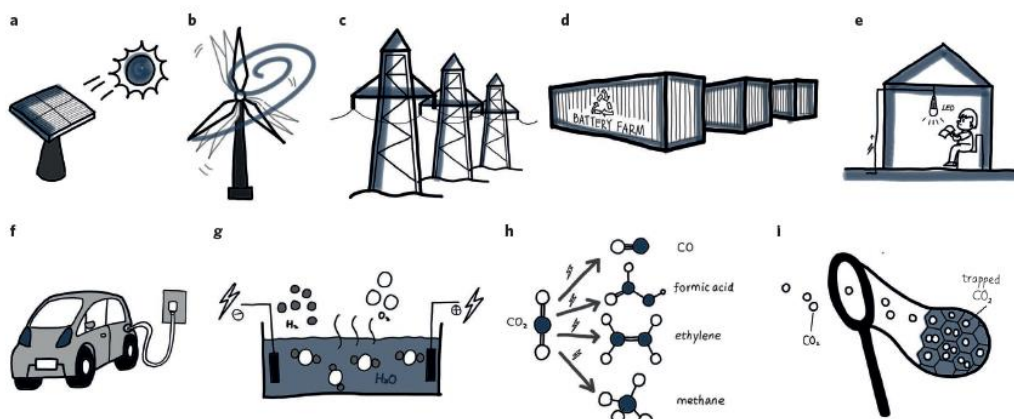


Figure 2.1 (a,b) Renewable energy sources, c) energy transport, d) energy harvesting, e) low-consumption lighting, f) electric vehicles, g) hydrogen production, h) CO₂ conversion to fuels, and i) CO₂ harvesting [47].

Among the BECCS, the electrochemical reduction of CO₂ to gases or fuels has been achieved mainly by the use of electrochemical cells ($E = e\Delta V$) at low potential regimes, although also thermochemical ($E = kT$) [22–24] and photochemical ($E = h\nu$) cells have been demonstrated using different nanostructures [25–31].

The first step in CO₂ electro-catalysis is generally the generation of carbon monoxide (CO) or formic acid (HCOOH) [58–60] which is common in the case of Ag or Au metals electrodes [61, 62], and amplified together with the oxidation of the metals and nanostructure formation [63–65]. CO₂ reduction to CO was also observed using Fe₂O₃ catalysts or iron oxide nanoparticles in heterogeneous catalysis [66, 67]

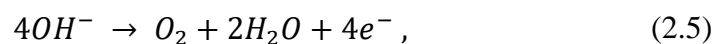
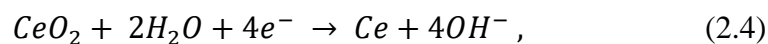
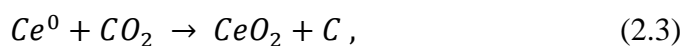
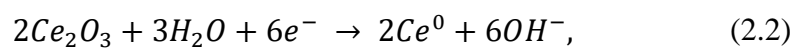
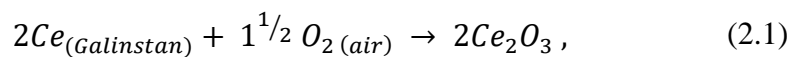
The use of particular nanostructured interfaces may allow the final formation of reduced species with $C \geq 2$, with the generation of fuels or fuels precursors in the water environment. This is the case of carbon-iron NPs films [68], N-doped nanodiamond-Cu interfaces [21], or CuNPs [69]. Interestingly, in this scenario, the AuNPs seems to play a unique role, since the non-radiative decay of the excited localized surface plasmon (LSPR) is associated with electron-hole pairs caused by the interband transition from the d-band to the sp conduction band, or by intraband transitions in the conduction band [70, 71], which are responsible for the triggering of different chemical reactions [30, 72]. In particular, the plasmonic excitation of AuNPs/solution interface generated by green light is favorable for CO₂ activation,

and when an ionic liquid stabilizes the charged intermediates created at the interface, it is possible to obtain multi-step reduction and C–C coupling [30].

Nevertheless, the reduction of CO₂ to solid carbon is now considered the most precious route for permanent storage of CO₂ in solution [34]. In fact, reduction of CO₂ to volatile species, although considered value-added chemicals useful for energy-related industrial processes, is not a definite route, since unwanted chemicals release in the environment still represents a negative issue from the ecological point of view.

Room temperature reduction of CO₂ to solid carbonaceous species has been recently demonstrated for the first time by Esrafilzadeh [35] by the use of liquid metal electrodes of Galinstan (liquid metal eutectic alloys whose composition is mainly consisting of gallium, indium, and tin) containing Ce⁽⁰⁾ and Ce⁽³⁺⁾ interfaces, with an activation potential as low as ~ 0.3 V Vs CO₂/C. Although depending on the applied potential, the electro-catalytic process involved in the unique CO₂/C conversion process is described thereby cyclic reaction in which cerium is continuously oxidized and further reduced to metallic species, in a process involving both electrons and OH species, as depicted in equations (2.1) - (2.5), taken from [35].

Equation (2.1) - (2.5) described the redox cyclic process between metallic and oxidized Ce [35], which is leading to the formation of solid carbon from CO₂ in water.



The process starts with the oxidation of the Ce based electrode by oxygen in air to Ce₂O₃, followed by reduction to metallic Ce⁽⁰⁾ during the application of the reductive potential. At this stage, metallic cerium reduces CO₂ to solid carbon and is oxidized to CeO₂. Subsequently the cerium oxide is again converted to metallic cerium, after which the redox loop continues, in parallel to the oxygen evolution reaction described by equation (2.5).

As explained in the introduction section, one of the most striking results of the research is the discovery that carbon-based nanostructures can be obtained by CO₂/C reduction during the PLA of targets of the transition metals Au, Ag and Fe. The general behavior of the observed CO₂/C reduction, which is not dependent on the particular transition metal target, let us suppose that a common property should be responsible for the formation of the carbonaceous material. Transition metals have all relatively good catalytic properties and are characterized by different oxidation states, comprising semiconductor oxides, so often used in NETs.

In our case, with the experimental configuration and parameters used during PLA in our experiments, we can estimate that about 75 µg of CO₂ is reduced per hour, corresponding to a BEECS added energetic value of $\sim 10^{-6}$ kW/h. As explained in detail in the *Conclusions* section, the choice of the proper parameters in terms of the target material, the geometry of the optical system, and the water container might enhance the energetic value of PLA product of 3 orders of magnitude.

2.1.2.

Possible transition metals oxides (Au, Ag, Fe)

Alkali/alkaline earth metals have one/ two electrons in their valence s-orbital, and they can only lose these one/two electrons, therefore their oxidation states are almost fixed (+1/+2). In contrast, the transition metals available and used in this research (Au, Ag, and Fe), have five unstable d-orbitals in a *d* subshell and one unstable s-orbital, therefore the number of possible oxidation states is higher and variable in transition metal as compared to alkali/alkaline. To understand the phenomenon involved in transition metal's oxidation states, it is important to understand how much are the un-pair *s* and *d*-orbitals electrons bonds [73, 74] The basic information about Au, Ag, and Fe oxidation states are summarized in Table 2.1 and Figure 2.2 [74–78], where the electronic configuration of both *s* and *d* orbital have been shown, since are the orbitals taking part in the oxidation reaction.

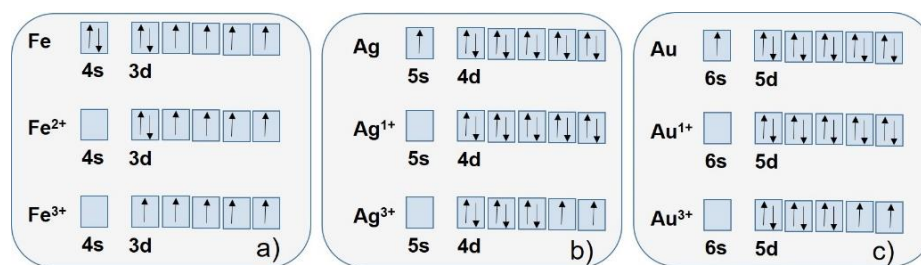


Figure 2.2 Schematic diagram of the most common oxidation states of Fe (a), Ag(b), and Au(c), and the corresponding electronic configuration of the last two orbitals.

Table 2.1 Atomic number, electronic configuration, and most common oxidation states of Au, Ag, and Fe.

Element Name and Symbol	Atomic Number	Electronic Configuration of Last Two Orbital	Most Common Oxidation States
Au	79	5d ¹⁰ , 6s ¹	+1, +3
Ag	47	4d ¹⁰ , 5s ¹	+1, +3
Fe	26	3d ⁶ , 4s ²	+2, +3

The presence of chemical species with their oxidation states is extremely important for the stability of the metal nanoparticles (MeNPs) in colloidal solution, as will be discussed in detail in Section 2.3. The most common oxidation states observed for NPs produced in water by PLA of Au, Ag, and Fe targets, are summarized in Table 2.2.

Table 2.2 Oxidation states of NPs synthesized by PLA of Au, Ag, and Fe targets in the water.

Target / Solvent (laser)	Laser wavelength / fluence or Energy per pulse	Metal /metal oxide NPs	Comments	Ref.
Au/water (ns laser)	1064 nm / 80 mJ	AuNPs with metal Au core and Au-Oxide surface	3.3-6.6% of the surface of AuNPs are oxidized (Au ⁺ , Au ³⁺) and were measured by XPS	[79]
Au/water (fs laser)	800 nm / 1 mJ	AuO ⁻ , AuOH ⁻ and CO ₃ Au ⁻	the oxidation states of gold were measured by FTIR and Raman.	[80]
Ag /water (ns laser)	1064 nm	Ag and Ag ₂ O		[6]
Ag /water (ns laser)	532 nm / 10-15 J cm ⁻²	Ag, Ag ₂ O, AgO, Ag ₂ O ₃	AgNPs have both metallic and oxidation structure and were determine via inter planer distance using SAED and HRTEM	[81]
Fe /water (ns laser)	1064 and 335 nm / 10 and 0.22 J cm ⁻²	Fe ₃ O ₄ = 94.0 % Fe ₂ O ₃ = 3.5%, FeO = 2.0 % Metal Fe = 0.5 %	94.0 wt% by weight of cubic spinel phase, with a fraction of 3.5 wt% of hematite, traces of wustite of 2.0 wt%, and metal a-Fe (0.5 wt%). The oxidation states and structure are examined by using FTIR, XRD, and Raman	[82]
Fe/ Water (ns laser)	1064 nm and 532 nm/2.5 – 8.0 mJ	Fe ₃ O ₄ and FeO	The magnetization decreased and the average size of NPs is increased if a 532 nm laser is used. The oxidation was examined by XRD analysis.	[83]
Fe, Fe ₂ O ₃ Fe ₃ O ₄ /water (ns laser)		Fe, Fe ₃ O ₄ and Fe ₂ O ₃	The oxidation was examined by XRD analysis.	[84]

2.1.2.1. Gold (Au)

Gold is one of the least reactive metals present in the periodic table, and its oxidation states are formed only by Au^+ and Au^{3+} species since Au^{2+} species are considered mixed-valence systems, consisting of equimolar portions of Au(I) and Au(III) [85]. Different techniques can be applied to oxidize the gold thin films, generally based on the interaction with high reactive gases, such as ozone or atomic oxygen [86, 87]. The experimental techniques involving electrochemical oxidation are [88], ion-oxygen sputtering [89, 90], and PLA in the molecular oxygen environment [91]. The particular oxide formed, depends principally on the chemical environment in which oxidation occurs. In an experiment of gold surfaces oxidation in the O_2 environment, mainly gold oxidation state +3 i.e Au (III) are found, due to the intrinsic instability of the Au_2O [92], where Au_2O_3 are the most stable pure oxide of gold, and decompose at temperatures around 450 K, and is also thermally unstable in air, even at room temperatures, with a typical lifetime of 1 or 2 days [93, 94].

In a water environment, different situations are found. The experiment of electrochemical water splitting by gold electrodes [95], revealed the formation of different kind of gold hydroxides, in both Au^+ and Au^{3+} form ($\text{Au}(\text{OH})_3$, AuOOH , Au_2O_3). Different results are obtained for the oxidation properties of AuNPs produced by the PLA process in water. Sylvestre *et. al.* [80], revealed by time of flight (TOF) and XPS studies that in an alkaline environment the Au-O single bonds of the oxidized AuNPs surface, react with and OH^- ions, and creates Au-O $^-$ and Au-OH surface oxides. In this case, also CO_2 has a particular role since surface studies revealed also the presence of carbonaceous oxides, such as Au- OCO_2H [80].

2.1.2.2. Silver

Silver (Ag) element is a transition noble metal, with atomic number 47 and atomic weight 107.87 u [75] and placed in group 11 (Ib) and 5th period of the periodic table. A different number of the oxidation state of Ag are possible, but the most common oxidation state of silver is +1 (Ag_2O and AgNO_3), while +2 oxidation states are rare [74]. Usually, the high valence containing silver compounds

synthesis required tough conditions as compare to lower valance containing silver compounds. The earlier know and most famous higher oxidation states of silver are AgO and Ag₃O₄ [77].

When AgNPs colloids are synthesized by using laser ablation of the metallic silver target in water, the surface of the AgNPs is oxidized [6, 81, 82], which produced a net negative charge over the AgNPs surface and provide stability against Van der Waals attractive force. As well as, these silver oxides can be useful as a photocatalytic [96], and can be used for the CO₂ conversion to other types of carbon [47].

2.1.2.3.Iron

Iron oxides richly exist in nature as a compound in different minerals. They exist in many crystal structures and with different magnetic properties [97, 98]. The most common oxides are iron oxide-III / hematite (α -Fe₂O₃) and maghemite (γ -Fe₂O₃), iron oxide-II / wüstite (FeO), and iron oxide II and III together / magnetite (Fe₃O₄) [97, 99].

- **Hematite**

Hematite is a rhombohedral phase α -Fe₂O₃ structure and the most stable oxide of iron with a +3 oxidation state. It is weak ferromagnetic or antiferromagnetic at room temperature and above 956 k (Curie temperature) it becomes paramagnetic. Hematite is mostly exist in nature in minerals (in rocks and soils) [82, 99, 100].

- **Maghemite**

Maghemite is a thermally unstable oxide and consists of a cubic spinel structure similar to magnetite, and also exists in minerals [82, 100]. It has typical ferromagnetic behavior at room temperature. The oxidation state of *Fe* is +3 in maghemite, and in an oxidative atmosphere at a temperature above 673 K, it converted to hematite [101]. Maghemite has a white to bluish-gray color in reflection, while brown to yellow color in transmitted light.

- **Wüstite**

Wüstite or iron (II) is a black color oxide of iron with a purely +2 oxidation state and a cubic crystal structure. It is thermodynamically unstable [102]. It has a gray color with a greenish tint in reflected light and exists in minerals.

- **Magnetite**

Magnetite exists in a black magnetic mineral form. It has the strongest magnetism than all-natural minerals existing on the Earth. It is ferromagnetic at room temperature and has an inverse spinel crystal structure. It is also called ferrous ferrite or iron (II, III) oxide. The molecular formula Fe_3O_4 of magnetite can be written as $\text{FeO}\cdot\text{Fe}_2\text{O}_3$, which consists both wüstite (FeO) and hematite (Fe_2O_3) [99, 103]. Both magnetite and maghemite are thermally unstable and converted to hematite at a temperature above 673 K [101].

The properties of these iron oxide become more interesting at the nanoscale. There are different kind of iron oxide-based NPs, namely hematite NPs [84], Wüstite NPs [82, 83] and magnetite NPs (Fe_3O_4 NPs) [82, 83, 104]. In literature [64] iron oxide-based NPs colloids have been synthesized by PLA of pure metal iron in water, and in most of the reported article major part (more than 90%) of these nanoparticles contain magnetite [82–84], therefore they have strong magnetization and have superparamagnetic properties [105], which can be useful for their applications [107].

2.1.3.

Transition metal oxide as semiconductors

Among the oxidized species of all the transition metals analyzed in the thesis, it is possible to find a particular configuration associated to semiconductors metals. Au_2O_3 for example, is a semiconductor with a band-gap (BG) variable between 0.85 eV / (1512.0 nm is the same BG in term of wavelength), while Au_2O is experimentally found to behave as a metallic conductor, although *ab-initio* DFT calculus predicts a direct-BG of about 0.83 eV / (1512.0 nm) [92]. Between Ag oxides, Ag_2O is reported to be a p-type semiconductor with a BG of 1.2 eV / (1033.2

nm) [108]. Similarly, the oxides of iron also have characteristics of a semiconductor, with the values of the energy BG reported in Table 2.3 [109].

Table 2.3 Value of the bandgap in different types of iron-based oxides, as measured by Giannakis, Stefanos. *et. al.* [109].

Iron oxide	Formula	Oxidation No.	Band-gap (eV/nm)
Wüstite	FeO	+2	2.4 / 516.6
Hematite	α -Fe ₂ O ₃	+3	2.2 / 563.5
Maghemite	γ -Fe ₂ O ₃	+3	1.9 / 652.5
Magnetite	Fe ₃ O ₄	+2, +3	0.5 / 2479.7
Nano-maghemite	γ - Fe ₂ O ₃	+3	1.9 / 652.5

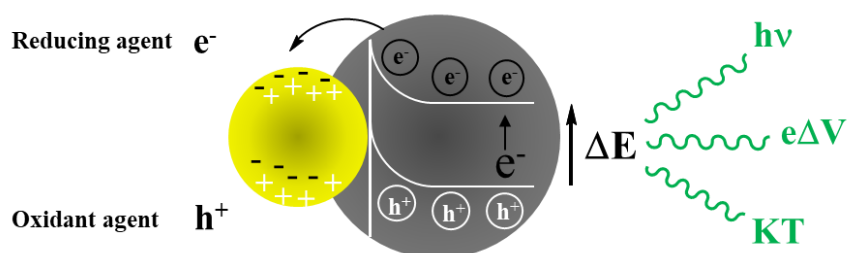


Figure 2.3 Creation of a hole-electron pair in metallic semiconductors, further used in redox processes. The bandgap may be excited by different routes: optically, electrically, or thermally.

The metal semiconductors above may act as catalyzing agents in different redox processes [92, 110–115]. As depicted in Figure 2.3, the binding energy (BG) of the metal semiconductors can be excited by three main different routes: optically (h), electronically ($e\Delta V$), or thermally (KT).

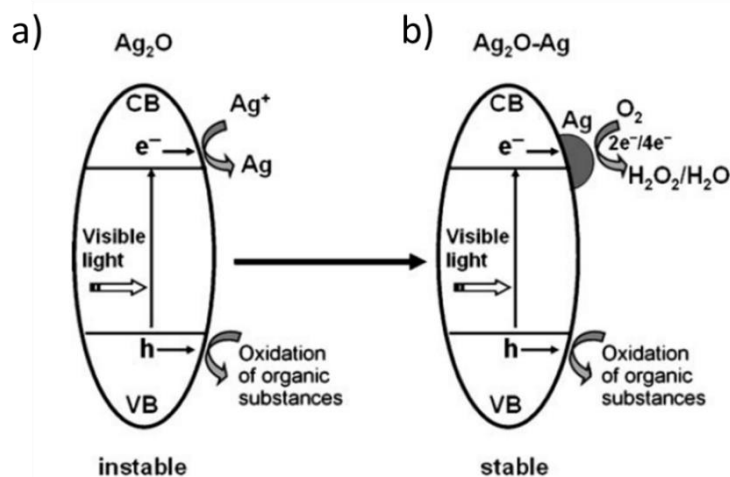


Figure 2.4 Schemes showing the photo-induced self-stabilizing process of the Ag/Ag₂O interfaces. a) The photogenerated electrons are taken by Ag⁺ ions of the oxide. b) The photogenerated electrons are taken from metallic silver and passed to molecular oxygen, formed in the first part of the process (a). The symbols h and e⁻ represent the photogenerated holes and electrons, respectively. CB and VB indicate the conduction and valence band, respectively [111].

The excitation induces the formation of a hole-electron pair which is particularly useful in redox processes, having the ability to act simultaneously as both reducing and oxidant agents.

When using noble-metals, heterogeneous catalysis is generally obtained using metal-oxides supports. In the case of Ag, hybrid Ag/Ag₂O interfaces are found to be catalytically active and stabilize the silver oxide Ag-O-Ag preventing its reduction [111]. In fact, Ag₂O without the presence of the metallic counterpart is characterized by a photo-instability, which limits its practical use in photocatalytic processes. Upon interaction with photons in the visible spectra, the photogenerated electrons (e⁻) in Ag₂O interact with the Ag⁺ ions of the oxide reducing them to metallic silver, following the reaction $\text{Ag}_2\text{O} \rightarrow \text{AgO} + \text{Ag}$, as represented in part a) of Figure 2.4. At the same time, the photogenerated holes (h⁺) oxidize the O₂⁻ lattice of the oxide and produce molecular oxygen, following the reaction $\text{AgO} \rightarrow \text{Ag} + \frac{1}{2} \text{O}_2$. However, as outlined in part b) of Figure 2.4, the presence of a metallic heterojunction forming a metal/metal-oxide interface, favors the passage of the photo-generated electron to the metal species, which also acts as an electron donor in redox processes, preventing the transformation of the O₂⁻ lattice.

As will be presented in the Conclusion Section, in our special case the surface of the transition metal NPs are composed at least by both $m^{(0)}$, m^{+1} , m^{+2} species (m stays for metal), creating a particular metal/metal-oxides interface which might be responsible for CO₂/C reduction [95, 116]. In fact, when a metal/metal-oxide interface is present, similarly as reported in Figure 2.4b, the transfer of the photo-excited electron to the metal enhances the exciton lifetime (typically sub ps) [117], and allow the use of the electron-hole pairs for chemical reactions.

In the next section, we start the description of the principal topic of the present research, the world of nanoparticles.

2.2. Colloidal nanoparticles

Living organisms are made the approximately 10- μ m size of unit cells, while the parts of these cells are in the sub-micron size. Even smaller are DNA, oligonucleotides, or proteins, with a typical size of just a few nanometers [118]. The control, manufacture, and exploration of new properties of structures with these dimensions are responsible for the development of a new branch of science called nanotechnology [119]. Nanostructured materials and NPs in particular [120] have a very large surface to volume ratio as compared to bulk material, which is an excellent playground for catalytic and bio-sensing applications. The high surface density of chemically active sites of NPs, may be used for selective chemical reactions [121], or the implementation of strategies for the complexation with biological analysts [122]. Although catalysis, alternative energy, and photonics represent branches of science heavily influenced by nanotechnology, it is in biology and medicine that nanostructured systems and nanoparticles are promising a revolution [122, 123]. Among a huge variety of NPs, noble MeNPs deserve special attention, due to their unique optical properties linked to the localized surface Plasmon resonance (LSPR) [124, 125]. The latter favors the application of MeNPs in optical diagnostic biosensors based on different enhanced spectroscopies, such as Surface-Enhanced Raman Scattering (SERS) or UV-Vis [124, 126], suitably described in the next sub-sections. It is in the field of diagnostic that the long-run stability of the of NPs colloid is essential, in order to avoid the risk of false diagnostic test results. The problem of stability is amplified when using the NPs

colloids directly in physiological media with high ionic force [20, 127], where generally steric stability solutions such as the stabilization with polymers [20, 127, 128] or metal-dielectric (carbon or SiO₂) core-shell nanocomposites (NCs) colloids are the best solutions [20, 129]. This is particularly important for the interaction of NPs with cells in the human body, where the NPs have to be stable in an extremely chemical-rich environment, with high ionic force [20, 129, 130].

Regarding the use of NPs colloids as alternate therapies, although small, these molecules generally used to specific body targets, have reduced toxicity. Therapeutic effectiveness cannot be guaranteed unless the medicine is able to selectively achieve in adequate doses (medicines are quickly degraded or eliminated from the system circulation). On the hand, nanoparticles can offer several advantages as compared to traditional therapies: i) fewer side effects of delivered drugs [131]; ii) increased versatility in the formulation [122]; and iii) display of optical or magnetic properties that can be tuned to detect early disease (molecular imaging) [132] or to damage tumoral or inflammatory cells (magnetic or optical hyperthermia in the near infrared) [133, 134].

As a matter of fact, the biological activity of NPs depends on chemical and physical factors such as material, size and shape, surface area, agglomeration state, chemical composition, surface chemistry (a charge, hydrophilicity, etc.), surface activity, solubility, dose, and so on. In particular, AuNPs, due to the gold chemically inert nature and easy chemical handling of the surface for downstream applications, received a lot of attention in the past decade. The control on the size and shape of the AuNPs is a crucial point for medical applications. For example, in the case of photodynamics (PDT) and thermal therapies for cancer treatments [135, 136] usually are needed nanostructures with particular resonant form and generally NPs with linear dimension > 10 nm, while NPs with dimensions less than ~ 5 nm are needed for the nuclear cell level, improving or hindering of the expression of selected genes [137, 138].

Summarizing, it appears clear how much it is important to find a new synthesis route that is able to produce NPs in colloidal dispersion with controllable dimensions, with a metallic core and an inert shell of SiO₂, polymeric, or carbon material, supplying the biocompatibility and the steric stability necessary for in-vivo applications (see Section 2.2.2).

In the following, we introduce the principal physical phenomena leading to the formation of nanoparticles by the PLA of solid targets in liquid, which will give to the reader the background to understand the process of formation of metals NPs and also its application for the CO₂/C reduction reported in the thesis

2.2.1.

Principles of pulsed laser ablation (PLA) in liquid

2.2.1.1 Introduction

Since the first example of the generation of nanomaterial by pulsed laser ablation in liquid in 1987 [1], an increasing number of laboratories started to dedicate their investigation to this fascinating field. As a matter of fact, the number of publications and citations per year in the field of generation of nanoparticles by laser in liquids, jumped from ~ 5 (publications and citations) to about 50 (publications) and 700 (citations) from 1998 to 2011, respectively [139].

Although it is not possible to show a comprehensive list of the numerous groups all over the world having an important role in the field in the past decades, we attempt to make a brief list of the groups which gave a fundamental contribution in: i) the control of nanoparticle size in water; and ii) the study of the chemical reactions happening in the liquid environment during the synthesis of the nanoparticles. From the point of view of the control of metal nanoparticles size and physics of the nanoparticles fragmentation by laser irradiation in water, a particular role is attributed to the groups of Prof. Fumitaka Mafune (Toyota Technological Institute, Japan) [140] and Dr. Emilia Giorgetti (Istituto dei Sistemi Complessi I.S.C-C.N.R, Italy) [141]. Concerning the Physico-chemical aspects affecting the composition of the resulting nanomaterial, and chemical reaction during the PLA process, we put in evidence the work of Prof. Vincenzo Amendola (University of Padova, Italy) [6], Prof. Giuseppe Compagnini (University of Catania, Italy), and principally of Prof. Stephan Barcikowski of the University of Duisburg Essen, in Germany, whose research is also dedicated to the bio-conjugation of nanoparticles and the relative use in biological applications [142].

Also, several groups in Brazil focused their attention in laser-assisted generation of nanoparticles in the past years, such as the groups of Prof. Ernesto Jiménez Villar (Federal University of Paraíba (UFPB)), Prof. Ricardo Rego Bordalo Correia (Technological Federal University of Rio Grande do Sul), and of Prof. Walter de Azevedo (Federal University of Pernambuco (UFPE)), whose results about the synthesis of semiconductor nanoparticles and complex chemical compounds during PLA in liquid [143] are particularly interesting for the experimental work shown in the thesis.

2.2.1.2 Principles of PLA in water

Laser ablation is a process of light-matter interaction where the material is removed from the surface of a target utilizing focused lasers [6, 144–146]. It finds several applications in modern technology: precise micromachining of materials [147], including dentistry applications [148], surgery [149, 150], conservation of cultural assets [151], and the production of different kind of nanostructures and deposition of thin films [6, 152, 153].

PLA is a very versatile technique, which may be performed both in gaseous or liquid environment, and by the use of both pulsed or continuous wave (CW) laser source, if the laser intensity is sufficiently high ($\sim 10 \text{ kW/cm}^2$). Laser ablation by CW lasers principally make use of high power infrared CO_2 [154] and UV excimer lasers [155], while pulsed laser ablation (PLA) can be performed by different kind of pulsed laser sources, essentially depending on the temporal length of the pulses (fs,ps,ns).

PLA process, is based on the absorption of the energy of the short laser pulse by the electrons of the surface of the targets, followed by phonon thermalization in times of the orders of ps [156].The mechanism related to the ejection of the material, strongly depends on the length of the laser pulses, and the nature of the external environment. Also, the depth over which the incoming laser pulse is absorbed, and thus the amount of material removed by a single laser pulse, depends on the environmental factors [157–159], but also on the material's optical properties and the experimental laser parameters, such as wavelength, energy and temporal length [6, 144, 145, 160]. Higher ablation efficiency (mass of material removed per

pulse energy) and lower threshold fluence F_{th} (the minimal fluence necessary to have ejection of the material) is obtained using shorter wavelength [159, 160], and shortest pulse duration [161].

From the physical point of view, while ultrashort pulses (fs, ps) mostly lead to multi-photon absorption processes and photo-ionization effect with Coulombic explosion and explosive boiling, PLA by the use of ns or longer pulses is instead dominated by thermal processes, such as melting and vaporization of the material [157, 162].

The use of ns pulses, like in the present work, strongly reduces the differences observed in the physical origin of material ejection in different environments, such as air and vacuum. In fact, in the latter case (vacuum), the use of ps or fs laser pulses gives a fundamental role to electron long-lifetime transient nonequilibrium surface states, whose thermalization times with hot phonons, is bigger than the surface cooling time [163]. Vice versa, when air or water is present, the collision of the gas or liquid molecules with the surface states, strongly reduces their life-time, so that thermal evaporation of the surface is allowed [163]. The use of ns laser pulses, whose duration is bigger than the phonon-electron relaxation times, strongly reduces the differences cited above, since the ejection of the material by PLA in a different environment is principally due to thermal effects.

The differences observed in PLA efficiency in air or water environment, are associated to the different behavior of the shock-waves generated by the expansion of the plasma [164]. While in an air environment, the shock-waves rapidly go apart from the target by expansion in the medium, in the case of a liquid environment they are responsible for the production of cavitation bubbles [164], which participate actively in the removal of the material from the targets, and are responsible for the higher rate of material removal in comparison with PLA in air or vacuum environment.

From a general point of view, PLA process in liquid represents a very complex light-matter interaction, whose theoretical physical description includes aspects of plasma physics, solid-state physics, plasmonic, non-linear optics, and low and high-temperature chemistry processes. In the following, we report a more

detailed description of the different physical processes having a fundamental role in PLA in liquid, starting from the absorption of the laser pulse from the target.

During laser and target interaction, the free electrons on the surface of the target material absorb the incoming laser energy, and two competing processes occur [165]. In the first stage, the excited electrons move with ballistic motion at the Fermi velocity (10^6 ms^{-1}) towards the deeper part of the target [165]. After that, the collision occurs among the excited electrons and the electrons around the Fermi level. Electron temperature is developed at the point of equilibrium among hot electrons. These hot electrons move to the deeper side of electron gas inside the metal target with a speed of $< 10^4 \text{ ms}^{-1}$, lower than ballistic motion. After, the hot electrons are cooled by the electron-phonon coupling with the lattice, with the corresponding heating of the crystal structure. In this way energy from the laser pulse is transferred to the target provoking the ablation process.

It is observed that electrons and phonons are not generally in thermal equilibrium with each other's, and can be described by a two-temperature model [166, 167] which was first time introduced in 1974 by Anisimov *et. al.* [168]. Here the two temperatures T_e and T_L are the functions of space and time, and can be described by the coupled equations [169] as below,

$$C_e \frac{\partial T_e}{\partial t} = \nabla \cdot \{ \kappa_e \nabla T_e \} - \Gamma \{ T_e - T_L \} + Q(r, t) , \quad (2.6)$$

$$C_L \frac{\partial T_L}{\partial t} = \nabla \cdot \{ \kappa_L \nabla T_L \} + \Gamma \{ T_e - T_L \} , \quad (2.7)$$

where κ_e and κ_L are thermal conductivity, and C_e and C_L are the heat capacity of electrons and lattice, respectively. The parameter Γ is associated with the coupling of electron and lattice systems, and $Q(r, t)$ describe the laser source term, which can be written as

$$Q(r, t) = \nabla \cdot \{ 1 - R \} I(t) e^{-2 r^2 / \omega^2} e^{-\alpha z} . \quad (2.8)$$

Here R , $I(t)$, ω , z and α are the reflectivity of the surface, the time-dependent intensity of the laser pulses, frequency of the laser, depth from the thin film surface, and absorption coefficient of the surface material respectively [169, 170]. Through the solution at those equations is possible to obtain the time dependence of the behavior of the electron and lattice temperature, at a different position inside the target. As represented in Figure 2.5, corresponding to a gold target, the typical

electron-phonon relaxation times are of the order of some ps , so that ns laser pulses are for most of their duration continuously interacting with a system where the heat is transported by thermalized electron and phonons, at least until we do not consider nonlinear absorption effects, which is one of the principal hypothesis in the model used for the calculus [169].

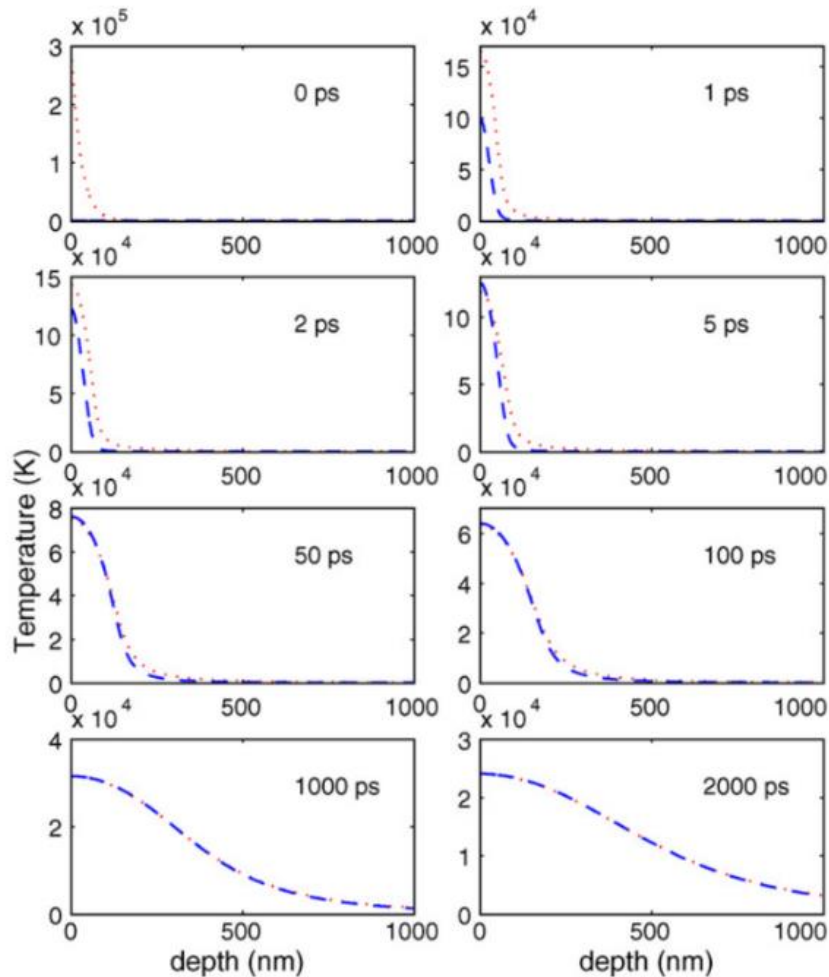


Figure 2.5 Temporal evolution of electron and lattice temperature of gold vs ablation depth. Thermal equilibrium between electron and lattice occurs approximately after 5 ps [169].

Figure 2.6 reports the theoretical ablation depth in a gold target in the function of the fluence F of the laser pulses, in the same range of fluence used in the present investigation. In the graph, two results are reported, considering a temperature-dependent (red line) and an independent (blue line) electron-phonon coupling constant. In the first case, the fluence threshold is about 0.3 J/cm^2 , the same value we observed experimentally along with the present research.

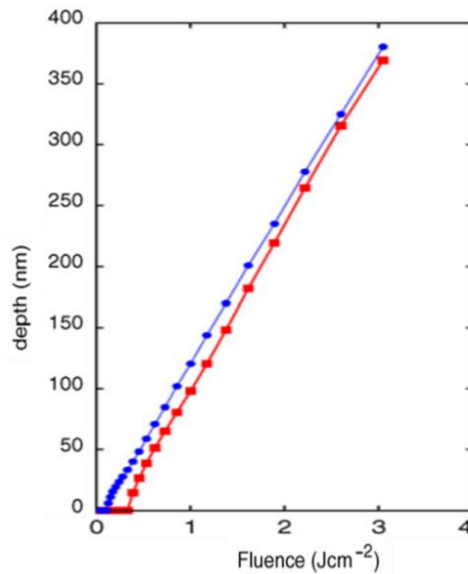


Figure 2.6 Theoretical ablation depth in a target of gold vs laser fluence F of the laser pulses. The red and blue lines are associated to the temperature-dependent and the temperature-independent electron-phonon coupling [169].

A schematic description of the different phases occurring during the PLA process of a metal target in the liquid is represented in Figure 2.7, adapted from Amendola *et. al.*[6].

PLA can be described by the following main three stages:

- (i) laser energy absorption by the target, material ejection from the target, plasma plume, and cavitation bubble formation;
- (ii) plasma plume and cavitation bubble expansion in the presence of the confining liquid environment;
- (iii) bursting of the cavitation bubbles, plasma plume mixing with the liquid, and formation of NPs by nucleation processes;

The target absorbs the incoming laser energy and, as described before, electron transfers the energy to the lattice in a few ps . Until $\sim 10^{-10}$ s, the energy absorption leads to the detachment of the ablated material. Although in non-thermal PLA (fs laser pulses) [171, 172], nonlinear optical absorption and direct photoionization of the material is the principal origin of the material detachment by Columbia explosion, in ps and ns based PLA in liquid, the material is ejected due to simultaneous thermal processes such as melting, vaporization and boiling [6].

The high ionization of the expelled material is typical of plasma with temperature and pressure of about 10^3 K and 10 GPa, respectively [173–175], where liquid pressure is responsible for plasma confinement above the target.

The formation of the plasma is followed by the generation of two shock waves in the opposite direction one moving into the solid target and the other going into the liquid, producing a cavitation bubble. In the second stage, the plasma plume expands adiabatically and follows the shockwave and the wall of the cavitation bubbles, heating the external liquid and forming eventual new materials by chemical interactions [6, 173, 174].

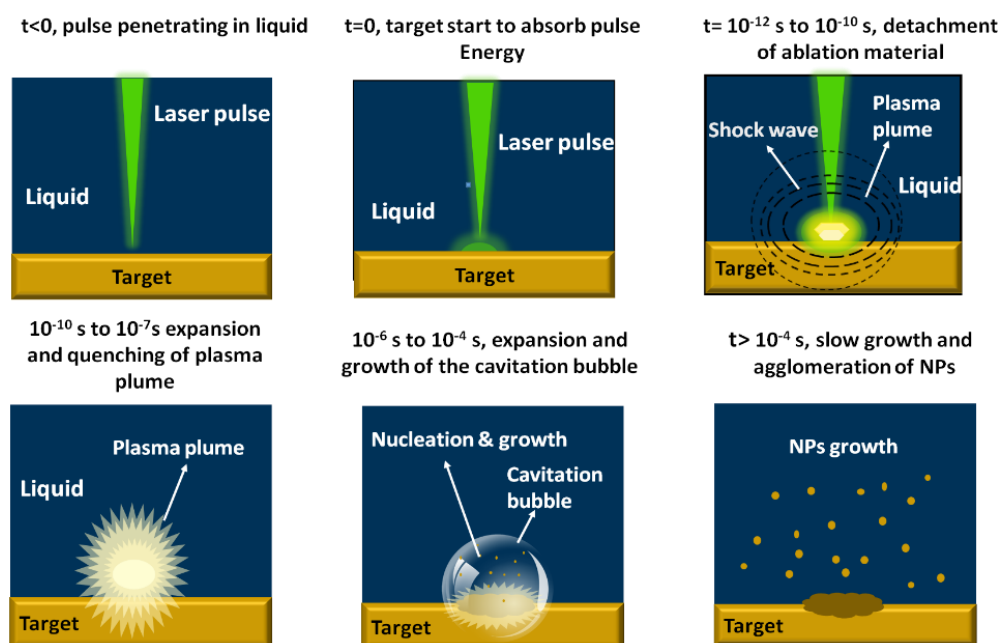


Figure 2.7 Schematic diagram representing the different stages in the process of formation of NPs by PLA in liquid (adapted from [7]).

The plasma plume has a typical lifetime of tens of 10^{-8} - 10^{-7} ns, during which it continues releasing energy to the target, provoking further ablation also after the effective temporal length of the pulse [7]. The plasma loses its energy also for the interaction with the liquid environment, which definitively leads to its cooling [173], and to the formation of a cavitation bubble expanding up to 10^{-4} s, after which it collapses emitting a final shock-wave [6, 176].

In literature, it is not clear if the nucleation stage of the NPs starts before or after the cooling of the plasma plume [6]. What is confirmed is that after nucleation

of the NPs in isolated crystals, the final NPs are formed by the coalescence of different nanocrystals, as suggested by the polycrystalline nature of nanomaterials produced by PLA [177, 178], as also observed in the TEM images reported in sections describing our experimental results.

The advantage in the use of *ns* laser pulses instead of performing non-thermal ablation with ultra-fast laser sources (*fs*) is in the control of the average size distribution of the synthesized NPs. As described before, the ejected material ablated from the target derives from different physical phenomena, such as photoionization, vaporization, or melting, so that the material designated for recombination and final formation of NPs is in a multiphase state, which is the principal cause of the quite large poly dispersivity of the colloidal nanoparticle synthesized by PLA [179] as compared to the chemical method of synthesis. This problem is less evident when using laser pulses with a duration of *ns*, where the plasma and material ejected in different phases are irradiated by the upcoming part of the laser pulse, and the size distribution of the NPs may be opportunely fit by a single-mode *log-normal* function [8], as described in details in the next subsections. A more detailed description of the parameter and techniques useful to control the dimension of the nanomaterial synthesized by PLA will be introduced in the section showing the experimental results, for both AuNPs, AgNPs, and iron-based NPs.

What is important to underline at this moment, is that although the nanoparticle composition is always the mirror of the target composition, the surface of NPs is instead marked by the presence of atoms coming from the PLA environment which, in the ultimate analysis, are responsible for their stability. In fact, in absence of surfactants or stabilizing agents, the PLA of metal targets in water or organic solvents leads to chemical reactions between the NPs atoms and the dissociated atoms or molecules of the solvent, which may form charged oxidized group on the NPs surface [79, 80], or even a shell of carbon material supplying steric stability [15], as depicted in Figure 2.8, taken from [6].

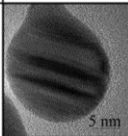
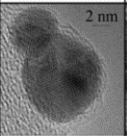
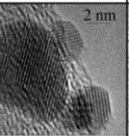
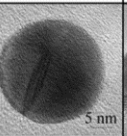
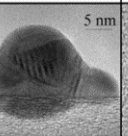
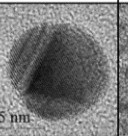
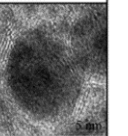
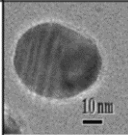
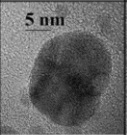
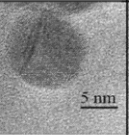
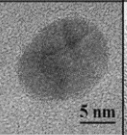
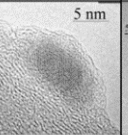
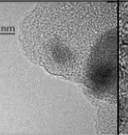
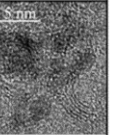
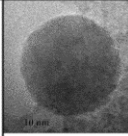
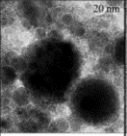
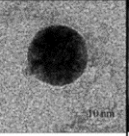
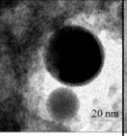
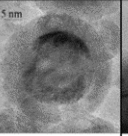
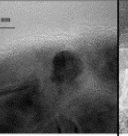
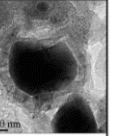
Target ↓	Solvent ↓	Water	Ethanol	Acetonitrile	Dimethyl- formamide	Tetra- hydrofuran	Dimethyl- sulfoxide	Toluene
		<chem>O</chem>	<chem>CCO</chem>	<chem>CC#N</chem>	<chem>CN(C)C=O</chem>	<chem>C1CCOC1</chem>	<chem>CSC(=O)C</chem>	<chem>Cc1ccccc1</chem>
Au								
		Metal Au	Metal Au	Metal Au/ Graphite				
Ag								
		Metal Ag/ Oxide AgO	Metal Ag	Metal Ag	Metal Ag	Metal Ag/ Carbon	Metal Ag/ Carbon	Metal Ag/ Graphite
Fe								
		Fe_3O_4 , Fe_2O_3 , $Fe(OOH)_2$	Fe_3O_4 , FeC_3	Fe_3O_4 , Carbon	Fe_3O_4 , Carbon	Metal Fe/ Fe_3O_4	Metal Fe/ Carbon	Fe-Carbide/ Graphite

Figure 2.8 Summary of the different kind of surface composition of MeNPs in colloidal dispersion obtained from PLA of Au, Ag, and Fe targets in water and different organic solvent) [6].

The new insight on PLA coming from our experimental results, put in evidence not only the effect of the liquid where PLA is performed, but also shows the importance of the gaseous species content. Nevertheless, in 2019 three articles were published on PLA of the metal target in pure water by the group of Prof. Stephan Barcikowski of the University of Duisburg Essen , putting in evidence the generation of different kinds of gases inside the water solution [32, 33, 180].

When the cavitation bubbles produced during the plasma expansion collapse, they give rise to the second type of bubbles, called persistent microbubbles. Both the cavitation and persistent bubbles can act as shadowing entities and may absorb a significative part of the energy of the laser pulse [181]. Persistent bubbles may have a big influence on the NPs productivity also when working at a low repetition rate (i.e 10 Hz) since their typical lifetime goes from hundreds of ms to s [32]. Figure 2.9 a), represent the shadowgraphs of the persistent microbubbles created by PLA of different metal targets after 100 ms from the arrival of the laser pulse [32]. The composition of the persistent bubbles has been recently analyzed by Kalus *et.*

al. [32] using gas chromatography. As represented in Figure 2.9 b, c), together with hydrogen and hydroxyl radicals, H_2 , O_2 , N_2 , and H_2O_2 can be found between the gaseous products inside the bubble. The results are explained in terms of laser-induced water break- and ultrasound-induced by laser pulses in the liquid [182], which, depending on the laser pulse fluence, naturally happens in PLA, also without the presence of any target.

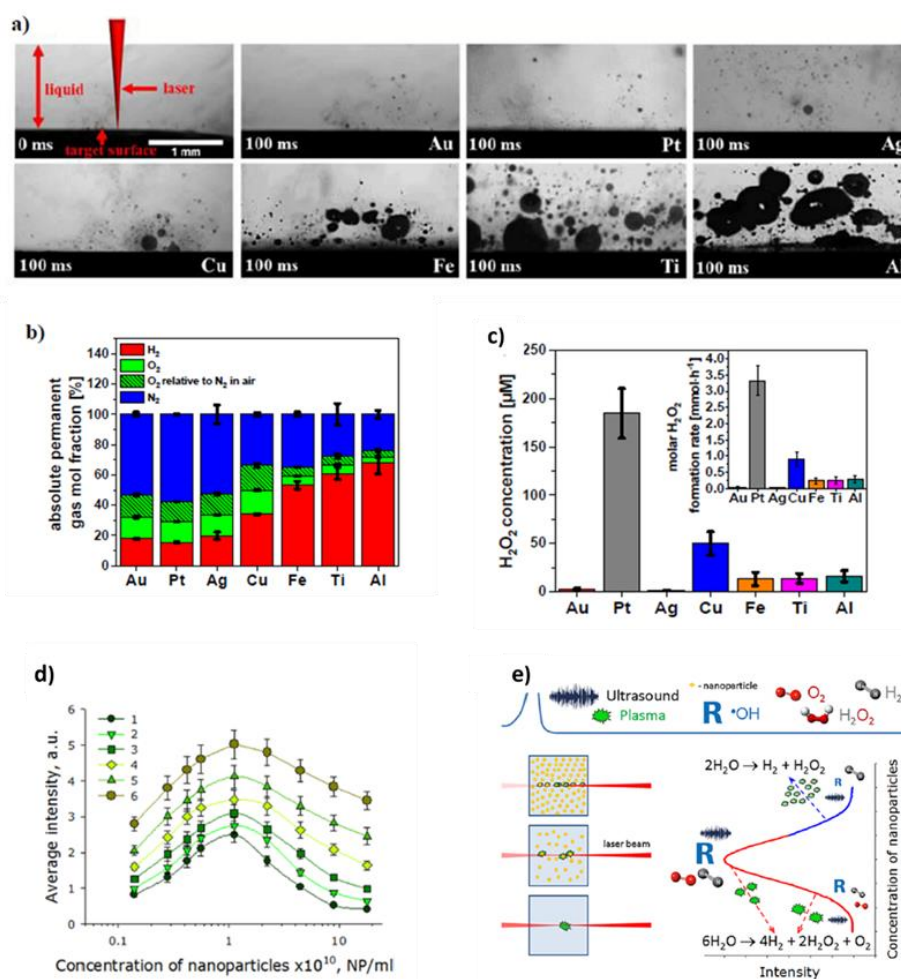


Figure 2.9 a) Shadowgraphs of the persistent microbubbles created by PLA of different metal targets after 100 ms from the arriving of the laser pulse [32]. b) H_2 , O_2 , and N_2 gas fraction in the permanent bubbles, depending on different metal targets [32]. c) Concentration of H_2O_2 produced during PLA in the water of different metal targets [32]. d) Intensity of the acoustic waves produced during PLA depending on AuNPs concentration [33], e) Gas production rate during PLA depending on AuNPs concentration [33].

Recent experiments by V. Sumakin *et al.* [33], demonstrate that both the water break-down probability and the relative gas production rate reach their maximum when an average concentration of about $\sim 10^{10}$ AuNP/ml is obtained. As represented in Figure 2.9 d,e, this particular value of NP concentration creates the maximum

intensity of the supersonic acoustic waves created after the cavitation bubble collapse.

Hence, the unique presence of metal NPs, enhances the gas production rate and is responsible for the activation of the reactions using the alternative energy channel of the supersonic acoustic waves.

The fundamental work of A. De Giacomo in collaboration with S. Barcikowski about the experimental study of the thermodynamic parameters P and T during the cavitation dynamics [183], put in evidence that most part of the NPs are near the target surface after the cavitation bubble collapse, suggesting their formation during this stage. The mechanism involving the formation of the NPs should happen on a time-scale of the order of $\sim 100 \mu\text{s}$, and involving a range of temperatures and pressure ranging from hundreds of K and $\sim 1 \text{ MPa}$, to about 10^4 K and 10^3 MPa , reaching the highest value at the moment of the collapse of the bubble on the metal targets [184]. Anyway, the authors do not exclude the possibility that a first part of the NPs may be formed by the cold external part of the plasma plume, before the birth of the cavitation bubble, and further transported into the latter. The transportation of the NPs into the cavitation bubble happens at the interface between the coldest part of the plasma and the layer of the surrounding vapors of the solvent [183]. In the light of these results, it is immediately before and after the collapse of the cavitation bubble that the formed NPs have the opportunity to interact with the gases and liquid present in the PLA environment, and be responsible for chemical reactions.

The dynamics of the cavitation bubble and supersonic acoustic waves created by the interaction of the laser pulse with the target and with the formed NPs, are hence probably responsible for the CO_2/C reduction process observed during our experiments.

In order to give a simplified vision of the PLA environment, we can identify three main regions during the temporal window of the plasma plume expansion and cooling, differentiated by the composition and state of the present elements. This schematic division is depicted in Figure 2.10.

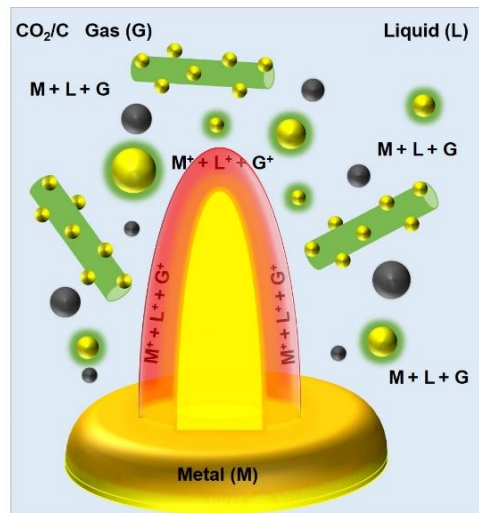


Figure 2.10 Schematic division of the PLA environment into different regions by the composition and state of the atoms. The picture shows the possible carbon nanostructures synthesized throughout our research, as defined in Section 1.

The hottest plasma near the target is essentially constituted by the metal ions and metal aggregates in an excited state, while the intermediate region finds the superposition of both, metal (M), liquid (L), and gas (G) atoms or molecules in the excited states. To the best of our knowledge [8], this is the first time that gaseous species different from N_2 and O_2 are included between the phases determining the final composition and functional properties of NPs synthesized by PLA.

2.2.2.

Stability of colloidal nanoparticles

Among the functional properties of the colloidal dispersion of NPs, the most important for NPs applications is stability. Two kinds of stability are generally introduced for the colloidal dispersion of NPs.

Stability with respect to oxidation (composition): when the colloidal NPs do not suffer further redox processes with time in the liquid environment where it is stored [185].

Stability with respect to aggregation (morphology): in this case, the NPs in the colloidal dispersion have enough repulsion to oppose the dipolar van der Waals (vdW) attractive force exists among them, without aggregation or

precipitation. In these conditions, no change occurs in the size and shape of the NPs with time [185]. Electrostatic stabilization and steric stabilization are the two main mechanisms for stabilization against aggregation.

In the first case, the mutual repulsion among the same electrostatic charge introduces electrostatic stabilization in colloidal dispersion of NPs. In a stable colloid of NPs, the latter is associated with the net charge of the NPs/external liquid interface, which is in general smaller than the charge on the NPs surface. The charge on the surface of the NPs is due to the functionalization of the particle surface with charged molecules, or to the ionization of surface groups. Because of electrostatic induction, the charged surface of a solid particle is hence readily surrounded by a thin layer of counterions, called the Stern layer, further surrounded by a diffuse layer of charges.

The electrostatic repulsion among the suspended colloidal NPs can easily be expressed in terms of the zeta potential, a measurable quantity describing electrical potential at the slipping plane in an electrical double layer (EDL, Stern and diffuse) around the particle. as represented in Figure 2.11. b.

When only electrostatic repulsion is considered (neglecting the steric repulsion), the stability with respect to aggregation is dictated by the balance between two opposites potentials, one deriving from the vdW attractive force (V_A) [5], and the other taking into account the overall electrostatic repulsion between the NPs (V_R). This theoretical approach follows the classical Derajuin-Landau-Verwey-Overbeek (DLVO) theory [186], which makes use of the following equations:

$$V_A = -\frac{H}{6} \left[\frac{2R_N^2}{h^2 - 4R_N^2} + \frac{2R_N^2}{h^2} - \ln \left(\frac{h^2}{h^2 - 4R_N^2} \right) \right] \quad (2.9)$$

$$V_R = \frac{\varepsilon \varepsilon_0 R_N \psi_o^2}{\frac{h}{R_N} + 2} \exp\left(-\frac{h}{\lambda_D}\right) \quad (2.10)$$

In equation (2.9) and (2.10), R_N is the radius of the NPs, and h is edge-to-edge distance between them. H is the Hamaker constant, ψ_o represents particle surface potential, and λ_D is the Debye's length [187]. The value of the latter diminishes

drastically in the presence of salts or other ionic species (physiological media), which provokes an effective shield effect of the electrostatic repulsion, with the final agglomeration of the NPs [89]. In this case, the Van der Waals force among MeNPs can be reduced by encapsulating the MeNPs in a material with a relatively lower value of Hamaker constant. Therefore, polymeric surfactant [188], silica [189] or carbon [190] are deposited over the surface of MeNPs by opportune chemical protocols, enhancing the stability with respect to both agglomeration and oxidation [191]. In the literature, a few studies were focused and dedicated to the control of the physicochemical properties of noble MeNPs synthesized by PLA in water with the simple addition of salts or hydroxides [20, 192]. In the latter cases, it is assumed that the negative charge and stability of the colloidal system is associated with the presence of hydroxyl and/or carbonates complexes on the oxidized portion of the metal surface [193] and, in the case of Au, to an excess of free-electron inside the metal core of the NPs [5]. In the case of Ag and Fe targets, oxidation is still the principal cause of the electrostatic stability, but the reactivity of the oxides may increase stability and dissolubility [194–196]. The charge and dissolution of AgNPs depended on the pH of the solution [197, 198]. In literature [199], AgNPs synthesized in water by PLA have a negative charge, due to oxidation of the surface [199]. The charge of iron-based NPs colloids synthesized by PLA are found to be pH-dependent and are positive in pH lower than 6 or 7, while their charge becomes negative if the pH of the solution is higher than pH7 [200].

Hence, transition metal NPs synthesized by PLA in water are definitively thought to be characterized by pure electrostatic stability, and there is no mention in the literature about the possibility of the simultaneous formation of carbon material supplying an electro-steric stabilization. Steric stabilization consists in fact, in covering the particles in polymers which prevents the particle to get close in the range of attractive forces, thanks to both elastic recoil effects and osmotic pressure [186], as sketched in Figure 2.11.

Figure 2.11.d, shows the dependence of the potential energy of the particles in function of their distance. The inclusion of the steric repulsion in the DLVO theory leads to the so-called extended DLVO model (X-DLVO), which considers a total potential energy (blue dashed curve) consisting of the attractive vdW contribution

(red curve, equation 2.9), and the repulsive EDL (green curve, equation 2.10) and steric (cyan dotted curve) contributions.

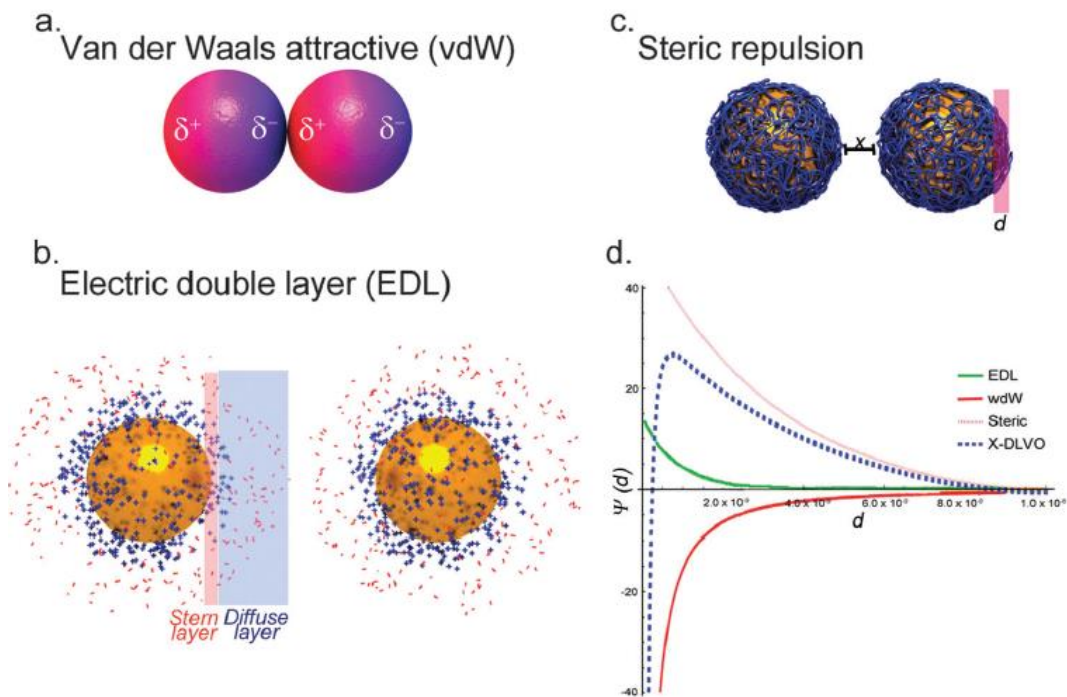


Figure 2.11 Scheme of the principal interactions between colloidal nanoparticles. a) vdW dipolar repulsive interaction. b) Steric repulsion, induced after functionalization of the particles with macromolecules or polymers. c) Electro-static repulsion, due to the net charge considering the EDL, consisting of the Stern and diffuse layer. d) Contribution of the EDL potential (green curve), repulsive vdW potential (red curve) and steric repulsion (dotted cyan curve) to the overall X-DLVO potential (blue dashed curve) in the function of the interparticle distance d . Adapted from [186].

The stability concepts discussed in the present sub-section apply to all the nanomaterials, independently of their particular composition. We will focus now our attention on a special kind of NPs, the noble MeNPs, whose optical properties are at the basis of the enhanced spectroscopies used along with the present research. We will introduce the concept of LSPR resonance in noble metal nanostructures and will show how to use the Mie theory for the optical modeling of the experimental UV-Vis spectra, with the theoretical calculus of the concentration of both metal atoms and MeNPs.

2.2.3.

Optical properties of noble metal nanoparticles colloids

Plasmons are a collective and discrete number of oscillations of the free electron gas density in metals. In the classical picture, Plasmon can be described as an oscillation of electron density with respect to the fixed positive ions in a metal. To understand plasma oscillation, let us consider a cube of metal placed in an external electric field directed to the right side. Electrons will move to the left side and will create enough positive charge on the right side until they produce an opposite induced electric field and cancel the field inside the metal. When the external electric field will be removed, they will move to the right again due to the mutual repulsion of electrons and the attraction of positive charge on the right side. Electrons will oscillate back and forth at the plasma frequency until the energy is lost in some kind of resistance or damping.

The quantized collective oscillation of quasi-free electrons on the metal-dielectric interface is known as surface Plasmon resonance (SPR) [201]. When these coherent electrons oscillations are coupled to electromagnetic radiation (EM), they generate a bound electromagnetic mode that propagates along with the metal/dielectric interface, which is called Surface Plasmon Polariton (SPP) [201]. This excitation depends on the polarization of incident radiation and the geometry of the metal and dielectric interface surface, which is extensively useful for sensing applications [202].

In contrast to SPP, LSPR is a non-propagative excitation of the Plasmon. When the sizes of the NPs are smaller than the wavelength of irradiating EM radiation used for excitation, the electromagnetic field of the incident light exert a uniform force on the free conduction electrons inside the MeNPs, and displaces them to one side of the surface, creating a positive charge on the opposite side. As a result, internal electric polarization dipoles are created, which have a net electric field opposite to the incident electric field as shown in Figure 2.12, providing an internal restoring force to displace back the electron. In this way, the electrons start oscillating inside the MeNPs, and act as a forced quantum oscillator.

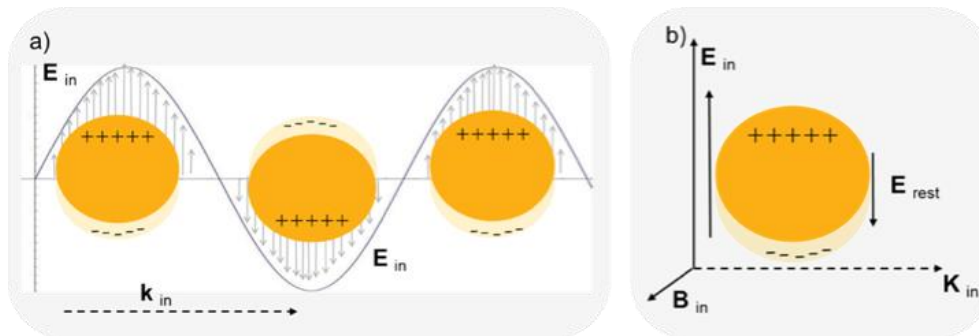


Figure 2.12 (a) Schematic diagram of collective oscillation of free electrons in MeNPs, arising from interaction with the incident EM planar wave. (b) The direction of the induced electric field (E_{rest}) and incident electric field (E_{in}).

The electrons inside the NPs are characterized by a natural frequency of resonance, called plasmonic frequency, or LSPR. When the frequency of incident EM radiation matches with the plasma frequency, it generates a stationary LSPR mode, with an enhancement of the near-field around the NPs which, depending of the particular geometry and material, may reach 4 or 5 orders of magnitude [201]. The increased EM near field is associated with both absorbed and scattered EM fields so that the MeNPs have very high absorption and scattering cross-section in the resonance, which are fundamental to obtain the high enhancement factors and high sensitivity in SERS and UV-Vis spectroscopy, respectively [203, 204].

Fortunately, the LSPR band for noble MeNPs exists in the visible region, which provides a specific color to their colloidal solution, due to resonantly enhancement effects of both scattering and absorption. This combined effect of absorption and scattering in the ultraviolet-visible absorption spectra is called extinction. While the basic characteristics of the LSPR phenomena, such as the Frolich condition [201] can be obtained using the simple Quasi-Static Approximation (QSA), in order to simulate the UV-Vis extinction spectra of a real colloidal dispersion of NPs, it is necessary to make use of the Mie's theory [205] and take in account the statistical polydispersity of the samples.

2.2.3.1.

Quasi-static approximation and Mie theory

- **Quasi-static approximation (QSA)**

When an EM field interacts with the MeNPs it can generate dipolar, quadrupole, and octupole modes in each NPs (depending on the sizes) If the size $r = a$ of the NPs is very smaller than the wavelength (λ) of the incident light ($a \ll \lambda$), the dipolar mode has a strong contribution to absorption and scattering as compared to other modes. In this case, the incident harmonically oscillating EM fields are approximately uniform inside the NPs, so that an electrostatic approximation can be used to solve the related problem[206].

To derive the mathematical equation for electric the polarizability (α), and the absorption (σ_{abs}) and scattering (σ_{scat}) cross-section of MeNPs , let us consider an isolated spherical NPs with radius $r = a$, as shown in Figure 2.13. Since $r \ll a$, the electromagnetic field phase will be considered uniform throughout the NPs, in a first approximation.

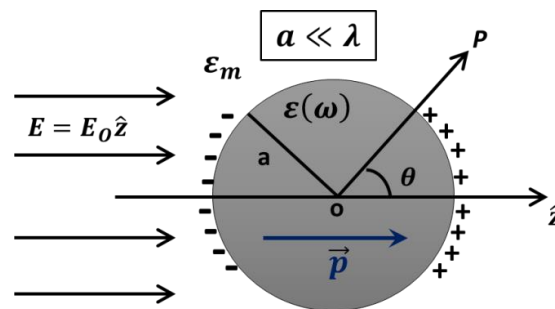


Figure 2.13 Schematic diagram of a spherical NPs of radius a , under the excitation a uniform static electric field polarized along the Z axis. In QSA we are considering $a \ll \lambda$.

The dielectric constant of the metal constituting the NPs is $\varepsilon(\omega)$, and the dielectric constant of the surrounding medium is ε_m . We consider an incident electric field $\vec{E} = E \hat{Z}$, and solve the Laplace equation $\nabla^2 \phi = 0$ for the electrostatic potential $\phi(\vec{E} = -\nabla \phi)$ with boundary conditions at $r \rightarrow \infty$ and $r = a$. We obtain the equations

$$\phi_{out} = -E_0 r \cos \theta + \frac{\varepsilon(\omega) + 2\varepsilon_m(\omega)}{\varepsilon(\omega) + \varepsilon_m(\omega)} \frac{E_0 a^3 \cos \theta}{r^2}, \quad (2.11)$$

and,

$$\phi_{in} = -\frac{3\varepsilon_m(\omega)}{\varepsilon(\omega)+2\varepsilon_m(\omega)} E_o r \cos \theta, \quad (2.12)$$

where ϕ_{in} and ϕ_{out} are electric potential inside and outside the sphere of radius a .

We recognize that (2.11) may be written as

$$\phi_{out} = -E_o r \cos \theta + \frac{1}{4\pi\varepsilon(\omega)\varepsilon_m(\omega)} \frac{p \cdot r}{r^3}, \quad (2.13)$$

$$\mathbf{p} = 4\pi a^3 c \varepsilon_m(\omega) \frac{\varepsilon(\omega)-\varepsilon_m(\omega)}{\varepsilon(\omega)+2\varepsilon_m(\omega)} E_o \hat{\mathbf{z}}, \quad (2.14)$$

where, \mathbf{p} is the induced dielectric dipole, proportional to applied field \mathbf{E}_0 inside the sphere.

Considering $\mathbf{p} = \varepsilon_0 \varepsilon_m \alpha(\omega) \mathbf{E}_o$, we derive

$$\alpha = 4\pi a^3 \frac{\varepsilon(\omega)-\varepsilon_m(\omega)}{\varepsilon(\omega)+2\varepsilon_m(\omega)}. \quad (2.15)$$

As shown in equation (2.15), the polarizability is enhanced when the real part of the denominator $\varepsilon(\omega) + 2\varepsilon_m(\omega)$ vanishes, that is

$$Re[\varepsilon(\omega)] = -2\varepsilon_m(\omega). \quad (2.16)$$

The optical cross-sections σ_{abs} and σ_{scat} maybe written as

$$\sigma_{scat} = \frac{k^4}{6\pi} |\alpha(\omega)|^2 = \frac{8\pi}{3} k^4 a^6 \left| \frac{\varepsilon(\omega)-\varepsilon_m(\omega)}{\varepsilon(\omega)+2\varepsilon_m(\omega)} \right|^2, \quad (2.17)$$

$$\sigma_{abs} = k Im[\alpha(\omega)] = 4\pi k a^3 Im \left[\frac{\varepsilon(\omega)-\varepsilon_m(\omega)}{\varepsilon(\omega)+2\varepsilon_m(\omega)} \right], \quad (2.18)$$

where k is the wave vector. Clearly, when the resonance condition 2.11 is fulfilled, the NPs experiment an enhancement in both absorption and scattering efficiency, so that a band with a clear peak appears in this spectral region [201]. Fröhlich's condition can explain also the typical red-shift obtained in the LSPR spectra of colloidal MeNPs when interacting with external analytes, used commonly as a detection method in LSPR optical sensing [201]. In the equations above, σ_{abs} is proportional to a^3 , while σ_{scat} scales with a^6 . This is the reason why the extinction spectra of relatively large size NPs will be dominated by scattering in comparison with absorption, while it is very difficult to pick out small particles in the large scattering background. The QSA gives accurate results only for small spherical NPs

($r < 4$ nm), but fails in describing the LSPR red-shift scaling with the NPs diameter, so that correct modeling of the optical properties of a real and polydisperse colloidal dispersion of NPs, needs the introduction of a more general electromagnetic theory, called Mie theory, used to retrieve the extinction spectra of metal NPs with all dimension, and both spherical or elliptical geometries[207].

- **Mie Theory**

The German scientist *Gustav Mie* in 1908 [208] proposed an exact analytical solution of Maxwell's equations for the scattering and absorption of EM radiation by spherical, homogenous, isotropic, and non-magnetic particles with an arbitrary size in a non-absorbing medium. His attention was to determine the extinction spectra of AuNPs of different sizes in solution and understand their color. In Mie's approach, Maxwell's equations are solved analytically by using appropriate boundary condition, and the calculated extinction cross-section are given by [205]:

$$\sigma_{ext} = \frac{2\pi}{|k|^2} \sum_{L=1}^{\infty} (1 + 2L) [Re(a_L + b_L)] , \quad (2.19)$$

where L is the integer used for the representation of dipole ($L=1$), quadrupole ($L=2$), and higher order multipoles and k is the light wave vector.

The a_L and b_L terms in equation (2.19) consist of the Riccati Bessel functions ψ_L and χ_L :

$$a_L = \frac{m\psi_L(mx) \cdot \psi'_L(x) - \psi'_L(mx) \cdot \psi_L(x)}{m\psi_L(mx) \cdot \chi'_L(x) - \psi'_L(mx) \cdot \chi_L(x)} , \quad (2.20)$$

$$b_L = \frac{\psi_L(mx) \cdot \psi'_L(x) - m\psi'_L(mx) \cdot \psi_L(x)}{\psi_L(mx) \cdot \chi'_L(x) - m\psi'_L(mx) \cdot \chi_L(x)} . \quad (2.21)$$

In the latter, $x = (|k| \cdot a)$ (a is the radius of the NPs), and $m = \tilde{n}/n_m$, where $\tilde{n} = n_R + in_I$, represents the complex refractive index of the metal, and n_m state for the refractive index of the surrounding medium and similarly complexes dielectric constant is $\varepsilon(\omega) = \varepsilon_R(\omega) + i\varepsilon_I(\omega)$, (where, $\varepsilon_R(\omega)$ is real and $\varepsilon_I(\omega)$ is the imaginary part). If we consider only the first term in equation (2.19) ($L = 1$), we obtain again the expression

$$\sigma_{ext} = \frac{24\pi^2 a^3 \varepsilon_m(\omega)^{3/2}}{\lambda} \frac{\varepsilon_I(\omega)}{(\varepsilon_R(\omega) + 2\varepsilon_m(\omega))^2 + \varepsilon_m(\omega)^{3/2}}. \quad (2.22)$$

To retrieve the correct extinction spectra of the NPs, retardation potential effects have to be considered, and the other terms with $L > 1$ have to be added in equation (2.19). In Appendix A.1 we report the code we developed using the software Matlab® R2017, consisting in the calculus of the extinction spectra of a colloidal dispersion of MeNPs with no limit of dimension, and characterized by an opportune statistical size distribution. The statistical size distribution is a *log-normal* function [207], which we will in principle consider monomodal due to the *ns* duration of the laser pulse, as explained previously in Section 2.2.1. The parameters of the *log-normal* function are fitted using the experimental statistical size obtained by TEM measurements, after which the theoretical extinction spectra may be calculated by our code, and compared with the experimental spectra.

Once obtained a good fitting on the experimental extinction spectra we have three important information:

- the statistical size distribution obtained by experimental TEM images is representative of the whole sample;
- the sample was no subject to a significative agglomeration or chemical activity (i.e oxidation), since the fitting is obtained on the hypothesis of non-interacting NPs and non-oxidized NPs [209].
- we have access to the theoretical value of both the metal and NPs concentration

2.2.3.2.

Theoretical calculation of metal and MeNPs concentration

The extinction efficiency, or the optical density, is an optical parameter of a sample (liquid or solid) representing the optical power lost by scattering and absorption of EM radiation at different wavelengths. The correct experimental measure and theoretical modeling of the optical density of a colloidal dispersion of MeNPs, can be used to determine both the molar concentration of NPs or the metal mass concentration.

To simulate the UV-Vis spectroscopy experiment, let's consider a general colloidal suspension of NPs irradiated by a plane wave EM radiation in a transparent cell of length d , as shown in Figure 2.14.

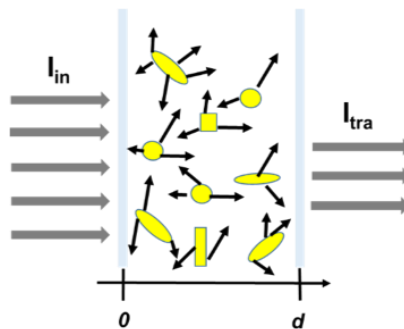


Figure 2.14 Schematic diagram used to explain the measurement of the extinction spectra of the NPs illuminated by plane EM radiation.

Let us neglect the multiple reflections by the cell wall. The ratio of transmitted to incident EM radiation is called transmittance and denoted by $T(\lambda)$, where λ is the corresponding wavelength of illuminating EM radiation [120]:

$$T(\lambda) = \frac{I_{tran}(\lambda)}{I_{inc}(\lambda)}. \quad (2.23)$$

The transmittance is related to the optical density $\tau(\lambda)$ through the relation

$$\tau(\lambda) = -\log_{10} [T(\lambda)]. \quad (2.24)$$

Equation (2.23) and (2.24) are appropriate for all particle shapes and can be used to determine the optical properties, concentration, and, indirectly, the topologies of NPs. The Lambert-Beer law is used to relate $T(\lambda)$ to $\tau(\lambda)$, considering that the irradiance of the EM radiation is exponentially attenuated from I_{in} ; to I_{tra} passing a geometrical distance d inside the sample. It holds the relation

$$T(\lambda) = \frac{I_{tran}(\lambda)}{I_{inc}(\lambda)} = e^{-e(\lambda)d}, \quad (2.25)$$

where $e(\lambda)$ is the extinction coefficient, which can be expressed as

$$e(\lambda) = \sigma_{ex}(\lambda) \frac{N}{V}. \quad (2.26)$$

In the latter, N / V is the NP number concentration, and the extinction cross-section is expressed in the unit of m^2 . Putting the equations (2.25) and (2.26) in (2.4), we obtain:

$$\tau(\lambda) = \sigma_{ext}(\lambda) \frac{N}{V} \log(e) d. \quad (2.27)$$

Equation (2.27) is a theoretical model applicable to compute the extinction spectra of monodispersed NPs, which is not the case of a real colloidal dispersion of NP, characterized by a finite value of the poly dispersivity, which can significantly alter the shape and intensity of the spectra. In the case of the statistical size distribution for the NPs, the optical density will be the sum of all the different contributions, expressed as

$$\tau(\lambda) = \sum_k \sigma_{ex}(\lambda, R_k) \frac{n_k(R_k)}{V} \log(e) d. \quad (2.28)$$

Above, R_k represents the particle size, and the concentration of the particles with such a radius in volume V is denoted by $n_k(R_k)/V$. We define the normalized statistical size distribution of particles as

$$n_{norm}(r) = \frac{n(r)}{\sum_k n_k(R_k)} = \frac{n(r)}{N_{total}}. \quad (2.29)$$

Using the normalization condition $\int_0^\infty n(r) = 1$, [205] we obtain

$$n_{norm}(r) = \frac{1}{\sqrt{2\pi}wr} e^{-\frac{[\ln r - \ln r_c]^2}{2w^2}}. \quad (2.30)$$

The parameters w and r_c (central value of the distribution) are linked to the mean value and standard deviation of the population, respectively.

In Figure 2.15 (a), we report the experimental statistical size distribution of Au@Cy NCs colloids [20] measured by TEM, and the corresponding Mie fit using the normalized *log-normal* function. From the experimental size distributions, we can calculate the statistical mean value $\langle r \rangle$ and standard deviation δ using the approach in (2.31) and (2.32), as

$$\langle r \rangle = e^{\ln r_c + \frac{w^2}{2}} \quad (2.31)$$

$$\delta = \sqrt{e^{w^2+2\ln r_c}(e^{w^2} - 1)}. \quad (2.32)$$

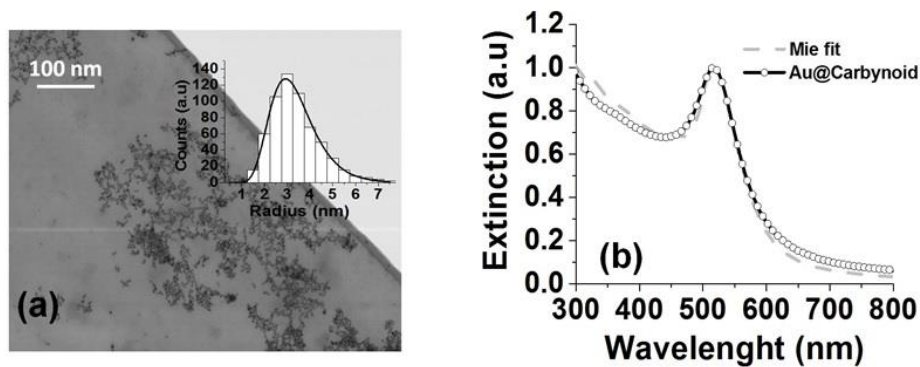


Figure 2.15 (a), TEM image of the Au@Cy NPs synthesized by PLA with NaOH concentration of 2 mM. In the inset is reported the experimental statistical size distribution of NPs. (b) Experimental extinction spectra of the synthesized NCs (black line with open circles), and Mie's theoretical fit (dashed grey line) obtained using the statistical distribution reported in (a) [20].

From the above example of Mie fitting, the exact concentration of gold in the water solution can also be calculated. The statistical extinction coefficient at λ can be expressed as [205]:

$$e(\lambda) = \int_0^\infty \sigma_{ext}(\lambda, r_k) \frac{N_{total}}{V} n_{norm}(r) dr. \quad (2.33)$$

In Figure 2.15 (b) are reported the experimental extinction spectra of the synthesized NCs (left term of equation (2.33) and the Mie's theoretical fit (left term of equation (2.33) obtained using the statistical distribution reported in Figure 2.15 (a), and the size-dependent dielectric function of small ($r < 5$ nm) MeNPs, for which an additional scattering term of the conduction electron with the boundary of the NPs has to be considered [210]. There is an almost perfect overlap between the experimental UV-Vis spectra and the theoretical Mie fit, which makes us confident about the experimental size distribution obtained by TEM measurements.

The metal mass concentration per unit volume of a monodispersed colloidal dispersion of NPs can be written as:

$$C_{Metal} = \frac{N_{total}}{V} \times V_{NPs} \times \rho_{Metal} = \rho_{NPs} \times V_{NPs} \times \rho_{Metal} , \quad (2.34)$$

where ρ_{NPs} is the concentration of NPs per unit volume, ρ_{Metal} is the density of the metal constituting the NP, and V_{NPs} is the volume of a single NP, the same for each one. In the more realistic case of an experimental polydispersed colloidal dispersion of NPs, we have to determine $N_{total}/V = \rho_{NPs}$, and to weight the single NP volume with the statistical *log-normal* size distribution.

The concentration of NPs ρ_{NPs} can be measured from the optical density and Mie fitting, using the relations:

$$\tau_{exp}(\lambda) = d_{exp} \log(e) \frac{N_{total}}{V} \left[\int_0^{\infty} \sigma_{ext}(\lambda, r_k) n_{norm}(r) dr \right]_{Mie\ fit} , \quad (2.35)$$

and,

$$\rho_{NPs} = \frac{N_{total}}{V} = \frac{\tau_{exp}(\lambda)/d_{exp} \log(e)}{\left[\int_0^{\infty} \sigma_{ext}(\lambda, r_k) n_{norm}(r) dr \right]_{Mie\ fit}} . \quad (2.36)$$

Here the path length of the cuvette containing NPs colloid is $d_{exp} = 1\text{cm}$, $\tau_{exp}(\lambda)$ can be measured experimentally, while the denominator can be calculated from Mie fitting.

The mass concentration is finally given by the expression

$$C_{mass} = \rho_{NPs} \rho_{Metal} \int_{r_{min}}^{r_{max}} n_{norm}(r) V_{NPs}(r) dr, \quad (2.37)$$

where $V_{NPs} = (4\pi r^3/3)$ is the volume of a single spherical NP with radius r , and $\rho_{Metal} = 19.32\text{ gm/cm}^3$. Using the code developed in the *Matlab® R2017a* framework (Appendix A.1), we calculated a mass concentration relative to the sample of Figure 2.15 of about 82 ppm, which matches extremely well with the experimental concentration measured by ICP-MS in chapter 4.

Considering the modeling of the optical cross-sections of colloidal dispersions of noble MeNPs we found problems relatively to two main aspects:

- 1) the oxidation and permanent chemical activity of AgNPs, so that a dielectric function different from the one of metal silver should be used;

- 2) a blue-shift up to about 10 nm in the LSPR peak position of the Au@Cy NPs in comparison to the theoretical one, the origin of which will be explained in the next sub-section.

2.2.3.3.

Effect of size on the extinction spectra of noble MeNPs

As explained in the previous sub-section, the extinction spectra are powerful experimental information [101], which can give direct access to different properties of the NPs in colloidal dispersion, such as size, material, and stability. This is particularly true in the case of noble MeNPs, characterized by a well visible LSPR band. In fact, most of the time is the spectral position and intensity of the spectra at the LSPR peak that is used to interpret the extinction spectra based on the NPs properties. The case of iron oxides is quite complicated cause not only to the absence of an LSPR peak as a reference but also to the high level of oxidation of the NPs, which alters completely the shape of the extinction spectra and eludes the possibility to perform a theoretical realistic optical model. Most of the literature is hence dedicated to the relation of the UV-Vis spectra of noble MeNPs (Au, Ag) with their size.

In Figure 2.16, the extinction spectra of AuNPs on their dimensions are shown theoretically, separating the NPs with a radius smaller (a) and larger than 10 nm (b) [210].

Herein, Scaffardi *et. al.*) [210] show both theoretically and experimentally that LSPR peak position of AuNPs with radii less than 10 nm is practically size-independent (Figure 2.16 (a)), while a clear red-shift occurs when increasing the size for radius bigger than 10 nm (Figure 2.16 (b)). When the size of AuNPs is comparable with the mean free path of an electron, the oscillating electron scatters on the boundary of the NPs, and damping occurs in its energy, with further broadening of the curve, resulting in a net increase of the Full-Width Half Maximum (FWHM) of the curve. As clearly visible in Figure 2.16 (a), we find that the extinction spectra of AuNPs with a radius smaller than 3 nm are size-dependent, where the ratio between the minimum intensity near to 450 nm and maximum intensity (near 520 nm) in extinction spectra, is linearly dependent on the mean size

of AuNPs. This effect is of particular importance for the Au derived NPs synthesized in the present research since, as will be shown in details in Section 4 and 5, all of them are characterized by mean radius ranging from 2.5 nm to 4.0 nm, and can be considered as ultrasmall NPs [137].

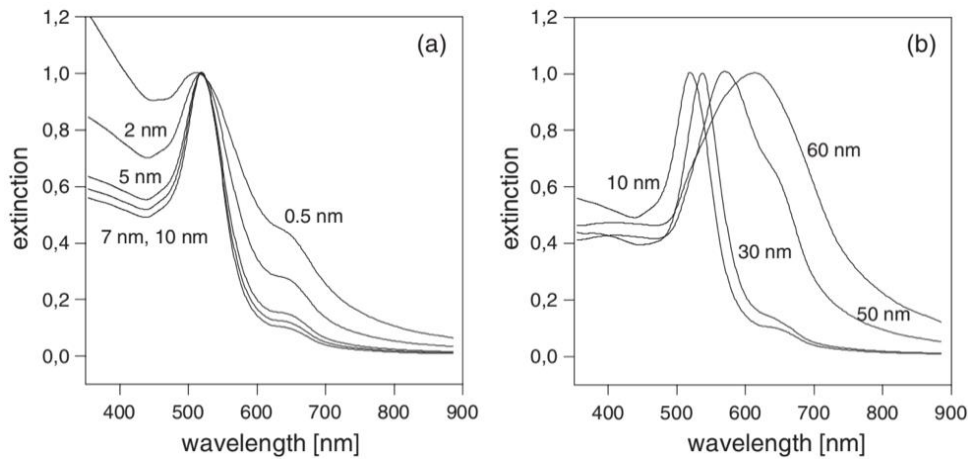


Figure 2.16. Normalized theoretical extinction spectra of AuNPs with a) $r < 10$ nm, b) $r > 10$ nm [210].

Ultrasmall AuNPs are also characterized by another interesting effect. The control in the LSPR peak position is generally done by changing the solvent refractive index, or synthesizing NPs of progressively bigger diameters, and obtaining the desired red-shift, as shown in Figure 2.16 (b). Uniquely for the case of ultrasmall AuNPs, exist examples in the literature of a blue-shift of the LSPR position, obtained by the control of the excess of charge in the metal core of the MeNPs [39, 213]. In this case, the shift in the LSPR peak is mathematically linked in a first approximation to the change in the number of free electrons, and can be expressed by the following equation by Templeton *et. al.* [213]:

$$\frac{\lambda_{LSPR}^{final}}{\lambda_{LSPR}^{init}} = \frac{N_{init}}{N_{final}}. \quad (2.38)$$

In the last, N_{init} and N_{final} represent the initial and final concentration of the free electrons participating in the plasma oscillation, while λ_{LSPR}^{init} and λ_{LSPR}^{final} stand for initial and final LSPR peak position. Equation (2.38) clearly shows that a blue shift occurs in LSPR peak when an excess electron is induced over the AuNPs surface ($N_{init} < N_{final}$). As will be discussed in details in Section 5, this is what might happen in the case of the ultra-small Au derived NPs, where the excess of

free electrons may be obtained by the interaction of the gold core with the electrons of the $sp-sp^2$ carbon atomic wires (CAWs) in the shell [214], and through Au-carbonyl species formed at the metal–dielectric interface of the NCs. Both the participation of the CAWs electron to the plasma oscillation and the π -back bonding in metal–CO system [213], enhances the number of available conduction electrons in the d-band of Au, participating to the observed blue-shift.

In the case of Au, as demonstrated before, it is possible to obtain very good matching between the theoretical and experimental extinction spectra, together with the correct value of both NPs and metal concentration. This positive result is associated to the chemical stability of AuNPs, which do not suffer further oxidation in the colloidal suspension, so that their dielectric constant doesn't change with time, and is available by different databases and articles present in literature. Completely differently from AuNPs colloids, AgNPs are subject to oxidation instability, which is responsible for the change of their dielectric constant during the time [215]. For this reason, it is difficult to extract the same analytical information as we obtained from of AuNPs colloids.

When dealing with AgNPs, some recurrent behavior of the UV-Vis spectra with the NPs dimensions has been observed [81]. Figure 2.17 shows the dependence on the mean size of the particles of the experimental extinction spectra of AgNPs synthesized by PLA [40]. As for AuNPs, in the case of AgNPs with a dimension between 10 nm and 20 nm, there is a progressive red-shift of LSPR peak (from 398 nm to 402 nm), and an increase of the FWHM, due to the enhanced scattering cross-section, as shown in Figure 2.17 (a). Herein, A1, A2, and A3 samples have an average size of 20, 19, and 15 nm, respectively. Differently than the case of gold, with further decreasing of the size from 15 nm to less than 5 nm, the LSPR peak shifts toward a longer wavelength, and the FWHM of the curve increases, as shown in Figure 2.17 (b) [81].

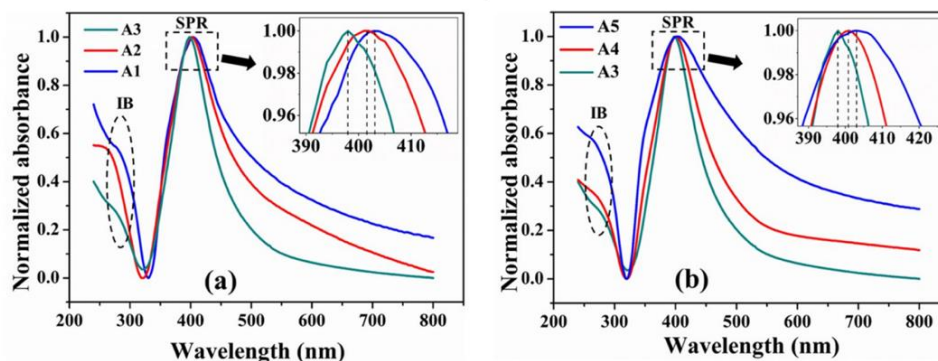


Figure 2.17 Experimental extinction spectra of a colloidal dispersion of AgNPs of different dimensions, synthesized by PLA. a) A1, A2, and A3 samples have an average size of 20, 19, and 15 nm, respectively [81]. b) A3, A4, A5 samples have an average size of 15, 12 and 10 nm, respectively [81].

The FWHM may become larger due to the scattering of the free electrons with the NPs boundary, as in the case of AuNPs, but the redshift may be attributed to a bigger effect that the oxidation of the silver surface has on the plasma oscillation in the case of small radius, where the ratio between the number of oxidized and metallic silver atoms may be higher, with an apparent loss of free electron density.

Both the blue and redshift occurring in the experimental LSPR peak of the small Au and Ag based nanoparticles synthesized in the present work might be well fit by theoretical curves obtained using Mie's theory for core-shell NPs [216]. A shell of carbynoid material and gaseous CO should be considered for the Au derived nanoparticles, while a thin oxide shell should be considered for the Ag derived particles. Although representing an interesting and alternative model to describe the optical properties of the synthesized small Au and Ag nanoparticles, this picture is far from reality. In fact, the oxide species in AgNPs are not necessarily uniformly distributed on the surface of the particle and are not necessarily confined in the external shell. In the case of Au derived nanoparticles, the simple Frolich condition [201] (equation 2.16), cannot explain alone the observed blue-shift since, as explained before, a core electron excess is expected from the particular interaction between the gold core and both CO and CAWs.

While UV-Vis spectroscopy gives important analytical and morphological information on the NPs, in most of the cases, it gives qualitative information about

their exact surface chemistry, which has to be collected by the use of vibrational spectroscopies, operating in a different range of optical frequencies and energies. The following sub-section will be dedicated to the vibrational spectroscopies used along the research, with special attention to Raman and SERS spectroscopies.

2.3.

Optical vibrational spectroscopy

IR and Raman spectroscopies are used to investigate the vibrational and rotational states of molecules or crystals and have been applied in the present research in the spectral range between 200 and 3500 cm^{-1} , corresponding to energies between 25 and 400 meV. Vibrational spectroscopies can give precise information on the chemical composition, functional groups, and hybridization of a different kind of NPs [217, 218]. IR and Raman are complementary spectroscopic techniques since different selection rules exist between them. While IR spectroscopy is effective only on the excitation of vibrational states with a non-zero transition dipole moment [219] the Raman response is obtained only by excitation of modes characterized by a net variation of the polarizability of the structure [220]. This is the reason why the IR cross-section is about 8 orders of magnitude higher than the one of the Raman process ($10^{-21} \text{ cm}^2 \text{ Vs } 10^{-29} \text{ cm}^2$) [221] so that a more concentrated sample or a bigger quantity of nanomaterial is needed to have a well definite Raman spectrum, in comparison to IR spectroscopy.

2.3.1.

Raman spectroscopy

To understand the origin of the Raman response let's have a look at Figure 2.18, where we suppose to excite the molecules of a certain material using laser radiation with a frequency ω_{laser} . When the molecules interact with the incident radiation, they are instantaneously excited to a virtual electronic state, and simultaneously fall back to its original energy state by emitting a photon with the same frequency of the laser source.

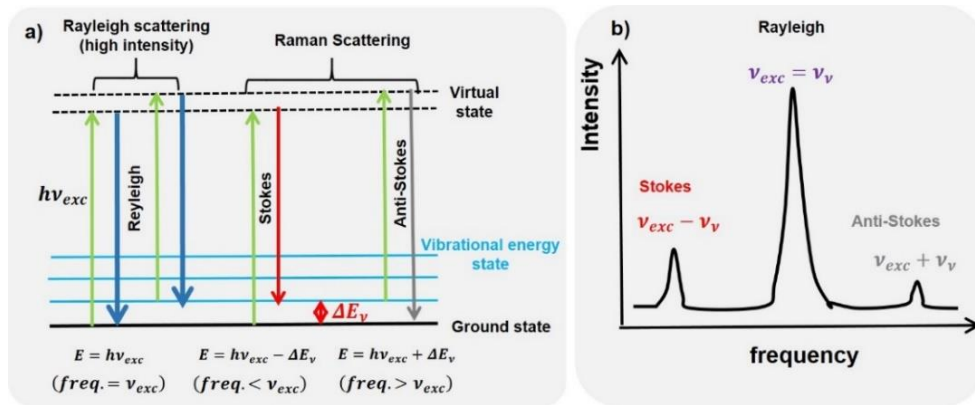


Figure 2.18 Energy level diagram representing the Raman response of a material. (b) Typical Raman spectrum showing the higher and weaker intensity peaks for Rayleigh, Stokes, and Anti-Stokes scattering respectively.

This phenomenon is called elastic Rayleigh scattering. However, a small fraction of photons (1 in 10^7 photons) may also return to a higher energy state (Stokes scattering) or lower (Anti-Stokes scattering) than the original state. This process leads to inelastic scattering, where the frequencies of the scattered photons are different from the frequency of the incident photons. This frequency modulation corresponds to the difference between the initial and final vibrational energy modes of the molecules and corresponds to the so-called Raman shift [220]. Part (b) of Figure 2.18, shows the typical difference in the intensity of the Stokes and Anti-Stokes scattered signals, which is not due to Raman optical process itself, but to the thermal equilibrium of the sample [217].

The Raman effect is based on the interaction between the external electric field of the monochromatic light with the electrons cloud of a sample, which can generate an induced dipole moment within the molecule based on its polarizability. When incident light interacts with a molecule, it induces a dipole moment \vec{p} , equal to the product of the polarizability α of the molecule and the electric field \vec{E} of the incident light source. This can be expressed as,

$$\vec{p} = \alpha \vec{E}. \quad (2.39)$$

We suppose that the nuclei of the molecules may vibrate around their equilibrium positions, where the variable Q_m represents the normal vibration mode, which is a collective vibration mode [201].

Using the small amplitude approximation, the polarizability can be described as a linear function of displacement. In this case, the variation in the polarizability with the vibration of the molecule can be expressed by the Taylor expansion of each element α_{ij} of the tensor α , with respect to the normal coordinates:

$$\alpha = (\alpha_{ij})_0 + \sum_m \left(\frac{d\alpha}{dq} \right)_0 Q_m + \frac{1}{2} \sum_{m,n} \frac{\partial^2 \alpha_{i,j}}{\partial Q_m \partial Q_n} Q_m Q_n . \quad (2.40)$$

Considering the molecular vibration along the m direction, we have

$$\alpha = (\alpha_{ij})_0 + \left(\frac{d\alpha}{dq} \right)_0 Q_m = (\alpha_{ij})_0 + (\acute{\alpha}_{ij})_k Q_m . \quad (2.41)$$

Considering that the m vibrational mode may oscillate at the frequency ω_m , it holds the expressions:

$$Q_m = Q_{m_0} \cos(\omega_m t + \delta_m) , \quad (2.42)$$

$$\alpha_m = \alpha_0 + \acute{\alpha}_m Q_{m_0} \cos(\omega_m t + \delta_m) , \quad (2.43)$$

where we insert in the polarizability tensor α_m the perturbation at the first order due to the particular molecular vibration m . Considering that the incident laser beam has a frequency ω_{laser} , we obtain the relations:

$$E(\omega_{laser}) = E_0 \cos(\omega_{laser} t) , \quad (2.44)$$

and,

$$P = \alpha \cdot E(\omega) = P^{(1)}(\omega_{laser}) + P^{(1)}(\omega_{Laser} - \omega_m) + P^{(1)}(\omega_{laser} + \omega_m). \quad (2.45)$$

From the latter equation, we understand that the excitation of the vibrational mode with frequency ω_m , leads to a Raman scattering of photons at the frequencies ω_{laser} , $\omega_{laser} + \omega_m$ (anti-Stokes), and $\omega_{Laser} - \omega_m$ (Stokes). Although the presented model cannot predict the different optical intensities in the Stokes and Anti-Stokes lines, it explains their origin in a simple mathematical frame and highlights the importance of the polarizability variation for the Raman activity of molecules or crystals.

The optical power P_{Raman} of the signal scattered at the frequency ω_s , can be written as

$$P_{Raman}(\omega_s) = KN \sigma_k^{free} I(\omega_{Laser}), \quad (2.46)$$

where K is the fraction of photon that is emitted from molecules and converted to the electron in the detector, N stands for the number of the irradiated molecule, σ_k^{free} is the Raman cross-section of the k^{th} mode of the free molecules, and $I(\omega_{Laser})$, is the laser intensity at the frequency ω_{Laser} [222]. Although the power of the Raman scattered radiation is proportional to the laser intensity (or optical irradiance in the case of a white lamp), it is never advised to use high optical irradiance, especially in the case of soft-matter carbon materials [20].

In Figure 2.19 we report the complete electronic energy diagram of a molecule, comprising of both the excited electronic and molecular states. Are also represented the main spectroscopic techniques used in the present research, together with their typical optical cross-section in cm^2 [221].

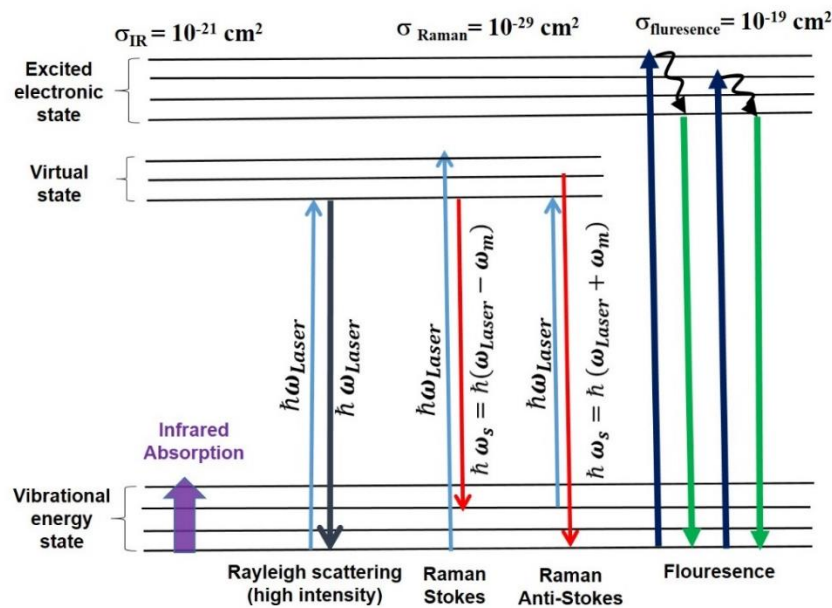


Figure 2.19 Complete electronic energy diagram of a molecule, comprising of both the excited electronic and molecular states. In the case of Raman spectroscopy, ω_{laser} is the frequency of the laser excitation, and ω_s is the frequency of the non-elastically scattered radiation after the activation of the Raman mode at frequency ω . For each kind of spectroscopy is reported the corresponding value of the optical cross-section in cm^2 [221]

Although Raman spectroscopy presents the less intense optical cross-section σ_{Raman} , we will show in the next sub-section that using noble metal nanostructures it is possible to enhance the scattered signals up to 10^{13} orders of magnitude, due to the amplification of the near field around a metal nanostructure in the LSPR condition [221]. In this case, the SERS effect may offer better sensitivity than IR spectroscopy, and used in the present scenario for the determination of the molecular groups complexed or adsorbed on the MeNPs themselves.

2.3.2.

SERS Spectroscopy

The chemical interaction (complexation) or the simple physical adsorption of molecules over the surface of noble MeNPs or nanostructures may lead, depending on the excitation frequency, to variations in both the Raman cross-section (polarizability tensor), and the Raman scattered power. As expressed in equation (2.47) in the case of the SERS effect [222], the overall optical power gain G_{SERS} is expressed as the product of two independent enhancement factors, an electromagnetic enhancement factor (G_{SERS}^{EM}) and a chemical enhancement factor (G_{SERS}^{chem}):

$$P_{SERS} = G_{SERS} \cdot P_{Raman} = G_{SERS}^{EM} \cdot G_{SERS}^{Chem} \cdot P_{Raman} \cdot \quad (2.47)$$

The chemical factor is generally negligible in comparison to the EM one, and its origins from the modification of molecular polarizability as a consequence of its physicochemical interaction with the metal surface [223]. In relation to equation (2.48), we can write,

$$P_{SERS}(\omega_s) = KN \sigma_k^{MeNP} \cdot I(\omega_L) \cdot |A(\omega_s)|^2 \cdot |A(\omega_L)|^2, \quad (2.48)$$

where $|A(\omega_s)|^2$ and $|A(\omega_L)|^2$ represent the square of the enhancement of the EM near-field around the MeNP at the scattered (ω_s) and absorbed (ω_L) wavelength. The product of these two factors is the electromagnetic enhancement factor G_{SERS}^{EM} of equation (2.48), while the chemical enhancement factor is hidden in the new Raman cross-section σ_k^{MeNP} , modified for the eventual chemical interaction of the analyte with the metal surface.

As a rule of thumb, the value of G_{SERS}^{EM} is about the fourth power of the electric field enhancement around the MeNPs, and depends on the kind of metal constituting the NP, the excitation wavelength, and the distance of the analytes from the metal surface. The maximum value of G_{SERS}^{EM} in the case of isolated non-interacting NPs, is obtained by the use of AgNPs excited in Forster resonance condition (Section 2.2.3.1), and can be of the order of 10^6 [224].

A schematic resume of the basic principle of SERS spectroscopy is reported in Figure 2.20. Herein, the noble metal nanostructure is represented as an agglomerate of NPs. The agglomeration process of a colloidal dispersion of MeNPs is highly desired in SERS spectroscopy and may be easily obtained by the deposition of drops of NPs on substrates, as explained in Section 3. This process may lead to the formation of metal nanostructures with different tailored optical properties, generally with a red-shifted LSPR band [20, 192]. In this case, the amplification of the electric field at particular junction sites between the NPs, called ‘hot-spots’ may be huge, and the SERS enhancement may reach values of 10^{12} [225].

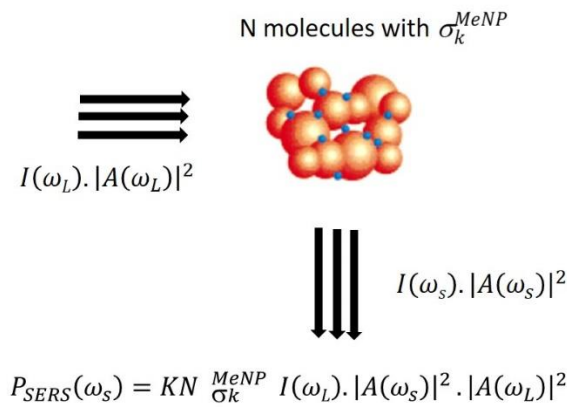


Figure 2.20 Principle of SERS spectroscopy. The N molecules of interest are placed in proximity (within a few nm) with a noble metal nanostructure. The incoming and scattered intensity are amplified by the factor $G_{SERS}^{EM} = |A(\omega_s)|^2 \cdot |A(\omega_L)|^2$.

The application of the SERS spectroscopy in the research is described in Sections 4 and 5, where it is used for the characterization of the noble MeNPs surface groups, the detection of sp^2 carbon nanomaterial, and also the identification of CO_2/C organic secondary product (carboxylic acids).

We finish the theoretical section by introducing a classification of different kinds of carbon-based nanomaterials, where the differentiation and identification parameters are the different hybridization states of the carbon atoms.

2.4.

Carbon Nanomaterials

2.4.1.

Hybridization states of carbon in nanomaterials

Orbital hybridization represents one of the most direct and simplest way to describe the changes happening in the single atom electron distribution when it forms bond with other elements to form molecules. The term orbital hybridization, describes the overlapping of the atomic orbitals of the atoms constituting the molecule under examination, which better represent the final electron density distribution observed experimentally. The concept of hybridization is very useful to explain the bond length, geometry and chemical reactivity of simple molecules, and has been introduced for the first time by Linus Carl Pauling [226, 227], in order to explain the different geometry of simple hydrocarbons. Based on the particular orbital mixing, the hybridization can be classified in sp , sp^2 , sp^3 , sp^3d^3 , sp^3d^2 , and sp^3d [228]. Degeneration of the energetic levels is obtained after hybridization, being four, three and two in sp^3 , sp^2 and sp orbitals, respectively.

All hybridized orbitals can make only σ -bond by direct linear overlapping, while non-hybridized orbitals can make π -bond as well [227]. The sp , sp^2 and sp^3 hybridizations are schematized in Figure 2.21, with examples of hydrocarbons with the corresponding hybridization (methan- sp^3 , ethylene- sp^2 , acetylene- sp).

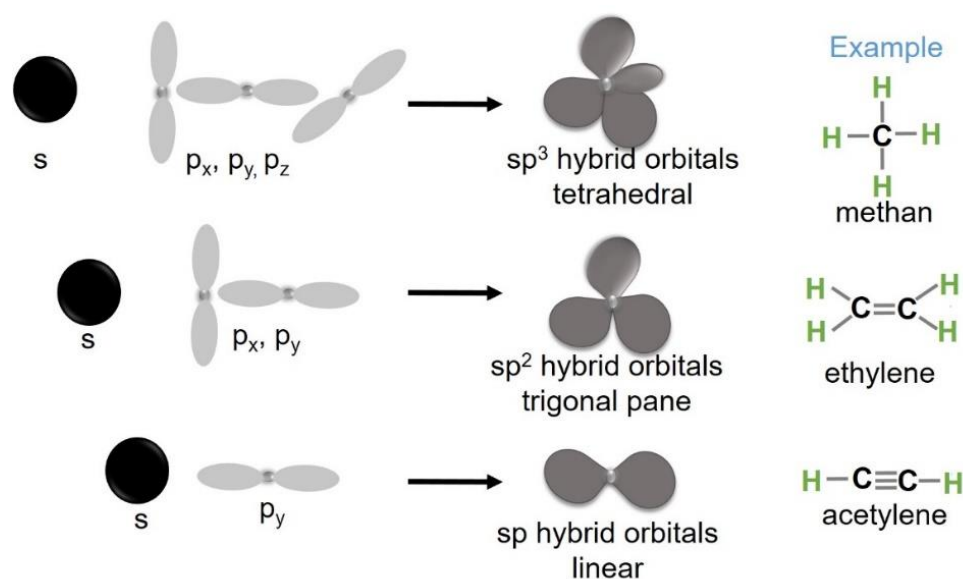


Figure 2.21 Diagram representing the concept of orbital hybridization in carbon atoms, with the formation of simple hydrocarbons (methane- sp^3 , ethylene- sp^2 , acetylene- sp).

Carbon is one of a few elements that are able to assemble in different geometries, such as linear, planar or tridimensional, and has different allotropic nanostructures, which can be classified on the basis of the hybridization of their atomic orbitals, as depicted in Figure 2.22 [41]. As shown in the latter, at the nanoscale it is possible to find carbon material in pure sp , pure sp^2 , pure sp^3 , and also in mixed hybridized states. For example, diamond, the tridimensional pure sp^3 hybridized carbon allotrope, can be found at the nanoscopic level as nanodiamond [229], while different kinds of sp^2 nanostructures are possible, with different portions of mixed sp^3 hybridization. Graphene [230] the 2-D carbon material, is the only pure sp^2 nanomaterial since, as illustrated in the diagram, both nanotubes [231], carbon onions [232], and fullerenes [233] have a portion of sp^3 hybridization, principally due to the curvature of their geometries.

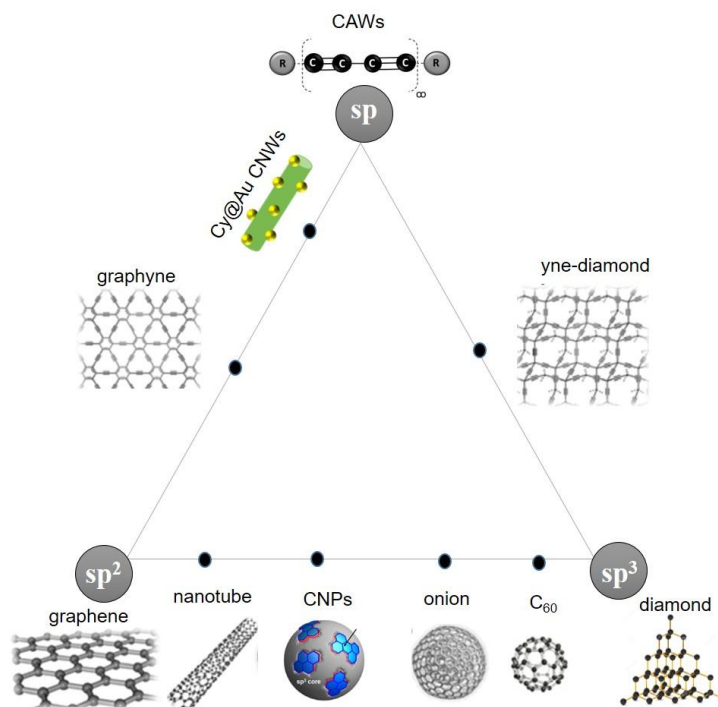


Figure 2.22 Schematic diagram of different kind of carbon nanostructures based on their hybridization [41].

We complete the diagram adapted from [41], locating luminescent carbon-based nanoparticles (CNPs) or CQDs in between sp^2 and sp^3 hybridization. Depending on their peculiarities, such as crystallinity or disorder, the CNPs take different names. CNPs constituted by a single flake on nm size graphene are called Graphene Quantum Dots (GQDs) [234], although authors do not respect this nomenclature in literature, and call as GQDs simple graphitic carbon dots, constituted by multiples

flakes of graphene, and named carbon quantum dots (CQDs). Luminescent CNPs with amorphous carbon is called finally as carbon nanodots (CNDs), as represented in Figure 2.23.

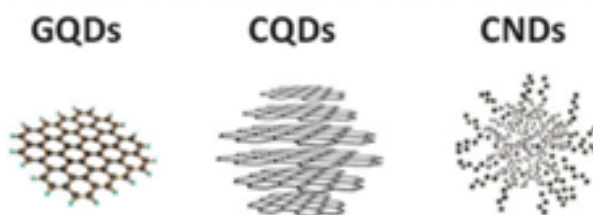


Figure 2.23 Different kinds of luminescent carbon nanomaterials [234].

The attribution of the effective hybridization of the carbon atoms of the CQDs is a hot theme of debate. Most of the authors attribute sp^2 hybridization only to GQDs and CQDs) [234], but a recent theory attributes to the CNDs a hybrid sp^2 - sp^3 hybridization, where sp^2 graphitic domains act as emissive units in an sp^3 amorphous carbon matrix [235].

We consider finally the last allotrope of carbon at the upper vertex of Figure 2.22, presented by sp -hybridized carbon materials. The unit elements of sp -carbon materials are called carbon atomic wires (CAWs). As represented in Figure 2.24, the CAWs can have two basic structures, namely polyynes, characterized by the alternating single and triple bond of carbon atoms [236], and cumulenes, characterized by carbon-carbon double bonds [237]. The stability of the CAWs is eventually assured by the choice of the proper capping group (R), such as noble metals, alkyl groups, or hydrogen [238]. What in literature is called carbyne, is an ideal single CAW, constituted by an infinite number of carbon atoms [236, 239].

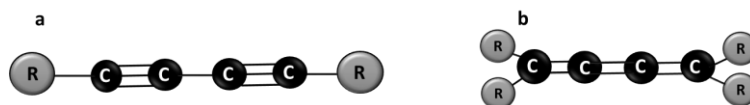


Figure 2.24 Schematic diagram of possible CAWs: a) polyyn structure, b) cumulene structure.

Cumulenic carbyne [237] is not stable for infinite chain lengths due to Peierls distortion [41], and are readily converted to less energetic polyyn like structures. When finite carbon chains are considered both of the polyyn or cumulenic configurations are energetically possible [41, 240], and the bond length alternation (BLA), electronic and vibrational properties of the CAWs are essentially determined by the chemical nature of the end group of the chains [41, 241]. Isolated finite polyynes with sp hybridization are traditionally synthesized by laser ablation of carbon target in water solutions [242–244], arc discharge method in liquids [245], or chemical routes [246, 247]. Recently, acetylenic linear chains with thousands of carbon atoms were synthesized inside double-walled carbon nanotubes, paving the way for the observation of ideal carbyne [248]. Carbynoid films with mixed sp , sp^2 , and sp^3 hybridization, are commonly fabricated by laser

or thermal assisted vapor deposition [249, 250], where interlinking between the linear carbon chains give rises to graphitic carbon and diminished order, like happens to CAWs exposed to oxygen or in high-temperature environments [249, 250], Graphene is considered as one of the most compatible sp^2 terminations for linear carbon chain, with the formations of the so-called graphynes or graph lines [251, 252], although these structures have been synthesized up to now only at the molecular level, and not like extended nanostructures. As reported in Figure 2.22, also hybrid $sp-sp^3$ nanostructures are theoretically possible, called one-diamond, and obtained (only theoretically) by inserting two carbon atoms into the C-C bonds of diamonds. All those mixed $sp-sp^3$ or $sp-sp^2$ infinite structures, together with CAWs of finite length are generally called carbynoid systems [41, 244], to differentiate them from the infinite carbene wire.

We conclude now the diagram in Figure 2.22 introducing the carbynoid nanocrystals (CyNCs). The CyNCs are semiconductors exactly like their building units, constituted by finite-length CAWs in polyyne form [40] Luminescent CyNCs have been synthesized by B.Pan *et. al.* [40] for the first and unique time during PLA of a gold target in alcohols, assisted by the catalytic properties of the small gold cluster in the cleavage of the carbon-hydrogen bond [40]. In this case, the NCs were automatically stabilized by the AuNPs synthesized during the PLA process of the gold target, which was found to decorate the carbynoid structures, acting probably as end terminal groups of the chains.

In Figure 2.25, we report the theoretical structure and the HRTEM images of the blue luminescent, hexagonal carbynoid NCs synthesized by B. Pan [40]. Along the *c*-axis of the linear crystal has an interplanar distance of about 0,99 nm (theoretical) against 0,91 (experimental), corresponding by DFT calculations to a number of carbon atoms between 8 and 12 [40]. The authors do not report any statistical distribution of sizes but report as represented in part *c* of Figure 2.25, a single isolated NC decorated by AuNPs, with the average lateral and longitudinal dimension of about 10 and 60 nm, respectively.

The CyNCs are inserted in the diagram of Figure 2.22 in between sp , sp^2 and sp^3 hybridization. While the presence of metal or benzene terminal group does not alter the degree of sp hybridization in theoretical infinite carbyne, it is expected that they have a bigger influence in the case of finite length sp NCs.

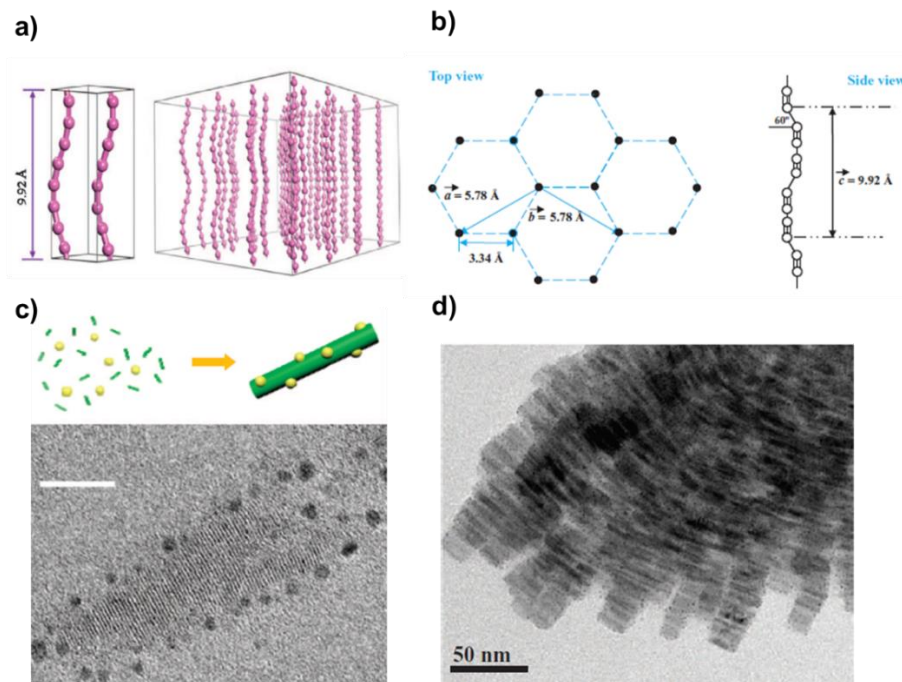


Figure 2.25 Theoretical structure of the finite length CyNCs [253]. a) Lateral view. b) Top view. c) HRTEM, and d) SEM image of an isolated CyNC decorated by AuNPs, synthesized by PLA of a gold target in alcohol.

2.4.2. Raman of Carbon Nanomaterials

The carbon structures we aimed to detect by Raman spectroscopy in the present research, are the CQDs and the Cy@Au NWs, both of them characterized by only single phonon processes. In the first case the single phonon processes are related to the broad Raman bands near to 1590 cm^{-1} and 1340 cm^{-1} , as visible in Figure 2.26 (a), called as G and D band, respectively. The G-mode is due to E_{2g} mode at the Γ -point [254] and arises from the stretching of the C-C bond in graphitic sp^2 materials. The D-mode is the disordered induced phonon [129], absent in graphene (see Figure 2.26 (b)), and seems principally due to the breathing modes of sp^2 atoms in rings [254]. For the reader interested in understanding the influence of chemical content or sp^2/sp^3 hybridization of the carbon material on the shape of the D and G band, we recommend the excellent work of A. C. Ferrari and J. Robertson [254].

Considering infinite polyynes type carbyne, its phonon dispersion is a classic example of phonons in a monoatomic infinite chain or a 1-D crystal. It is possible to demonstrate that the energy of the mode for $q = 0$ depends essentially on the so-called bond length alternation (BLA), which is the difference in bond lengths for adjacent bonds [41]. The latter parameter is 0 for cumulene and 0,039 for polyynes type carbyne, and varies with the number of carbon atoms constituting a finite CAWs, together with the particular kind of terminal group [41]. As a consequence of the different BLA, the Raman modes assume different frequencies, as represented in Figure 2.26 (c) for hydrogen capped polyynes of with a different number of carbon atoms [255].

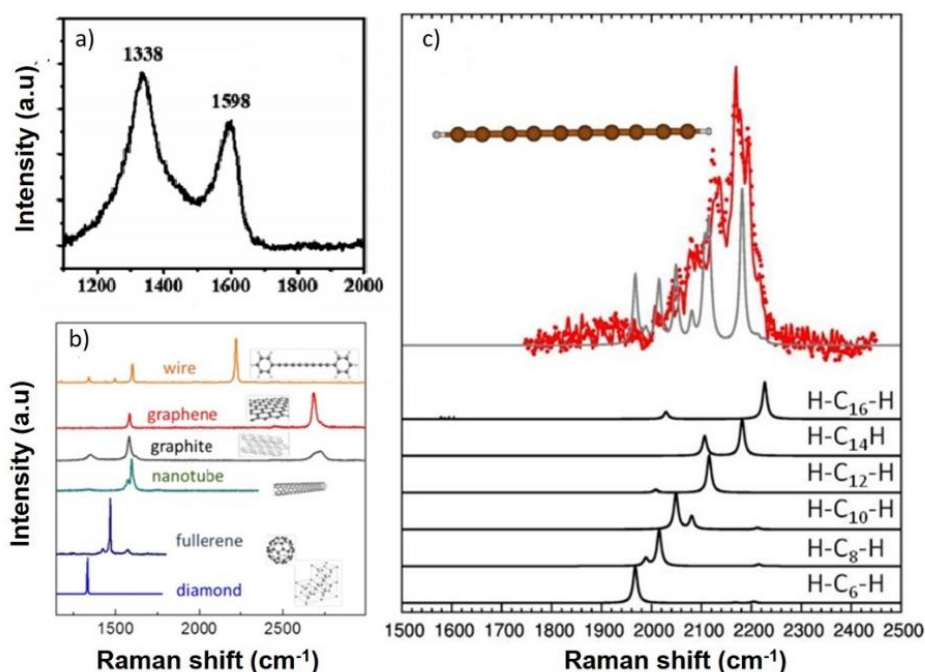


Figure 2.26 a) Experimental Raman spectra of GQD synthesized by electrochemical method. D band and G band are observed at 1350 and 1590 cm^{-1} , respectively [259]; b) Theoretical Raman spectra of different types of carbon nanomaterials[41], c) DFT computed theoretical Raman peaks for hydrogen capped polyynes (continuous lines) of different lengths, and comparison with the experimental spectrum (red points) [255]. The polyynes have been synthesized by the arc discharge method.

Independently on the length of the CAWs and their particular terminal group, the Raman spectra of the sp hybridized polyynes is always characterized by this

strong longitudinal phonon peak in the region 1800-2300 cm^{-1} , often called α -line, associated with triple bond carbon stretching vibration [214].

The carbon nanostructures synthesized in the presented research, are characterized by a quite low concentration, so that enhanced Raman spectroscopies were necessary. Considering the experimental facilities disposable for the spectroscopic characterization of the nanomaterials, UV Resonant Raman [256] or tip-enhanced Raman scattering [257] were excluded from the possible experimental approaches, and plasmonic nanoisland films [258] was chosen as analytical platform to perform SERS spectroscopy in the visible and near IR region.

In the next subsection, we introduce another peculiar characteristic of carbon-based nanomaterials investigated during my research, the photoluminescence (PL), which presents both similarities and differences with the one associated with traditional semiconductor quantum dots (SQDs) [234].

2.4.3.

Luminescence of Carbon Nanomaterials

For the first time the term “quantum dots” was introduced by M. A. Reed *et al.* [260] in 1988 for the semiconductor NPs of size in the quantum confinement range. The semiconductor quantum dots (SQDs) are semiconductor NPs with the size of the same of the order of the exciton Bohr radius, which is the distance between the excited electron-hole pair. Due to the quantum confinement effects, the electron-hole in SQDs behave like a particle in an infinite potential well, and the energy spectrum turns to discrete energy level, like in atoms or molecules [260, 261], as shown in Figure 2.27 (a), adapted from [262]. When the size of the bulk semiconductors turns to SQDs size range, the energy bandgap E_g between valence (VB) and conduction bands (CB) increases, so that for smaller SQDs, E_g will be relatively higher than larger SQDs [263, 264] as shown in Figure 2.27 (b).

Most recently in 2004, X. Xu *et al.* [265] for the first time discovered carbon quantum dots (CQDs) or carbon dot (CDs) accidentally, during the purification of the arc-synthesized single-wall carbon nanotube. This discovery is one of the most recent breakthroughs in the fields of nanotechnology.

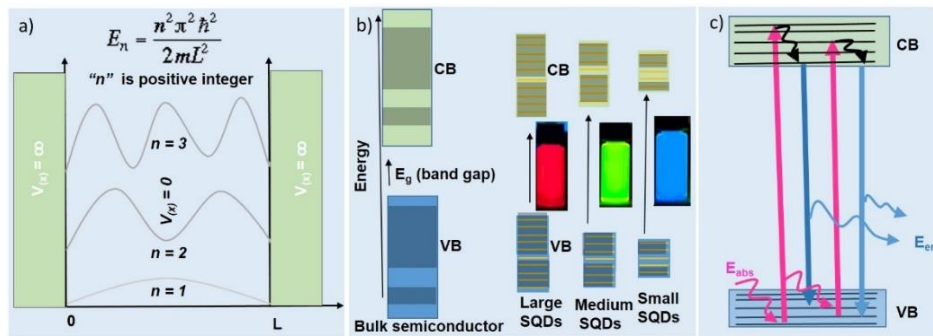


Figure 2.27 a) Discrete energies states of a particle in a one-dimensional infinite potential well or box, where E_n stands for the total energy of a particle and $V(x)$ represents the potential energy; b) Transformation of E_g as we pass from bulk semiconductor to SQDs of different dimension; b) and c) scheme of excitation and emission of luminescence in SQDs, adapted from [262, 263].

A. Cayuela. *et. al.*[234] in a review article, divides these fluorescent nanodots in SQDs and carbon fluorescent nanodots (CFNDs). The CFNDs are further divided in three different categories named graphene quantum dots (GQDs), carbon quantum dots (CQDs), and carbon nanodots (CNDs), as represented in Figure 2.28. The GQDs are small sp^2 hybridized carbon graphene sheet of 2-10 nm, and CQDs are quasi-spherical NPs, containing both sp^2 - sp^3 hybridized carbon. The quantum confinement effect exists in SQD, CQDs and GQD, while CNDs are amorphous quasi-spherical CFNDs with a lack of quantum confinement [234], where PL is due to the superposition of the responses of assembled individual emitters on the surface of the particle.

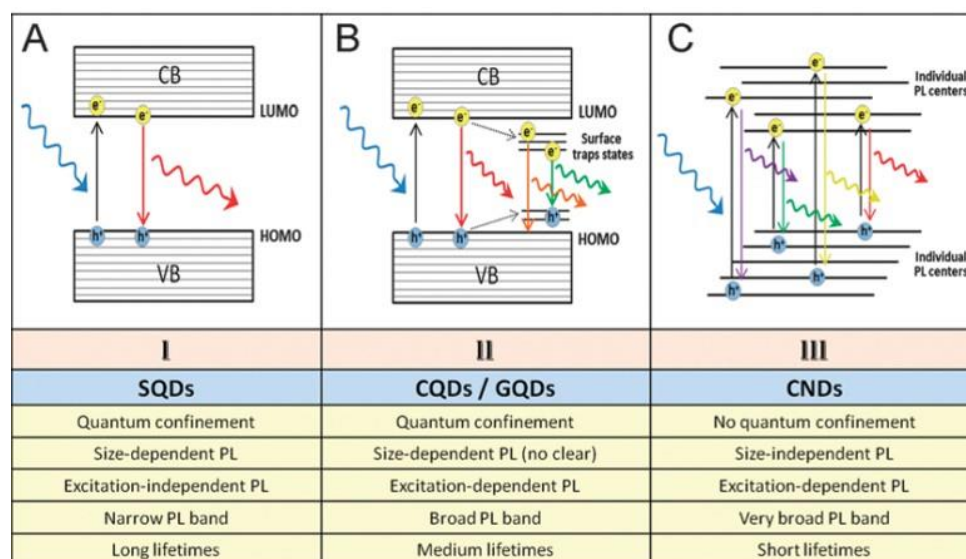


Figure 2.28 Schematic diagram of different PL mechanisms in NPs [234].

Despite the great amount of research on the CFNDs, the physic-chemical mechanism standing behind their PL is still the theme of debate. Hence, there are several proposals about the source of PL in semiconductor or carbon nanoparticles which, according to A. Cayuela. *et. al.*[234], can be summarized by the three main mechanisms reported in Figure 2.28.

- (I) The origin of PL in pure quantum dots is the electron-hole pair recombination. This type of emission is called intrinsic fluorescence (or luminescence) and it purely exists in impurity-free and defects free quantum dots, without intermediate states between energy gap. This type of PL property is governed by the quantum confinement effect. The PL emission band in a pure quantum dot is narrow, with a full width half maximum (FWHM) of the order of 40 nm, and is size-dependent and excitation independent [234]. Furthermore, the SQDs have a bigger PL lifetime τ than CQD, GQDS, and CNDs. τ is found to depend on the size of the particles, and big SQDs have longer lifetime [266]. For example, Cheng Cheng. *et. al.* [267] determined lifetimes from 2.57 to 0.71 μ s for octadecylamine capped PbS/SQDs depressed in toluene, with the corresponding size from 2.35 to 5.61 nm, respectively.

The second and third kind of PLs are characterized by the trapping or scattering of the electron-hole pair in states with the lower value of the energy band-gap E_g . The final emission is size-independent so that there are no quantization size effects. The trapping states have different origins, depending on the structure of the carbon core of the NPs (relative content of sp^2 and sp^3 carbon atoms) and the particular functionalization of the surface with certain chemical groups [235, 268]. This electron-hole pair (e-h) recombination mediated by defect or surface states, is characterized by a typical life-time bigger than the fast direct e-h recombination described in the processes of type I [268].

- (II) The second kind of PL arises, together with the type I, in sp^2 -hybridized carbon NPs with oxidized surface groups [268]. In this case, the PL response is the combined effect of two sources: (1) the intrinsic quantization effect of the core, and (2) the surface states on the particle. Surface states

produce a trapped state in between the intrinsic core CB and VB, as shown in Figure 2.28 (b). The energy difference between the trapped states will be smaller than the E_g between CB and VB [234]. Most of the reported research about CQDs and GQDs are presenting in this type of PL. The PL, in this case, maybe both excitation and size-dependent, and the presence of both direct and mediated e-h recombination can be revealed by time-resolved PL with the appearance of two independent lifetimes [234].

- (III) The third type of PL may occur in carbon NPs without quantum confinement effects and electron-hole recombination. They also have excitation dependent and size-independent PL, and their PL is associated to surface properties. In this case, the PL comes from the overall response of an ensemble of individual emitters, which are considered small domains of partially sp^2 -hybridized carbon atoms or functional group on the surface of the NPs, or inside an amorphous sp^3 carbon core, as represented in Figure 2.29. In this case, the emission is a pure type III process, characterized by very high life-times (of the order of μs) and a very broad PL band-

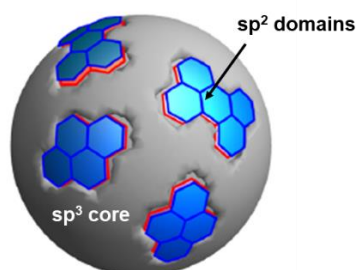


Figure 2.29 Representation of the mixed sp^2 - sp^3 carbon NPs, responsible for the PL of type III. Adapted from [235].

An alternative and powerful technique, used to understand the contribution of the particular PL mechanism, is to measure the dependence of the life-time τ on different emission wavelengths, in the PL emission spectra of the sample [268]. In fact, in type-I emission, CNPs with bigger dimensions emit at longer wavelengths (quantum-size effect) with shorter lifetime, while in process of type II and III, the higher emission wavelength is associated with progressive lower-energy radiative

recombination, with a prolonged charge carrier relaxation. It is worth noting that this technique has been used to investigate the origin of the emission of the QCDs synthesized by PLA of the gold target during my investigation, as reported in Section. 4.

CQDs composed of only carbon, oxygen, and hydrogen atoms, like the ones synthesized in the present investigation, generally are functionalized with surface carbonyl, carboxylic, and/or hydroxyl groups. These NPs are hence hydrophilic and water-soluble which, together with their excellent biocompatibility [269], is responsible for the large use of the NPs as a diagnostic system for bio-interactions and cell imaging [270]. This trend is contrary to the use of SQDs, generally hydrophobic, and extremely toxic to the environment and health system of the human body, due to the release of toxic heavy metal ion from the core [271].

Beyond the water solubility and biocompatibility, the other two important parameters of the CFNDs are related to their emission properties and are the spectral purity (FWHM) and photo luminescence quantum yield (QY), the latter defined as “*the number of emitted photons as a fraction of a total number of absorbed photons in the material*” [272].

Spectral purity and QY are particularly important for applications in optical biosensors and optoelectronics [273–276]. Luminescent CNPs have lower QY as compared to SQDs, and the scientists are still struggling to develop chemical synthesis methods to obtain better performances [277–279]. Although many chemical synthesis routes might lead to typical values of QY between 5% and 30% [280–284] and FWHM of about 70–100 nm [285, 286]. There are a few rare examples of CNPs with giant QY near to the 90% [270, 287, 288] and FWHM as small as 30 nm [289, 290].

Y.P. Sun *et al.* [291] successfully synthesized for the first time in 2006, CQDs by PLA of carbon target in the presence of water vapor and argon. In the following different authors attempted the synthesis of efficient CNPs by PLA of various carbon-based targets in water or organic solvents, both in bulk or powder form [37, 292]. For all the examples reported in the literature, the reported QYs until now for CNPs synthesized by one or even two-step PLA process, are limited to values between 1% and of about 10% [37, 293].

Interestingly, the unique synthesis of luminescent CNPs by PLA without solid carbon target is very recent, [294], and was obtained by non-focusing pulsed laser irradiation on the toluene solution. There is no report until now, about the synthesis of carbon nanomaterial by PLA starting from the gaseous species diluted in the liquid environment.

2.5.

Applications of nanomaterials

2.5.1.

Photodynamic therapy

The phenomenon of “photodynamic action” was first time discovered by PhD student *Oscar Raab* under the supervision of Professor *Hermann von Tappeiner* in the Munich Pharmacological institute in 1900 [295]. *Raab* used a microscope illuminated by sun light and observed that, if the light intensity was high enough, paramecium cells were killed by fluorescing dyes (quinine, eosin, methyl phosphine, acridine, and others).

Photodynamic therapy (PDT), is a phototherapy based on the interaction between photons, a photosensitizing chemical agent and molecular oxygen. As represented schematically in , in PDT the photosensitizer (PS) is optically excited in its short-time living singlet state, and decay by intersystem crossing (ISC) to the long life-time triplet state [296]. Since the spin of the electron is reversed during the ISC process, due to the Pauli exclusion principle it cannot decay rapidly, but only through the slow process of phosphorescence, during which its spin state can be reverted again to the initial one in times of the order of μs . During this large temporal window, the excited electron has the opportunity to interact with the molecules in the surrounding environment. This interaction is particularly interesting in biological tissues and cells, where molecular oxygen is one of the few molecules in the triplet ground state ($^3\text{O}_2$) [136].

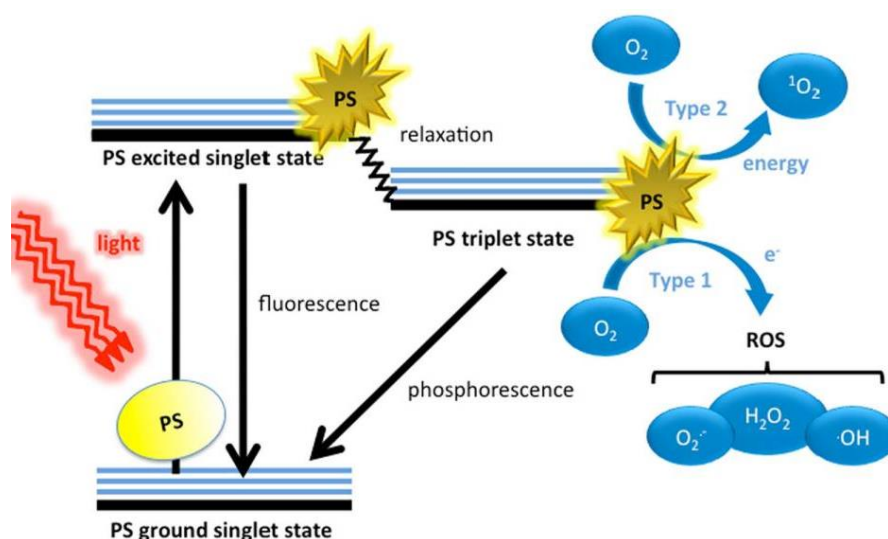


Figure 2.30 Scheme representing the principle of work of the photo-dynamic activity. Adapted from [136].

The interaction between $^3\text{O}_2$ and the PS can follow two principal pathways, denominated type-1 and type-2, with the final production of different reactive oxygen species (ROS). In the type-1 mechanism, the excited PS in the triplet state transfer an electron to the oxygen, with the formation of hydroxyl radicals ($\cdot\text{OH}$), hydrogen peroxide (H_2O_2) and superoxide anions ($\text{O}_2^{\cdot-}$) [296]. The type-2 mechanism, involves a collisional energy transfer between the outermost unpaired orbitals of the oxygen and the excited triplet state of the PS, with the final production of unstable and highly reactive singlet oxygen ($^1\text{O}_2$) [136].

PTD has proven in the last decade to be a valid alternative to both chemotherapy and radiotherapy for treatment of cancer in specific regions of the body, such as skin, head, neck, lung, mouth or esophagi [297]. Its use is actually not limited to cancer treatment, but also applied in some particular skin diseases, such as fungi infection and acne [136, 298, 299].

As explained before, when the PS absorbs electromagnetic waves at the proper wavelength, it is able to produce ROS, which can kill specific cells by apoptosis and necrosis caused by irreversible oxidization [300]. Methylene Blue (MB) [301] and chlorin e6 (Ce6) [300], the latter used in the present research, are between the most used PS in literature [300, 301].

For a better description, Rekha R. Avirah *et. al.*[302] divided PDT into four stages, as shown in the schematic diagram in Figure 2.31. In the first stage, the PS is injected into the human body and then it is conducted to tumors cells. After that, the affected body region part is irradiated by suitable light for the destruction of cancer cells.

An innovative strategy for PDT is combining the PS with MeNPs colloids with LSPR resonances in a spectral region overlapped with the absorption band associated to the excitation of the PS singlet state [300, 301, 303]. The use of MeNPs amplifies the rate of excitation of the PS, and accelerates the production of ROS, allowing a diminishing in both the medicinal dose and the light source irradiance.

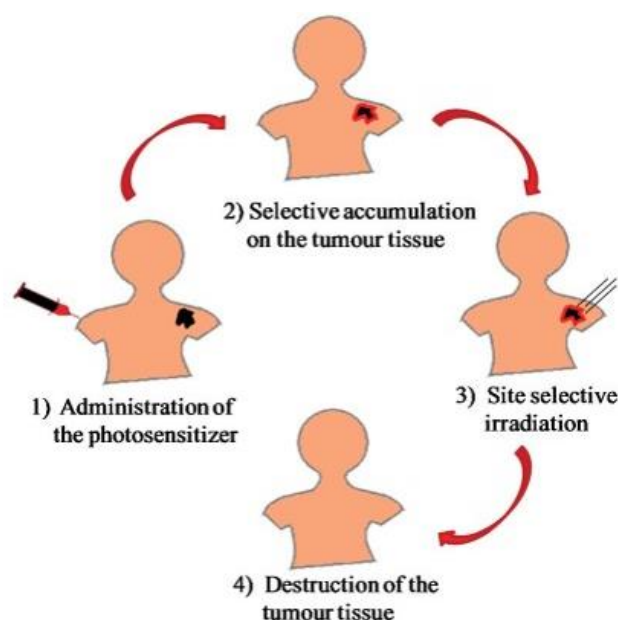


Figure 2.31 Schematic diagram of the different stages of PDT [302].

A proof of principle of this approach is demonstrated experimentally in Section 4, where it is shown the plasmonic enhancement of the photodynamic activity of Ce6-PS combined with colloidal dispersion of AuNPs synthesized by PLA, and further agglomerated and stabilized by the proper combination of NaCl and the copolymer Pluronic PF-127 [20].

2.5.2.

Gene therapy with nanoparticles

The particular dimension of nanomaterials gives them the appealing property to be able to enter in a different part of the cells and, depending on their nature, dimension, and gene functionalization, to activate determinate gene expression patterns [137, 304]. The primary challenge for gene therapy is to develop a method to deliver a therapeutic gene (both directly or indirectly) to selected cells, in order to produce a therapeutic gene expression [305].

The most used route for non-viral gene delivery is the incorporation of DNA in NPs containing cationic lipids or polymers [306]. The draw-back of this approach is the inability of these vectors and DNA fragments to maintain their stability in the extracellular space, and also in the biological membranes, before reaching the nucleus [307].

To facilitate the possibility for the non-viral vectors to reach the nucleus cells, recently ultrasmall AuNPs have been tested in genic therapy on breast human cancer cells with excellent results [137]. The interesting results, in this case, are obtained only for the colloid of AuNPs smaller than 6 nm, with best results when the average dimension reaches down to 2 nm. In this case, the tiopronin-covered gold nanoparticles (Au-TIOP NPs) were used to deliver the POY-2T triplex-forming oligonucleotide (TFO) by conjugation, which binds to specific proto-oncologic genes, quenching the transcription process. The scheme of this process is shown in Figure 2.32 adapted from [137].

But AuNPs based gene therapy does not need necessarily to use ultrasmall AuNPs. Recently, Jun-sang Yoo *et. al.* [138] obtained astonishing results in the therapeutic use of electromagnetic stimulated AuNPs with an average dimension of about 20 nm. The electromagnetic stimulation of the AuNPs with magnetic fields at frequencies of hundreds of Hz provoked the extra nucleus acetylation of the histone H3K27, and following robust activation of neuron-specific genes, with possible therapeutic applications in Parkinson's disease.

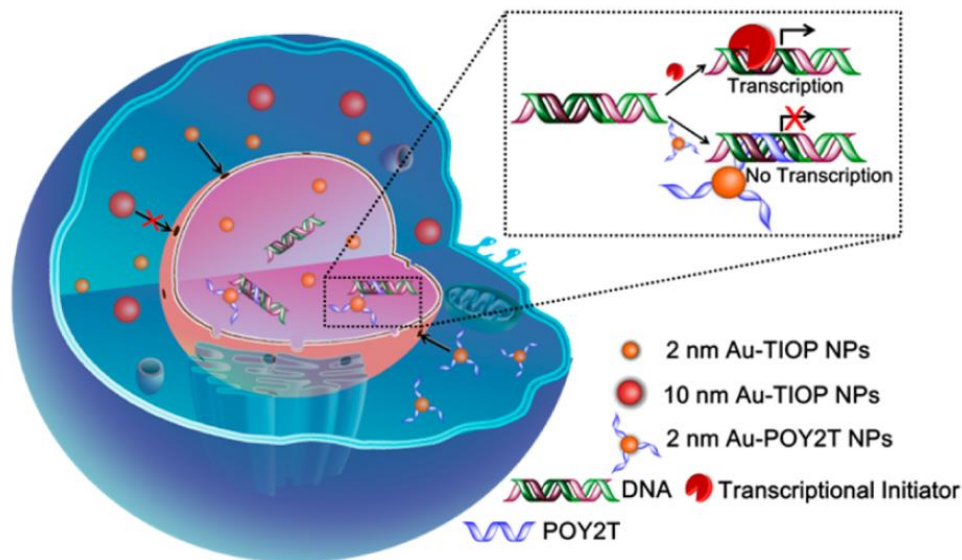


Figure 2.32 Schematic and specific example of gene therapy by the use of ultra-small AuNPs, adapted from [137]. The AuNPs functionalized with the TFO are able to block the DNA transcription of selected pro-oncologic genes.

The description of the application of our particular Au@Cy NPs in gene therapy is reported in the final part of Section 4. Before starting to show our experimental results, we describe in the next Section 3 the principal experimental techniques and methodologies used for the development of the research, with the exclusion of the medical part, which do not enter in the know-how of the *NanoLaser* Laboratory in the Department of Physics of PUC-Rio, and is not an activity where we supervised the experimental measurements.

3 Instrumentations and experimental methods

This chapter discusses the description of materials, instrumentations, and the experimental methods used in this thesis. It begins with the list of the different materials used for the synthesis of nanoparticles and the main method of cleaning both metallic targets and glassware used for PLA. After that, I introduce the *NanoLaserLab* and the different experimental set-up and laser sources used to perform the PLA in liquid. We will continue with the description of all the instruments dedicated to the analytical, chemical, and morphological characterization of the synthesized nanomaterial. Furthermore, we will describe the multiple separation techniques used for the separation of the carbon nanomaterial from the metal species, and conclude with the description of steady-state and time-resolved luminescence measurements.

It is worth noting that in each section related to the different experimental techniques, we will also describe the corresponding preparation of the samples.

3.1. Materials and cleaning processes

3.1.1. Materials

Analytical grade NaOH, H₂SO₄, HCl, NaCl, NaOH, acetone, ethanol, trichloroethylene, Acetic acid, Pluronic F127 (PF127), and HNO₃ were purchased from Sigma-Aldrich. Clorin e6 (Ce6) with purity higher than 95 %, 1,3-Diphenylisobenzofuran (DBPF), and Phosphate was obtained from Frontier Scientific. The gold (Au), silver (Ag), and iron (Fe) disk with purity better than 99% used as a target for PLA in water and gold used for thin film deposition was bought from Kurt J. Lesker Company. Dried dialysis cellulose membranes of 3.5 KD molecular weight cut-off, containing 10% glycerol, 0.1%, sulfur, and heavy metal traces were purchased from Fisher Scientific Company. Ultrapure deionized

(UPD) water (with 18.2 M Ω cm of conductivity) was obtained from the Milli-Q gradient A10 ultra-purifier (Milipore, USA) “*Laboratory of Applied Spectroscopy, Electroanalysis and Elemental Analysis Department of Chemistry PUC Rio*”.

3.1.2. Cleaning of targets

The Cleaning of the ablated metallic targets and glassware, where PLA in a liquid is occurring is extremely important for the stability of the colloidal system. Hence, particular attention was kept in this sense, and a rigorous discipline was maintained in the daily cleaning of all the accessories which were used to manipulate the NPs.

The following are the main steps used for the cleaning of metallic targets before PLA:

- the disk of the pure metal target was first rubbed by sandpaper to remove surface oxides and rinsed with distilled or ultra-pure deionized (UPD) water.
- Au or Ag targets were placed in a clean vessel containing 40% H₂SO₄ solution in water and put in ultrasound for 10 minutes. Then we replaced the H₂SO₄ with ultra-pure deionized (UPD) water and left again in ultrasound for 10 minutes. The targets were finally rinsed in UPD water at least five times to remove the acids.

The iron target was cleaned in ultrasound with ethanol and UPD water before each use. H₂SO₄ was not used for the Fe target to avoid the oxidation of the Fe target before the PLA process.

After the above cleaning process, the target is ready for PLA in liquid. While Fe and Ag targets were cleaned before each ablation due to the high rate of oxidation in water (also without ablation) as compared to gold, the target of Au could be used for several days, since it oxidized only in the area corresponding to the small spot of the pulsed laser beam.

3.1.3. Cleaning of glassware

The beakers, small glass bottles, and other glassware that we are used in the PLA process and storing of synthesized NPs colloids have been first cleaned with detergent solution or with soap, and then rinsed thoroughly at least three times in common water to remove all the traces of detergent or soap. Next, the vessels were rinsed three times with distilled water, followed by immersing in 10 % nitric acid solution in water for 24 hours. The glassware was after rinsed three times with distilled water and milli-Q water, and put for 10 minutes in an ultrasonic bath in milli-Q water. At this point, the glassware was dried in the oven at 50 °C, after which we applied multiple 10 minutes-long ultrasound bath in the following solvents: trichloroethylene, acetone, and ethanol. The as-treated vessels were ready to be used for the synthesis or storing of the colloidal system of NPs.

3.1.4. Preparation of the aqueous solution of NaOH

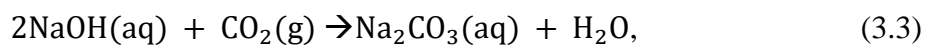
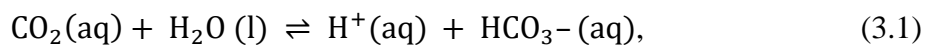
To prepare the NaOH water solutions with different concentrations, a 100 mM aqueous NaOH stock solution in UPD water was stirred in a closed falcon tube for twenty minutes. The hydroxide water solution should not store in glassware, because it reacts with the silica that exists in the glass and will produce silicon hydroxide, which will make contamination in the synthesizing colloidal dispersion of NPs. After, the same stock solution was diluted to the desired concentration C_{NaOH} by adding aliquots to 50 ml of UPD water, further stirred in the open air for a fixed time of 10 minutes. After that, the aqueous NaOH solution is left for 1 hour in the open air before starting the PLA. At this stage, the pH was measured using the pH meter, and also calculated theoretically by using the formulas $pOH = -\log_{10} [OH^-]$ and $pH = 14 - pOH$, for the corresponding concentration of NaOH. The temperature was maintained at a value of 23 °C with a humidity of about 45%. The average (along 1 year) CO₂ concentration in the environment inside the laboratory for aqueous solution preparation, was (800 ± 400) ppm, and was measured using an ambient CO₂ monitor (*Testo 535*). The as-prepared NaOH water solution was used for the ablation of the noble metals targets. Table 3.1 report the NaOH concentration (C_{NaOH}) and corresponding pH of the solution during the preparation, and the

volume of aqueous solution NaOH (V_{NaOH}) used in the present investigation to prepare the final PLA environment.

Table 3.1 Concentration of NaOH in the aqueous NaOH mother solution used in the present investigation to prepare the final PLA environment; Volume (V_{NaOH}) of stock solution added to 50 ml of UPD water; Experimental and theoretical pH.

C_{NaOH} (m mol/L)	V_{NaOH} (μl)	Experimental pH	Theoretical pH
2.0×10^{-2}	10.0	7.4	8.3
6.0×10^{-2}	30.0	9.2	8.8
2.0	1.0×10^3	11.1	11.3
4.0	2.0×10^3	11.3	11.6
8.0	4.0×10^3	11.8	11.9
12.0	6.0×10^3	12.0	12.1
20.0	1.0×10^4	12.2	12.3

The pH decreased continuously over time, because of the convention of absorbed CO_2 and NaOH in water to carbonic acid, sodium carbonate, and sodium bicarbonate, therefore we measured it just after preparation. After solving of NaOH and absorption CO_2 from the environment, the following well-known reaction is shown in (3.1) - (3.4) [308] may occur.



Also because of this CO_2 absorption, the theoretical pH was always bigger than the experimentally measured pH.

3.2. Synthesis of the colloidal solution of nanomaterial by PLA

3.2.1. Experimental setup for PLA in liquid

The synthesis of the nanomaterial has been accomplished in the Laboratory of Optical Synthesis and Characterization of Nanomaterials (*NanoLaserLab*) of the Department of Physics of PUC-Rio. The laboratory is equipped with a Pulsed Laser Deposition (PLD) system of *Intercovamex*, with a Q-Smart 850 laser source from Quantel (U.S.A), represented in Figure 3.1.

The NG:YAG pulsed-laser has a duration of 6 ns duration, a constant repetition rate of 10 Hz, and can be operated at both the fundamental ω (1064 nm) and second-harmonic 2ω frequency (532 nm), with a maximum energy of about 500 mJ/pulse.

Figure 3.1 shows the optical path of the system, equipped with mirrors (M) and beam splitters (BS) which allow performing simultaneously PLA in both vacuum and liquid. PLA in vacuum was not used in the presented research so that we will describe in more detail only the first part of the equipment, dedicated to the optical synthesis in liquid. The part of the system dedicated to PLA in the liquid was optimized and upgraded along the time dedicated to my research, and the actual version of the instrument is represented in Figure 3.2. All the optics of the set-up have been designed for high power applications and have anti-reflection coatings for ω or 2ω frequencies, and have been purchased from *ThorLab* and *Lambda research* companies (U.S.A). We thought about an original and versatile configuration, represented in Figure 3.2 (a). The laser pulse is directed on a beam splitter (BS) and deviated in two perpendicular directions, where two mirrors M_1 and M_2 deflects them towards the lenses L_1 and L_2 , with focal lens f_1 and f_2 . The two laser pulses are finally focused on the corresponding targets t_1 and t_2 , immersed in the liquids 1 and 2. This configuration may allow us to synthesize a bigger quantity of material if necessary, and it is perfect to make an accurate comparison of the PLA process conducted on different targets, or with different optical parameters.

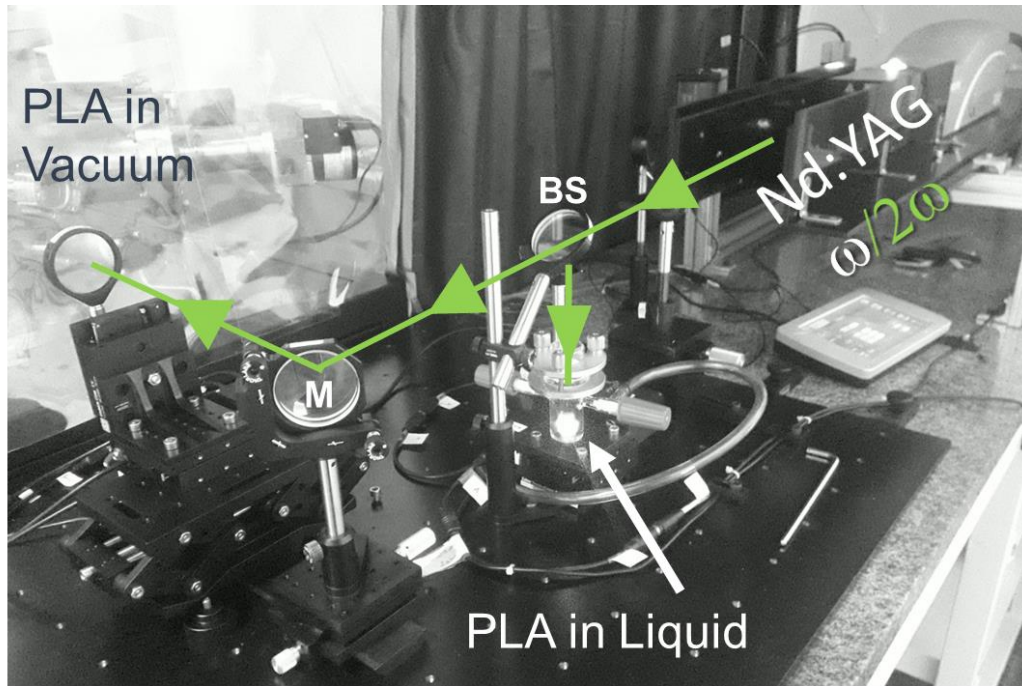


Figure 3.1 PLD system installed in the *NanoLaserLab* of the Department of Physics of PUC-Rio, where it is possible to perform simultaneously PLA in both vacuum and liquid environment.

The Q-Smart 850 laser source described above was used to perform the synthesis at the fundamental ω (1064 nm) or second-harmonic 2ω (532 nm) frequencies separately, while experiments of synthesis by simultaneous irradiation of ω and 2ω pulses were performed using a Nd: YAG laser from *Quantel* (U.S.A) model *Big Sky Laser*, emitting simultaneously pulses at both the frequencies, with a repetition rate of 10 Hz, located in the LOEM Laboratory of PUC-Rio. The scheme of this second optical set-up is represented in Figure 3.2 (b).

Figure 3.2 (a) shows the configuration used for PLA at one single frequency, ω or 2ω . For bigger production of colloids per unit time, and for accurate comparisons of the PLA products using different water environments, the laser pulse is directed in two orthogonal directions by the use of a beam splitter (BS). Two mirrors M_1 and M_2 deflect them towards the lenses L_1 and L_2 , with focal lens f_1 and f_2 . The laser pulses are then focused on the corresponding targets t_1 and t_2 , immersed in the liquids 1 and 2. Figure 3.2b) represents the scheme of PLA by simultaneous irradiation of pulses at both ω and 2ω frequencies, and Figure 3.2 c) shows a photo of the PLA set-up corresponding to the configuration represented in a). Figure 3.2

d) highlights the the last upgrade of the PLA system, where a mechanical base of *Zaber* (Canada) with micrometer accuracy is controlled remotely to scan the beam over the moving target, and the target and the liquid environment are put inside a sealed glass container, previously filled with a controlled partial pressure of CO_2 .

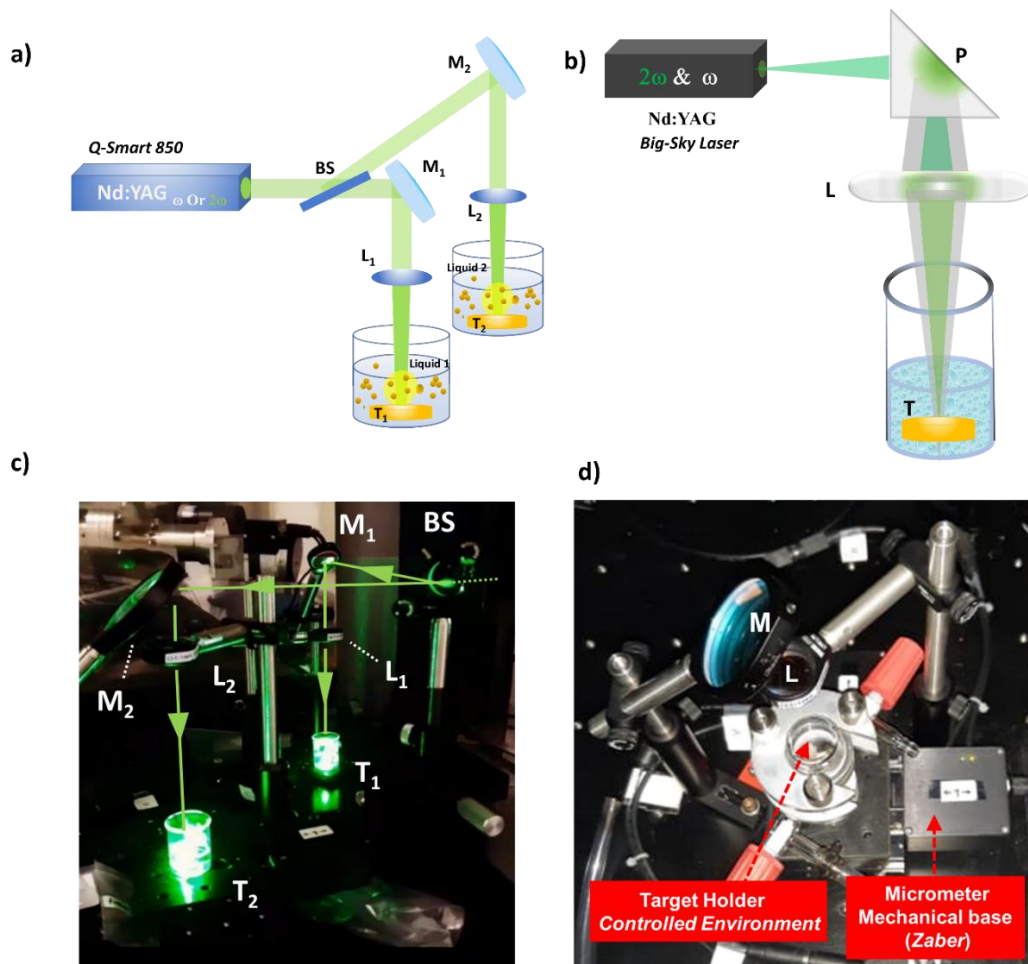


Figure 3.2 a) Configuration used for PLA at one single frequency ω or 2ω ; b) Scheme showing the PLA by simultaneous irradiation of pulses at both ω and 2ω frequencies; c) Photo of the PLA set-up corresponding to the configuration represented in a); d) Photo highlighting the last upgrade of the PLA system, with the mechanical moving base of *Zaber* and a sealed glass container, used to perform PLA in controlled CO_2 partial pressure.

In both setups as shown in Figure 3.2 (a), and (b), the NPs colloids were synthesized at different fluence F by changing both the distance between the convex lenses L and the targets T and the energy per pulse of the laser sources. The latter was measured by a *ThorLab* detector model *ES220c*, with a range from 2 mJ to 2 J/pulse energy).

Preliminary experiments were also performed by doing PLA on a moving target, in which the target holder was located on the mechanical base of *Zaber* (Canada) with micrometric precision-controlled remotely by *LabView* software. The micrometer base is visible in Figure 3.2 d), where it also shown an alternative target holder used to perform initial tests of irradiation of nanomaterial in a controlled gas environment.

3.2.2. Calculation of laser spot size and fluence

To the best of our knowledge, for the first time, we are showing an optical model used to calculate the correct value of the laser fluence F on the surface of the target, by considering the height of the liquid environment over the metal. This model is particularly important since the laser pulse fluence has a significant effect on the properties of synthesized NPs [309].

The fluence of the laser pulse ablating the samples follow the well-known definition $F = 4E/\pi\phi_T^2$, where E is the energy of the pulse and ϕ_T is the diameter of its spot on the target. Hence, it appears fundamental the measurement or, alternatively, the theoretical calculation of the laser pulse spot-size on the ablated target.

Figure 3.3 (a), illustrates the laser pulse focused through a convex lens (L) onto the target surface plane. α and β are the incident and refraction angles normal to the air/liquid interface, respectively. The pulse with a diameter ϕ_{Laser} before focusing, has a focusing point at Y (near to lens) in air, while in water it is focused at point Z (large distance from the lens). According to the manual of the Q-smart 850 laser source, the laser pulse diameter at the output of the head is $\phi_{\text{laser}} = 0.7$ cm (radius of pulse $r_p = 0.35$ cm). Consider the Snell's law and a focal length of the lens in the air $f = 14.9$ cm, we have

$$\alpha = \tan^{-1} \left(\frac{r_p}{f} \right) \simeq 0.0235 \text{ rad} , \quad (3.5)$$

and

$$\beta = \sin^{-1} \left(\frac{n_{air}}{n_{water}} \sin \alpha \right) \approx 0.0177 \text{ rad} . \quad (3.6)$$

To calculate the laser spot size and fluence in air, let us suppose that φ_T is the diameter of the laser pulse on the target in water, located at a distance $d = l_\alpha + l_\beta$ from the L as shown in figure 3.3 (b). l_α is the lens/water distance, and l_β the distance between the water/air interface and the surface of the target. The distance from the lens L at which a laser pulse focused in the air has the same dimension as the spot of the real laser pulse on the target in liquid, is called equivalent optical path $EOP = l_\alpha + l_\alpha^*$, it holds the geometrical relation

$$l_\alpha^* = \left(\frac{\tan \beta}{\tan \alpha} \right) l_\beta = 0.76 l_\beta, \quad (3.7)$$

so that we have

$$EOP = d_{real} - 0.24 l_\beta. \quad (3.8)$$

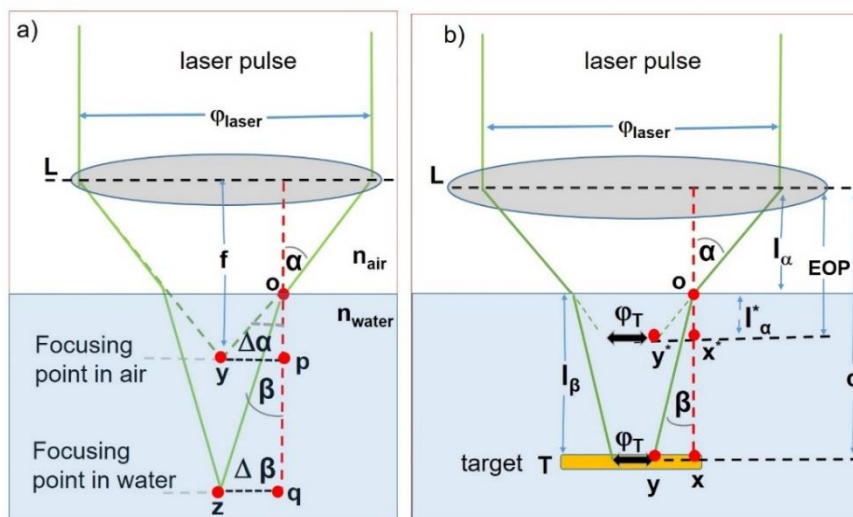


figure 3.3 a) Schematic diagram representing the effect of water on the laser focusing position. b) Scheme used for the calculus of the laser spot size and fluence F on the target.

The *Q-Smart 850* laser source (Quantel U.S.A), which can be operated separately with laser pulses at ω or 2ω frequency, is characterized by a nearly TEM₀₀ ($M^2 \approx 1$)

beam [310], and a very small angular divergence of about 0.2 mrad at 1064 nm. In this case, defining of φ_T the diameter of the laser pulse on the target, and considering the laws of optical geometry, we can write

$$\varphi_T = \varphi_{laser}(EOP - f)/f. \quad (3.9)$$

3.2.3. Effect of the water column over the target

In Table 3.2 reported the theoretical data of φ_{target} and F for different values of the water column height l_β , depending on the lens/target distance d used along with the experiments. The values of F are relative to a pulse energy of 2 mJ per pulse, which was mostly used experimentally. We consider three hypothetical heights of the water column over the target, 0 cm (no water), 0.5 cm, and 1.1 cm.

In Figure 3.4, are plotted the theoretical data of φ_{target} and F for different values of the water column height l_β , depending on d . It is evident that a significant variation of F is obtained when considering correctly the presence of the water column. These results do not take into account the possible presence of non-linear effects such as autofocusing of the beam, which is negligible in the ns regime at the present values of fluence. The effects of the water column height l_β over the target on the size of AuNPs has been investigated by [311], but the effects were not interpreted based on the optical properties of the beam on the target but on the changes in the local water pressure.

The parameter used for the synthesis of our nanomaterial varied in terms of volume based on the particular application. To produce NPs for biological applications or a massive quantity of CQDs for sensing applications, generally, we used the simultaneous ablation of two targets Figure 3.2 (a) for a total volume of 2 x 12 ml = 24 ml of nanomaterial using $F = 3.9 J.cm^{-2}$ and shown in the last row in Table 3.3.

For analytical characterization such as TC, UV-Vis or ICP-MS aliquots of 2 ml were prepared most of the time. Independently on the volume of the liquid (2 ml or 5 ml), the value of l_β was kept fixed at 0.5 cm by the use of beakers of different diameters. Most of the time the energy of the pulse was kept fixed at 2 mJ per pulse

but was raised to 8 mJ for the massive production of the CQDs from the ablation of the Au target.

For the case of noble metal targets, the ablation was stopped when the extinction of the samples reached the value of 1, so that the ablation time t_{abl} varied in function of F . When dealing with the iron target, the PLA process was stopped after a time of 2 hours, independently on the value of F .

Table 3.2 Size φ_T and fluence F of the laser pulse for l_β of, 0.0 cm, 0.5 cm, and 1.1 cm, considering different values of the lens/target distance d . The values of F are relative to a pulse energy of 2mJ.

distance between lens and target d (cm)	laser spot size on target φ_T (cm)			fluence of the laser F (J/cm ²)		
	$l_\beta = 0.0$	$l_\beta = 0.5$	$l_\beta = 1.0$	$l_\beta = 0.0$	$l_\beta = 0.5$	$l_\beta = 1.0$
	(cm)	(cm)	(cm)	(cm)	(cm)	(cm)
14.6	0.14	0.30	0.32	12.79	2.90	2.45
14.1	0.38	0.44	0.51	6.76	1.33	0.98
13.6	0.61	0.67	0.74	4.16	0.56	0.46
13.2	0.80	0.86	0.93	3.18	0.34	0.29

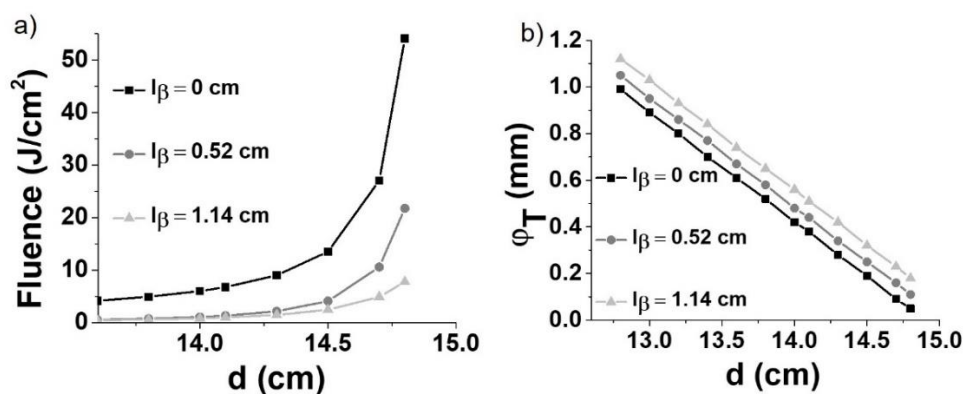


Figure 3.4. Dependence of F (a), and φ_T (b) on the lens/target distance d , for different heights of the water column over the target: $l_\beta = 0$ cm (black square), $l_\beta = 0.5$ cm (grey circle) and $l_\beta = 1.0$ cm (grey circle)). The values of F are relative to a pulse energy of 2mJ.

Table 3.3 Energy per pulse and fluence, and ablation time used for the PLA of the different transition metal target in water.

Metals Target	Laser Frequency	E (mJ)	F (J/cm ²)	t _{abl} (min)	Laser
Au / Ag	2 ω	2	1.3	60 / 25	Q-Smart
Au / Ag	2 ω	2	0.6	180 / 60	Q-Smart
Au / Ag	2 ω	2	0.3	420 / 200	Q-Smart
Au / Ag	2 ω	3.5	1.3	60 / 25	Q-Smart
Fe	ω	3.5	2.3	120	Q-Smart BIG SKY
Fe	2 ω	3.5	2.3	120	Q-Smart
Fe	2 ω + ω (simultaneous irradiation)	4.8	0.9 3.2	120	BIG SKY
Au / Ag/ Fe	2 ω	8	3.9	300	Q-Smart

In Table 3.3 are listed the values of the energy E per pulse, fluence F for all the optical conditions used in the synthesis of the different nanomaterials, and the corresponding time of ablation. The fluence F and ϕ_T are calculated using eq. (3.5) - (3.9).

3.2.4.

Procedure for the measurement of F_ω and $F_{2\omega}$ during simultaneous ablation by fundamental and second harmonic frequencies

As previously explained, the Nd:YAG laser source *Big Sky* (Quantel U.S.A, model) was used to perform PLA using pulses containing simultaneously both the wavelength of 1064 nm (frequency ω) and 532 nm (frequency 2ω). This experimental set-up, the same one reported in Figure 3.2 b, is represented also in Figure 3.5a, where it is indicated as first PLA system (PLA-S₁).

In this case the equation of the fluence per pulse can be written as

$$F_{pulse} = F_\omega + F_{2\omega} = \frac{E_\omega}{\pi/4 \phi_\omega^2} + \frac{E_{2\omega}}{\pi/4 \phi_{2\omega}^2} . \quad (3.10)$$

The pyroelectric detector cited before was used to measure the energy of the laser pulses. To measure E_{ω} and $E_{2\omega}$ we firstly measured the total energy of the pulses, $E_{\text{pulse}} = (E_{\omega} + E_{2\omega})$. After, we inserted a high power dichroic mirror (DM) between the focusing lens and the target, as depicted in Figure 3.5a. The dichroic mirror had the function to properly separate the pulses at ω and 2ω frequency. The ω and 2ω pulses were reflected and transmitted, respectively, (or vice versa, depending of the choice of the particular DM) with an efficiency better than 90% (EK SMA Optics, Lithuania). In this way, it was possible to measure separately the energies E_{ω} and $E_{2\omega}$, and to compare their sum with the total energy measured without the DM. Since the laser pulses come out from the head of the BIG SKY laser with a high divergence (full angle ~ 8 mrad at 1064 nm), and since the beam quality factor M^2 [310] of the beam may change during years of operation of the lasers, it is hard in this circumstances to calculate with good accuracy the spot size of the laser pulses by the application of the laws of propagation of Gaussian beams [312].

Not provided of a proper camera to measure the dimension of the laser spot [159], we used an alternative comparative method. To do that, we synthesized gold nanoparticles (AuNPs) by PLA in NaOH enriched water using two different laser sources: the BIG SKY laser (with high angular divergence and years of operation), and the recently acquired Q-Smart 850 (Quantel U.S.A, 5.8 ns pulse duration). The latter experimental set-up is called second PLA system, and it is indicated in Figure 3.5 as PLA-S₂. When using the PLA-S₂, we can easily calculate the dimension of the spot of the laser pulses by considering the approach described in the previous section.

The AuNPs were synthesized by the use of both ω and 2ω pulses, independently. The shape of the extinction spectra of the resulting NPs, whose intensity is proportional to their concentration in the water, is well known from our research [20, 192]. Since the PLA environment condition of the two experimental set-up shown in Figure 3.5, were the same (3 mm height of water with 2 m mol/L NaOH), the production rate of the NPs in the two cases will be the same only when the fluence F_{ω} or $F_{2\omega}$ of the laser pulses coming from the different laser sources are the same [6].

Hence, the following simple protocol was applied:

- 1) a proper lens-to-target distance (LT_1) was chosen for the PLA-S₁, the DM was inserted (Figure 3.5 a), and E_ω and $E_{2\omega}$ were measured;
- 2) the ω and 2ω pulses with the energy values of point 1) were used (separately) to synthesize AuNPs with the PLA-S₁;
- 3) laser pulses of the same energy of point 1) were used in the PLA-S₂ to synthesize AuNPs, at both ω and 2ω frequency.
- 4) The lens-to-target distance (LT_2) of the second experimental set-up was varied, and point 3) was repeated until we reached the geometrical condition for which the same concentration of NPs (same extinction spectra) were synthesized in the same time (~ 1 hour) using the different laser sources. This procedure was repeated for both ω and 2ω frequencies.

The nominal focal distances f_1 and f_2 of the lens L_1 and L_2 were 13.8 cm and 14.8 cm, respectively.

Once reached the condition of point 4, the diameter of the spot of the laser pulses at the two different frequencies (ϕ_ω , $\phi_{2\omega}$) was calculated, together with their fluence F_ω and $F_{2\omega}$. The condition for which $F_\omega \approx F_{2\omega}$, was found by simply varying LT_1 in the first experimental set-up, and repeating the procedure described above (point 1-4). This condition was found for a lens to target distance minor than the focal length of the lens L_1 , where the dimension of the spot of the ω laser pulse is bigger than the dimension of the one associated to the 2ω frequency, coherently with the well-known dependence of the diffraction-limited beams on the wavelength of electromagnetic waves [313].

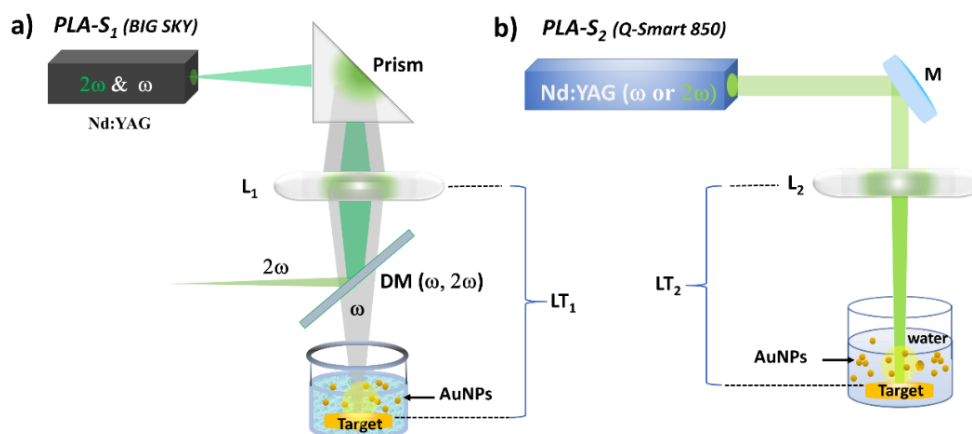


Figure 3.5 PLA experimental set-up (PLA-S₁ and PLA-S₂) used for the determination of the energies (E_{ω} , $E_{2\omega}$) and fluence (F_{ω} , $F_{2\omega}$) associated to the ω and 2ω frequency laser pulses during the experiments. a) PLA system emitting simultaneously ω and 2ω pulses indicated as PLA-S₁. DM($\omega, 2\omega$) represents a high power dichroic mirror, transmitting only laser pulses at one of the two frequencies (ω in this case), and reflecting the other one (2ω in this case). b) PLA system with a low divergence angle of the laser pulses, indicated as PLA-S₂. M is a high power mirror. LT₁ and LT₂ represent the lens-to-target distances in the two experimental set-ups. In both cases, the PLA systems are used for the synthesis of gold nanoparticles in water enriched with NaOH 2 m mol/L, indicated as AuNPs.

3.3. Analytical characterization of the nanomaterials

3.3.1. UV-visible spectroscopy

UV-Visible spectroscopy was used to measure the extinction optical coefficient of the samples, which are related to the nature of the metal, concentration, shape, and agglomeration state of the colloidal system of NPs. Along with the research, we used a Lambda 950 spectrophotometer from Perkin Elmer (U.S.A). Most of the measurements were performed in a cuvette of quartz with an optical path of 1.0 cm, and the samples were generally analyzed in the spectral range between 200 nm and 800 nm.

3.3.2. Inductively Coupled Mass spectroscopy (ICP-MS) analysis

Inductively coupled plasma mass-spectroscopy (ICP-MS) was used for the direct measurements of the metal concentration C_{metal} of the NPs. It is an extremely sensitive analytical technique used to measure the low concentration of elements, with a resolution of less than 1 part per billion (ppb). The quantification process was conducted by using ICP-MS with reaction cells (NexIon 300X and DRC II) from PerkinElmer (USA).

Prior to ICP-MS measurement, the sample of synthesized MeNCs colloidal solution and CQDs was placed in ultrasound bath for 10 minutes and then diluted 20000-time. The minimum volume required for the measurement is about 10 ml, and the concentration of salt and organic compound must be lower than 0.2 %.

3.3.3. Total Carbon Analysis (TC)

The total concentration of carbon element TC in our samples was measured by a Carbon Analyzer model TOC-VCPN (Shimadzu, Japan). The total carbon analyzers can detect and measure both the total organic carbon (TOC) present, and the complementing total inorganic carbon with a concentration in the ppb (part per billion) range.

Inorganic compounds are those compounds that do not have a carbon-hydrogen (C-H) bond. As compared to organic compounds, the inorganic compounds are quite simpler and shorter [314, 315]. Inorganic compounds exist in minerals and the atmosphere primarily in the form of carbon dioxide (CO₂), where the average concentration at the sea level in the atmosphere is approximately 380 ppm and is increasing about 2 ppm per year [316].

In contrast, the organic compounds are those compounds containing C-H bonds, although there are some exceptional cases. As compared to inorganic compounds, they have a more complex structure and contain many carbon atoms connected in chain or ring form [315]. Table 3.4. lists the common examples of organic and inorganic carbons.

Table 3.4 Examples of organic and inorganic compounds [314, 315].

Organic Carbon compounds	Inorganic Carbon compounds
Alkane, Alkene, Alkyne	diamond, graphite, amorphous carbons
Carbyne, polyynes, cumulene etc	carbon dioxide, carbon monoxide
Ketones, alcohol, phenol,	Carbides (silicon carbide)
Protein, lipid, nucleic acid	Carbonate & bicarbonate (sodium carbonate & bicarbonate)
Graphene, Graphene oxides,	Cyanides (sodium cyanide [NaCN])
Aldehydes	Sodium cyanate (NaCNO)
carboxylic acid, formic acid	Carbon tetrachloride (CCl ₄)
Ester	Trimethylphosphine (P(CH ₃) ₃)

The Carbon Analyzer (model TOC-VCPN) has a CO₂ detector, which is used to measure organic and inorganic carbon in the water-based solutions. The following three steps are used by the instrument to measure these carbons in the water.

- **Total Carbon (TC):** In order to measure the TC in a solution, a 50 µl of solution is automatically injected in the instrument, where it is burned in the presence of oxygen gas. The total carbon present in the solution (sample) is converted to CO₂, which is finally detected. The instrument repeats the measurements three times, and as result gives the average value [317].
- **Inorganic Carbon (IC):** highly concentrated (2 M) HCl is used to remove the inorganic carbon present in the sample. In this step, the equipment dissolves 12 µl of HCl solution in 800 µl solution of the sample. Hence, inorganic carbon in solution are converted to CO₂, and again measured by the detector [317].

Total Organic Carbon (TOC): TOC of the solutions is measured by indirect method. The measured IC is subtracted from the TC of the same solution, and as a result, the TOC is obtained [317].

We have different type of organic and inorganic carbon in our metal NP (MeNPs) colloidal solution, for example, sodium carbonate, bicarbonate, carboxylic acids, Cy@Au CNWs, and CQDs. Few of them are clear to be classified in organic or inorganic carbon, but it is difficult at that moment to categorize the presented CQDs or Cy@Au CNWs in organic or inorganic carbon. However, the equipment counts them in the organic carbon because they are relatively slow reactive with HCl as compared to inorganic, and are not easily convertible to CO₂.

In order to show the limitations of the equipment, we introduce here the TC measurements of a water solution containing different concentrations of NaOH. The results are shown in Figure 3.6.

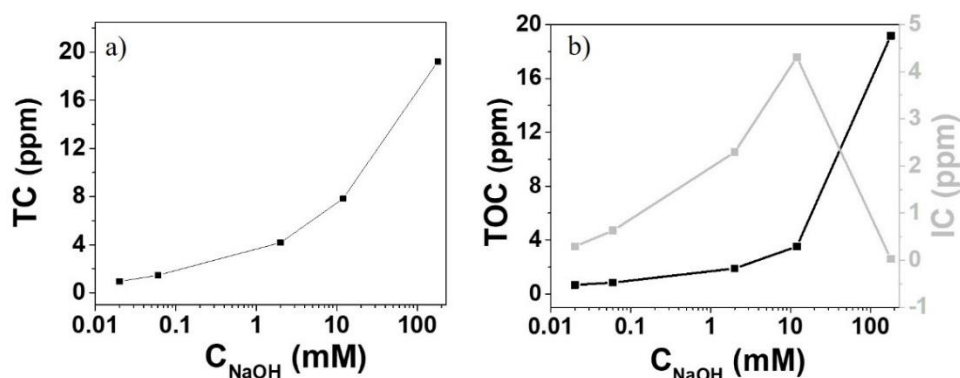


Figure 3.6 Dependence of a) TC, b) IC and TOC on the concentration of NaOH in the water solution.

Figure 3.6 show that all TC, TOC and IC are increasing with the rising of NaOH concentration in solution, but above than 20 m mol/L NaOH the behavior of IC changes trend. We observed that the molar concentration of the NaOH in the measured solution must be lower than the net concentration of HCl in the solution inside the equipment, otherwise when acid concentration is comparable or less than NaOH, the present HCl will react with NaOH, and there will be not enough concentration to convert inorganic carbon to CO₂. In the equipment the net concentration of the HCL solution during measurement was 20 m mol/L, therefore this was the maximum allowed NaOH concentration.

3.3.4. Dynamic light scattering (DLS) and ζ -potential

A nanoparticle analyzer model SZ-100 (Horiba, Japan) was used for the measurement of hydrodynamic size and surface potential (ζ -potential) of NPs in the colloidal dispersion. More details about the principle of working of the instrument are explained in appendix A.2.

The fresh synthesized Au, Fe, and Ag derived nanomaterials in liquid form were used for the measurement of both DLS size and ζ -potential. For both Au and Ag derived nanomaterials in colloidal dispersion, the extinction at the corresponding LSPR wavelength was fixed at a value of 1. In the case of Fe derived nanomaterial, without a LSPR peak, the ablation was fixed for 2 hours. The ζ -potential of the CQDs was measured after their separation from MeNPs by induction or magnetization methods, as explained in Section 2.6.

3.4. Chemical characterization of the nanomaterial

3.4.1. Raman spectroscopy

Raman and SERS spectroscopy were performed both by the candidate in the Analytical Center of the Department of Chemistry of PUC-Rio, and by Prof. Gino Mariotto from the University of Verona, as explained in Section 1.

In the Analytical center we used a confocal micro Raman apparatus model XploRA, from HORIBA, equipped with a CCD detector with a thermoelectric cooling system (working temperature of $-50\text{ }^{\circ}\text{C}$), and three solid-state laser sources at the wavelengths of 532 nm, 638 nm, and 783 nm.

The iron-based NPs were instead characterized by our colleague from the University of Verona using a Horiba Jobin-Yvon (model LabRAM HR800) Micro Raman spectrometer, equipped with a He-Ne laser ($\lambda_{\text{exc}} = 632.8\text{ nm}$).

The experimental conditions used to measure the samples by the different Raman spectrometer were similar. In both cases, mostly the excitation wavelength in the red region was used (638 nm and 632.8 nm), and the laser beam was focused

onto the sample surface through a 100× objective lens to produce a spot size of approximately 1 μm. Unless specified, the optical irradiance was kept in the range of 10⁻² kW/mm², in order to not modify the characteristics of the carbon soft materials [20].

In Verona, the scattered radiation was dispersed by a diffraction grating of 600, lines/mm, the average spectral resolution was approximately 1 cm⁻¹ /pixel over the spectral range of interest, and the notch filter produce a low wavenumber limit of approximately 200 cm⁻¹. Under these excitation conditions, very long integration times (typically 1800s) were required to collect spectra with an optimal signal-to-noise ratio.

During Raman and SERS spectroscopy in the Analytical Center, also different gratings were used, specifically of 1200 and 1800 lines/mm. The entrance and output slits were put at 100 μm, and the final spectral resolution were 2.5 cm⁻¹ and 1.8 cm⁻¹ for 532 nm and 785 laser excitations, respectively. Also in those cases the typical time to collect the spectra were of the order of a few hours.

MicroRaman measurements were carried out on different aggregates of both types of MeNPs under the experimental conditions described above, and the recorded spectra exhibited very good reproducibility. Moreover, repeated measurements over the same sample grain produced overlapping spectra, indicating that there was no structural damage to the sample surface from the laser beam.

- **Preparation of the samples**

The solid state samples for SERS and Raman spectroscopy were prepared by the following two different methods.

a) **Colloids drops on gold thin film (SERS)**: we put several 3 μl volume drops of nanomaterial obtained from ablation of Au or Ag targets on a thin film of gold, and let evaporate one after the other, to create a nanoisland film (NIF) of agglomerated MeNPs characterized by potential hot-spots for SERS effect.

Powder (Raman): in order to measure the Raman spectra of the iron based NPs, a considerable quantity of material was needed. In this case, 40 ml of colloidal solution was prepared, after which the iron oxide-based NPs were separated by the application of a 0.5 tesla magnet for 4 days. After the separation of precipitant and

supernatant, the latter was attracted for further 6 days with the magnet, and ultra-small iron-based NPs were obtained as new precipitant. In both cases, the precipitants were dried through evaporation in the oven at 55 K temperature, to obtain the powder of MeNPs. Because of their small concentration, at that moment we are not able to prepare the quantity of CQDs in powder form necessary for the Raman characterization.

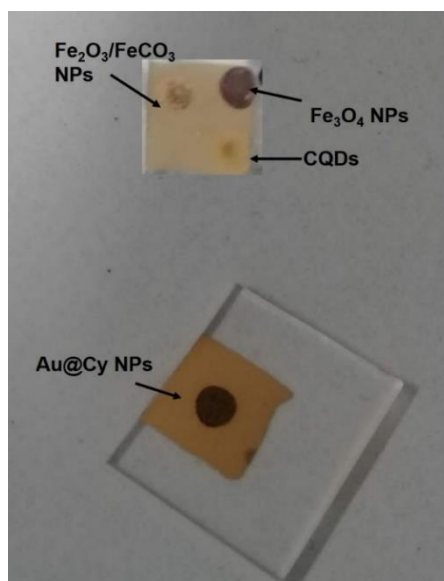


Figure 3.7 Appearance of the samples for SERS and Raman spectroscopy. Drops of MeNPs are deposited and dried on a gold thin film.

3.4.2. Infrared spectroscopy

The infrared spectra of the samples were measured by FTIR spectroscopy using a spectrophotometer model Spectra-Two (Perkin Elmer, U.S.A) with a resolution of 0.5 cm^{-1} , in the spectral range between 400 to 4000 cm^{-1} . The apparatus is equipped by module which allow to enhance the signal by an attenuated total reflection (ATR) configuration. All the samples were analyzed in powder form, produced following the method described in the previous sub-section.

To obtain a well reproducible signal from the samples of CQDs derived from Au and Fe, we concentrated in a volume of $400 \text{ }\mu\text{l}$ the CQDs obtained from about 40 ml of as synthesized nanomaterial before the separation process, and deposited in several drops on the active diamond surface ($2 \text{ mm} \times 2 \text{ mm}$) of the ATR configuration. The deposition process took about 8 hours.

In the case of Au derived CQDs, before the concentration, the colloidal dispersion of nanomaterial was subjected to a dialysis process of about 3 weeks, to eliminate NaOH and its derivatives in water. After evaporating all the water, we successfully measure FTIR spectra in the range from 400 to 4000 cm^{-1} .

3.4.3. X-ray photo-electron Spectroscopy (XPS)

A Magnesium K_{α} -ray and VG Thermo Alpha 110 cm hemisphere analyzer were used in the XPS measurements, conducted under the supervision by Prof. Marcelo Maia da Costa of the Van der Graaf Laboratory of the Department of Physics of PUC-Rio. The spectra range was kept from 0 eV to 1100 eV with 0.5 eV energy steps, while local energy spectra at the position of carbon, iron, oxygen and gold, were done with 0.1 eV energy step.

- **Preparation of the samples**

For the Au derived CQDs, we applied the same deposition technique as in the FTIR analysis. The NPs were deposited on copper disks, and before the concentration process, were subjected to a dialysis process of about 2 weeks, to eliminate NaOH and its derivatives in water.

The iron based NPs were analyzed after deposition of a few drops of 100 μl on pure silicon substrates. As for IR characterization, dialysis was not necessary in this case, since the ablation was conducted without the addition of NaOH in the water environment.

3.5. Morphological and structural characterization of the nanomaterial: transmission electronic microscopy

The working principle and structure of transmitting electronic microscope in high resolution TEM (HRTEM) mode, scanning transmitting electronic microscope (STEM), and energy dispersed spectroscopy (EDX or EDS) mode have been discussed in detail in appendix A.3.

In this research work, for the analysis of the structure and composition of carbynoid materials, CQDs, and MeNPs, TEM was used in diffraction electron pattern mode, HRTEM, STEM and EDS configurations.

3.5.1. Used TEM apparatus

Different types of equipment were used to perform the TEM characterization of the samples:

a) (*LABNANO/CBPF*)

1) JEOL JEM-2100F operated at 200 kV in both STEM, HRTEM and selective area electron diffraction (SAED) modes.

2) Field emission scanning electron microscope (FE-SEM) (JEOL, JSM-6701F) operated in transmission (TSEM) mode at 30 kV.

b) (*INMETRO*)

1) FEI Tecnai –Spirit G2 operating at 120 kV.

2) FEI Titan 80-300TM microscope operating at 80 kV, equipped with FEG, and Cs probe corrector.

c) (I.N.L) - FEI Titan 80-300TM microscope operating at 80 kV, equipped with FEG, and Cs probe corrector.

d) (USP) - Tecnai G2 Spirit TWIN FEI microscope, USA, operating at 120 kV with a LaB6 (lanthanum hexaboride) filament.

3.5.2. Preparation of samples

To prepare the TEM grid for the analysis, different methods were used, depending on both the kind of grid and sample. We mostly used two kinds of TEM grids, the so called flat carbon (FC) and holey-carbon (HC). In both cases we used a 300 mesh of copper or gold. Before the deposition of the carbon based nanomaterials,

the carbon flat TEM grids were treated for 75 s by a plasma cleaner (with shield), in order to enhance the contrast.

When the analysis of the same sample was performed on both FC and HC films, the concentration of the drop deposited on the HC type was always approximately two times (optical extinction = 0.4) the one used for the flat ones (optical extinction = 0.20). This is because part of the liquid sample passes through the holes and is missed during the deposition procedure.

Depending on the concentration of the sample, two deposition techniques were used: grid-on-drop (GOD), and drop-on-grid (DOG). The first case has to be applied for samples without problems of low concentration and low contrast on the grid, and minimize the quantity of water on the grid, diminishing the agglomeration of the NPs during the deposition process. The TEM grid is placed over a drop of colloidal solution for about three minutes, after which is placed over a drop of ultra-pure water for 10 second, and let dry in a clean environment at ambient temperature. The water on the sample generally disappears in a few hours, although it is always better to wait at least one night in order to allow the optimal evaporation of the water.

In the DOG method, a drop is placed on the TEM grid, and let evaporate slowly for 48 hours. This method has to be privileged to the GOD when the sample has a very low concentration of NP, or the NPs are weakly interacting between them so that there is no danger of enhancing their agglomeration during the drying process.

Although different combination of grid, method of deposition and concentration of the NPs has been investigated for the different kind of NPs, we resume in the following Table 3.5, the details for the optimal preparation of the different samples analyzed in the present research.

Table 3.5 Preparation technique and TEM grids used for the different samples analyzed in the present research.

<i>z</i>	extinction at LSPR /or t_{abl}	dilution or concentration factor	TEM grid	technique
Au@Cy NPs	1	3 time diluted	HC	GOD
Au@Cy NPs	1	4 time diluted	FC	GOD
Ag@Cy NPs	1	3 time diluted	HC	GOD
Iron NPs	2 hours	10 time diluted	HC	DOG
Carbon (CNM)	5 hours	15 time Concentrated	HC	DOG

3.6. Carbon/metal separation methods

The process of synthesis of carbon nanomaterial during PLA of transition metal targets in water is a process which naturally happens in normal thermodynamic conditions of pressure and temperature of the liquid, as will be clear after the presentation of the experimental results. The great number of scientist which dedicated their scientific activity in the past 40 years on the investigation of the synthesis of nanomaterial by PLA in liquid, never had realized this simultaneous synthesis due to the spectral overlap between the emission bands of the emissive carbon nanostructures and the extinction spectra of the MeNPs, as visible in Figure 3.8, where are represented the LSPR bands of Au and Ag based nanomaterials, together with the emission spectra of the QCDs. It is clear that the emission of the CQDs is strongly attenuated by the optical density of the colloidal dispersions. Also in the case of iron targets, the quenching of the luminescence by the presence of metallic species [11], impedes the detection of any luminescence by the carbon material.

Generally, carbon-based (nano) materials are separated from metals and selected on the basis of their typical retention time inexpensive analytical techniques such as high-performance liquid chromatography (HPLC) [253, 318], but the MeNPs may precipitate in the filtering column and cause the relative damage.

Therefore, we tested different new and non-expensive methods aimed to the separation of the CQDs and carbonyoid NWs from the metal NPs, namely: amalgamation, precipitation by salt, centrifugation, filtration, heating, grounding and magnetization. Some of the previous techniques were mixed together in multistep processes, to enhance the performances of the separation process. The results were compared in terms of the residual percentage concentration of metals (ρ_{residual}) inside the final colloidal dispersion.

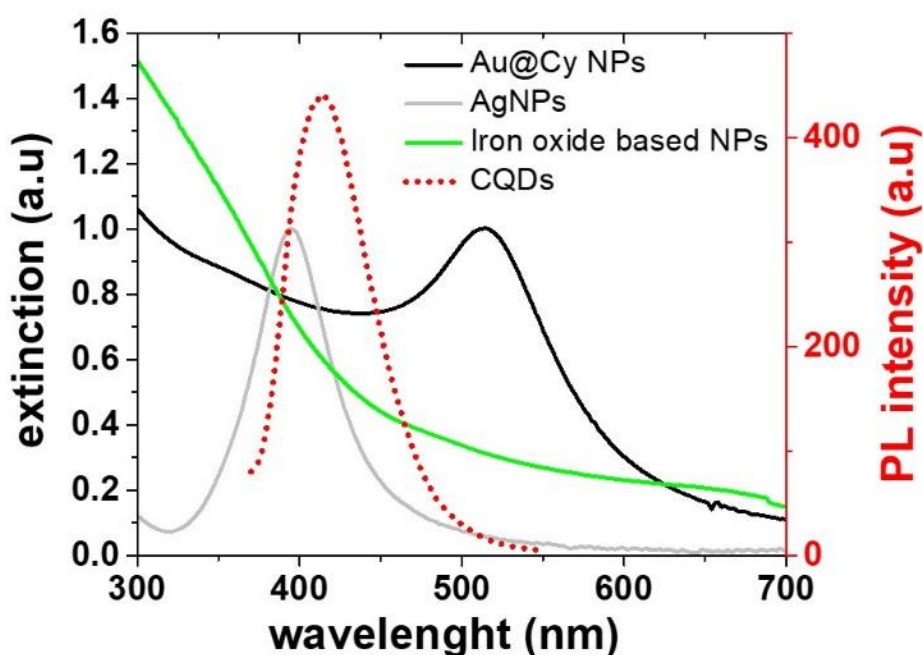


Figure 3.8 Emission spectra of the CQDs (red line) overlapped with the extinction spectra of the Au (black line), Ag (grey line), and Fe (green line) derived nanomaterials.

As an example, in Figure 3.9 we report a TEM image of the Au-derived nanomaterial before and after the separation by the multi-step process consisting of heating, filtration and centrifugation. Consistently with the TEM images, the residual concentration of Au was below 0.1 ppm (0.1 %), and the process was considered successful.

In the following, we describe in more detail the methodology and the results relative to the different separation processes.

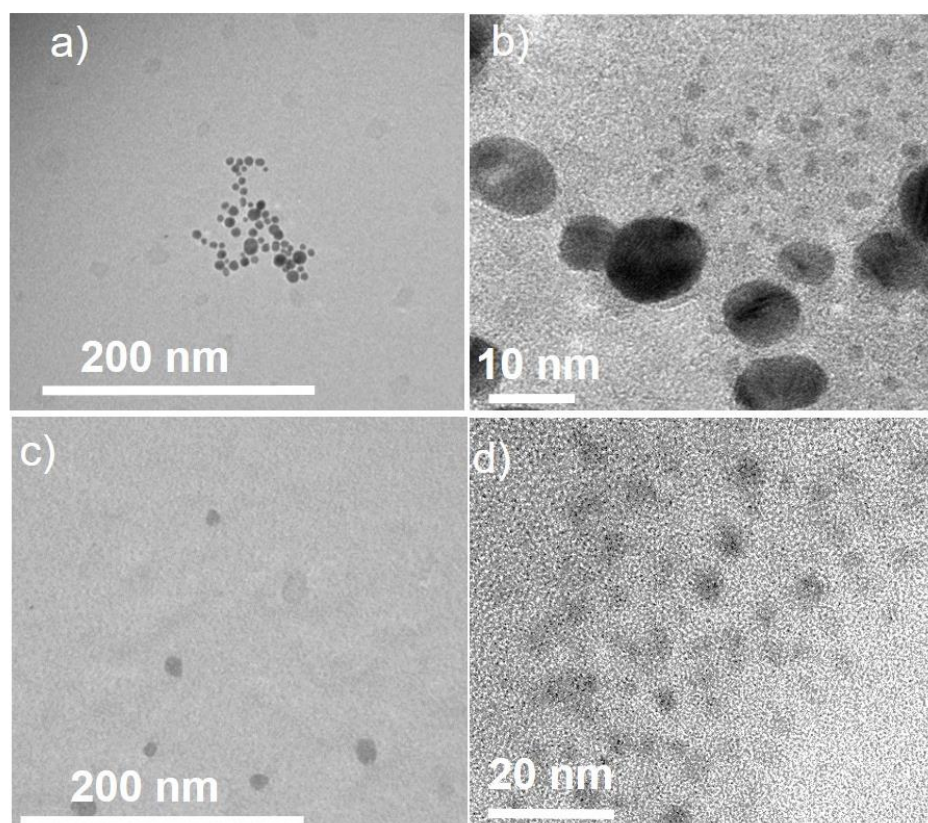


Figure 3.9. TEM image of the fresh Au derived nanomaterial (a,b), and the material after separation (c,d).

3.6.1. Magnetization

This method was applied only for the Fe derived nanomaterial. A 0.3 T magnet is placed aside a glass containing the colloidal solution of magnetic NPs. The case of iron-based synthesized at the fundamental frequency (ω) is shown in Figure 3.10. After 10 days, a transparent supernatant is separated from the precipitated magnetic material. The successful separation can be confirmed by eye in this case. Anyway, when the Fe based nanomaterial is synthesized by the second-harmonic radiation 2ω ($\lambda = 532$ nm) or both the ω and 2ω frequencies, the NPs are not all agglomerated by the unique magnetization. After different experiments, we realized that heating the colloidal dispersion of NPs at a temperature above ~ 55 °C leads to precipitation of the residuals iron-based nanostructures. The obtained precipitant is easily agglomerated by magnetization, and a transparent supernatant is obtained.

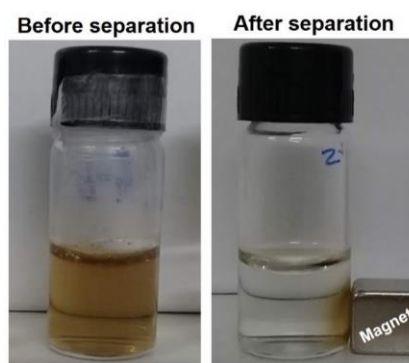


Figure 3.10 Photo of a colloidal dispersion of Fe derived nanomaterial before and after the separation by magnetization. The NPs were synthesized by fundamental frequency (ω) laser pulses.

Table 3.6 ICP-MS measurement before and after separation with magnet

Sample	Au (ppm)
Fe derived nanomaterial (ω) (before)	32.0
After separation	0.0

3.6.2. Amalgamation

This method was applied only to Au derived nanomaterial. Metallic mercury is placed in the sample, after which the sample is put in agitation by a shaker for 30 minutes. During the shaking the existing Au@Cy NPs and mercury form the amalgam [319] and the colloidal dispersion loses its ruby red color and precipitate. The quantity of gold and mercury in the supernatant before and after the separation was measure by ICP-MS, and the results are reported in Table 3.7.

Table 3.7 Concentration of gold and mercury before and after the separation by amalgamation, as measured by IC-PMS.

Sample	Au (ppm)	Hg (ppm)
Fresh Au derived nanomaterial	71.3	0.0
After amalgamation	3×10^{-12}	16.0
After amalgamation and centrifugation	1×10^{-2}	6.0

This method was not proved to be successful, since the residual presence of mercury contaminates significantly the obtained nanomaterial.

3.6.3. Precipitation by dialysis and centrifugation

In a good extent, is the double layer charge on the surface of the noble MeNPs which drives their stability, as discussed in Section 2 [5]. We induced an electrostatic instability on the double layer of the Au derived nanomaterial by the application of a dialysis process. The dialysis has been initially carried on for about 2 days, changing the deionized water every 12 hours. After dialysis, the obtained liquid was centrifuged for 1 hour at 14000 rpm rotation speed, and the supernatant was separated carefully. The metal concentration before and after the separation is reported in Table 3.8.

Table 3.8 Gold concentration before and after the separation by dialysis and centrifugation.

Sample	Au(ppm)
Fresh Au derived nanomaterial	80.3
After dialysis and centrifugation	5.1

The ICP-MS measurement shows that still there is a significant quantity of gold in the supernatant. Hence, also this method has not been proven successful.

3.6.4. Precipitation by salt

The electrostatic instability of the double layer of the Au derived nanomaterial was induced by the addition of 0.33 M NaCl in water. The colloidal dispersion changes rapidly the color from ruby red to purple because of this agglomeration [320], and start to precipitate. After 24 hours the supernatant and the precipitant are separated. Because of the high concentration of salt (0.33 M NaCl) which quenches the PL of the CQDs, the supernatant was subjected to four dialysis process of 24 hours.

Table 3.9 ICP-MS measurement of the Au derived nanomaterial before and after precipitation by salt.

Sample	Au (ppm)
Fresh Au derived nanomaterial	80.3
After precipitation by salt and dialysis	1×10^{-1}

The ICP-MS measurement before and after separation, are shown in the above Table 3.9. The results indicate a successful separation. After dialysis, the concentration of salt ions decreases, and we can see a good PL emission of the CQDs colloidal solution. Although this method is efficient in order to see a good PL, the measurements of the TC on the colloidal dispersion of nanomaterials after multiple dialysis steps, indicated a progressive enhancement of the carbon content, as indicated in Table 3.10. In the dialysis process we used two types of membranes, both with 3500 dalton molecular weight cut-off. One type contains glycerin as a humectant (Spectra/Por™ 3 Dialysis Tubing with 3500 d Molecular weight cut-off), and the second contains cellulose. We understood only in the last weeks dedicated to the experimental research, that the enhanced TC resulted is because of a non-efficient initial cleaning of the dialysis membranes described above. In order to obtain a dialyzed colloidal dispersion without carbon contaminants, a cleaning process of 1 week of the membranes is needed prior to dialysis. The latter has to be performed for the other 2 weeks, changing the deionized water every 8 hours.

Table 3.10 TC of Au derived CQDs after different number of dialysis processes.

Au derived CQDs	TC (ppm)
Before dialysis	10.1
After 1 dialysis of 20 hours	15.8
After 5 dialysis of 20 hours	53.1

Nevertheless, this method was used to synthesize QCDs derived from Au target, and used for chemical sensing applications.

3.6.5. Heating

The colloidal dispersion of Au derived nanomaterial was heated at temperatures varying from 40⁰ to 65⁰ C, in order to let slowly evaporate the liquid of the colloidal dispersion, which was concentrated as a rule of thumb of about 10 times.

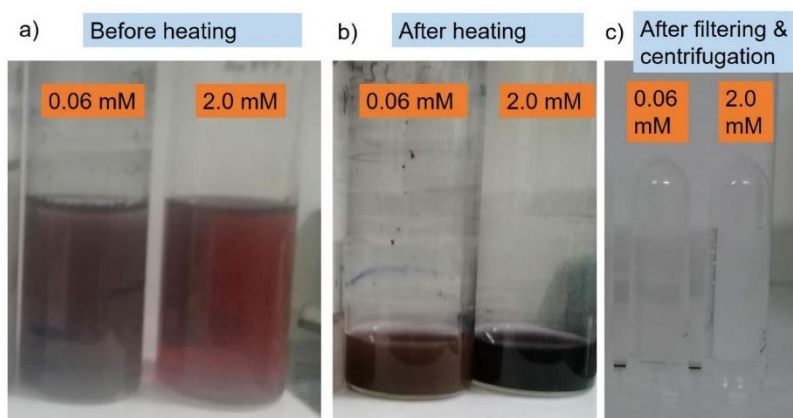


Figure 3.11 Au derived nanomaterial synthesized in 0.06 and 2.0 m mol/L NaOH solution a) before heating, b) after evaporation induced by heating, and c) after filtering and centrifugation.

At very high concentration, the MeNPs become close to each other and hence the Van der Waals forces become increased, which results in an induced agglomeration among MeNPs in colloid and become unstable, as shown in Figure 3.11. The concentrated colloidal dispersion is filtered with a PES (Polyethersulphone) Sterile syringe filters of 0.2 μm pore size, and centrifuged for 1 hour at 13000 rpm at -5 ⁰C . The obtained transparent supernatant has a low metal concentration, a good PL, and does not present any contaminant.

Table 3.11 Metal Au concentration before and after separation.

Sample	Au (ppm)
Fresh Au derived nanomaterial	81.3
After evaporation by heating and filtering	2×10^{-2}

3.6.6. Electromagnetic induction

MeNPs dispersion synthesized by PLA in water has an excess of charge in their metallic core contribution in their stability [5]. This excess charge is decreased by the grounding of the NPs colloidal dispersion through the conductor (due to electromagnetic induction), which arise the agglomeration and eventual precipitation. In this method, the colloidal dispersion was grounded with the help of a clean copper wire, as shown in Figure 3.12. The NPs partially or completely lose their charge, and start to agglomerate with final agglomeration, as shown in Figure 3.12. (b) and (d). To enhance the agglomeration and precipitation process, the colloids were stirred continuously.

After agglomeration, the transparent solutions were separated carefully and characterized by UV vis and ICP-MS spectroscopies. The results are shown in Table 3.12. The UV-vis absorption shows no presence of AuNPs.

Table 3.12 ICP-MS measurements on Au derived nanomaterial before and after separation by grounding.

Sample	Au (ppm)
fresh Au derived nanomaterial	81.3
after grounding	5×10^{-2}

The principal problem of this method is that it is successful only in the case of Au derived material since the stability of Ag and Fe derived nanomaterial is mostly because of oxidation and not due to excess of core charge [5]. Hence, we cannot agglomerate efficiently the AgNPs and iron oxide NPs by electromagnetic induction.

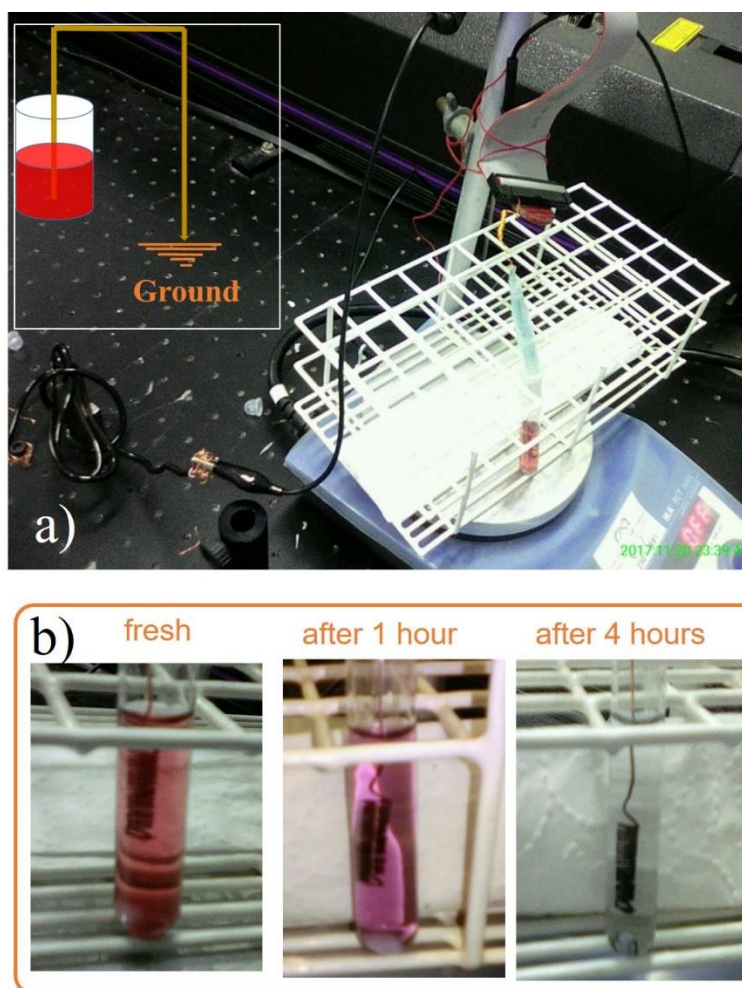


Figure 3.12 Photos representing the grounding technique for the Au derived nanomaterial. a) Experimental set-up; b) Temporal evolution of the color of the Au derived nanomaterial during the grounding.

3.6.7. Conclusions on the separation methods

All the methods described above are clean, easy and cheap, and any of them can be applied if the aim is the simple observation of the PL.

Anyway, considering the small concentration of carbon nanomaterial, the most important aspect remains the absence of possible contamination, so that that the evaporation process induced by heating followed by filtering seems the best option, if a long cleaning process (1 week) of the dialysis membranes wants to be avoided.

The separation method by heating and filtering is very useful to control the maximum possible dimension of the separated nanomaterials and has been applied

for the morphological study by TEM investigation. Resolved the contamination problem during dialysis, in the future we will have the possibility to analyze dialyzed samples with confidence, investigating the possible presence of bigger nanostructures.

3.7. Photoluminescence spectroscopy

The properties of photoluminescence (PL) of the synthesized QCDs were investigated by both steady-state and time-resolved PL spectroscopy (STPL, TRPL).

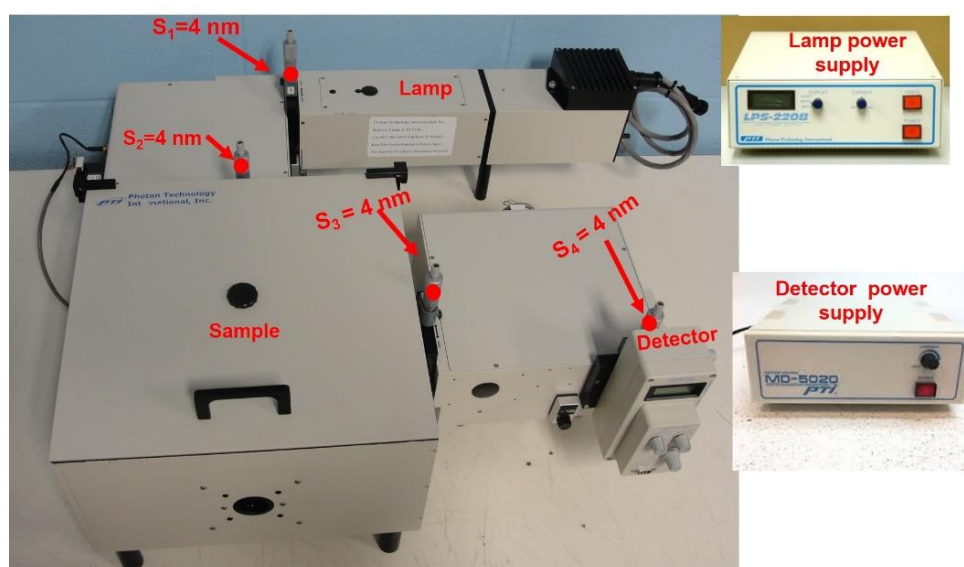


Figure 3.13 Photo of the spectrofluorometer model QM1 of PTI (Canada) used for STPL in the Department of Physics of PUC-Rio. The opening of each slits was set at 4 nm, as indicated. The slits S_1 and S_2 are used to modulate the intensity of incoming excitation light, while S_3 and S_4 are the slits to control the intensity of emitting light.

STPL spectroscopy was the most powerful tool used to confirm the presence of CQDs in the supernatant of MeNPs colloidal solution synthesized by PLA of metal target in water. In fact, due to the high optical cross-section of the PL process in comparison to both IR and Raman spectroscopy, we could detect the production of luminescent material also at concentration for which Raman, IR or even SERS response was not obtained.

STPL spectroscopy was performed using different spectrofluorimeters in the Department of Physics and Chemistry of PUC-Rio. Most of the characterization measurements were performed using the spectrofluorometer model QM1 of PTI (Canada). A few measurements for samples at lower concentration were executed using a fluorimeter (PTI) QuantaMaster™ 8000 in the LOEM of the Department of Physics of PUC-Rio. For the chemical sensing application of CQDs, we also used a spectrofluorometer model LS 55 of Perkin Elmer (U.S.A), located in Laboratory of Applied Spectroscopy, Electroanalysis and Elemental Analysis Department of Chemistry PUC Rio, under the supervision of Prof. Ricardo Aucelio.

The optical chemical sensing measurements were performed using a 1000 nm min⁻¹ scan rate, 10.0 nm spectral bandpass (slit opening size), 4 nm spectral resolution and a 1 cm optical path length quartz cuvettes. In this case, a thermostatic system with stirring (PTP-1 Fluorescence Peltier System with a PCB1500 Water Peltier System, Perkin-Elmer) was used to keep the dispersions in the cuvette at specific constant temperatures during the measurements.

TRPL spectra were measured with pulse width < 1.2 ns at the excitation wavelength of 335 nm, varying the emission on the whole PL band of the CQDs, with steps of 25 nm. The decay curves were fitted to obtain the lifetime using a double exponential function.

The quantum yield (QY) of the CQDs was evaluated by the comparative method, similarly as reported in [287]. The unknown QY_s is determined from the known QY_r of a reference material through the following formula (“s” and “r” stand for “sample” and “reference”, respectively)

$$QY_s = QY_r \frac{I_s A_r}{I_r A_s} \left(\frac{n_s}{n_r} \right)^2, \quad (3.11)$$

The integrated emission intensity is recorded as a function of the absorbance A of the sample, and n is the refractive index of the buffer solution. For the measurements to be reliable and to minimize the non-uniform radiation, the absorbance of the sample was kept below 0.1. For the quantification, Rhodamine 101 (QY_r = 100%) was used as a reference. As for the emission intensity I, the PL area at the FWHM was considered.

3.8. Magnetic characterization

The scanning magnetic microscope (SMM) [321–323] used to perform the magnetization curves of the iron-based nanomaterials, is shown in Figure 3.14. The principal part is constituted by a powerful electromagnet (Model 3470 of the GMW brand) which, in the current configuration, is capable of applying in the sample a magnetic field of up to 0.5 T. The field is applied between its 40 mm diameter poles and a movement system composed of a pair of linear actuators (Model T-LLS260C brand Zaber). The reading system consists of a pair of Hall effect sensors (Model HQ-0811 brand AKM), installed in an axial gradiometric configuration in order to cancel the magnetic field applied by the electromagnet, and reduce ambient magnetic noise [321, 322]. Each sensor is soldered to a printed circuit board that is connected to a thin acrylic structure attached to one of the surfaces of the electromagnetic pole [321–323].

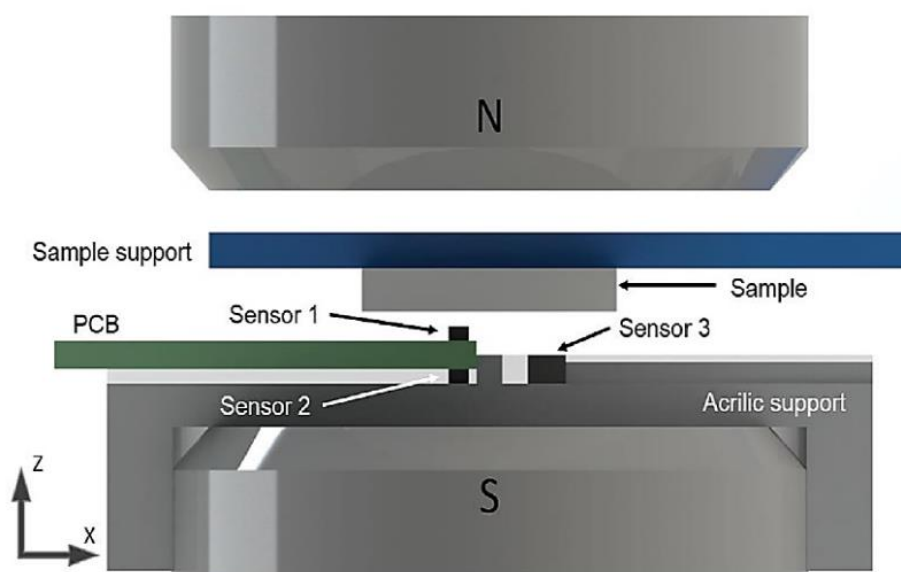


Figure 3.14. Reading system of the scanning magnetic microscope [322].

For the measurements of magnetic nanoparticles synthesized by PLA, the used na acrylic sample holder. After this stage, small cylindrical cavities (400 μm diameter and 400 μm depth) were made in the center of each sample holder. Within this cavity, 50 μg of magnetic nanoparticles were added [322]. To obtain the

magnetic moment of the nanoparticles, several magnetic maps were mapped for each magnetic field applied by the electromagnet in the sample. Through these maps, it was possible to obtain the magnetization curve of the samples [322]. In addition to the magnetic characterization, the microscope was used to estimate the average diameter of the magnetic core of the nanoparticles [322].

4. Results of Au derived nanomaterial

4.1. UV-Vis stability Investigation of Au derived nanomaterial

In Figure 4.1, we report the temporal evolution of the UV-Vis extinction spectra of the Au derived nanomaterial colloids synthesized at $F = 1.3 \text{ J/cm}^2$ and different values of NaOH concentration (C_{NaOH}), ranging from 0,02 mmol/L to 20,0 mmol/L (initial pH 7.2 to 12.4). The PLA process was stopped when a maximum extinction coefficient of 1 was reached. The ablation times were slightly different for the different concentrations, ranging from 55 to 65 min.

We observe three distinct phenomena with the passage of time: the Ostwald ripening [324], agglomeration, and precipitation. Ostwald ripening is particularly observable in the first days after PLA. The Au ions and clusters dispersed in the colloidal dispersion, slowly enrich the core of pre-existing small metal NPs, contributing with a spectral red-shift, and an enhancement of the Plasmon peak. This phenomena is not observable in the samples synthesized at low ($< 0.5 \text{ mM}$) or high ($> 12.0 \text{ mmol/L}$) values of C_{NaOH} . As explained in the theory section, in both cases the electrostatic repulsion between the NPs is lower than the attractive long-range forces, with final precipitation of the nanomaterial.

The long-term use of the Au derived nanomaterial is hence opportune for samples synthesized in a range of C_{NaOH} between 0.06 mmol/L and 12.0 mmol/L. In this case, we do not observe any precipitation of the samples along 3 months, although some small aggregation phenomena is visible by the enhancement of the FWHM of the LSPR curves for the samples at the extremes of the stability window (0.06 mmol/L, 12.0 mmol/L). In $C_{\text{NaOH}} = 50 \text{ mmol/L}$ solution the production rate of AuNPs is very low as compared to lower C_{NaOH} samples, and the synthesized colloidal dispersion is highly unstable. Due to this agglomeration and a relatively small concentration of AuNPs, the 50 mmol/L NaOH sample has light gray purple

color. Similarly, the 0.02nmol/L samples are also unstable, but with higher metal concentration, showing a dark gray purple color, as shown in Figure 4.2.

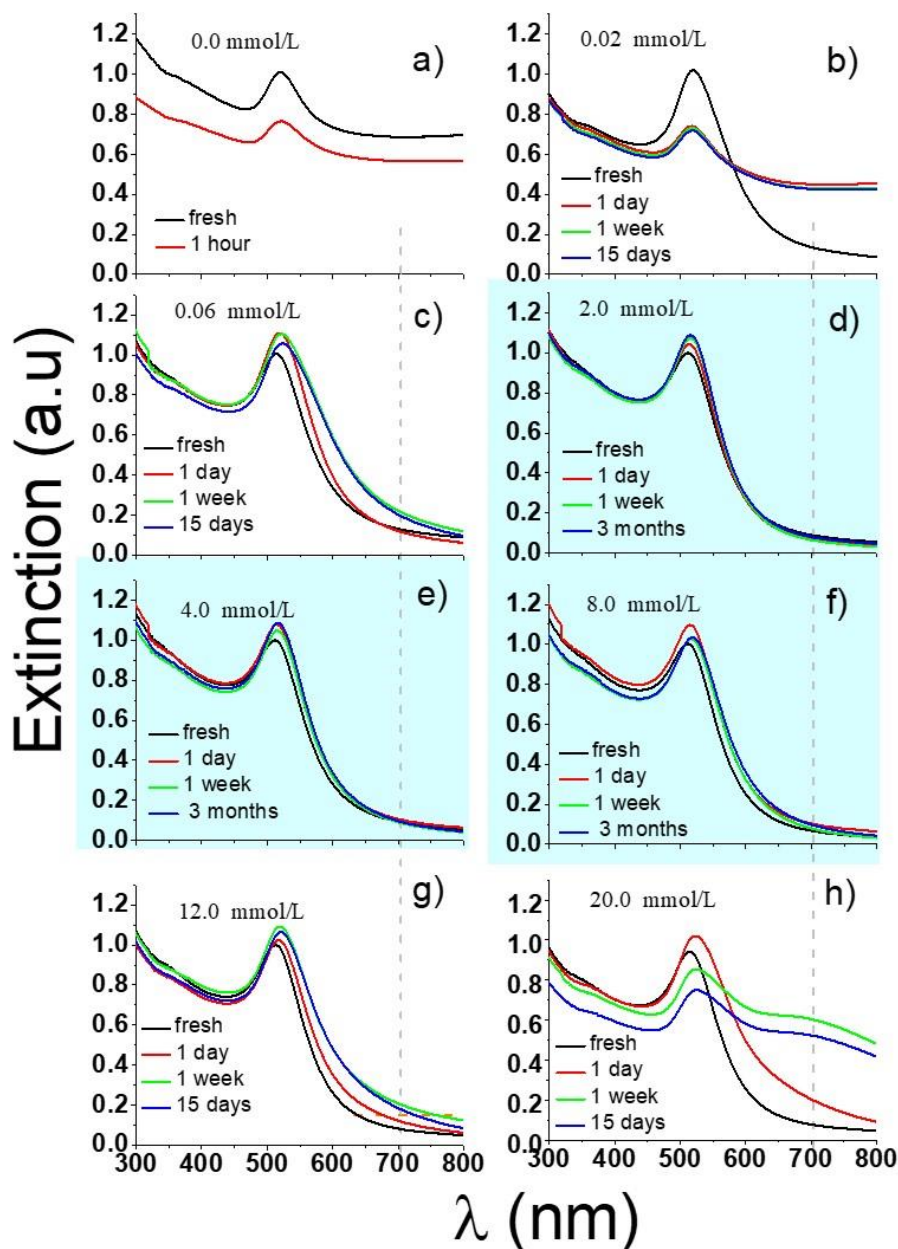


Figure 4.1 Temporal evolution of the UV-Vis extinction spectra of the Au derived nanomaterial synthesized at $F = 1.3 \text{ J/cm}^2$ and different values of c_{NaOH} , ranging from 0,02 mmol/L to 20,0 mmol/L. The figure highlighted, is relative to the condition of best stability, with almost no aggregation after more than 90 days.

In Figure 4.2 we document, by the use of photographs, the stability of the different colloidal solutions with the passage of time.

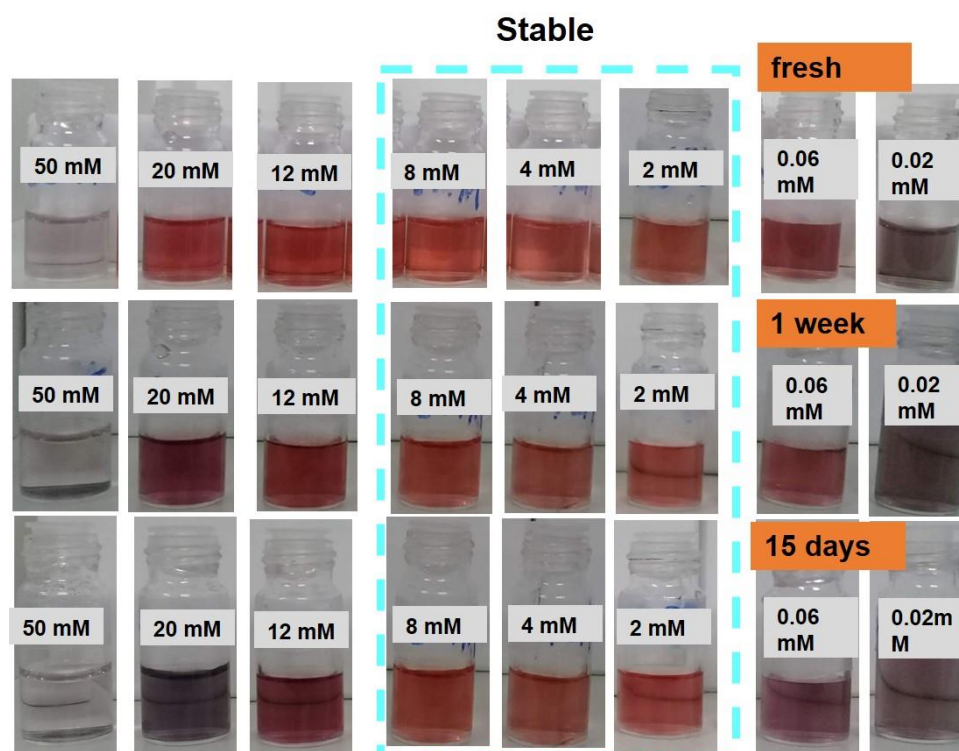


Figure 4.2 Photos showing the color aspect of the colloids of Au derived nanomaterials with passage of time, synthesized at different values of c_{NaOH} .

In Figure 4.3 we finally report the temporal evolution of UV-Vis extinction spectra of the Au derived nanomaterial synthesized at $c_{\text{NaOH}} = 2,0 \text{ mmol/L}$ and different values of F . The total time of ablation necessary to reach an extinction value of ~ 1 , was 45 min, 180 min, and 520 min, for fluences of 0.3 J/cm^2 , 0.6 J/cm^2 , and 1.3 J/cm^2 , respectively. Interestingly, the low fluence samples show impressive stability, and also Ostwald ripening was almost not observable.

In Figure 4.4, we also report the comparison in the ablation efficiency depending on the value of F , expressed in terms of the value of optical extinction reached in the different experimental conditions by a PLA process of about 45 minutes.

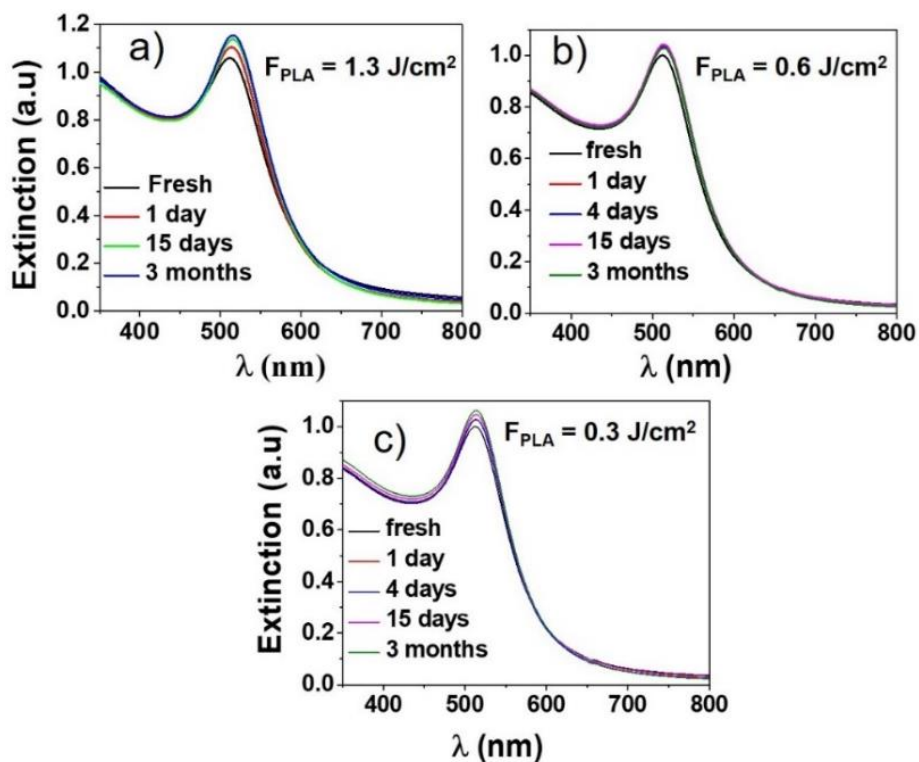


Figure 4.3 Temporal evolution of the UV-Vis extinction spectra of the Au derived nanomaterial synthesized at $c_{\text{NaOH}} = 2.0 \text{ mmol/L}$ and different values of F . The smaller fluence of $F = 0.3 \text{ J/cm}^2$ correspond to the threshold PLA value for Au target [169].

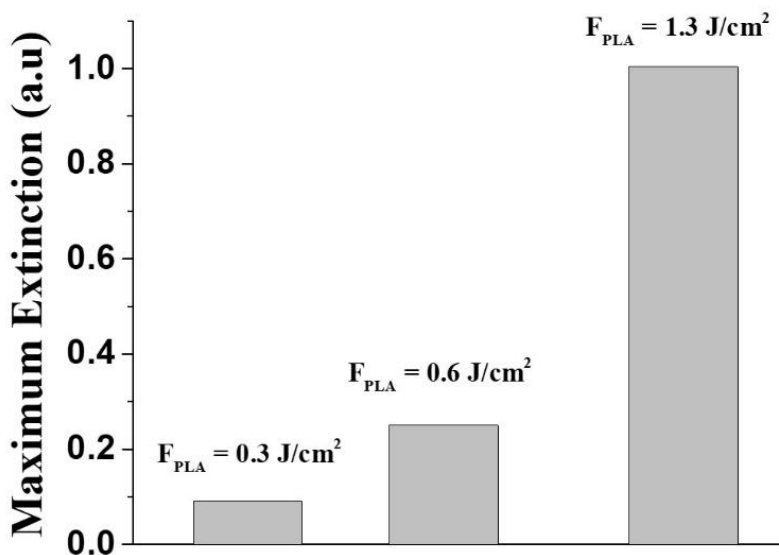


Figure 4.4 Optical extinction value of the Au derived nanomaterial at λ_{LSPR} , synthesized in a time $t_{\text{PLA}} = 45 \text{ min}$ using different values of F .

Hence, we can conclude that in the case of Au derived nanomaterial, the best method to obtain high stable colloidal dispersion, is the use of a low value of fluence, with $0.06 \text{ mmol/L} < c_{\text{NaOH}} < 12,0 \text{ mmol/L}$.

4.2.

Characterization of the Au derived nanomaterial (dimension, λ_{LSPR} , charge, total carbon)

Figure 4.5 show TEM images, statistical size distribution, and the corresponding UV-Vis spectra of the Au derived nanomaterial, synthesized at $c_{\text{NaOH}} = 0,02 \text{ mmol/L}$ (a,b) and 2.00 mmol/L (c,d). Due to the low stability of the samples synthesized at a lower value of c_{NaOH} , in this case, the deposition on the TEM grid was performed immediately after the end of the PLA process, and with the grid-on-drop (GOD) method described in Section. 3.

As is visible from Figure 4.5, the Mie theoretical fit perfectly overlaps with the experimental data, with the exclusion of a progressive blue-shift of the localized surface Plasmon resonance (LSPR) peak for higher values of c_{NaOH} . Hence, for the best overlap between the experimental and theoretical spectra, the latter have been opportunely blue-shifted.

In Figure 4.6, we show the evolution of the UV-Vis spectra and the dimension of the nanomaterial depending on both the NaOH concentration and fluence . The linear dimensions, as explained in the theoretical Section 2.2.3.3, are linked to the value of the ratio of [325, 326] the extinction at 440 nm and 520 nm, which is smaller for the higher concentration of NaOH and lower values of F. In the latter case, the values of the statistical mean radius have been accomplished only theoretically, without experimental comparison with the TEM statistical distribution.

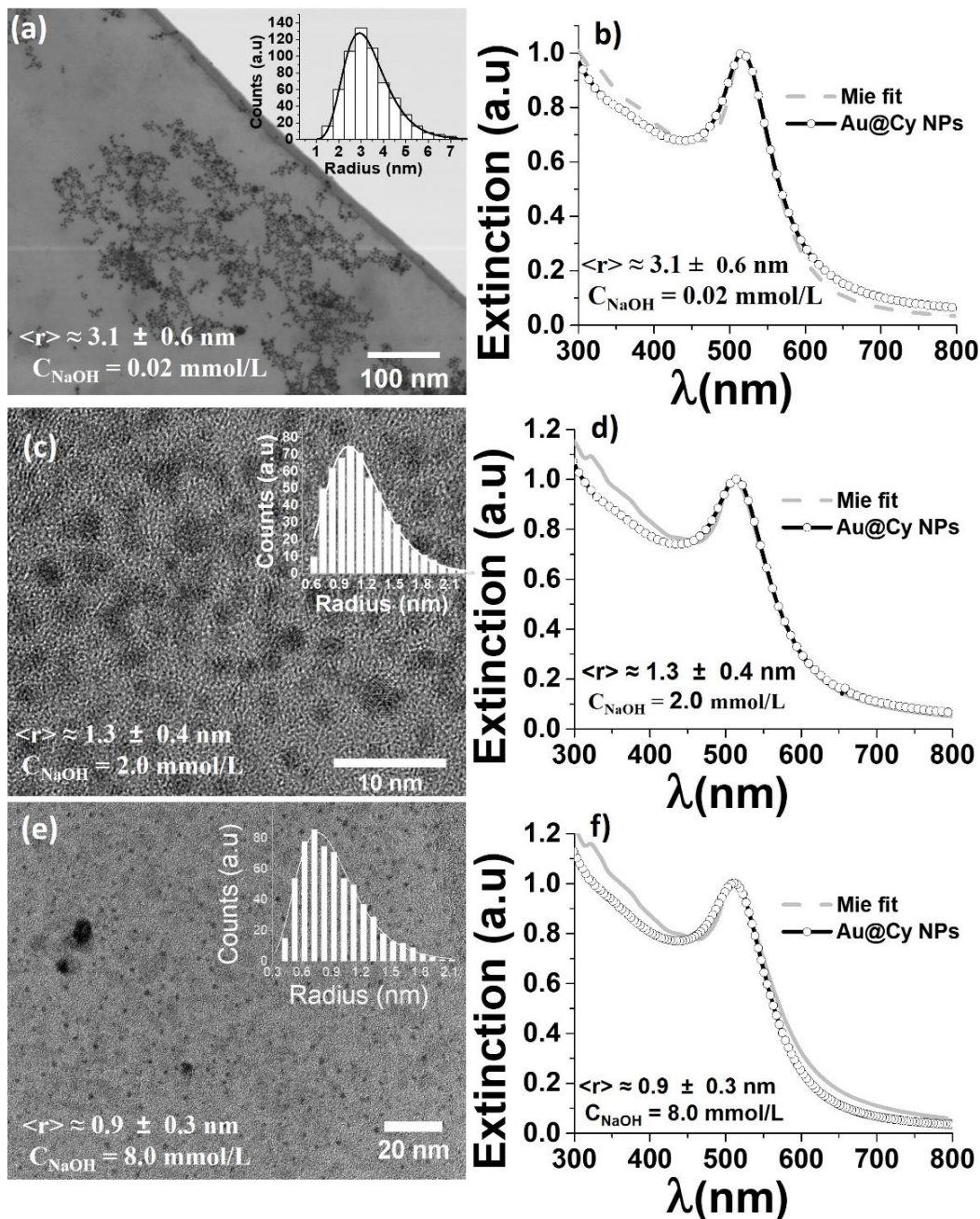


Figure 4.5) TEM images of the Au derived nanomaterial synthesized at $F = 1.3 \text{ J/cm}^2$ and in a) $C_{\text{NaOH}} = 0.02 \text{ mmol/L}$, c) $C_{\text{NaOH}} = 2.00 \text{ mmol/L}$ and e) $C_{\text{NaOH}} = 8.00 \text{ mmol/L}$.

The electron acceleration voltage was 80 keV. The inset represents the experimental statistical size (radius) distribution. The UV-Vis extinction spectra of the corresponding colloidal dispersion are represented in (b), (d) and (f). The grey dotted lines represent the Mie fit obtained in the multipolar approximation using the experimental size distribution shown in (a), (c) and (e).

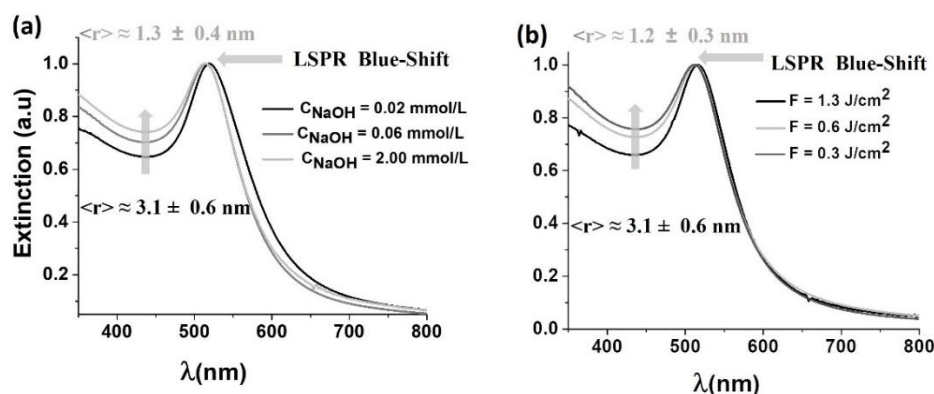


Figure 4.6 the UV-Vis extinction spectra of the colloidal dispersion of Au derived nanomaterial synthesized at different values of C_{NaOH} (a) and F (b). In the figure are highlighted the optical extinction around 440 nm and the spectral blue-shift.

The spectral appearance of the Au nanomaterial depending on the experimental conditions (C_{NaOH} , F) is represented in Figure 4.7.

We also did a comparison between the UV-Vis experimental spectra of the Au based nanomaterial derived by PLA using the different laser pulse frequencies ω (first harmonic laser pulse) and 2ω (second harmonic laser pulse). The normalized extinction spectra for both wavelengths is reported in Figure 4.8. The samples were ablated using a fluence of 1.3 J/cm^2 , at $C_{\text{NaOH}} = 2.00 \text{ mmol/L}$.

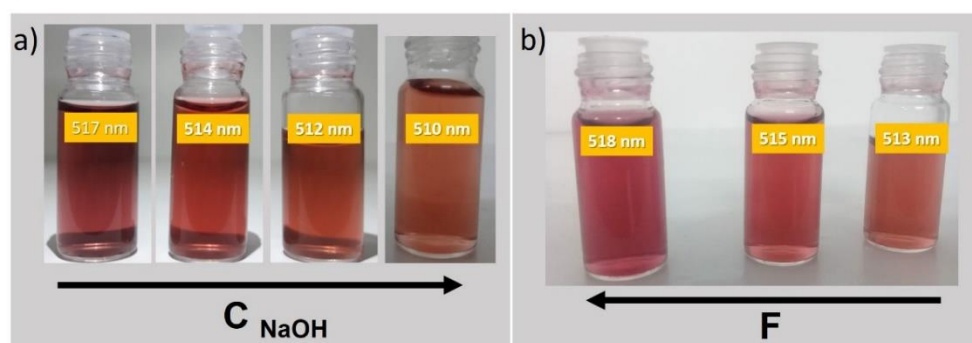


Figure 4.7 Color aspect of the Au derived nanomaterial depending on the experimental conditions (C_{NaOH} , F), where the direction of the arrow corresponds to increasing values in C_{NaOH} or F .

As reported in the literature, the size of AuNPs synthesized by ω frequency pulses is of the order of tens of nm [327], and the 2ω frequency pulses are mostly used to perform fragmentation of the NPs pre-synthesized at the fundamental frequency. Most of the research was and is in fact dedicated to the control of the dimensions of the AuNPs by post-irradiation processes at different wavelength

[141, 328], obtained by the introduction of opportune surfactants [325, 326, 329], to guarantee the stability of the nanomaterial, and the control on the recombination of the metal clusters produced during the fragmentation of the gold core [326]. Hence, a few studies were focused and dedicated to the control of the physicochemical properties of AuNPs synthesized in water with the simple addition of salts or hydroxides [20, 80, 128], principally by the use of pulses at the second harmonic frequency.

When a colloidal dispersion of AuNPs is irradiated by laser pulses at the wavelength of 532 nm, neutral or charged gold clusters are produced, and a continuous simultaneous fragmentation and recombination into new reshaped AuNPs occurs, caused by the resonance between the laser pulse and the LSPR band of the nanomaterial [141, 330].

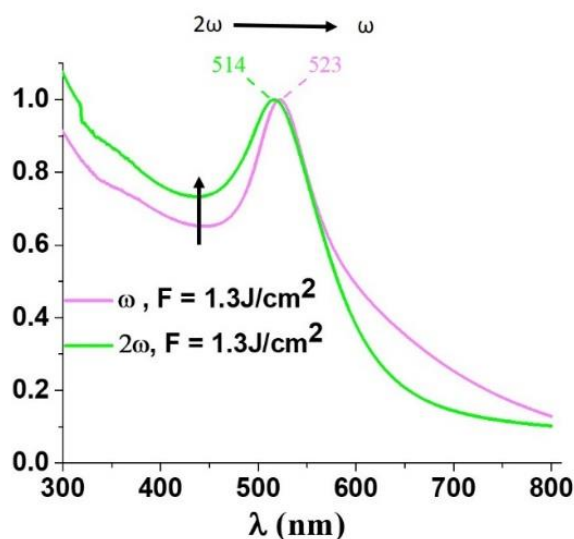


Figure 4.8 UV-Vis extinction spectra of the Au derived nanomaterial synthesized at the laser pulse frequencies ω and 2ω , in the same experimental condition ($F = 1.3 \text{ J/cm}^2$, $C_{\text{NaOH}} = 2.00 \text{ mmol/L}$).

An interesting work of *Mafune et al.* [331], shows how the dimension and aggregation of AuNPs pre-synthesized at the fundamental frequency, depend on both the sodium dodecyl sulfate (SDS) concentration (used as a surfactant and stabilizing agent), and the fluence of the pulses at the 2ω frequency, used to make a post-irradiation with 12,000 laser shots. The results of cited work are resumed in Figure 4.9, which shows (as 2D color map) the intensity of the agglomeration band at the wavelength of 800 nm observed in the experimental UV-Vis spectra, due to the formation of bigger nanoparticle and complex nanonetworks.

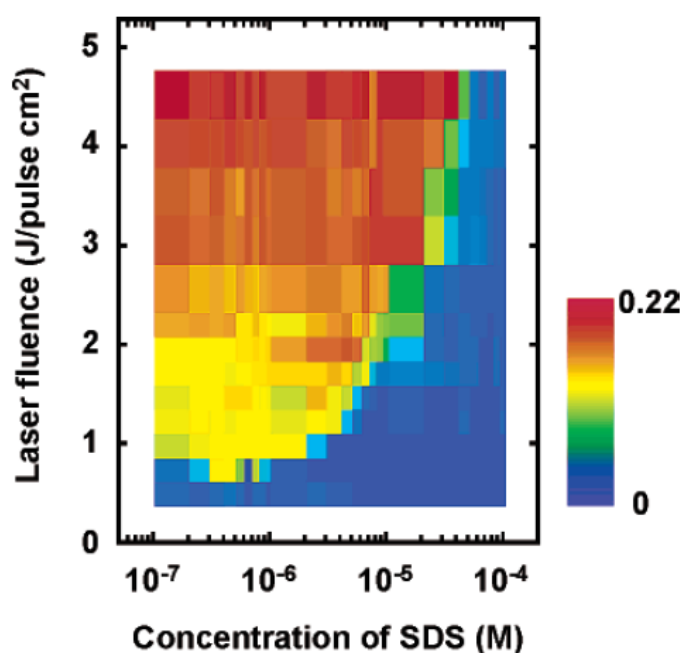


Figure 4.9. 2D color map representing the intensity of the agglomeration band at the wavelength of 800 nm observed in the experimental UV-Vis spectra of AuNPs pre-synthesized at the fundamental frequency ω . Both the sodium dodecyl sulfate (SDS) concentration (used as a surfactant and stabilizing agent), and the fluence of the pulses at the 2ω frequency, used to make a post-irradiation with 12,000 laser shots, have a clear effect on the optical and morphological properties of the final NPs. Adapted from [331].

When SDS is absent, as in our case, the irradiation by 2ω frequency pulses with a fluence lower than $\sim 1 \text{ J/cm}^2$ leads to not agglomerated NPs, as we observed in our experimental study. Increasing of the fluence is accompanied by the formation of bigger NPs, and also aggregates in the form of nanonetworks.

The day after the synthesis by PLA, we performed a post-irradiation experiment on the samples in the range of fluence between 0.1 J/cm^2 and 0.4 J/cm^2 , and verified that differently from what reported in the literature [141], it was not possible to modify the extinction spectra of the Au derived nanomaterial, with a further decrease of the size of the nanomaterial and photobleaching effect [332], with a perfect balance between fragmentation and recombination effects [325].

This unicity may be associated to the experimental parameters used to perform PLA in our research, which is different from all other works reported in the literature. The particularity of our study stands in both the introduction of NaOH, the irradiation with unique 2ω laser pulses, the fixed position of the laser

pulse over the target, and the long ablation time, where only 2 ml of liquid were irradiated for about 45 to 50 minutes.

In Table 4.1 we report the complete analytical characterization of the samples synthesized at $F = 1.3 \text{ J/cm}^2$, for different values of C_{NaOH} . In the table, c_{Au} is the metal concentration, ζ -represents the surface potential, λ_{LSPR} is the wavelength of the LSPR resonance, TC_0 is the total carbon of the water solution used to perform the ablation, and ΔTC represents the increment (when different from 0) of the TC during the PLA process of the metal target. Here, we highlight that PLA was performed in the open air, so that CO_2 , continuously diffuses into the liquid environment, and in order to correctly measure ΔTC we used the experimental set-up shown in Figure 3.2 a. In this case, one ablation line is occupied by the NaOH water solution with the Au target, while in the second one is simply put the aqueous NaOH solution, without any target. In both cases, the focusing condition was the same as reported in

Table 3.2. At the end of the PLA processes, the TC of the two samples are measured, and ΔTC is calculated.

Information from different characterization techniques is contained in Table 4.1. The matching between the experimental and theoretical values of the metal concentration tells us that the degree of the oxidation of the NPs is low and that the TEM images shown along the text are really representative of the whole samples. The theoretical value of AuNPs concentration were calculated using the Mie theory, as explained in detail in Section 2.2.3.2. The MatLab based code used for the simulations and fit is reported in Appendix A.1. The mean values and corresponding standard deviations have been calculated considering tens of samples measured along the past 4 years.

Table 4.1 Complete analytical characterization of the samples synthesized at $F = 1.3 \text{ J/cm}^2$, for different values of C_{NaOH} .

C_{NaOH} (mmol/L)	TC_0 (ppm)	ΔTC (ppm)	λ_{LSPR} (fresh) (nm)	λ_{LSPR} (15 days) (nm)	TEM Radius (nm)	ζ - potential (mV)	C_{Au} Exp. (ppm)	C_{Au} Theory (ppm)
0.02	3.5 ± 1.1	< 0.1	517.7 ± 1	520.7 ± 1	3.1 ± 0.6	-65.0 ± 3.7	65.4 ± 7.6	64.4
0.06	6.0 ± 1.6	0.5 ± 0.1	515.9 ± 1.5	518.1 ± 1	2.3 ± 0.7	-116.2 ± 2.0	71.6 ± 0.9	69.9
2.0	18.0 ± 5.3	2.7 ± 0.8	513 ± 1.3	515.7 ± 1	1.3 ± 0.4	-119.6 ± 3.2	81.2 ± 2.6	81.1
4.00	22.5	3.8	512.5 ± 1	517 ± 1		×	×	×
8.00	27.3	5.7	511.2 ± 1	518 ± 1	0.9 ± 0.3	×	87.5 ± 4.5	84
12	32.1 ± 8.3	7.9 ± 2.3	513.8 ± 1	521 ± 1	×	×	×	×
20	41.0	10.25	514 ± 1	524 ± 1	×	×	×	×

What it is surprising in Table 4.1, is the detection of a positive variation of the total carbon ΔTC for higher values of C_{NaOH} . The latter observation, indicates that the $\text{CO}_{2\text{water}} / \text{CO}_{2\text{air}}$ equilibrium is broken during the PLA process, suggesting that chemical transformations to the gas are occurring in the liquid environment.

A higher concentration of NaOH, acting as the CO_2 carrier in the liquid environment, lead to noble MeNPs with a smaller radius, allowing the control of both the dimension and LSPR position of the NPs.

The Au derived nanomaterial, is characterized by a progressive blue-shift of the resonance down the wavelength of 512 nm, in contrast with the Mie's theory, on which basis we expect a minimum value of λ_{LSPR} near about 521 nm [210]. Hence, the observed values smaller than this wavelength, cannot be simply explained by a variation in the size. The keys to the interpretation of the observed blue shift are equations (2.16) and (2.38). The first one represents the Fröhlich's condition, which may predict a blue-shift down 520 nm of the LSPR peak of the AuNPs in case they are surrounded by a media with a refractive index smaller than water, such as gases. The second equation represents instead the effect on the LSPR

wavelength of the electron transfer from an external ligand to the metalcore. As it will be clearer from the SERS spectroscopy and HRTEM results shown in Section 4.3, both carbon monoxide (CO) and traces of sp-hybridized carbon material are detected over the surface of the Au derived nanomaterial. In both cases, the participation of the CAWs electrons to the plasma oscillation and the π -back bonding in metal–CO system [213], enhances the number of available conduction electrons in the d-band of Au, participating to the observed blue-shift, as already explained in Section 2.2.3.3.

In Figure 4.10, we report the blue shift in λ_{LSPR} with increasing TC_0 and decreasing F. The TC_0 gets higher with the content of NaOH, due to the increasing CO_2 absorption capability of NaOH aqueous solutions [333].

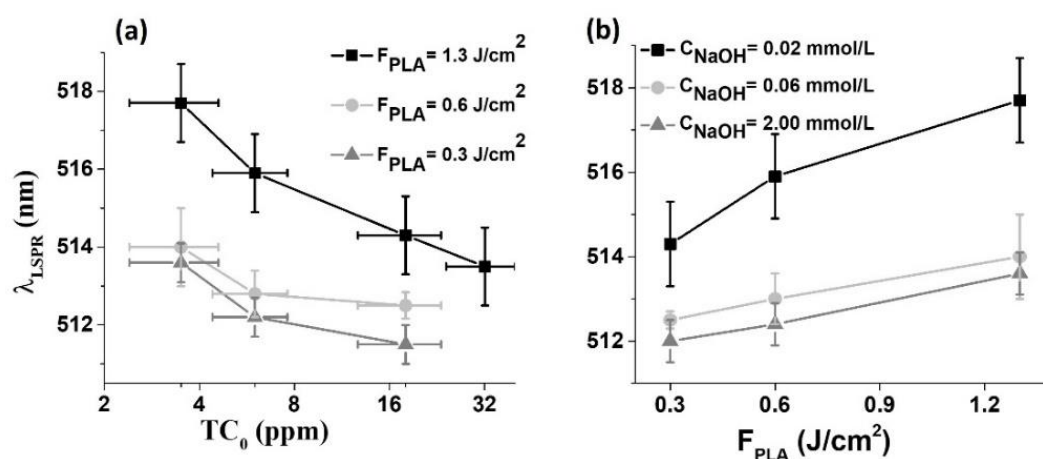


Figure 4.10. Dependence of the central position of the LSPR band (λ_{LSPR}) on (a) TC_0 (i.e. C_{NaOH}), and the fluence F (b).

4.3.

Characterization of carbon nanomaterial derived from Au target

4.3.1.

SERS measurements on Au derived nanomaterial

The presence of solid carbon is firstly detected in the SERS spectra of the Au derived nanomaterials (before separation) in dried powder form, represented in Figure 4.11. Herein, sp² carbon collective Raman modes (D and G bands) are observable, overlapped with several molecular vibrations. Also a sharp line is

dominant around 2124 cm^{-1} , in the typical spectral region of Au-carbonyl [39], which grows more intense with the addition of NaOH, which is our CO_2 carrier in the water solution.

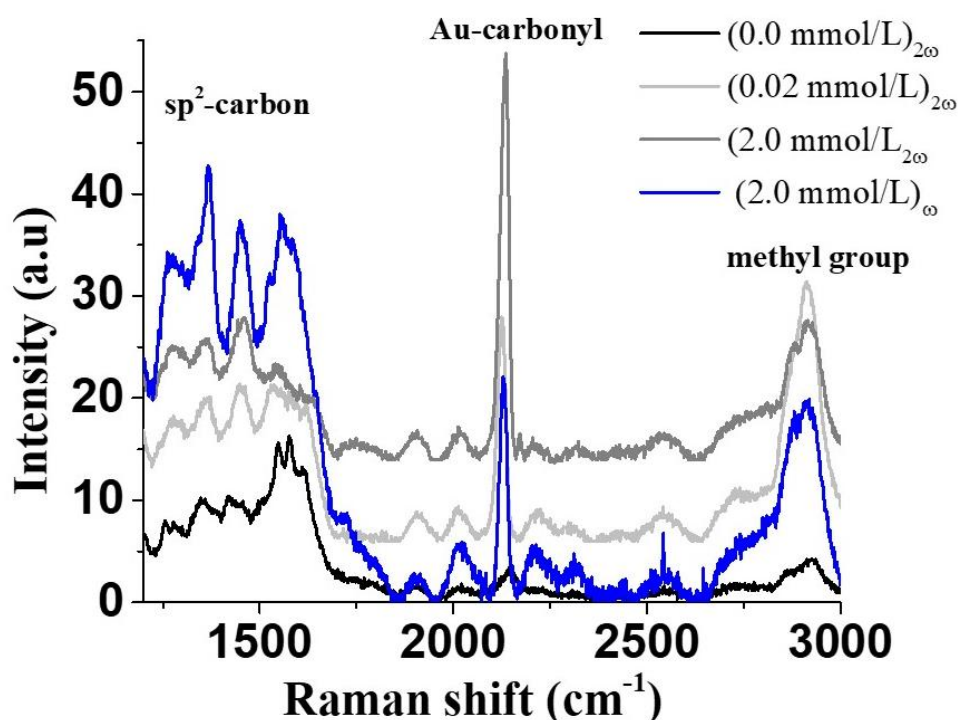


Figure 4.11 SERS spectra of Au derived nanomaterial in powder synthesized at 2ω with different values of C_{NaOH} . As a comparison, we also report the SERS spectra of the samples obtained by the use of laser pulses at the frequency ω (blue curve), for $C_{\text{NaOH}} = 2.00\text{ mmol/L}$. The excitation wavelength in the SERS measurements was 638 nm .

Due to the presence of high-intensity molecular features, the detailed structure of the D and G band of sp^2 carbon, which is important in order to identify graphitic or amorphous carbon structures, could not be identified, and high-resolution transmission electron microscopy was used for such identification.

A possible interpretation of the molecular features of the SERS spectra shown above, together with the one obtained from the powder of the Ag derived nanomaterial, is reported in Section 7, taking in account the CO_2/C reduction occurring during the PLA process.

4.3.2.

TEM Measurements

We report in the following the detailed analysis of the Au derived nanomaterial by HRTEM, where the most significant images were selected.

As explained in the introduction section, we found three different populations of carbon-based nanomaterial with different compositions and structures. The most concentrated species, visible only before the separation process, were the Au@Cy NPs. After the separation processes described in Section 3, we detected both CQDs, and Cy@AuNWs. The latter, differently from the CQDs, were not easy to be detected on the TEM grid, demonstrating that the synthesis of the carbynoid NWs is secondary to the production of CQDs.

The images of the Cy@AuNWs and CQDs were taken from samples after the separation process based on concentration by heating, followed by a filtering process of 0.2 μm , as described in Section 3.

4.3.2.1

Au@CyNPs

In Figure 4.12, we report the HRTEM images of the Au@CyNPs. The interline spacing in the core of the NPs are typical of metallic gold, with the distances of near to 0.23 nm and 0.283 or 0.273 nm corresponding to the (111) and (110) planes, respectively [20, 39, 334].

Some of the NPs appears surrounded by a thin layer of carbon nanomaterial, with the interplanar distances of 0.44 nm, 49 nm, and 0.91 nm, corresponding to the planes (110), (100), and (001) of carbynoid material [20, 40], respectively. The thickness of the carbynoid shell seems to be proportional to the dimension of the metallic nuclei so that it was not possible to observe the formation of the crystal carbon structure on the typical smallest Au cores.

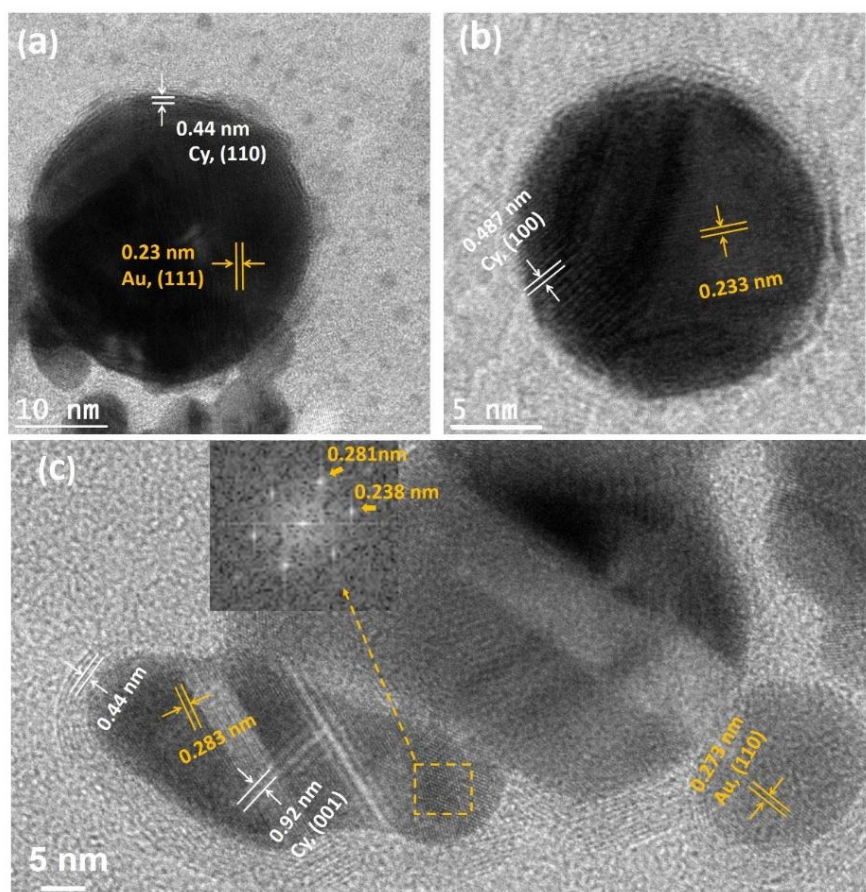


Figure 4.12 (a,b) HRTEM of Au@Cy NPs synthesized at $C_{\text{NaOH}} = 0.06$ mmol/L. (c) A few agglomerated NPs, synthesized at $C_{\text{NaOH}} = 2.00$ mmol/L. The electron acceleration voltage was 80 keV.

4.3.3. CQDs

Figure 4.13 a and b represent the ensemble of the CQDs derived CO_2/C from Au target, at TC_0 of 3.5 ppm and 18 ppm, respectively. A variation of $\langle R \rangle$ from 1.7 nm to 2.4 nm is observed depending on TC_0 , indicating that the last parameter has a small influence on the structure of the CQDs, at least in the investigated range of concentration.

The EDX spectra in the inset of TEM images shows the presence of C and O atoms, and residues of Na coming from NaOH. Interplanar distances of 0.33 nm, 0.21 nm, and 0.18 nm, relative to the planes (002) [335, 336], (100) [270, 337] and (102) [338] of graphitic carbon, were observed in the samples by HRTEM. Together with the small CQDs, we also observed sparse bigger carbon

nanoparticles, both in circular and carbon-onion (CO) structure [338], as represented in c and Figure 4.13 d, respectively

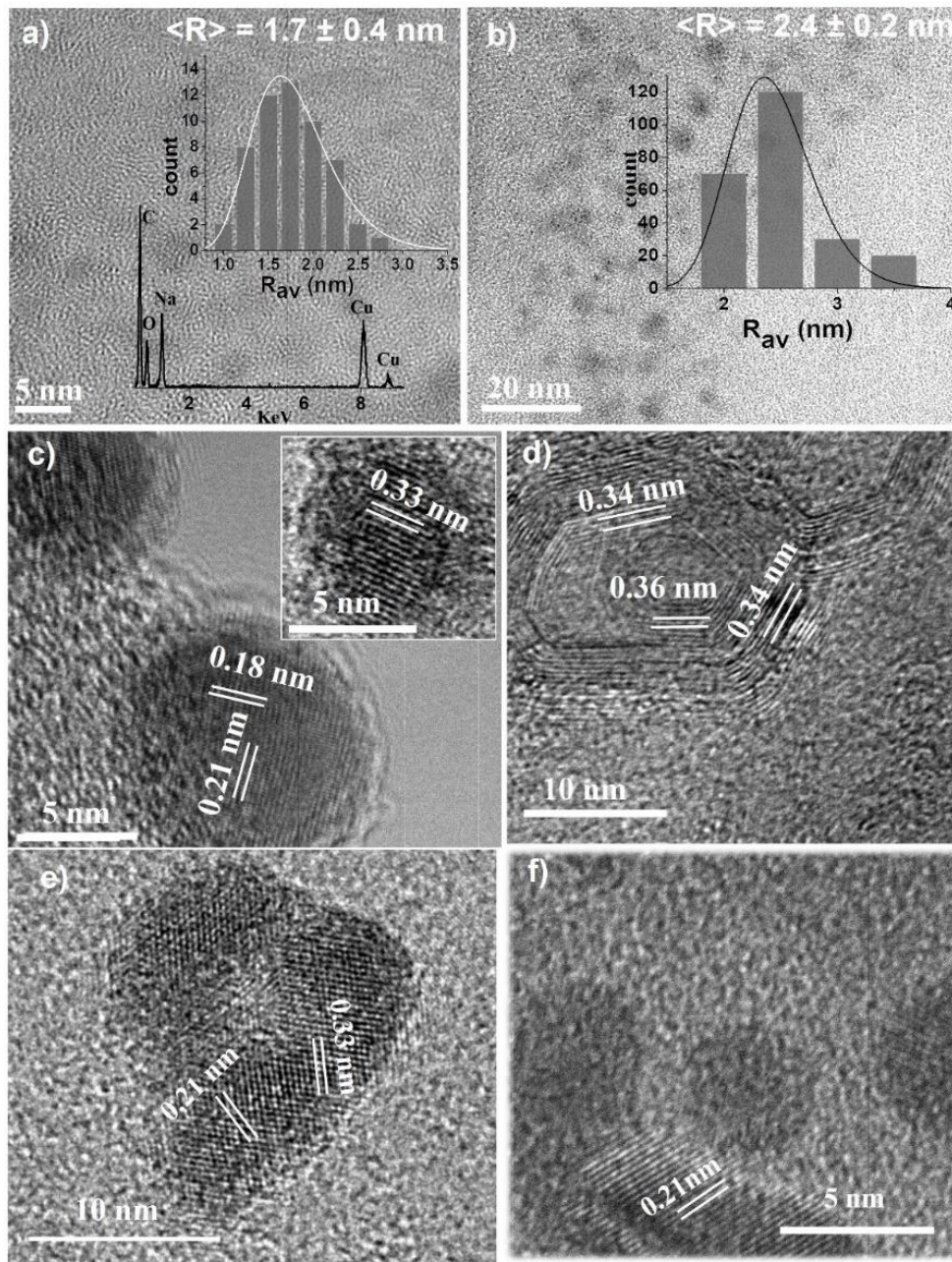


Figure 4.13 TEM images of the CQDs derived by CO_2/C with Au target, synthesized at $\text{TC}_0 = 3.5 \text{ ppm}$ (a), and 18.0 ppm (b). In the inset are shown the statistical size distribution of the nanomaterial and the corresponding EDX spectra. c,d) Sparse bigger carbon nanoparticles, both in circular and carbon-onion structure. The electron acceleration voltage was kept at 80 keV .

4.3.4.

Cy@Au NWs

Various regions of the Au derived samples were recognizable by ensembles of carbon nanowires decorated by AuNPs (Cy@AuNWs), as represented in Figure 4.14 a,b,c. The inset in the latter represents the EDX spectra of the Au-carbon nanocomposites, where Au, C, and O appear as the most abundant elements, together with Na residuals. Figure 4.14 (d) reports the statistical distribution of the longitudinal (L) and transversal (W) dimension of the Cy@AuNWs, centered around 101 nm and 16 nm, respectively. These dimensions are similar to the results reported in [40], although the presence of structures bigger than 200 nm cannot be excluded, taking into consideration the filtering step in our separation process. In fact, the existence of bigger Cy@AuNWs is demonstrated in Figure 4.14, representing a low-resolution TEM image of isolated NWs detected before the separation processes.

HRTEM images of typical isolated Cy@AuNW are presented in Figure 4.15 (a-d), where are highlighted the interplanar distances of 0.91 nm, 0.91 nm, 1.00 nm, corresponding to the c-axis of the nanocrystal [40]. The Cy@AuNWs are grown around small AuNPs, which seems to play the role of nucleation sites of the carbynoid crystals, and are known to preserve their stability against oxidation process and sp to sp² conversion [41, 339]. Figure 4.15 f). represent the selected area electron diffraction (SAED) pattern and HRTEM of another Cy@AuNW, showing the interplanar distances of 0.91 nm, 0.51 nm, and 0.26 nm along the (001), (100) and (203) planes of the nanocrystal, respectively [11, 20, 40, 340].

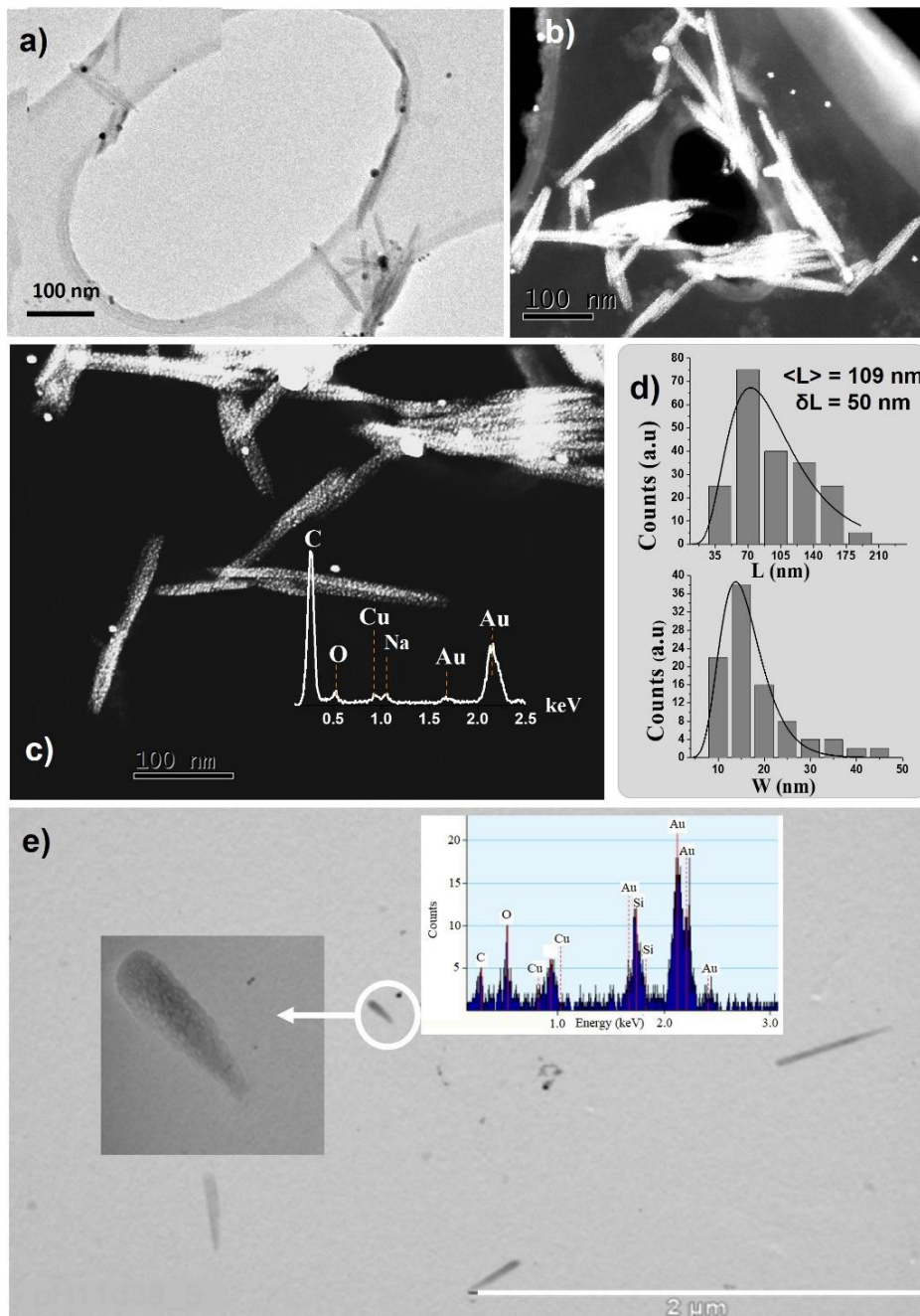


Figure 4.14 a) TEM and STEM (b,c) images of the Cy@AuNWs derived by CO_2/C with Au target, synthesized at $\text{TC}_0 = 18.0$ ppm and $F = 1.3$ J/cm². The inset in (c) shows the corresponding EDX spectra. (d) Statistical log-normal distribution of the longitudinal (L) and lateral (W) linear dimensions of the Cy@AuNWs. e) TEM image of Cy@AuNWs before the separation process, demonstrating the existence of carbynoide structures bigger than the filter pores.

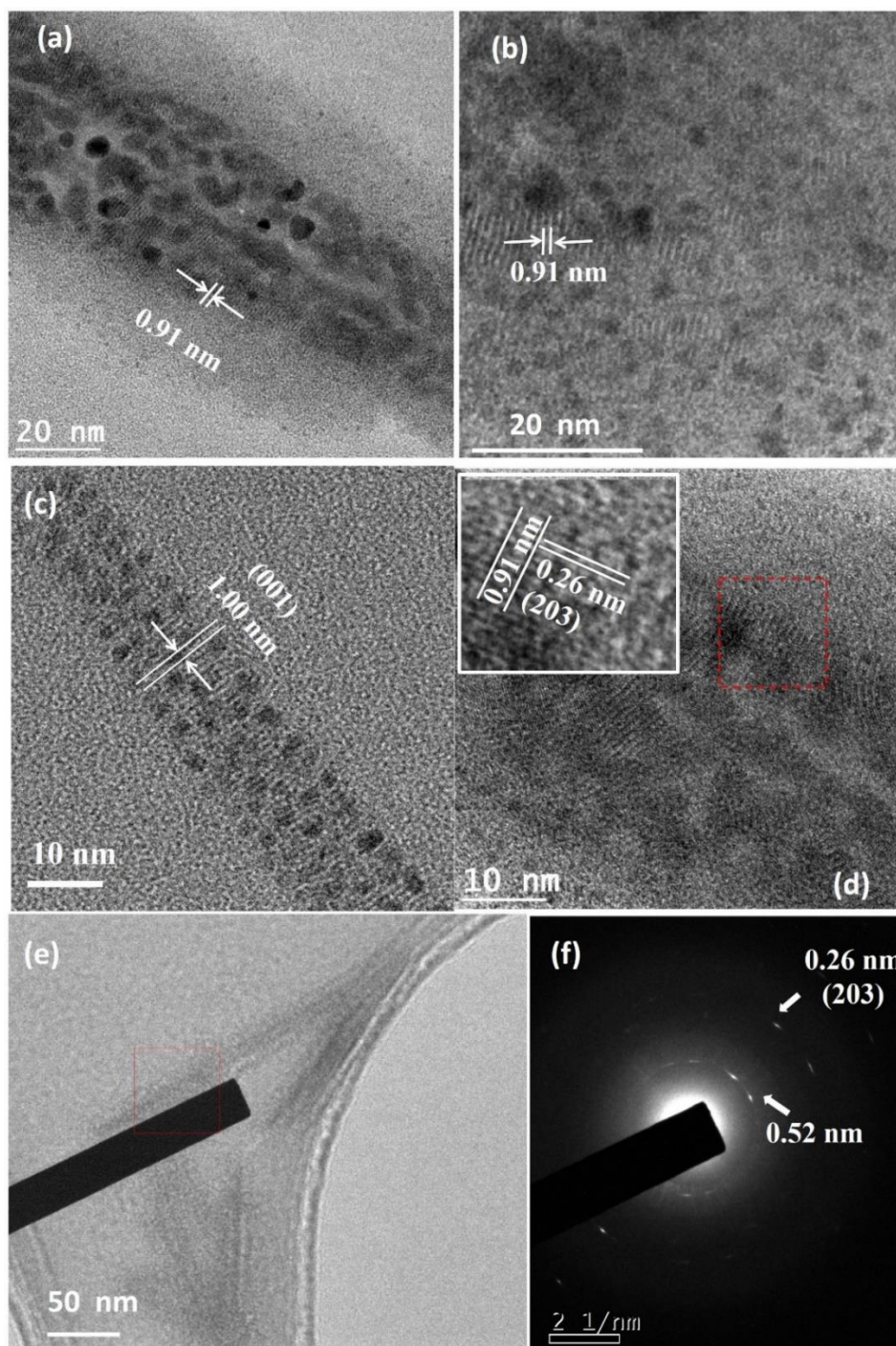


Figure 4.15 (a)-(d) HRTEM images of the Cy@AuNWs derived by CO₂/C with Au target, synthesized at TC₀ = 18.0 ppm and F = 1.3 J/cm². The images were taken at an acceleration voltage of 80 kV. e) Bright-field (BF) TEM image of an isolated Cy@AuNWs and f) the corresponding SAED pattern.

It is worth noting that the application of a low accelerating electron voltage of 80 kV it was not an option, but was verified to be essential to avoid sp-sp² conversion of the soft carbynoid nanomaterial, Figure 4.16 (a) show the HRTEM image of an Au@CyNCs taken at 300 kV. When using this acceleration voltage,

we were not able to observe the typical interplanar distance of the carbynoid nanomaterial around the gold core. In this case, the shell appeared or as amorphous carbon, or as sp^2 carbon material, with the typical interplanar distance of 0.33 nm. In order to confirm our hypothesis, in Figure 4.16 (b,c) we show the variation of the interplanar distance along the c-axis during the electron irradiation at 200 kV. During the time, the interplanar distance passes from the typical values around ~ 1 nm, to smaller values, with final amorphization.

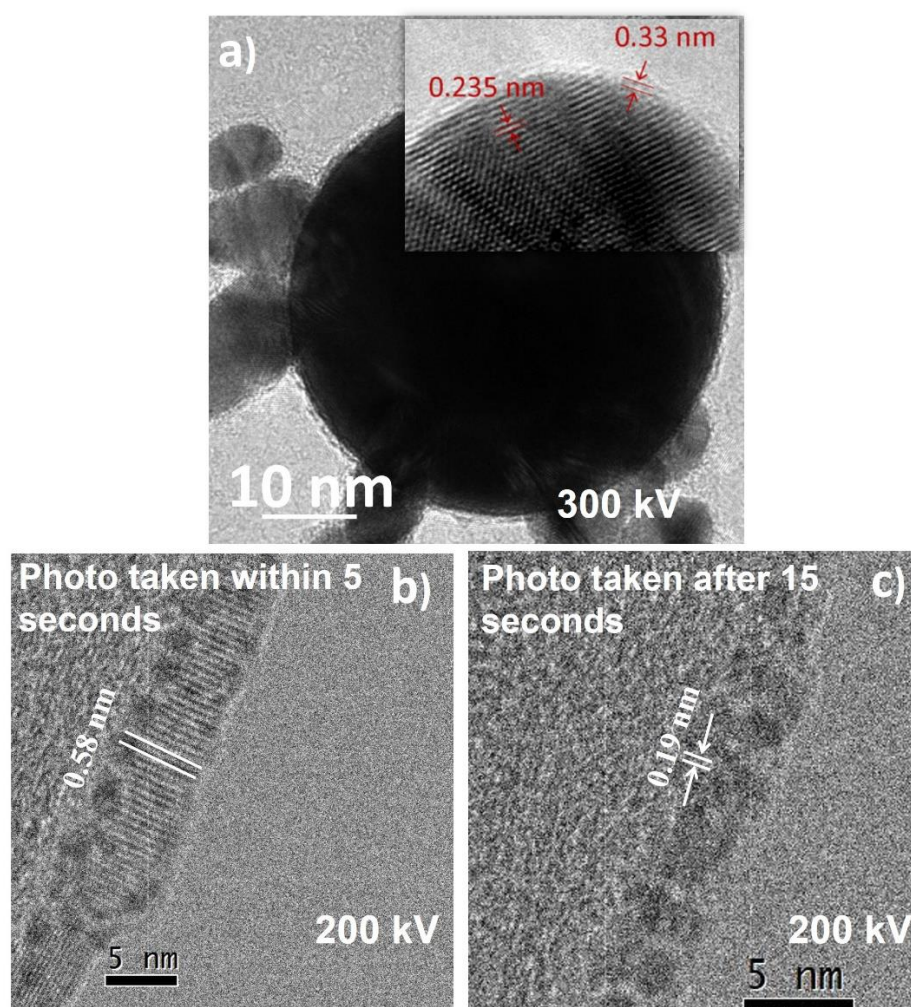


Figure 4.16 a) HRTEM image of an Au@Cy NP taken at an acceleration voltage of 300 KV. There is no trace of sp hybridization in the carbon shell of the NCs. (b,c) Change of the interplanar distance along the c-axis of the Cy@AuNWs during the irradiation at the electron acceleration voltage of 200 kV.

In order to enhance the content of the Cy@AuNWs in the samples, we also prepared samples by the use of a PTFE (polytetrafluoroethylene) membrane filter with relatively bigger pores of ($0.45 \mu\text{m}$). Unfortunately, the observed sample was

too much concentrated, and was not possible to distinguish the different carbon-based nanostructures. Anyway, we observed the consistent presence of big amorphous carbon wires, as represented in Figure 4.17. In this case, the measurements were taken at 200 kV, and constant degradation was observed on the nanostructure.

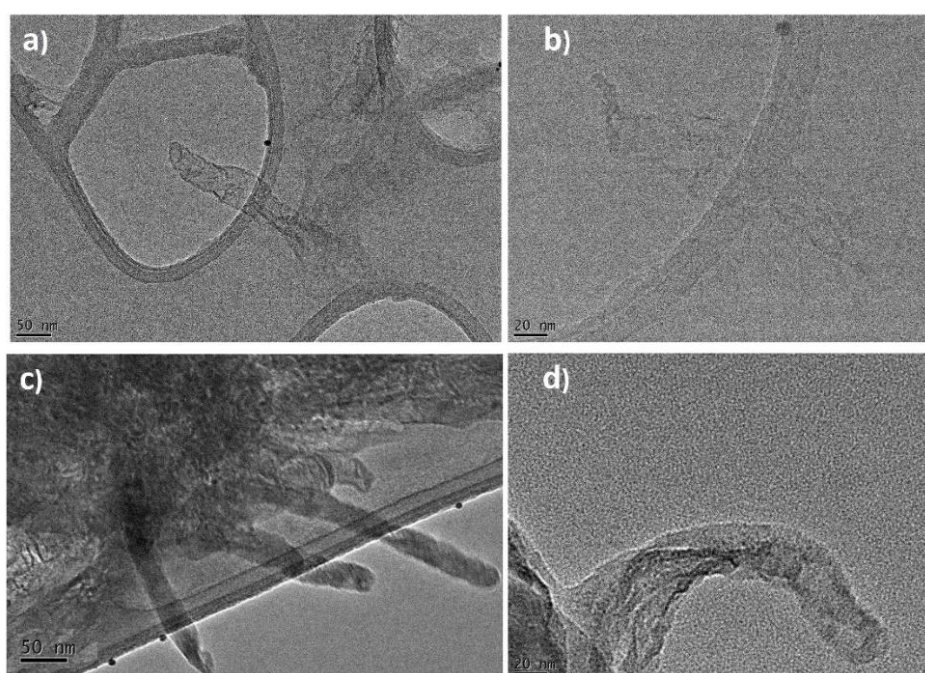


Figure 4.17 Amorphous carbon NWs observed after performing the separation process with a filter of 0.4 μm . The acceleration voltage of 200 kV provoked the real time degradation of the carbon nanostructures.

So we found Au@cy NPs, Cy@AuNWs, CQDs and some amorphous carbon in the TEM images. The CQDs and Cy@AuNWs can be observed very well after separation.

4.4. Surface Composition of the CQDs Obtained by CO₂/C with Au Target

The surface composition of the CQDs obtained by CO₂/C with Au target and separated by heating and filtering, was investigated by SERS, FTIR and XPS spectroscopies. We do not show the results of SERS spectroscopy, performed at the *Department of Energetic of the Politecnico of Milano*, since the concentration of CQDs was too low in order to observe the signal of the collective Raman modes.

In Figure 4.18 a,b we show the FTIR and the C1s XPS spectra of the CQDs after the dialysis process, respectively. The FTIR spectra is characterized by typical bands of oxygen-rich CQDs. At 464 cm^{-1} , 1409 cm^{-1} , 1590 cm^{-1} and 1650 cm^{-1} , we observe the bands associated to the bending, symmetric and anti-symmetric stretching $\nu(\text{COO})$, together with carbonyl $\nu(\text{C}=\text{O})$ stretching in carboxylic groups [341–344]. The most intense band at 1035 cm^{-1} is associated to $\nu(\text{C-O-C})$ antisymmetric stretching of epoxide groups on the CQDs [345], covering a shoulder around 1220 cm^{-1} associated to the $\nu(\text{C-OH})$ stretching of hydroxyls group, just as the broad $\nu(\text{OH})$ band centered at 3380 cm^{-1} [345–347]. Other minor characteristic bands are $\nu(\text{C}=\text{O})$ of carbonyl at 1720 cm^{-1} [346] and $\nu(\text{CH})$ around 2920 cm^{-1} . The XPS spectra confirms the results of FTIR spectroscopy. The most intense band at 284.4 eV is associated to the C-C/C-H content, while the bands at 286.0 eV , 287.8 eV , 289.4 eV are associated to C-O-C(epoxide)/C-OH(hydroxyl), C=O (carbonyl) and O-C=O (carboxyl), respectively [292, 348, 349]. Interestingly, we notice also the contribute of the π -Plasmon peak (shake-up) of π - π^* transitions at 290.8 eV , which indicates the presence of π -electrons rich materials, and enhanced order of the graphitic structures [350].

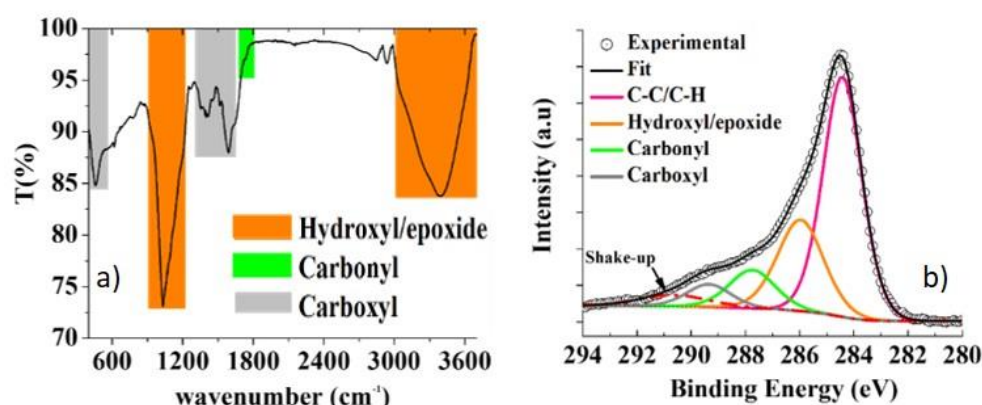


Figure 4.18 FTIR (a) and C1s XPS (b) spectra of the dialyzed CQDs derived from Au target by CO_2/C .

To facilitate the reader in the visualization of the surface chemistry of the Au derived CQDs, in Figure 4.19, we report the schematic representation of all the chemical groups detected by FTIR and XPS spectroscopy on the surface of the carbon nanoparticle, together with a scheme (f) representing the external surface of the CQDs.

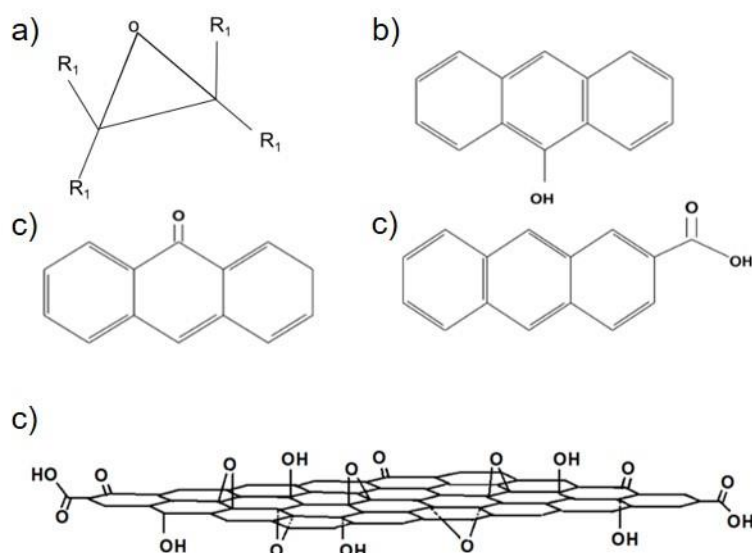


Figure 4.19 Schematic representation of all the chemical groups detected on the surface of the carbon nanoparticle: (a) epoxide, (b) hydroxyl, (c) carbonyl, (d) carboxylic acid, (e) all the groups.

4.5.

PL of The CQDs obtained by CO₂/C with Au target

4.5.1. Steady-state PL

In Figure 4.20 (a) we report the extinction, excitation, and photoluminescence spectra of the emissive carbon nanomaterial derived from Au for different total carbon concentrations. Two peaks in the excitation spectra near to 315 nm and 265 nm have been observed, while in the UV-visible extinction spectra two clear extinction bands at about 225 nm and 265 nm are present. For UV extinction spectra, pure water is used as a blank to correct the background. The extinction band near 225 nm represents π - π^* transition of aromatic sp^2 domains in the graphitic core of the CQDs [351, 352], while the absorption near 265 nm might be associated with the n - π^* transition of C=O on carboxylate CQDs [353]. The relative surface density of the CQDs and Cy@AuNWs during TEM investigation suggests that the population of the NWs is substantially negligible if compared with CQDs so that the contribution of the carbonyl NWs to both the extinction and emission spectra is negligible.

It was observed that neither the total carbon TC, nor the wavelength or fluence of the laser pulse during the synthesis Figure 4.20 influence the position of the

excitation and emission band, centered around 415 nm, but only on the intensity of the corresponding PL. Moreover, for all the analyzed samples we find that the spectral position of the PL band has a weak dependence on the wavelength of the excitation radiation (5 nm shift), as reported in Figure 4.20 (c). This characteristic is quite rare in CQDs [354], and suggests a carbon core contribution to the overall PL, with the possible presence of single energy level surface states [268, 270].

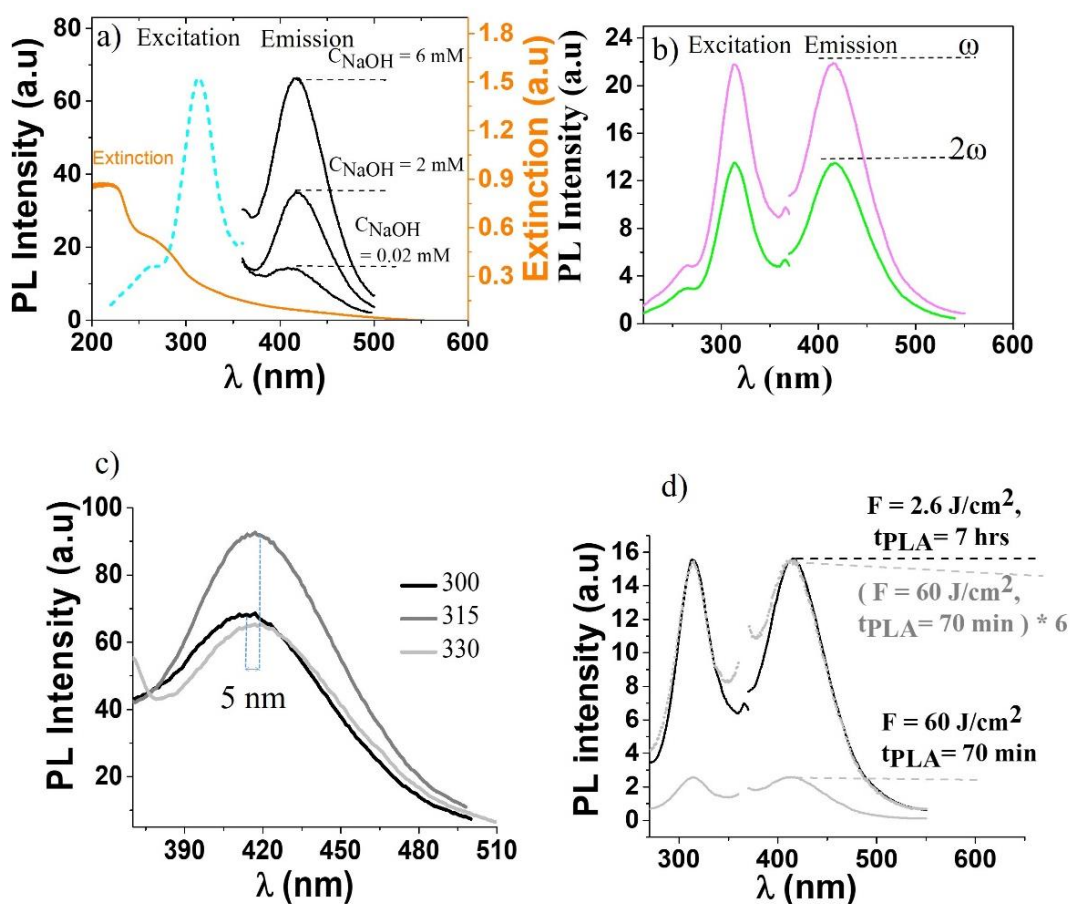


Figure 4.20 a) Extinction (orange continuous line), excitation (cyan dotted line), and photoluminescence emission spectra (black lines) of the CQDs derived from Au target, synthesized at different values of TC_0 : 3.5 ppm (dotted), 18.0 ppm, and 25.3 ppm. b) PL spectra (normalized to the ablation time) of the Au derived CQDs synthesized by the laser pulse ω and 2ω laser pulses. c) Dependence of the PL spectra on the excitation wavelength. The PL spectra were excited at the wavelengths of 300 nm (black line), 315 nm (grey line), and 330 nm (light grey line). d) Dependence of the PL spectra on the value of F used during the PLA of the Au target by $F = 60 \text{ J/cm}^2$ (gray line) and $F = 2.6 \text{ J/cm}^2$ (black line), where the laser pulse spot size on target was constant. The dotted grey line represents the PL curve normalized to the ablation time.

As explained in Section 3, different methods were used for the separation of the CQDs. In Table 4.2 we resume the performance of each method in terms of its feasibility and the residual metal concentration C_{Au} .

Table 4.2 Concentration of gold (C_{Au}) in the solution after separation of CQDS from Au-derived nanomaterial

Method of Separation	C_{Au} (ppm)	Comments
None	80.3	We cannot observe PL in presence of AuNPs
Amalgamation and subsequent centrifugation.	1×10^{-2}	16 ppm and 0.3 ppm of mercury and gold are found after separation. The concentration of both mercury and gold decreased to 6 ppm and 0.01 ppm after centrifugation. It is a method with a high risk of toxic metal contamination. Good PL.
precipitation by dialysis and centrifugation	5.1	The PL intensity was visible but very low.
precipitation by salt and subsequent Dialysis	1×10^{-1}	good PL, but we lose CQDs during the dialysis process and relatively time more consuming at least 1 week.
electromagnetic induction	5×10^{-2}	good PL, clean, cheap method, only need few hours
Heating and filtering	2×10^{-2}	good PL, clean and cheap method, can finished in one day but very easy.

The concentration by heating, followed by filtering, was selected as the default separation method for its simplicity, because it is cheap, clean, and give a relatively good PL.

As represented in Figure 4.21, the residual gold concentration might also be detected by LSPR resonance monitoring. We found that a final metal concentration of 3.61 ppm, provokes approximatively the same quenching on the PL found for the samples with a lower metal concentration (0.55 ppm), as shown in Figure 4.21.

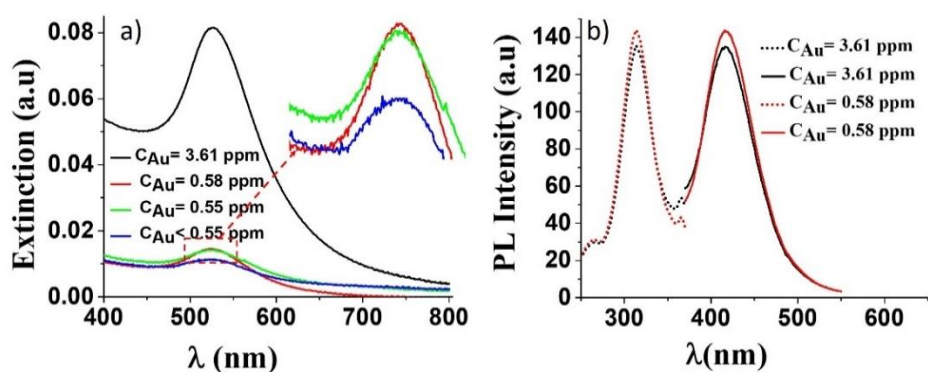


Figure 4.21 a) Monitoring of the residual Au concentration by UV-Vis extinction spectroscopy. b) Effect on the PL of the residual gold concentration.

4.5.2.

Time-Resolved PL (TRPL)

As explained in the introduction section, the TRPL measurements on the CQDs derived from Au target by CO_2/C were performed by the group of Prof. Nicola Daldosso, *Department of Computer Science from the University of Verona (Italy)*.

The PL decay was investigated by excitation with 304 nm and 335 nm. The decay curves are reported in Figure 4.22 in panel a) and b), respectively. The emission wavelength is varied over the whole PL emission band.

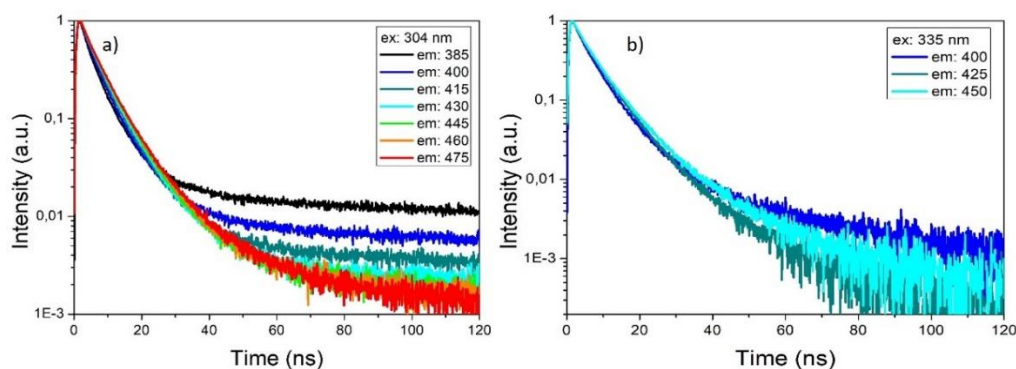


Figure 4.22 PL decay curves of CQDs derived from Au target by CO_2/C in water. a) Excitation at 304 nm. b) Excitation at 335 nm.

The lifetime was determined by fitting each PL decay curve with single ($I = I_0 e^{-(t/\tau)}$), double ($I = I_1 e^{-(t/\tau_1)} + I_2 e^{-(t/\tau_2)}$) and stretched ($I = I_0 e^{-(t/\tau)^\beta}$, with β the stretched parameter) exponential.

Figure 4.23 shows two representative decay curves, for 304 nm and 335 nm excitation, with emission at λ_{\max} . The fitting exponentials and the obtained parameters are reported. As it can be observed, the curve that better fits the data of PL decay is the double exponential, which has been used for the definitive results on the life-time.

The possible presence of surface states mediating the electron-hole recombination was investigated by TRPL measurements over selected spectral regions inside the CQDs emission band. The multi-emission TRPL spectra were excited at both the wavelength of 304 nm and 335 nm. The corresponding results of the life-time τ , are reported in Table 4.3. where I_1 and I_2 are constant for any investigated emission wavelength, and we obtained $I_1=1.0\pm 0.2$ e $I_2=0.4\pm 0.1$

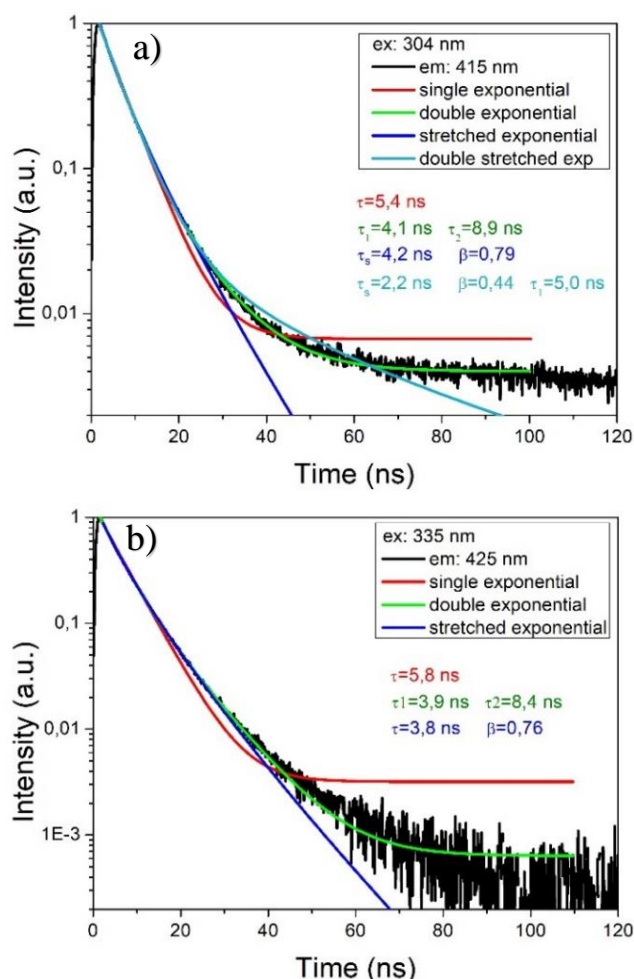


Figure 4.23 PL decay curves of CQDs derived from Au target by CO_2/C in water. (a) Excitation at 304 nm at λ_{\max} . (b) Excitation at 335 nm at λ_{\max} . The fitting exponentials and the obtained parameters are reported.

We obtained similar results for different excitation wavelengths, concerning both the lifetime values and their dependence on the emission wavelength. The average lifetime value increases as the emission wavelength increases. As an example, the value of the constants τ_1 and τ_2 at the emission wavelength of 415 nm with excitation of 304 nm was 4.1 ns and 8.9 ns, respectively. τ_2 has a very small increase, while τ_1 has a clear increase depending on the emission wavelength. The opposite behavior is expected by direct electron-hole recombination processes [268, 355], and the results suggest that the emission of our CQDs is mostly associated with surface states (surface trap states) with two different lifetimes.

Table 4.3 Decay parameters as a function of the emission wavelength for the best fit (i.e. the double exponential).

λ_{EM} (nm)	λ_{EX} 304 nm		λ_{EM} (nm)	λ_{EX} 335 nm	
	t_1 (ns)	t_2 (ns)		t_1 (ns)	t_2 (ns)
385	3.1±0.1	8.5±0.2	400	3.7±0.1	9.0±0.2
400	3.7±0.1	8.6±0.2	425	3.9±0.1	8.4±0.2
415	4.1±0.1	8.9±0.2	450	4.1±0.1	9.0±0.2
430	4.2±0.1	8.8±0.2			
445	4.2±0.1	8.8±0.2			
460	4.2±0.1	8.8±0.2			
475	4.3±0.1	9.3±0.2			

The quantum yield (QY) of the CQDs was evaluated by the comparative method [287], as described in Section 3.7. The results are obtained by calculating the slopes of the lines represented in Figure 4.24, where the integrated PL area is reported as a function of the sample absorbance, for CQDs and Rhodamine, used as a standard reference. By considering the maximum and minimum slopes that better fit the QCDs data, we obtained a QY of about 45%.

The full width half maximum (FWHM) of the emission is of the order of ~ 45 nm, quite smaller than the typical FWHM reported for other kinds of CQDs

soluble in water emitting in the visible region, which is in the range between 80 nm and 110 nm [286, 356, 357].

The measured value of the QY is, at the best of our knowledge, one order of magnitude higher than the typical values reported for luminescent carbon nanomaterials synthesized by both one or even two-step PLA processes [37, 292, 293].

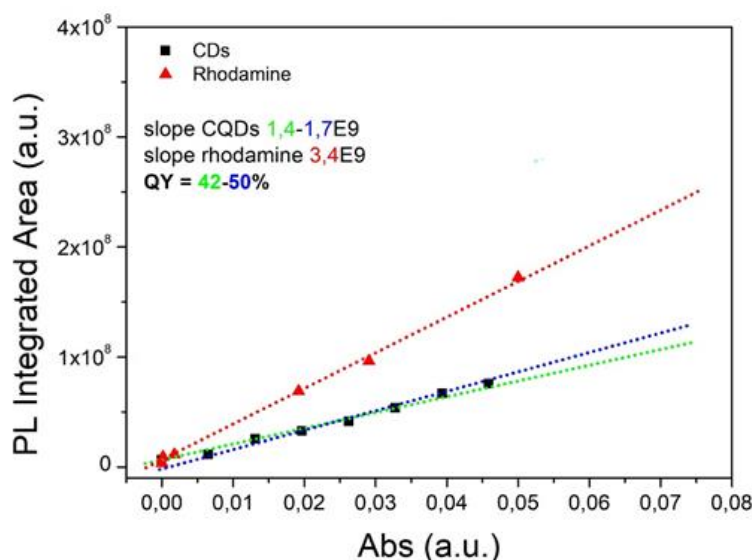


Figure 4.24 QY determination. Integrated PL area (at the FWHM) in function of the sample absorbance, for CQDs obtained from CO_2/C reduction by Au and Rhodamine.

Such a low FWHM and high QY may be associated to the different source of carbon atoms in CO_2/C assisted synthesis [292, 358]. In traditional PLA, the atoms constituting the nuclei of the upcoming NPs are ejected from the solid carbon target in multiphase form, such as vapors, liquid, solids pieces, which after condense together giving rise to a quite broad size distribution [292, 358]. In CO_2/C assisted synthesis, the building elements of the carbynoid NWs and CQDs might be 'C2' molecular units [40] or small polycyclic aromatic hydrocarbons [359], and is reasonable to suggest that part of the units of nucleation recombine in highly ordered structures.

Another key of interpretation of the results, is constituted by the functional groups attached on the surface of CQDs (those are mostly responsible for PL). In fact, the surface states decrease the energy gap of CQDs, and in result the probability of electron transition from ground state to lowest excited singlet state

may increase. Additionally, the electrons trapped by the CQDs surface states are able to quench the non-radiative recombination, and enhance the radiative path [341].

The discussion on the carbon nanostructure nucleation process will be described in the *Conclusions* Section.

4.6. Application of the Au derived nanomaterial

4.6.1.

Interaction of The Au derived nanomaterial with the copolymer pluronic-F127: stability in media with high ionic force

The applicability of the Au derived nanomaterial in biomedical applications was evaluated by examining their cytotoxicity with different epithelial and endothelial human cells, and studying its interaction with the amphiphilic block (chemical compound possessing both hydrophilic and lipophilic properties) copolymer Pluronic-F127 (PF127). PF127 is commonly used for drug or gene delivery [360], and recently has been associated to metal nanoparticles to create bifunctional NCs for theranostic (combined diagnostic and therapeutical functions), due to its thermodynamic stability, low immunogenicity, and enhanced cellular internalization at tumor site [361, 362]. It has been recently approved by the Food and Drug Administration for clinical use. In this part of the thesis, the Au derived nanomaterial will be named temporarily as Au@Cy NCs (NCs stands for nanocomposite). The study with the copolymer PF-127 has two main goals: to assure the stability of the colloidal dispersion in a high ionic force environment and to check the possibility to use the nanomaterials as a drug carrier in photodynamic therapy.

The interaction of PF127 with the NCs has been studied by ζ -potential, dynamic light scattering (DLS), UV-Vis, and SERS spectroscopy. The potential use of the NCs as Ce6 carrier and sensitization-aid in photodynamic activity driven by the LSPR resonance [300, 363] was evaluated.

The Au@Carbynoid/PF127 NCs were obtained by incubation of the laser-ablated material using the copolymer at different concentrations (0.03–0.6 mg/mL or 2.4–48 $\mu\text{mol/L}$).

In Figure 4.25, it is shown the dependence of the surface charge, hydrodynamic radius, and spectral stability of the Au derived nanomaterial on the concentration of PF-127. No variations are observed for concentrations higher than 0.3 mg/ml, indicating that the interaction between the two species is saturated. As visible in the (c) panel, for this value of concentration, no distortion of the LSPR band is observed in a 0.15 M NaCl water solution, indicating that the colloidal solution of NCs can be used in biological applications without the risk of agglomeration and precipitation.

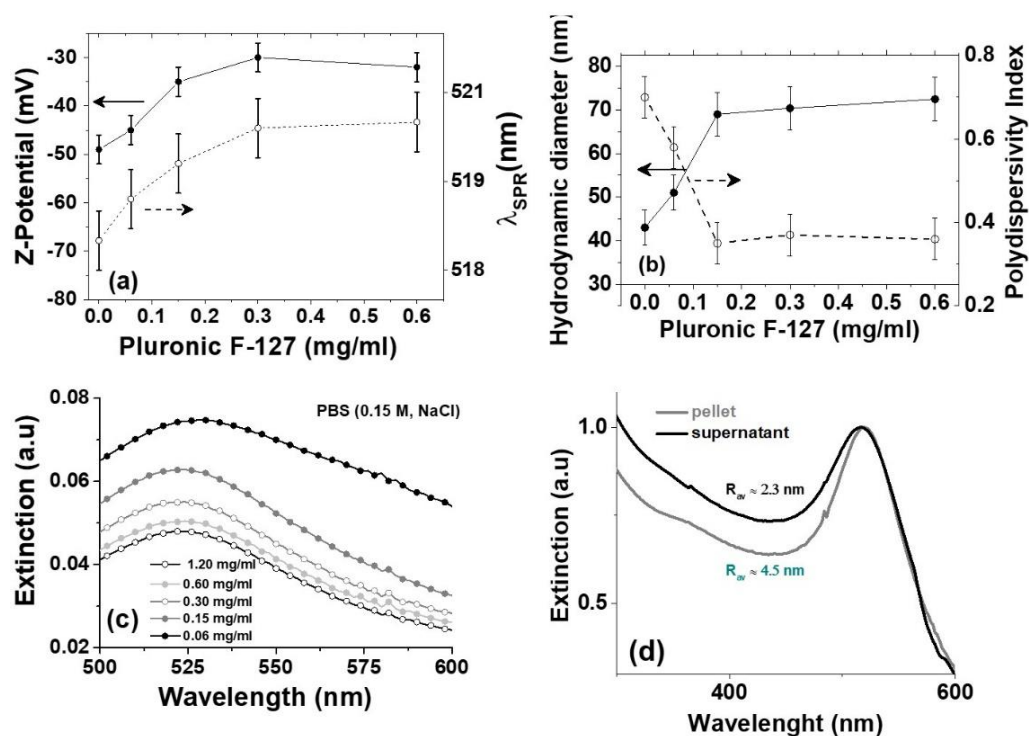


Figure 4.25 (a) ζ -potential and LSPR wavelength, (b) hydrodynamic diameter and polydispersity index (PI) of the Au@Cy/PF127 NCs in the function of the concentration of the copolymer. (c) UV-extinction spectra of Au@Cy/PF127 NCs in a 0.15 M NaCl water solution with different concentrations of PF127. (d) Extinction spectra of pellets and supernatant after centrifugation of the colloidal dispersion of NCs with copolymer at the reference concentration of 0.3 mg/ml.

4.6.2.

Effect of the agglomerated Au@Cy/PF127 NCs On the photodynamic activity of Ce6 photosensitizer

For photodynamic activity measurements, Ce6 was added to the Au@Cy/PF127 colloidal suspension of non-agglomerated and agglomerated NCs (agg-NCs). To obtain a colloidal dispersion of agg-NCs with an SPR band overlapped with the 650 nm band of Ce6, agglomeration was induced by adding 100 μ L drops of a NaCl 5 mol/L solution to the fresh synthesized colloidal dispersion of NCs. The agglomeration was blocked by rapid introduction of PF127 at a concentration of 0.8 mg/mL, using a global procedure similar as reported in [362]. Finally, the sample was centrifuged at 13000 rpm, and the pellets were extracted from the solution in the agglomerated form. on Figure 4.26, we represent the TEM images of the agglomerated Au@Cy/PF127 NCs before and after the centrifugation process.

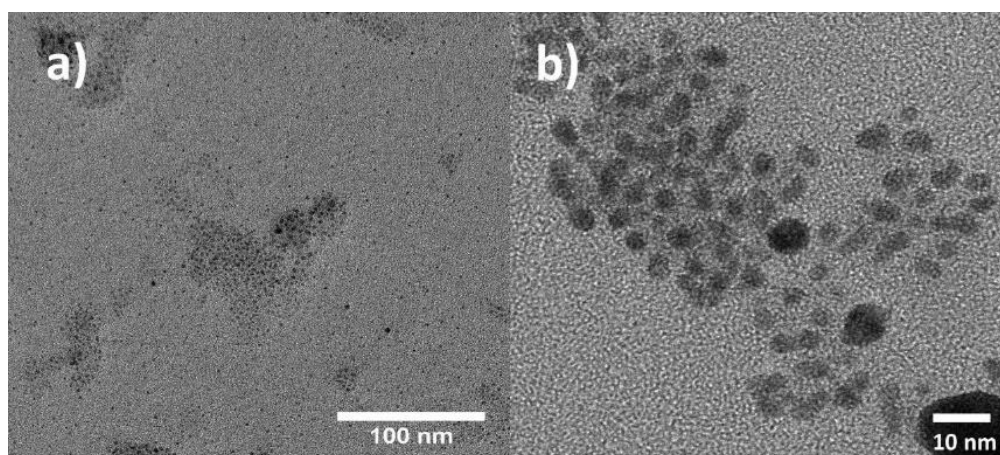


Figure 4.26 TEM image of the Au@Cy/PF127 NCs at the reference concentration of PF127. a) Before centrifugation. b) After centrifugation.

Photodynamic activity of Ce6 loaded Au@Carbynoid/PF127 NCs was demonstrated using both isolated and agglomerated NCs. Figure 4.27 a and b show respectively the extinction spectra and HRTEM image of the aggregated nanocomposites (agg-NCs). The SPR band is widely broadened, with a good overlap with S1 singlet state of the photosensitizer. In fact, as evident from the

HRTEM image, the NCs are in a well-defined agglomerated state, with dimensions ranging between 20 nm and 50 nm, and consequent redshift and broadening of the SPR band due to near field interaction. The comparison of the photodynamic activity of Ce6 in PF127 solution and isolated or agglomerated Au@Cy/PF127 NCs is reported in Figure 4.27. The concentration of Ce6 in each case was about 1 mol/L and was determined spectrophotometrically. Singlet oxygen production by illuminated Ce6 is proportional to the decrease in the 1,3-diphenylisobenzofuran probe (DBPF) absorption at the wavelength of 418 nm, indicated with parameter $\Delta A = (A_0 - A)$. Figure 4.28 shows the decrease of DPBF absorbance normalized to the concentration of photosensitizer [Ce6] in each sample. It can be noted that 1O_2 production by Ce6 in presence of Au@Carbynoid/PF127 NCs is similar to that in PF127. The presence of aggregated NCs, however, increases the 1O_2 production, similarly as reported in [362].

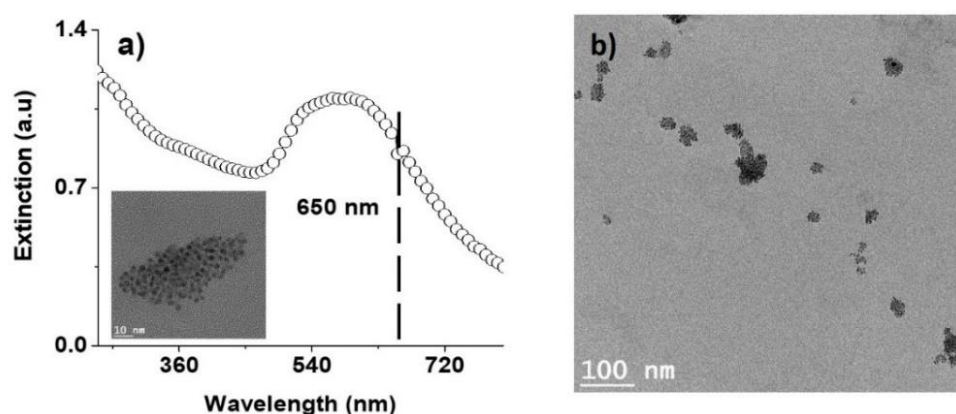


Figure 4.27 a) Extinction spectra of the agg-NCs. The dashed line represents the central wavelength of the optical source used in photodynamic activity measurements. The inset is the HRTEM image of a single agg-NC. b) HRTEM image of the ag-NCs.

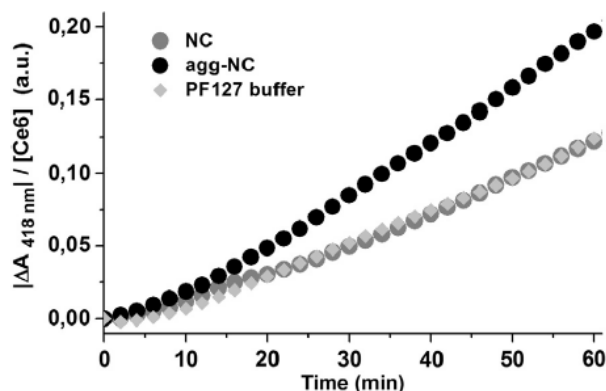


Figure 4.28 Absorbance decay of DPBF (A_0-A) at 418 nm normalized to [Ce6] as a function of time. The concentration of the NCs both in the normal (NC) and agglomerated state (agg-NC) was about 25 ppm. The concentration of Ce6 was about 1 $\mu\text{mol/L}$.

4.6.3. Citotoxicity of the Au derived nanomaterial

As explained in the *Introduction* Section, organic material is produced during the synthesis of the Au derived nanomaterial, together with the solid carbon nanostructures. Here, we put in evidence that the possibility of secondary reactions being produced during the PLA of the metal target in water has never been taken in account until now in literature [6, 82]. Vice versa, the conviction of its absence is commonly the main argument reported by different authors to catalog PLA as green-technique and defend the minor cytotoxicity of the nanomaterials when compared to the chemically synthesized homologs [8]. Our experimental results reveal a completely different scenario and shine a light on the importance to check the biocompatibility of nanomaterial obtained by PLA in water. Due to the central role of AuNPs in biological and medical applications, the cytotoxicity of the Au derived nanomaterial was evaluated in different kind of human cells: skin fibroblasts, keratinocytes (NCTC), human metastatic melanoma (A375-M6), dermal microvascular endothelial (HMVEC), and Endothelial progenitor cells (ECFCs).

The cells were exposed to colloidal dispersion of nanomaterial containing $10\mu\text{g/ml}$ of Au for 24 hours, and cell viability was monitored with Trypan blue assay. Morphologic examination by optical microscopy, showed the internalized

metal loads as black areas inside the cells, as represented in Figure 4.29 b) for the uptake of the melanoma cells. As shown in Figure 4.29 a), the nanomaterial did not exert any obvious cytotoxicity on all examined cell lines at the tested concentration.

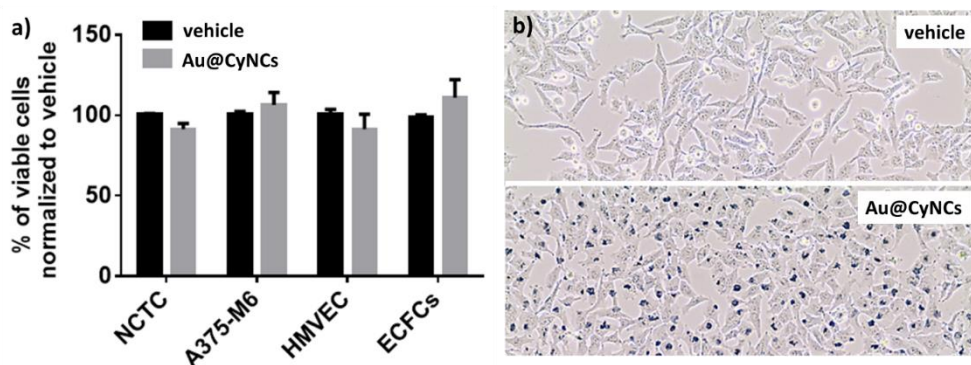


Figure 4.29- a) Viability histograms relative to the cellular uptake of the Au derived nanomaterial by cheratinocytes (NCTC), human metastatic melanoma (A375-M6), dermal microvascular endothelial (HMVEC), Endothelial progenitor cells (ECFCs). b) Optical images representing the uptake of the Au derived nanomaterial by A375-M6 melanoma cells after 24 hours (bottom panel). The concentration of gold was 10 µg/ml.

4.6.4. Gene therapy with Au derived nanomaterial

The physiological process of forming new blood vessels from preexisting vessels is known as angiogenesis and requires a finely balanced equilibrium between pro-angiogenic (growth factors, chemokines, angiogenic enzymes, endothelial specific receptors, and adhesion molecules) and antiangiogenic factors. Historically, abnormal angiogenesis was only implicated in a few diseases, such as cancer, arthritis, and psoriasis. However, in the last decades, the contribution of insufficient, excessive, and abnormal angiogenesis has been correlated to the pathogenesis of many more disorders [38]. Therapeutic angiogenesis can be induced mainly by two methods. Either angiogenic proteins or endothelial progenitor cells synthesizing angiogenic growth factors can be injected directly into a site to stimulate blood vessel growth, or the right genes can be activated to induce a signaling cascade that would lead to angiogenesis [364]. However, genetic studies have shown that the angiogenic program can be initiated but not completed. Thus, there are still many challenges before gene therapy can be applied to clinical

settings. The alternative approach to overcome these drawbacks might be engaged by nanomedicine, relying on the use of NPs.

The present study has surprisingly identified pro-angiogenic properties of the Au derived nanomaterial, which is heavily taken by endothelial cells, as visible in the optical images reported in Figure 4.30.

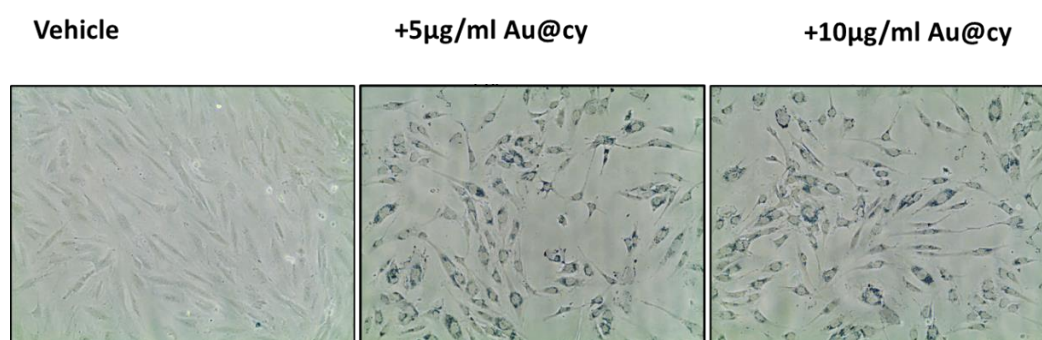


Figure 4.30 Images acquired with optical microscope for Endothelial cell (ECs) loaded with the Au derived material at different metal concentrations (5 ppm, 10 ppm). The internalized metal loads into the ECs are identifiable as the dark areas inside the cells.

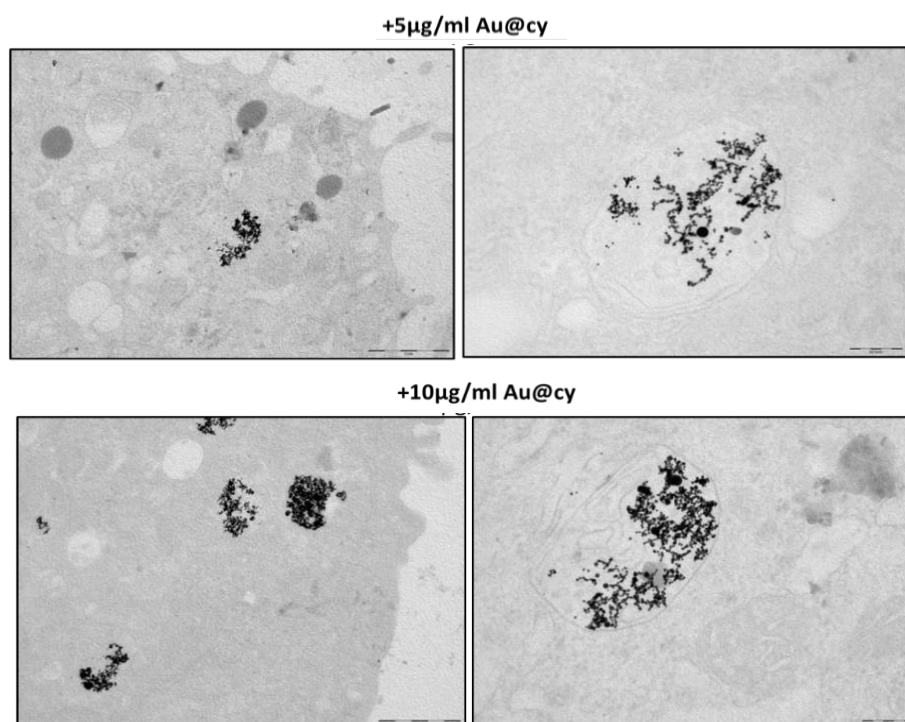


Figure 4.31 TEM images of the ECs loaded with the Au derived nanomaterial at different metal concentrations (5 ppm, 10 ppm).

TEM images of the loaded ECs, shown in Figure 4.31, demonstrate that the Au derived nanomaterial is well internalized by the cells, and packed in phagosomes, without introducing cellular damage for the used concentrations.

The endothelial cells, loaded with the Au-derived nanomaterials show an improved angiogenic phenotype *in vitro*, such as the enhanced capability to form vessel-like structures in the presence and absence of extracellular matrix coating (matrigel), as shown in Figure 4.32. The capillary morphogenesis is enhanced by the presence of the Au derived nanomaterial, after only 24 hours. In fact, the number of meshes, nodes, and master junctions, is higher after treatment with NPs, suggesting a pro-angiogenic activity. Since the encouraging results *in vitro*, *in vivo* tests have been conducted by the insertion of a matrigel plug assay in mice. Mice were subcutaneously injected in the flanks with matrigel containing a mixture of pro-angiogenic factors and heparin, and in the presence or absence of the Au derived nanomaterial. Indeed, at body temperature matrigel polymerizes to a solid gel, which becomes vascularized within 5 days in response to proangiogenic substances. In Figure 4.33 are represented the results of the *in vivo* experiments.

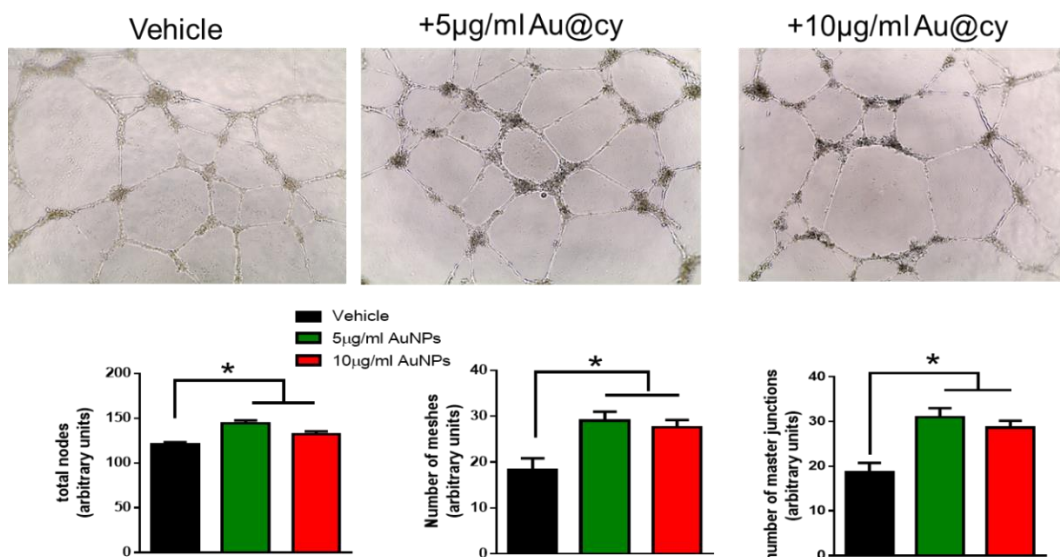


Figure 4.32 Optical images of the ECs after 24 hours of treatment by the Au derived nanomaterial. The first image on the left, represents the vehicle (control). In the down-series, the histograms with the number of nodes, meshes and master junction for all the cases.

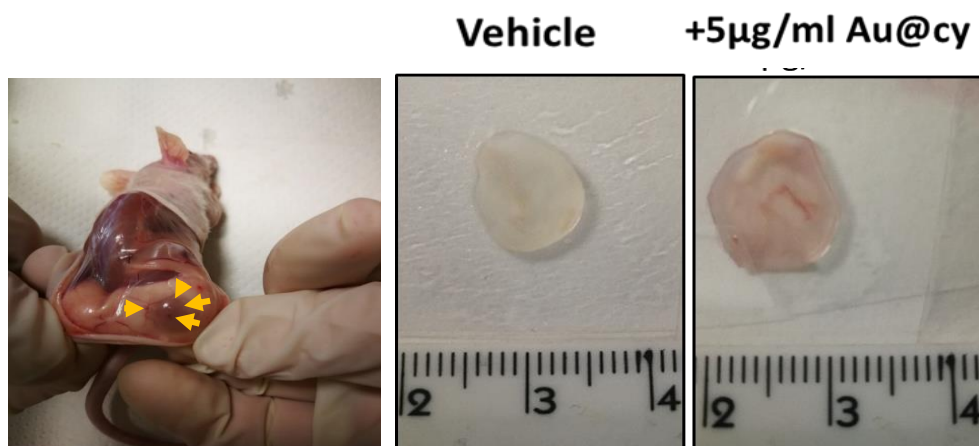


Figure 4.33 Images of matrigel plug removed from nude mice after 5 days. Without the nanomaterial (center image), with the Au derived nanomaterial (right image).

As evident from the photos of the matrigel, the quantity of blood vessels created by along 5 days, is hugely higher in the case of the injection of the Au derived nanomaterial. In literature, there is no mention of the use of metal nanoparticles for the enhancement of angiogenesis, so that is not possible to make any comparison with pre-existing data.

Anyway, the SERS measurements reported in Figure 4.10, together with the observed blue-shift of the LSPR peak of the Au derived nanomaterial, are coherent with the presence of carbon monoxide (CO) absorbed on the surface of the NPs.

Nitric oxide (NO), hydrogen sulfide (H₂S), and CO are at today considered as the ‘gas triumvirate’, being an ensemble of gases with huge biological effects in both the cardiovascular system and inflammation [365].

CO for example, which at high concentration definitively provokes apoptosis and death of human cells, is able at low therapeutically doses to provoke a vascular remodeling and enhanced angiogenesis [365]. This property has been verified in the last decade by the experimentation of different carbon monoxide releasing molecules (CORMs), which have the general form of metal-carbonyl species, where CO is generally released in the biological environment by light irradiation of the CORMs [118].

Further investigation is hence needed in order to detect the possible release of CO by the Au derived nanomaterial in physiological conditions. The research is

actually in progress in the *Laboratory of Cell Therapy and Nanomedicine* of the University of Florence, in order to understand if pro-angiogenic gases such as NO and CO are produced during the NPs loading in different kinds of human cells.

4.6.5.

Optical Sensing of methylmercury in Water by CQDs

Methyl mercury is an organic metallic compound and is generated from inorganic mercury through the living microbes existing in different aqueous systems. It is highly toxic, even more than other heavy metal ions (Hg^{2+} , Fe^{2+} , Pb^{2+} , Cd^{2+}) for the human body [366–368]. In literature, carbon quantum dots (CQDs) or graphene quantum dots (GQDs) are often used as photoluminescence nanosensors for the detection of toxic metal ions or methyl mercury in water [286], where PL quenching generally occurs. The limit of resolution is very low in the range of a few ppm [286, 369].

For the reasons cited above, the CQDs derived from the Au target were tested as luminescent nanosensors for the detection of methyl mercury (MeHg). Since the NaOH content in the colloidal dispersion of CQDs may shield the negative charge of the carbon nanomaterial by positively sodium (Na^+) ions, a dialysis process has been performed three times prior to the sensing measurements.

Differently from most of the CQDs presented in the literature, a spectral blue shift occurred additionally with PL quenching after interaction with MeHg. The limit of detection and sensitivity were measured using the method reported in [286, 370], and are 18 ppb and 1.3×10^{-2} nm/ppb, respectively. These values are much lower than the ones reported for chemically synthesized graphene quantum dots, which are of the order of 60 ppb [286]. The results are shown in Figure 4.34, where the measurement were repeated at least five-time, and the spectral resolution of the fluorimeter was set at 0.4 nm.

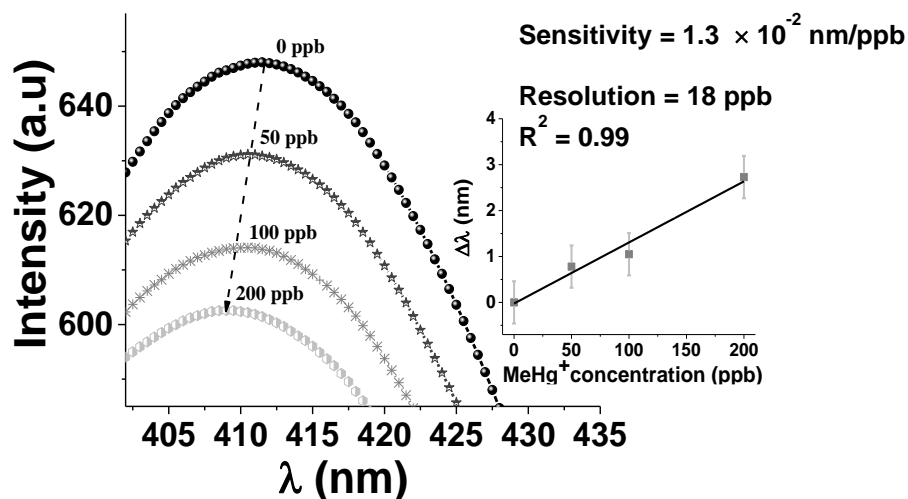


Figure 4.34 PL emission spectra of Au derived CQDs after dialysis in different concentration of MeHg. The inset represents the linear change in the wavelength ($\Delta\lambda$) corresponding to the maximum PL emission, depending on the concentration of MeHg.

4.7.

Conclusions

Differently from all literature available at the moment on the ligand-free PLA of gold target in water, we observe the simultaneous synthesis of gold based nanostructures together with carbon based material, both in nanostructured and molecular form. The latter, are observed as a molecular fingerprint in the SERS spectra of Figure 4.10. The possible nature of those organic products in molecular form will be discussed in Section 7.

The solid carbon nanomaterial is detected in the forms of carbynoid nanowires supported by gold nanoparticles (Cy@AuNWs), graphitic carbon quantum dots (CQDs), and gold nanoparticles partially covered by a shell of carbynoid material (Au@CyNPs). The three types of populations cited above are not present in the colloidal solution with similar concentrations. Most of the colloidal dispersion is constituted by the Au@CyNPs, followed (in terms of concentration) by the CQDs, and finally the Cy@AuNWs. Although the concentration of the latter is very small, HRTEM images revealed their presence in a repeatable way and pointed out to the typical interplanar distances of CAWs sp-hybridized nanowires, similarly as reported in [40].

In order to better identify the different synthesized carbon structures, different low-cost separation techniques have been proposed and tested. The most practical, effective, and clean methods were the ones based on electrical induction and concentration process by heating (followed by filtering). Anyway, independently of the used separation technique, it was not possible to separate the CQDs from the Cy@AuNWs.

The concentration of the latter is too small in order to have proper spectroscopic identification in terms of extinction, Raman or PL spectroscopy, at least with the infrastructure disposable in Departments of Physics and Chemistry of PUC-Rio. For this purpose, different samples containing the mix of CQDs and Cy@AuNWs will be analyzed by tip-enhanced Raman spectroscopy (TERS) at the *InMetro* Institute (Rio de Janeiro, Brazil), after proper deposition on SiO₂(50 nm)/Si substrates. In fact, TERS is characterized by the proper nanometer spatial resolution needed for the localized excitation and SERS response of the single nanowires.

The PL of the CQDs is characterized by the highest value of QY (~ 50%) reported until now for luminescent carbon nanoparticles obtained by PLA of solid targets. The intensity of the PL can be controlled by changing experimental parameters such as C_{NaOH} , F , or the frequency of the laser pulse. Anyway, none of the cited parameters was effective in the control of the spectral properties of the emissive species, characterized by a PL emission in the blue region. The CQDs presents the typical chemical groups of oxocarbons carbon dots, which were investigated by both FTIR and XPS spectroscopy. TRPL was used to understand the nature of the PL, which seems not to have any carbogenyc contribution, and mostly depends on the recombination of the electron-hole pairs at the surface states of the carbon nanoparticles.

We also observed that both the size and λ_{LSPR} of the Au derived nanomaterial may be controlled by changing the experimental parameters C_{NaOH} and F . The results are coherent with the literature, although a strict comparison cannot be done, due to the particular and unusual experimental conditions used to observe CO₂/C reduction during the PLA process: NaOH is introduced in the liquid environment to stabilize the NPs and carry more CO₂ inside the solution, the laser-target relative

position is kept fixed, and a very long ablation time is considered (45 minutes) in a quite small volume of liquid (2 ml) using a quite low value of fluence (from 0.3 J/cm² to 1.3 J/cm²).

In fact, there is no mention in literature about the blue-shift in the LSPR peak of the Au derived nanomaterial which we observed experimentally. One of the key points for the correct interpretation of the spectral blue-shift, is the detection of Au-carbonyl species in the SERS spectra of the dried powder of the nanoparticles. The presence of CO adsorbed on the AuNPs, which has a refractive index minor than the water, may in fact be responsible for the observed blue-shift, together with the possible formation of the π -backbonding in metal-CO system, with the enhancement of the number of electrons participating to the localized plasma oscillations. An analog transfer of electrons may also happen from the shell of CAWs observed around some of the Au nanoparticles and their metallic nuclei, contributing to the overall observed blue-shift.

The applicability of the Au derived nanomaterial has been tested in different applications related to medicine. The mixing of the Au derived nanomaterial with the copolymer PF-127 assures stability in liquid with high ionic force. The PF-127 based nanocomposites present no cytotoxicity, at the tested concentration, for both fibroblast and endothelial human cells.

The PF-127 based NCs were firstly tested in photodynamic activity, showing that the opportune engineering of the LSPR band of the aggregates can enhance the production of singlet oxygen.

More importantly, the Au-derived nanomaterial greatly enhances the capillary morphogenesis of endothelial cells, with interesting potential applications in regenerative tissue medicine. The results may be explained by the biological activity of the CO adsorbed on the AuNPs. The latter, may in fact generate CO by the reduction of the CO₂ present in the physiological environment, and further release the gas into the cells, similarly as it happens in CO-based therapy with carbon oxide-releasing molecules (CORMs). In order to understand this fundamental point, measurements of NO and CO production in endothelial cells charged with Au derived nanomaterial, are being performed in the *Laboratory of Cell Therapy and Nanomedicine* of the University of Florence (Italy).

As a final remark, in Figure 4.35 we report a scheme representing the different ‘phase’ regions of the PLA environment (similarly as in the Theoretical Section 2),

together with all the principal carbon-based nanostructures which were observed during the investigation.

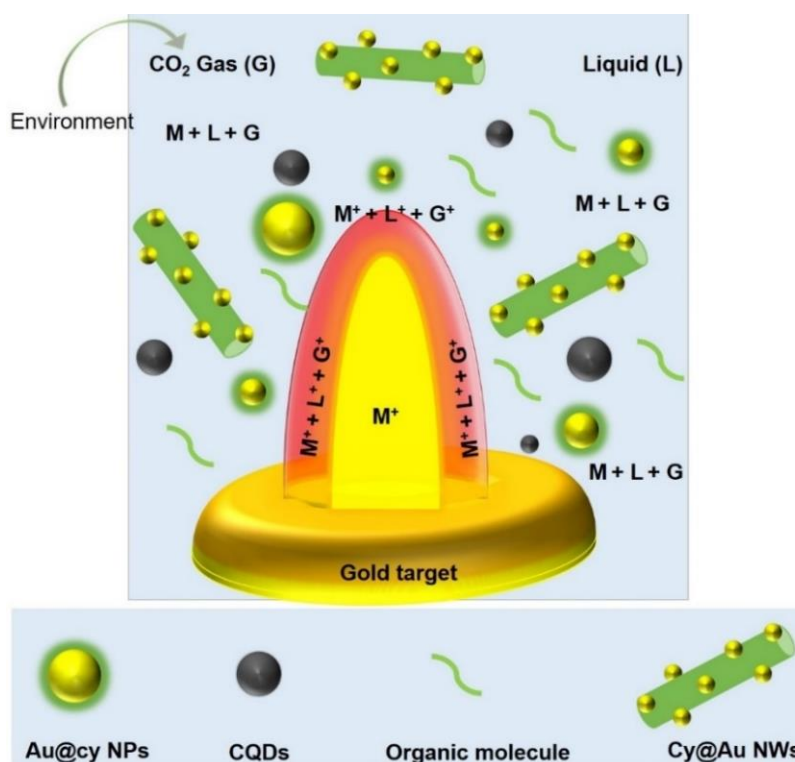


Figure 4.35 Schematic diagram representing the different 'phase' regions present in the PLA environment, together with all the materials synthesized during CO₂/C reduction by the use of Au target. M =Metal; L=Liquid; G=Gas. The reaction takes place in the interface between the plasma plume and the liquid environment.

As explained in Section 2.2.1, the transportation of the NPs into the cavitation bubble happens at the interface between the coldest part of the plasma (red in Figure 4.35 and the layer of the surrounding vapors of the solvent, and it is immediately before and after the collapse of the cavitation bubble that the formed NPs have the opportunity to interact with the gases and liquid present in the PLA environment and be responsible for chemical reactions leading to the formation of the CO₂ reduction products

5 Ag Derived Nanomaterial

Different sizes and shapes of AgNPs with different properties can be synthesized by PLA in liquid by just varying the material or laser parameters. For example, Tsuji *et. al.* [371] synthesized AgNPs by PLA of a silver target in the water at three different wavelengths (1064 nm, 532 nm, and 355 nm), with a corresponding change in their sizes. Similarly, R. M. Tilaki *et. al.* [372], demonstrated the effect of solvent on the average size, size distribution, and stability of AgNPs.

These variations in sizes, structures, and properties of NPs in dispersion by changing PLA parameters make it a versatile method for the synthesis of AgNPs and encourage us to test the PLA process for the production of AgNPs colloids with controlled sizes and shapes [373].

Interestingly, big (~ 20 nm) AgNPs having photoluminescence were reported recently, where two emission peaks at 399-409 and 440 nm were observed [81]. According to them, the luminescence is due to both the radiative decay of LSPR and the radiative recombination of the Fermi level electrons with sp- or d-band holes. In the cited research, there is no mention about the possible presence of carbon nanoparticles or CQDs.

In the present chapter, we will show that similarly to the case of Au target, the ablation of Ag targets in a water environment enriched with NaOH, leads to the synthesis of luminescent CQDs, which can be easily separated from the metal species by the same experimental procedures reported for the case of Au.

5.1.

UV-Vis stability investigation of Ag derived nanomaterial

The Ag derived nanomaterial in colloidal form was synthesized by PLA of silver target in ultra-pure deionized (UPD) water with different values of C_{NaOH} , at the frequency 2ω , and at fixed laser pulse fluence of $F = 1.3 \text{ J/cm}^2$.

As for the case of gold, the laser-target relative position was kept fixed, and ablation was performed for a minimum time of 45 minutes when considering liquid volumes of about 2 ml.

To study the stability of Ag-derived nanomaterials, UV-Visible spectroscopy is used as a primary technique. The time-dependent extinction spectra of the Ag-derived nanomaterials in the function of the C_{NaOH} in water, are shown in Figure 5.1.

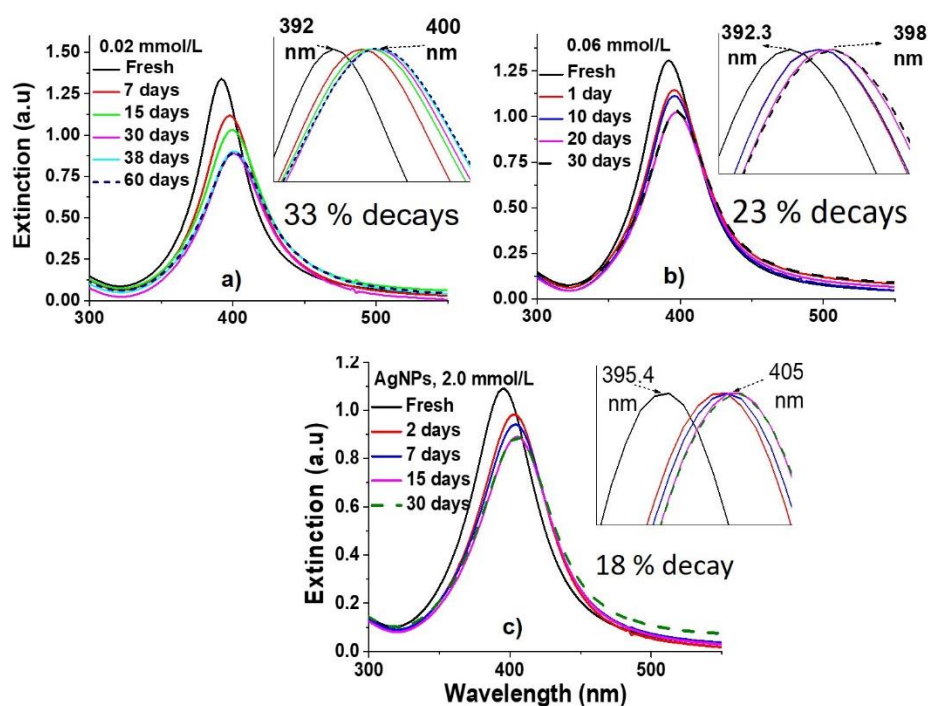


Figure 5.1 Temporal evolution of the UV-Vis extinction spectra of the Ag derived nanomaterial synthesized at $F = 1.3 \text{ J/cm}^2$ and different values of C_{NaOH} , ranging from 0,02 mmol/L to 2,0 mmol/L.. The inset in each figure represents the corresponding normalized extinction spectra.

It can be seen that the Ag-derived colloids are not stable in the first 15 to 30 days. The colloids synthesized at higher NaOH concentration (up to 2 mmol/L), are relatively more stable as compared to lower values of C_{NaOH} . For a 2mmol/L NaOH concentration, 18 days were necessary to stabilize the colloidal dispersion, while lower C_{NaOH} took 32 days to become stable.

Oppositely to the Au derived nanomaterials, in this case, the intensity of the LSPR peak decreases since the first hour after PLA, instead of growing up. This behavior is followed by a well visible broadening of the curve and a progressive redshift of the spectra position of the LSPR peak. This behavior can be coherently explained by the time-dependent oxidation of the NPs, which increases the losses of the LSPR band, and may create an oxide shell around the NPs [193, 374]. The latter phenomena, together with a possible increase in the NPs diameter, may contribute to the overall red-shift of the LSPR resonance.

AgNPs in relatively higher C_{NaOH} (in 2.0 mmol/L) are probably more stable (18% decreased) and more red-shifted than the 0.06 or 0.02 mmol/L analogs, as they may be subject to a faster oxidation process [193, 374], due to the more suitable environment for oxidation.

5.2.

Analytical characterization of the Ag derived nanomaterial (dimension, λ_{LSPR} , charge, total carbon, HRTEM)

Figure 5.2 show TEM images, statistical size distribution, and the corresponding UV-Vis spectra of the Ag derived nanomaterial, synthesized at $C_{\text{NaOH}} = 0.2$ mmol/L (a), 2.00 mmol/L (b), and 8.00 mmol/L (c). Due to the low stability of the samples, the deposition on the TEM grid was performed immediately after the end of the PLA process, and with the grid on the drop (GOD) method described in Section 3.

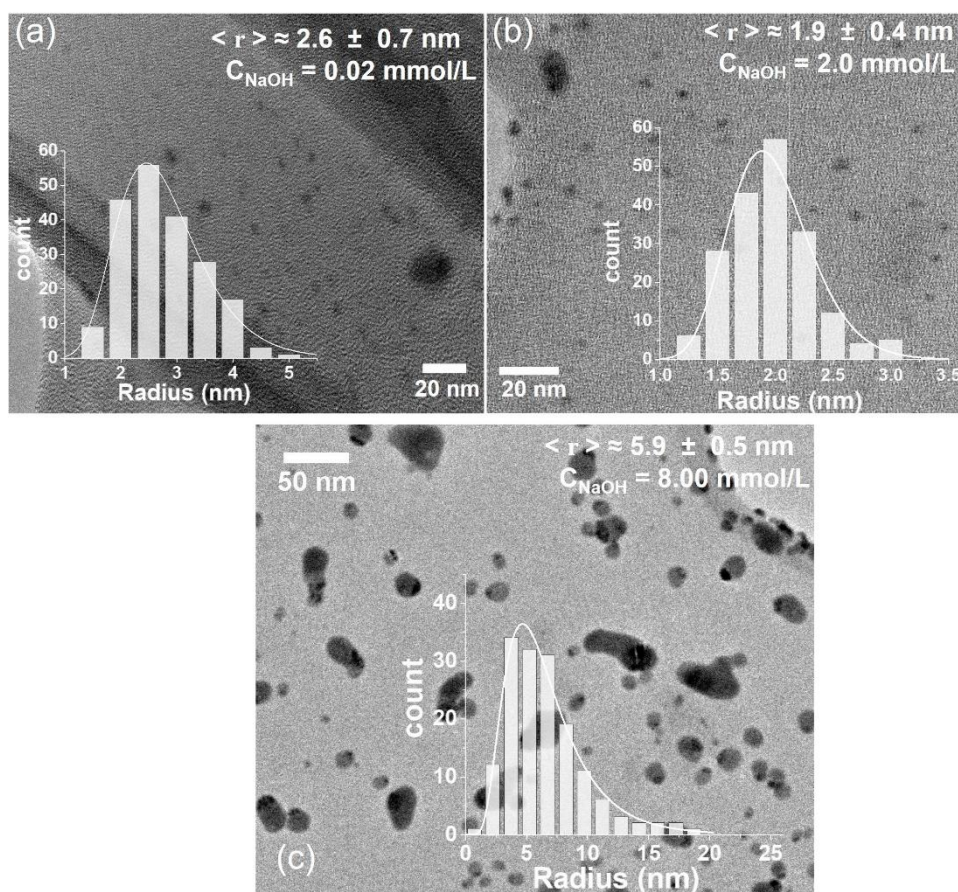


Figure 5.2 TEM images of Ag derived nanomaterials synthesized in a) 0.02 mmol/L and b) 2.00 mmol/L, c) 8.00 mmol/L. The inset in each figure shows their corresponding statistical size distribution with Lognormal fit, average size $\langle r \rangle$, and standard deviation.

In Table 5.1 we report the complete analytical characterization of the samples synthesized at $F = 1.3 \text{ J/cm}^2$, for different values of C_{NaOH} , similarly as reported for the case of Au target in Table 4.1. In literature [81, 375], redshift occurs in λLSRP of AgNPs colloids smaller than 15 nm with the decreasing of the size [81]. A similar redshift has been observed along our research in Ag derived nanomaterials, by increasing C_{NaOH} from 0.02 nmol/L to 2.0 mmol/L as shown in Figure 5.3 a) and b), and in Table 5.1. The Ag derived nanomaterials were found to be more unstable and in agglomerated form for C_{NaOH} values higher than 2.0 mmol/L.

Table 5.1. Complete analytical characterization of the Ag derived nanomaterial synthesized at $F = 1.3 \text{ J/cm}^2$, for different values of C_{NaOH} .

C_{NaOH} (mmol/L)	TC_0 (ppm)	ΔTC (ppm)	λ_{LSPR} (nm)	Radius (nm)	ζ -potential (mV)	C_{Ag} (ppm)
2×10^{-2}	3.5 ± 1.1	< 0.1	392 ± 1	2.6 ± 0.8	-82.0 ± 1	3.7 ± 0.8
6×10^{-2}	5.7 ± 1.6	1.1 ± 0.1	393 ± 1	2.4 ± 0.9	-93.2 ± 1.5	3.9 ± 0.8
2.00	19.1 ± 5.3	3.3 ± 0.9	395 ± 2	1.9 ± 0.4	-115.6 ± 5.2	6.2 ± 0.6
8.00	27.3	6.5 ± 0.9	397 ± 2	5.9 ± 0.5	×	×

As represented in Figure 5.3, it was not possible to make a good theoretical Mie fit for of the UV extinction band in the case of Ag derived nanomaterial, because the theoretical value of the dielectric constant of metallic silver, does not take in account the oxidation of the NPs.

While a progressive charging of the NPs is expected from literature for higher values of C_{NaOH} , again what it is surprising in Table 4.1, is the detection of a positive variation of the total carbon ΔTC for higher values of C_{NaOH} . The latter observation indicates that the $\text{CO}_2(\text{water})/\text{CO}_2(\text{air})$ equilibrium is broken during the PLA process, suggesting that chemical transformations to the gas are occurring in the liquid environment.

A higher concentration of NaOH (proportional to TC_0), acting as the CO_2 carrier in the liquid environment, leads to noble MeNPs with a smaller radius (inside the stability region ($0.02 \text{ mmol/L} < C_{\text{NaOH}} < 2.00 \text{ nmol/L}$), allowing the control of both the dimension and LSPR position of the NPs. When TC_0 is increased, contrary to the Au derived nanomaterial, the AgNPs are characterized by a progressive red-shift of the LSPR peak, suggesting a more relevant role of the oxidation, and the absence of a significant electron transfer from ligands (eventually created during the PLA) and the metal-core.

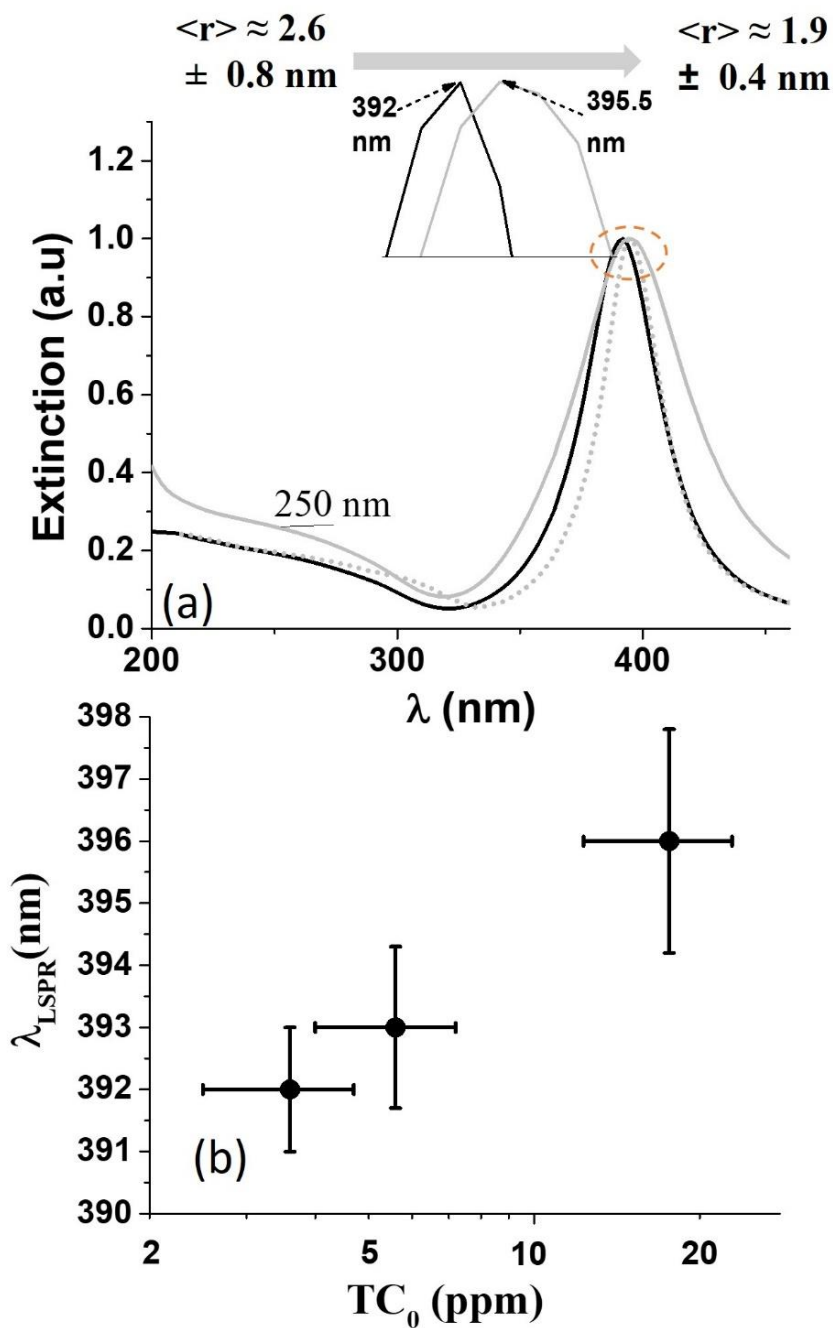


Figure 5.3 Normalized extinction spectra of Ag derived nanomaterials synthesized in $C_{\text{NaOH}} = 0.02$ mmol/L (black line) and $C_{\text{NaOH}} = 2.0$ mmol/L (gray line). The grey dotted line represents the Mie fit obtained in the dipolar approximation using the lognormal fit of experimental size distribution shown in Figure 5.3 (b).

5.3.

Characterization of carbon nanomaterial colloid derived from Ag target

5.3.1.

SERS measurements on Ag derived nanomaterial

As in the case of Au, also for Ag, the presence of solid carbon is firstly detected in the SERS spectra of the nanomaterial in powder form. In Figure 5.4, we report a comparison of the SERS spectra obtained from both Ag and Au colloids.

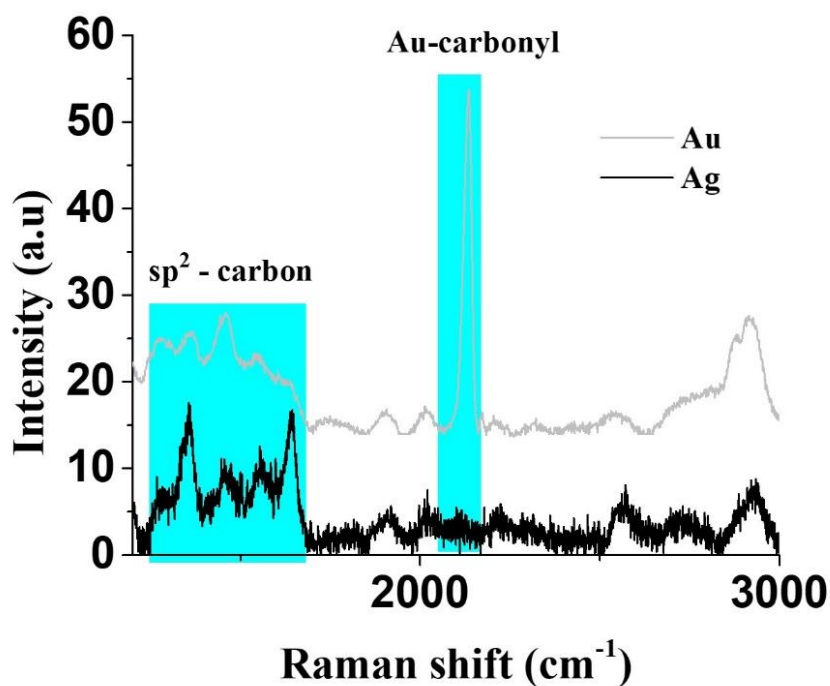


Figure 5.4 SERS response of nanomaterials in solid form synthesized by PLA of Au (black curve) and Ag (grey curve) targets with $c_{\text{NaOH}} = 2.00$ mmol/L. The excitation wavelength was 638 nm.

For both noble metals, sp^2 carbon Raman modes (D and G bands) are observable, overlapped with several molecular vibrations. As explained in the previous chapter, the overlap prevents the quantitative analysis of the D and G bands, so that the amorphous or crystalline nature of the carbon nanostructures is

not identifiable by SERS spectroscopy. In the unique case of gold, also a sharp line is dominant around 2120 cm^{-1} in the typical spectral region of Au-carbonyl, as explained in Section 4. Interestingly, we notice here that the molecular fingerprint overlapped with the carbon collective modes is the same for both Au and Ag derived nanomaterials, suggesting that similar molecular organic products are synthesized during PLA of both the noble metal targets.

To investigate the nature of the carbon nanomaterial (CNM) present in the colloidal dispersion, the separation processes described in Section 3.6.5 were applied. Differently than gold, after separation the supernatant of the Ag-derived nanomaterial still has the presence of a significant quantity of residual metal, as confirmed by UV-Vis spectroscopy, HRTEM and EDS, reported in Figure 5.5.

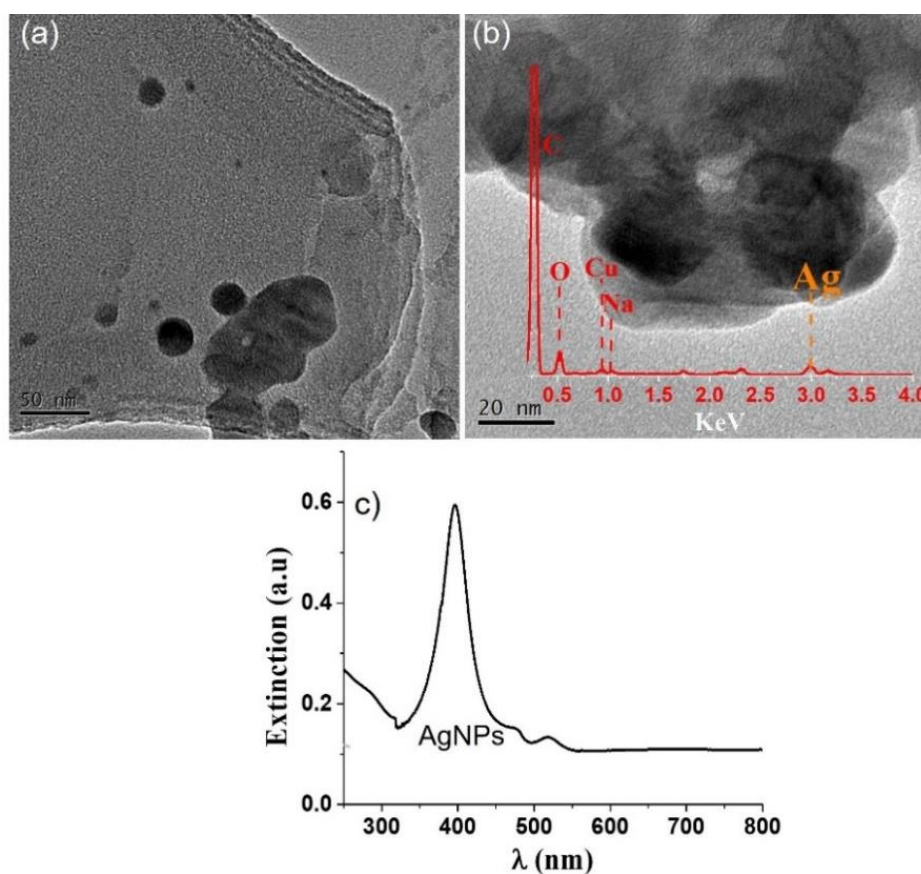


Figure 5.5 a)-b) HRTEM images of the nanomaterial derived from Ag target after the separation procedure. In b), the inset represents the EDS spectra confirming the presence of silver. c) UV-Vis spectra of the Ag derived nanomaterial after the separation process, confirming the presence of a significant concentration of the metal.

5.3.2 TEM Measurements

5.3.2.1 CQDs

Figure 5.6 a) and b) represent the two kinds of CQDs derived from the CO₂/C reduction by PLA of Ag target, at TC₀ of 6 ppm and 18 ppm, respectively. As in the case of Au, together with small circular nanoparticles, we also observed a few and sparse bigger carbon nanoparticles in the form of carbon-onions [338].

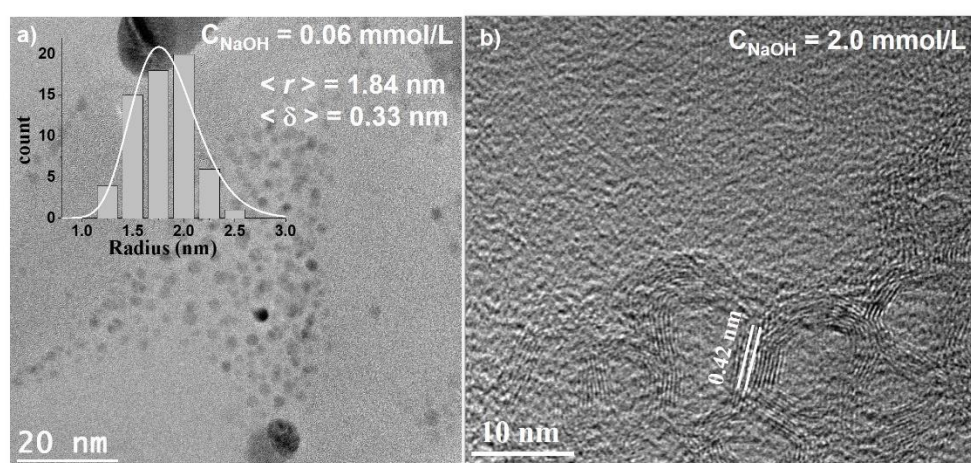


Figure 5.6 a) TEM image of small spherical CQDs obtained by CO₂/C process from Ag target. The inset shows the LogNormal fit of the statistical distribution with standard deviation $\langle \delta \rangle$ and average radius $\langle r \rangle$. b) Carbon onion nanoparticles.

The dimension of the CQDs, centered around 1.8 nm, is very similar to the one obtained by Au target in all the different conditions of NaOH concentration.

5.3.2.2

Cy@Ag Nanocrystals

Although quite rare, it was possible to identify a few carbynoid nanocrystals stabilized by AgNPs (Cy@AgNC), together with the CQDs after the separation.

Those metal-carbynoid NCs are not organized in nanowire (NWs) like in the case of Au, but seems to be present as larger crystals, stabilized and grown over relatively big AgNPs. The HRTEM images of the rare Cy@AgNCs are represented

in Figure 5.7. The inset in the latter represents the EDX spectra of the Ag-carbon nanocomposites, where Ag, C, and O appear as the most abundant elements, together with Na residuals. Similarly to the case of Au, we observe an interplanar distance ranging from 0.93 nm to 0.95 nm in the central region, which would be coherent with the central axis (c-axis) of sp-hybridized materials of the plane (001) [40].

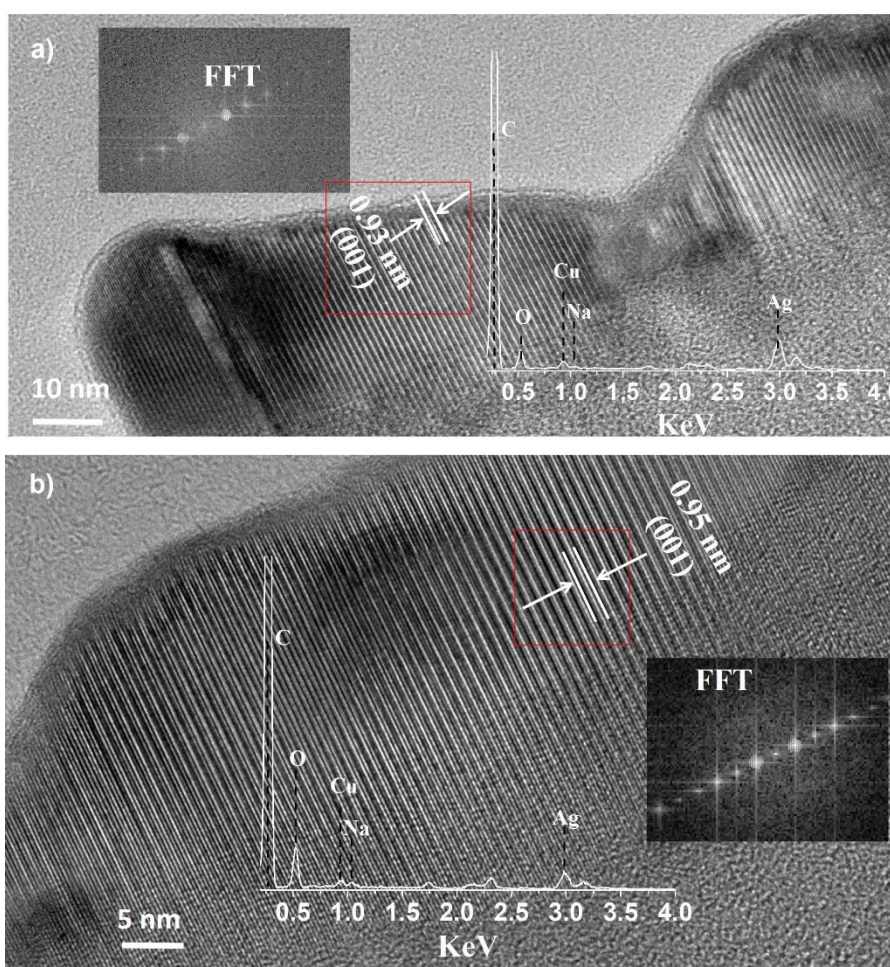


Figure 5.7 a,b) HRTEM image of the rare Cy@Ag NCs. The inset shows the corresponding EDX spectra, together with the FFT pattern.

5.4.

PL of the CQDs obtained by CO₂/C with Ag target

The PL spectra of the CQDs derived from Ag (CQDs/Ag) and Au (CQDs/Au) were compared. As observed in Figure 5.8, the PL intensity of the CQDs/Ag is

much smaller than the PL intensity of the CQD/Au, probably due to the presence of the residual silver quenching the corresponding emission. The emission peak position in both CQDs/Ag and CQDs/Au is the same, without any spectral differences, which can be related to the same surface functional groups and the similar sizes of the Ag and Au derived CQDs.

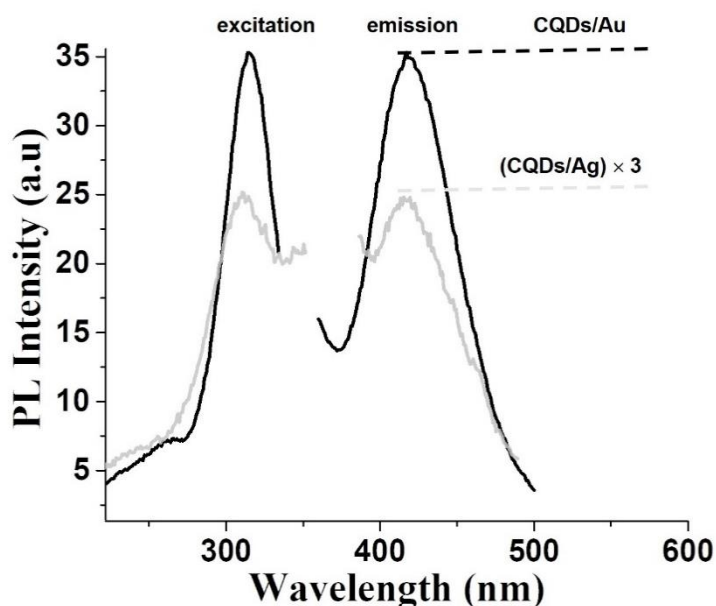


Figure 5.8 Comparison of the PL spectra of CQD obtained by CO_2/C reduction with Ag (grey curve) and Au (black curve) targets. TC_0 was 18 ppm for both the samples. The PL intensity of the CQDs/Ag has been multiplied by a factor 3.

5.1.

Conclusions

Also in the case of Ag targets, differently from all literature available at the moment on the ligand-free PLA of Ag target in water, we observe the simultaneous synthesis of silver-based nanostructures together with carbon-based material, both in nanostructured and molecular form. The latter is observed as a molecular fingerprint in the SERS spectra of Figure 5.4, the same one reported for the Au derived samples. The possible nature of those organic products in the molecular form will be discussed later in Section 7.

The solid carbon nanomaterial is detected in the forms of carbynoid nanocomposites supported by silver nanoparticles (Cy@AgNCs), graphitic carbon

quantum dots (CQDs), and silver nanoparticles (AgNPs). The three types of populations cited above are not present in the colloidal solution with similar concentration. Most of the colloidal dispersion is constituted by the AgNPs, followed (in terms of concentration) by the CQDs, and finally the Cy@AgNCs.

The concentration of the latter is very small; they have been uniquely observed until now in the samples synthesized at $C_{\text{NaOH}} = 2.0$ mmol/L, and it is not clear at this stage of the research what are the main experimental factors which might control their production rate. Together with the important experimental parameters characteristic of the PLA process (NaOH concentration, laser pulse characteristics, liquid volume, ablation time), also the quality and details of the separation process, and also the quality of the deposition of the separated nanomaterial on the TEM grid (too low or too high concentration of the dispersion), may influence the detection of such rare carbonyd structures by HRTEM.

What we can conclude with the actual experimental results, is that such as in the case of Au target, the carbonyd nanomaterial is less concentrated between the different nanomaterials observed, and is not detectable at the moment by the optical spectroscopies used along the research (UV-Vis, SERS, PL).

The average size of the AgNPs can be controlled by changing C_{NaOH} , with the linear dimension getting smaller when increasing C_{NaOH} from 0.02 to 2.00 mmol/L. Unlike the Au derived nanomaterial, the synthesized AgNPs become stable with respect to oxidations after 15 to 30 days, and a redshift has been observed in the λ_{LSRP} when increasing the NaOH concentration up to 2 mmol/L, due to the progressive oxidation of the NPs.

Indirect evidence of the large oxidation of the AgNPs is the difficulty to provoke their precipitation by the induction method, which instead is highly efficient for the case of Au derived nanomaterial, due to the low surface coverage of the oxides [5].

The PL of the CQDs/Ag after separation, was very low as compared to the CQDs/Au. In fact, a significant concentration of AgNPs is present also after the separation procedure, and the corresponding LSPR resonance absorbs most of the PL emission.

As final remark, in Figure 5.9 we report a scheme representing the different ‘phase’ regions of the PLA environment (similarly as in the Theoretical Section 2),

together with all the principal carbon-based nanostructures which were observed during the PLA of Ag targets.

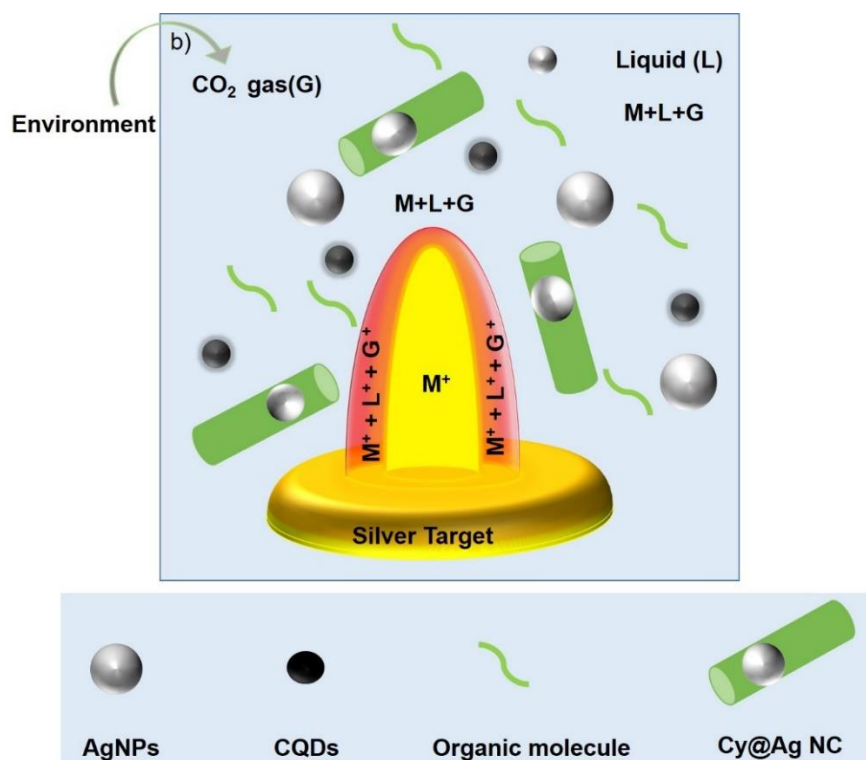


Figure 5.9 Schematic diagram representing the different 'phase' regions present in the PLA environment, together with all the materials synthesized during CO₂/C reduction by the use of Ag target.

6 Fe Derived Nanomaterial

6.1.

Separation of the different constituents present in Fe derived nanomaterial

As in the case of PLA on noble metal target (Au, Ag), the ablation of a pure iron target in water has been performed with the principal objective to prove the CO₂/C reduction process, and identify solid carbon nanostructures.

Iron was the unique transition metal for which we observed the formation of luminescent material without forcing the entry of the CO₂ in the water solution through the NaOH addition. In comparison to the case of the noble metal target, a special investigation has been performed using the Fe target. The PLA process has been performed not only by irradiation of laser pulses at the fundamental (ω) or second harmonic frequency (2ω) but also by the simultaneous irradiation of ω and 2ω frequency laser pulses. In the latter case, unique results were obtained, both in terms of dimension of the resulting NPs and also in terms of the PL spectra of the associated transparent CNMs. A possible explication of these experimental observations will be presented in Section 7, where we propose our hypothesis on the mechanism of the CO₂/C reduction happening during PLA. The other experimental conditions of the PLA process were similar to the ones used for noble metal targets: a fixed laser pulse-target relative position, 2 ml of pure water without surfactants or ligands, and a long ablation time (120 minutes in this case) at a fixed repetition rate of 10 Hz.

Another important experimental difference in comparison to the procedures used for the Au and Ag derived nanomaterial, is constituted by the metal/carbon separation process. PLA of the iron target in water leads in fact to the synthesis of magnetic NPs, which can be successfully separated from the non-magnetic (carbon)

counterparts by the simple magnetization process. In fact, it is known from the literature that PLA of an iron target in water is characterized by the simultaneous synthesis of different magnetic phases, such as magnetite (Fe_3O_4) (in the major part), hematite (Fe_2O_3), wustite (FeO), and metal iron (Fe) [82, 83].

In the light of the results from the literature, it is clear that the magnetization process is not only effective for the separation of the magnetic and non-magnetic (carbon) material, but it is also a powerful method which can be used for the selection of magnetic nanoparticles with different sizes and different phases (magnetization). In fact, although all iron oxide NPs are superparamagnetic for a size smaller than 10-20 nm, their magnetic properties depend on both size and composition [376].

Hence, we decided to give a general definition for the different constituents of the colloidal dispersion of the Fe derived nanomaterial, based on the product obtained after the application of different separation steps. Precipitant (FeNPs^{pr}), supernatant (FeNPs^{sp}), and carbon nanomaterial (CNM) were hence defined following the schematic diagram shown in Figure 6.1.

The Fe derived nanomaterial was first placed for 4 days near a strong permanent magnetic bar of 0.25 T (Figure 6.1 b). At this time, the magnet attracts a part of the iron oxide-based nanoparticles on the wall of the glass container, which we will call precipitant (FeNPs^{pr}). After the collection of the precipitant in fresh deionized water, the nanoparticles which were not attracted in the first 4 days, are located for further 10 days in the proximity of the magnet, or heated at 55-60 °C degree for 2 hours, with final precipitation. The nanomaterial precipitating in this second separation step is called supernatant (FeNPs^{sp}), and it is further collected and finally suspended in fresh deionized water. After separation of both (FeNPs^{pr} and (FeNPs^{sp}), the remaining transparent liquid does not present a significant quantity of magnetic nanoparticles, and contains in major part the carbon-based material (CNM), constituted of carbon quantum dots (CQDs) and eventually of the molecular organic compound, synthesized during the CO_2 reduction.

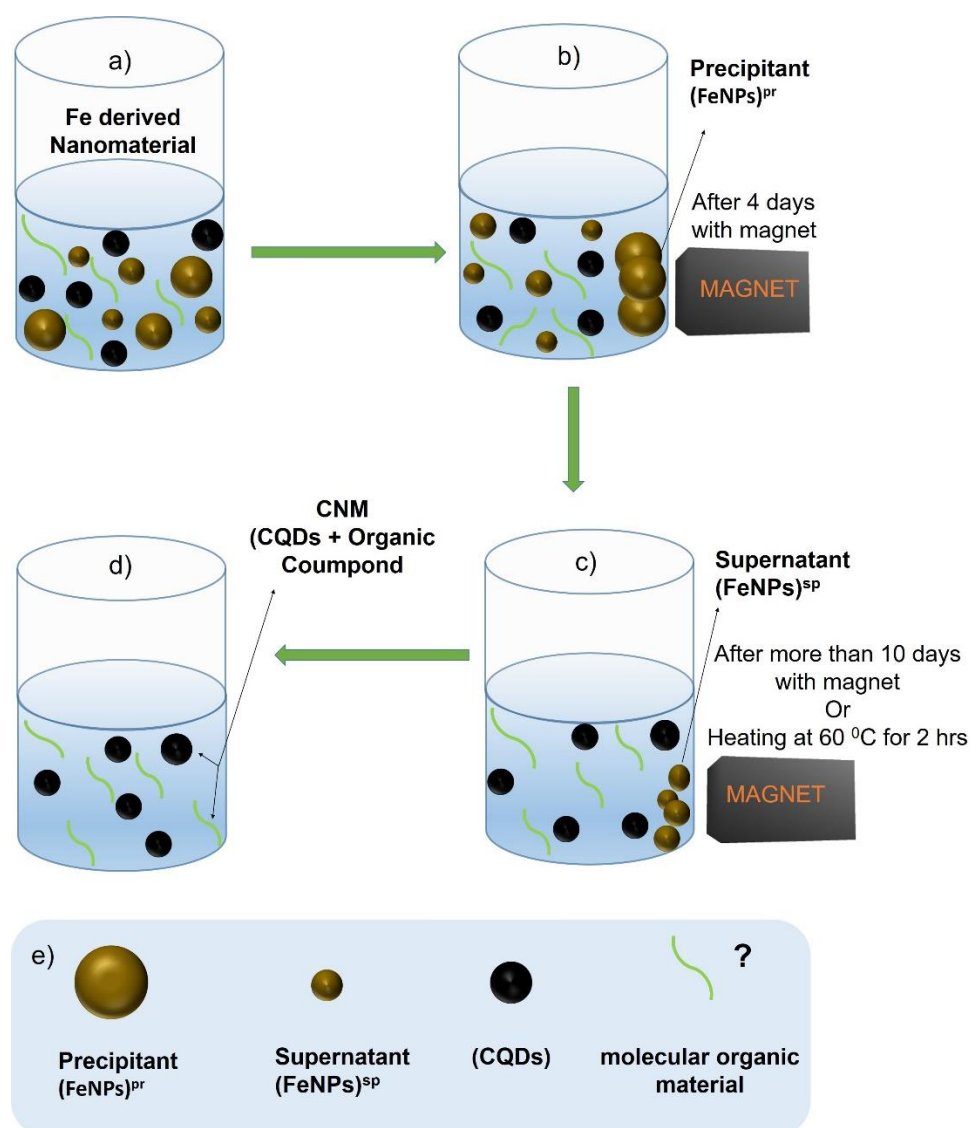


Figure 6.1 a-d) Different steps of the separation process used to identify and isolate the different species in the sample. e) The different species present in the Fe derived nanomaterial. An interrogation point has been placed aside the symbol of the molecular organic material since its presence has still to be detected.

Before starting the presentation of the experimental activity, we put in evidence that the correct interpretation of some of the results still needs further investigation, which has been slowed down due to the limited access to most of the laboratories infrastructure, due to the spreading of the pandemic COVID-19 virus [377].

6.2.

Stability and analytical characterization of the Fe derived nanomaterial (dimension, charge, ζ -potential, magnetization)

6.2.1.

Fe Derived nanomaterial synthesized by PLA with simultaneous ω and 2ω pulses

When PLA is performed by the use of simultaneous ω and 2ω frequency pulses coming from the *BIG SKY* laser source, both the energy and fluence of the pulse are characterized by two components, so that $F_{\omega+2\omega} = F_{\omega} + F_{2\omega}$, and $E_{\omega+2\omega} = (E_{\omega} + E_{2\omega})$. Using the experimental procedure reported in Section 3.2.4, the optical system was calibrated in such a way that about 70% of the overall fluence $F_{\omega+2\omega}$, was due to the component of the pulse at the fundamental frequency ω . Two values of total fluence were considered, $F_{\omega+2\omega} = 0.9 \text{ J/cm}^2$, and $F_{\omega+2\omega} = 3.2$, as reported in Table 3.3. In both cases, we observed that the 2ω component of the laser pulse had a negligible effect on the production rate of the NPs, so that its role in the PLA process was not in the direct synthesis of NPs, but rather in the simultaneous irradiation of the nanoparticles synthesized by the ω component of

Figure 6.2 represents the photos of Fe derived nanomaterial synthesized at the different value of fluence, for a total ablation time of 120 minutes, before and after the magnetization along 4 days. The image is clearly showing that the optical density and the concentration of the Fe derived nanomaterials get higher when the fluence is raised. Also, it is clear in Figure 6.2 (c,d), that it is not possible to precipitate all the nanomaterial even after 4 days of magnetization, so that (FeNPs)^{SP} may be obtained.

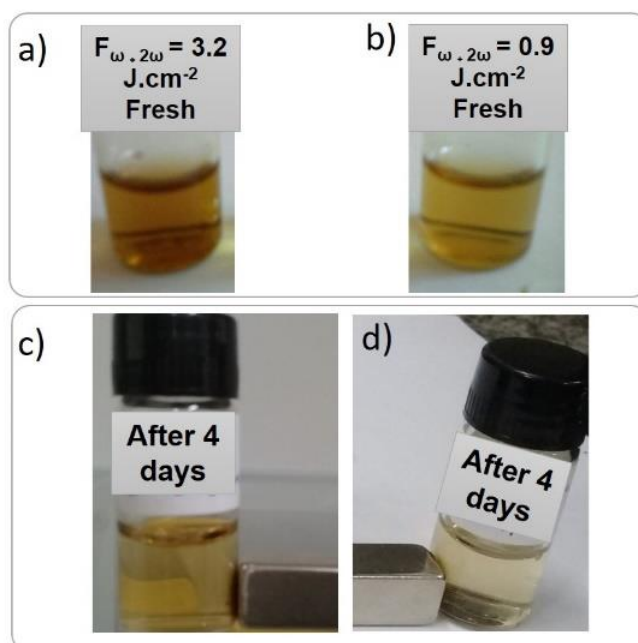


Figure 6.2 Photos of Fe derived nanomaterial synthesized by laser pulses with both ω and 2ω frequency, at $F_{\omega+2\omega} = 0.9 \text{ J/cm}^2$ (left side), and $F_{\omega+2\omega} = 3.2 \text{ J/cm}^2$ (right side) .

(a,b) Fresh nanomaterial. (c,d) After 4 days of magnetization.

In Figure 6.3, we report the temporal evolution of the UV-Vis extinction spectra of the fresh Fe derived nanomaterial synthesized at $F_{\omega+2\omega} = 0.9 \text{ J/cm}^2$ before separation, and of the corresponding $(\text{FeNPs})^{\text{Pr}}$ obtained after 4 days of magnetization.

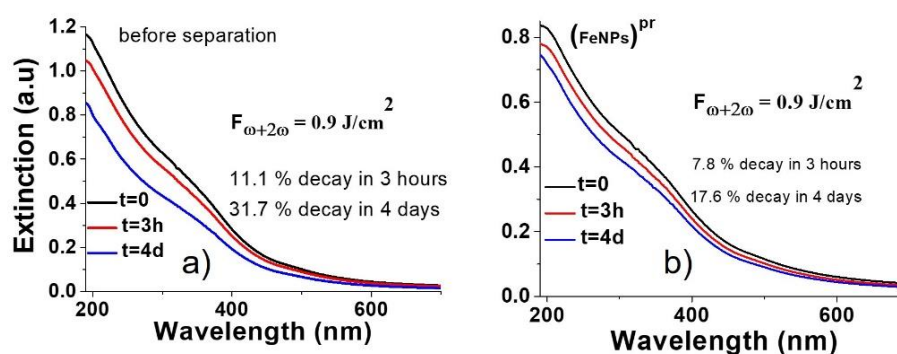


Figure 6.3 Temporal evolution of the UV-Vis extinction spectra of the Fe derived nanomaterial synthesized at $F_{\omega+2\omega} = 0.9 \text{ J/cm}^2$. a) Fresh nanomaterial; b) $(\text{FeNPs})^{\text{Pr}}$ obtained after 4 days of magnetization.

The value of the optical extinction at the wavelength of 350 nm was chosen as indicator of the stability. Interestingly, the $(\text{FeNPs})^{\text{Pr}}$ presented higher stability

in comparison to the fresh Fe derived nanomaterial before separation (coherently with the ζ -potential measurements reported in the next Table 6.1, and similar results were obtained also for the samples synthesized at the higher fluence $F_{\omega+2\omega} = 3.2 \text{ J/cm}^2$.

In order to collect the $(\text{FeNPs})^{\text{SP}}$, the samples obtained after the first 4 days magnetization step (Figure 6.2) were placed more than 10 in the proximity of the magnet. The extinction spectra of $(\text{FeNPe})^{\text{Pr}}$, $(\text{FeNPe})^{\text{SP}}$, and the completely transparent CNM are shown in Figure 6.4. The samples synthesized at the higher fluence, with higher NPs concentration, were selected for this representation, in order to have a clearer and more intense optical signal. It is clearly evident the obtained CNM is characterized, such as the case of CQDs/Au, by two distinct peaks, at the wavelength of 240 nm and 275 nm, respectively. The interpretation of those bands will be discussed later at the end of the section

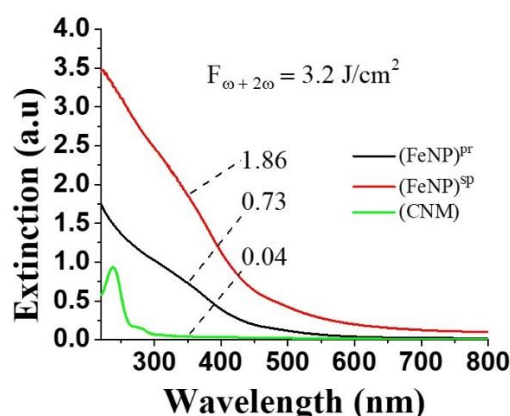


Figure 6.4 UV-Vis extinction of $(\text{FeNP})^{\text{Pr}}$, $(\text{FeNP})^{\text{SP}}$, and transparent CNM obtained by PLA with laser fluence $F_{\omega+2\omega} = 3.2 \text{ J/cm}^2$.

Figure 6.5. shows the change in time of the ζ -potential of the Fe derived nanomaterial before separation, synthesized at different values of the laser fluence. Together, is also reported the value of the ζ -potential of the CNM. The latter is characterized by a negative charge, contrarily to the positive charge of the fresh nanomaterial, which contains the magnetic nanoparticles. After 4 days, a decrease in the ζ -potential of the material before separation is clearly observable (and repeatable over different samples). At the light of the results, we think that during the time the negative charged CNM may migrate by diffusion in the proximity of

the positively charged magnetic nanoparticles, shadowing the overall surface charge. In this sense, the presence of the CNM in the colloidal dispersion may be a source of instability during the time, and its separation should improve the stability of the magnetic NPs. This hypothesis is coherent with the stability results reported in Figure 6.3 where the $(\text{FeNPs})^{\text{PF}}$ show relatively better stability in time if compared to the Fe, derived nanomaterial without any separation.

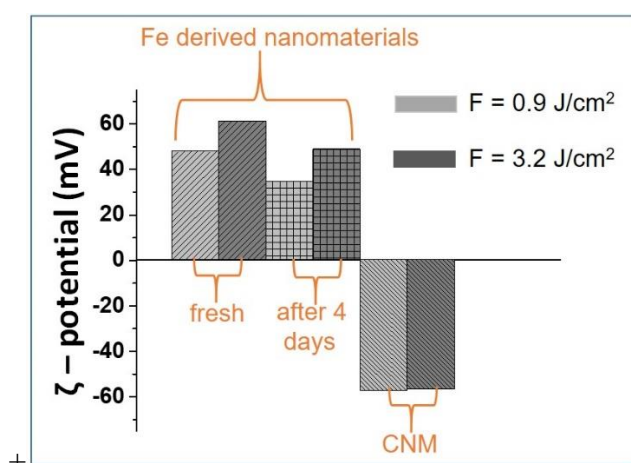


Figure 6.5 ζ -potential of the CNM obtained after separation (negative), and of the fresh and 4 days aged Fe derived nanomaterial before separation (positive). The colors dark and light grey are used for the representation of samples synthesized at $F_{\omega,2\omega} = 3.2 \text{ J/cm}^2$ and $F_{\omega,2\omega} = 0.9 \text{ J/cm}^2$, respectively.

After the separation process described above, both the $(\text{FeNPs})^{\text{PF}}$ and $(\text{FeNPs})^{\text{SP}}$ were characterized by TEM. The results are shown in Figure 6.6. Herein, panels a) and b) show that the value of $F_{\omega+2\omega}$ has a negligibly small effect on the dimension and polydispersivity of the $(\text{FeNPs})^{\text{PF}}$. In both cases, the average diameter $\langle\phi\rangle$ and standard deviation σ is of the order of 4.5 nm and 1.8 nm, respectively. Figure 6.6 (c) shows the TEM image and statistical size distribution of the $(\text{FeNPs})^{\text{SP}}$ obtained at higher fluence. In this case, the average diameter and standard deviation of $(\text{FeNPs})^{\text{SP}}$ are $\langle\phi\rangle = 1.8 \text{ nm}$ and $\sigma = 0.8 \text{ nm}$, respectively.

In literature there is no mention of iron oxide NPs with diameters smaller than $\sim 5 \text{ nm}$ synthesized by PLA in water. Hence, the result obtained for the $(\text{FeNPs})^{\text{SP}}$ represents a breakthrough, which can only be explained on the basis of the unique experimental parameters used in this peculiar synthesis: small volume of liquid, long ablation time of hours, fixed target/pulse relative position, and simultaneous

irradiation by pulses at different frequencies. As will be explained in the next Section 7, one possible key of interpretation is constituted by the synthesis of intermediate organic molecular material, which might reduce the nucleation time of the NPs, with a final reduction of their size [106].

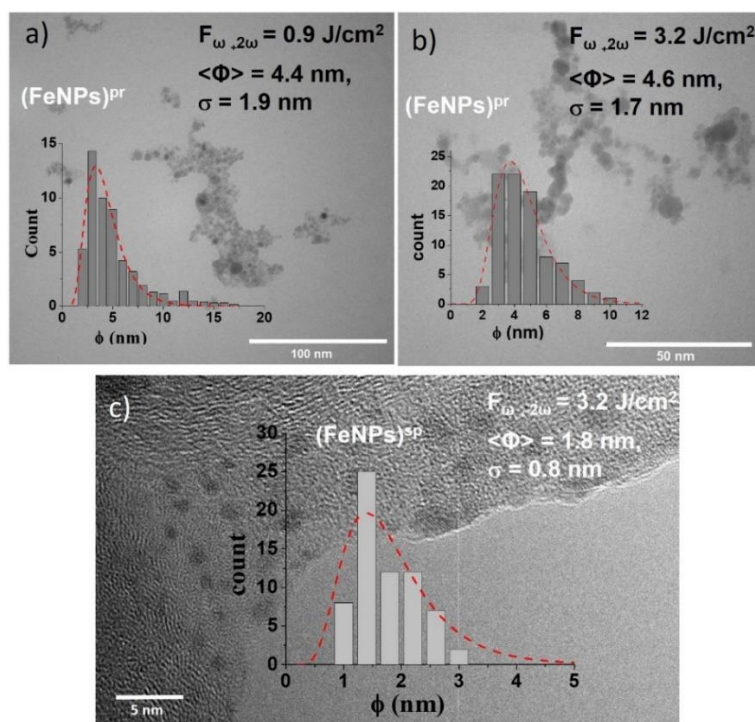


Figure 6.6 TEM images of the $(\text{FeNPs})^{\text{pr}}$ synthesized by a) $F_{\omega+2\omega}=0.9 \text{ J/cm}^2$ and b) $F_{\omega+2\omega}=3.2 \text{ J/cm}^2$. c) TEM image of $(\text{FeNPs})^{\text{sp}}$ synthesized by $F_{\omega+2\omega}=3.2 \text{ J/cm}^2$. The inset in each figure shows the statistical size distribution with LogNormal fit, and the average diameter (ϕ) and standard deviation (σ).

The size of the $(\text{FeNPs})^{\text{pr}}$ was also verified by scanning magnetic microscopy, using the approach reported in [322]. The measurements were performed by Prof. Jefferson Ferraz (Department of Physics of PUC-Rio, *Laboratory of Non Destructive Magnetic Measurements*) using the experimental apparatus described in Section 3.8. The results are shown in Figure 6.7. Herein, the magnetization curves are similar for both the fluence, and demonstrate that the $(\text{FeNPs})^{\text{pr}}$ have superparamagnetic behavior [322]. As we will see in the next sub section, Raman analysis confirm the presence of a majority of magnetite phase in the $(\text{FeNPs})^{\text{pr}}$. In this case, from the analysis of the characteristics of the magnetization curves, it is possible to extract the average size of the magnetic nanoparticles, which was found to be of about 4 nm, in good agreement with the TEM experimental results [322].

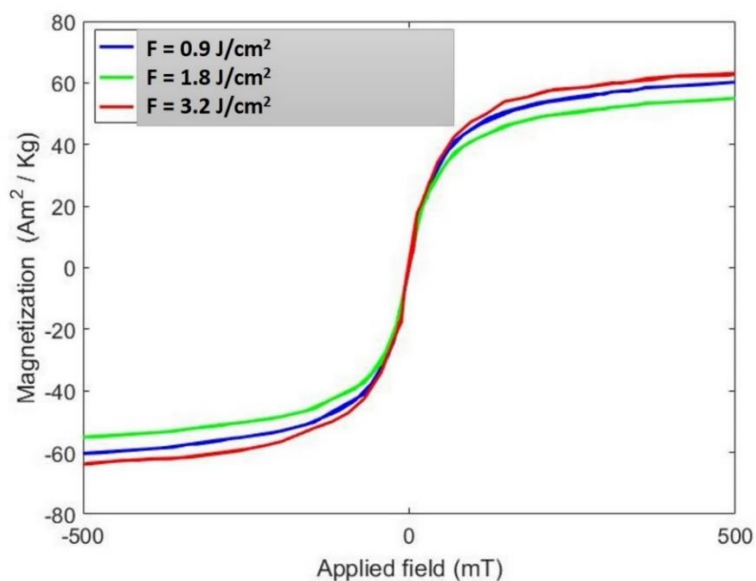


Figure 6.7 Magnetization curves of (FeNPs)^{pr} synthesized at different laser fluence by simultaneous irradiation with ω and 2ω frequency laser pulses.

For clarity, the experimental values measured for the extinction intensity, ζ -potential, TEM size, and metallic iron concentration (C_{Fe}) of the samples before and after the separation, are listed in Table 6.1

Table 6.1 Complete analytical characterization of the different species present in the Fe derived nanomaterial, synthesized at $F_{\omega+2\omega} = 0.9 \text{ J/cm}^2$ and $F_{\omega+2\omega} = 3.2 \text{ J/cm}^2$. The iron concentration of the sample in ppm is indicated as C_{Fe} .

Sample	$F_{\omega,2\omega}$ (J/cm ²)	ζ -potential (mV)	Extinction at 350 (a.u)	C_{Fe} (ppm)	TEM radius (nm) <i>Iron-based NPs</i>
Fe derived nanomaterial (no separation)	3.2	49.0	2.47 <	55	×
	0.9	34.9	1.13 <	31	×
(FeNPs)^{pr}	3.2	×	2.47	×	4.6 ± 1.7
	0.9	×	1.13	×	4.4 ± 1.9
(FeNPs)^{sp}	3.2	×	1.03	×	1.8 ± 0.8
	0.9	×	0.03	×	×
CNM	3.2	-56.7	< 0.04	0.0	×
	0.9	-57.3	< 0.03	0.0	×

6.2.2.

Fe derived nanomaterial synthesized with pulses at single-frequency laser (ω , or 2ω)

For the reasons cited at the end of the previous Section 6.1, the temporal stability, ζ -potential, and magnetization of the Fe derived nanomaterial, has been performed only in the case of the PLA synthesis by simultaneous pulses at ω and 2ω frequency, so that will not be shown in the present section.

The fluence of the ω pulses were set to 2.3 J/cm^2 , which is the same value of the fluence of the component at the fundamental frequency used during the PLA at both frequencies (72% of 3.2 J/cm^2). The fluence of the 2ω pulses were not set at 0.9 J/cm^2 (28% of 3.2 J/cm^2) because, as explained in the previous section, the production rate was too low in order to observe any visible product in the first 2 hours of ablation. Hence, the same value of 2.3 J/cm^2 was also chosen for the PLA performed with the 2ω pulses.

Figure 6.8, reports the comparison of UV-Vis extinction spectra of Fe derived nanomaterial synthesized by different laser pulse frequency (ω , 2ω or $\omega + 2\omega$), considering the values of fluence cited above, and a total ablation time of 120 minutes. The results show that the production rate, which is proportional to the optical extinction, is higher when PLA is performed at the fundamental frequency ω . This result is coherent with the enhanced absorption of both the synthesized NPs and the persistent microbubbles generated during the PLA process in water, which is particularly evident in the UV and visible region of the spectra [106, 142].

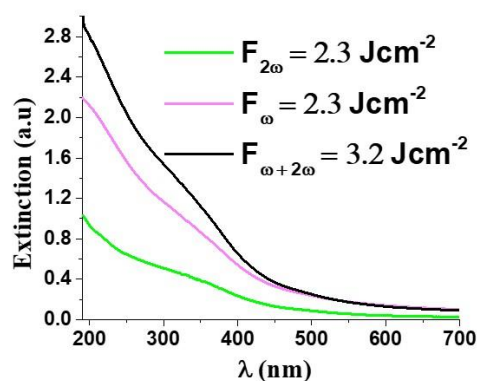


Figure 6.8 Extinction spectra of Fe derived nanomaterial synthesized by pulses with a single frequency (ω or 2ω), and pulses with both frequencies ($\omega + 2\omega$). The total ablation time was 120 minutes.

Figure 6.9 shows instead the photos of the Fe derived nanomaterial before and after the magnetization along 4 days. A comparison has been made considering the synthesis using single frequency (ω or 2ω) or dual frequency (ω and 2ω) laser pulses. To have a good contrast in the photo, the samples synthesized with 2ω laser pulses have been ablated for 8 hours, differently from the 2 hours of ablation performed in the other configurations.

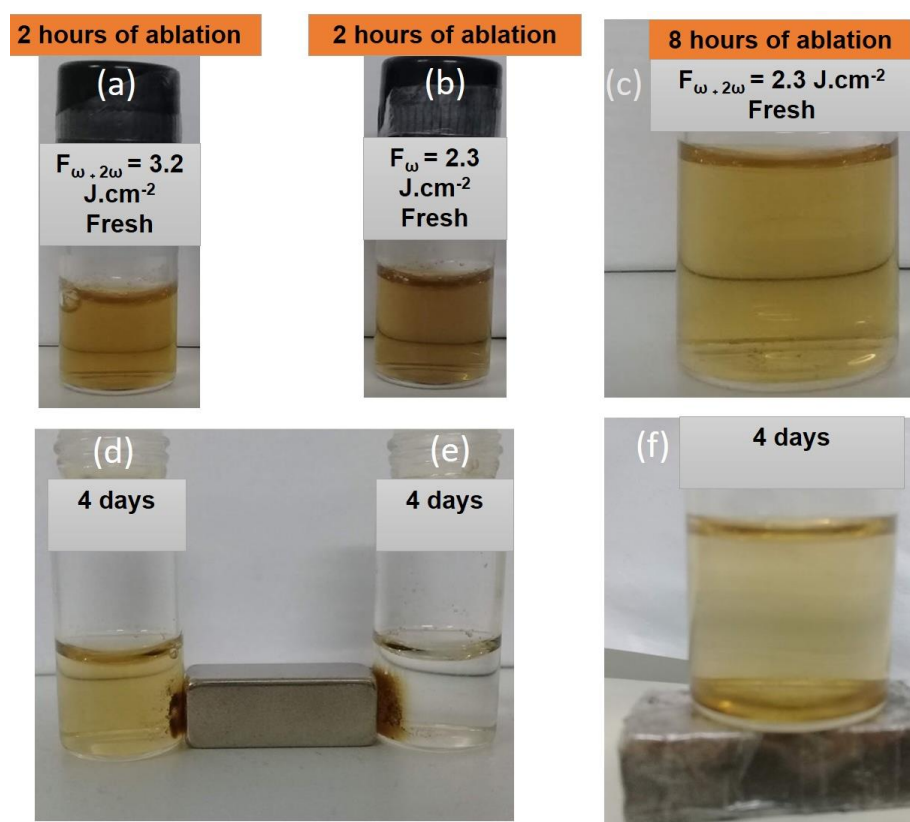


Figure 6.9 Photos of the Fe derived nanomaterial before and after the magnetization along 4 days. A comparison has been made considering the synthesis using single frequency (ω or 2ω) or dual frequency (ω and 2ω) laser pulses. (a,d) $F_{\omega+2\omega} = 3.2$ J/cm²; (b,e) $F_{\omega} = 2.3$ J/cm²; (c,f) $F_{2\omega} = 2.3$ J/cm².

It has been perceived that Fe derived nanomaterials synthesized by ω laser pulses can easily be precipitated with the magnet, and a completely transparent supernatant (without iron oxide NPs) is obtained. In contrast, the Fe derived nanomaterials synthesized by 2ω laser pulses, do not precipitate completely after

this first magnetization step, similarly as for the samples synthesized by dual-frequency laser pulses.

These results are coherent with the literature, which reports that iron oxide nanoparticles synthesized by 2ω , generally presents a minor magnetization than the one synthesized by ω frequency [83], although a clear explication of these observations is not present.

In Figure 6.10 we report the TEM images of both the (FeNPs)^{SP} and (FeNPs)^{PR} synthesized by ω or 2ω laser pulses. As explained before, in the first case it is not possible to obtain any supernatant nanoparticles. Concerning the (FeNPs)^{PR}, we did not observe significant differences in the average size (~ 11 nm) or polydispersity (~ 5 nm) in the function of the frequency of the laser pulses, as shown in panels a) and b). In literature [83], it is reported a significant enhancement in the dimension of the NPs from 7 nm to 17 nm, when ω or 2ω frequency pulses are used, respectively. Anyway, in [84], the laser pulse fluences are about one order of magnitude higher than the typical fluences used in the present research, so that a strict comparison cannot be done. Moreover, we highlight again the unique experimental parameters of the PLA process we propose (fixed target/pulse relative position, a small volume of water, large ablation time of hours) which, to the best of our knowledge, have never been experimented before, also for the case of Fe target.

Figure 6.10 (c), reports the TEM image and size distribution of the (FeNPs)^{SP} for which, similarly to the case of dual-frequency irradiation, smaller sizes are obtained, with an average diameter of about 6.0 nm, and a deviation standard of 1.6 nm.

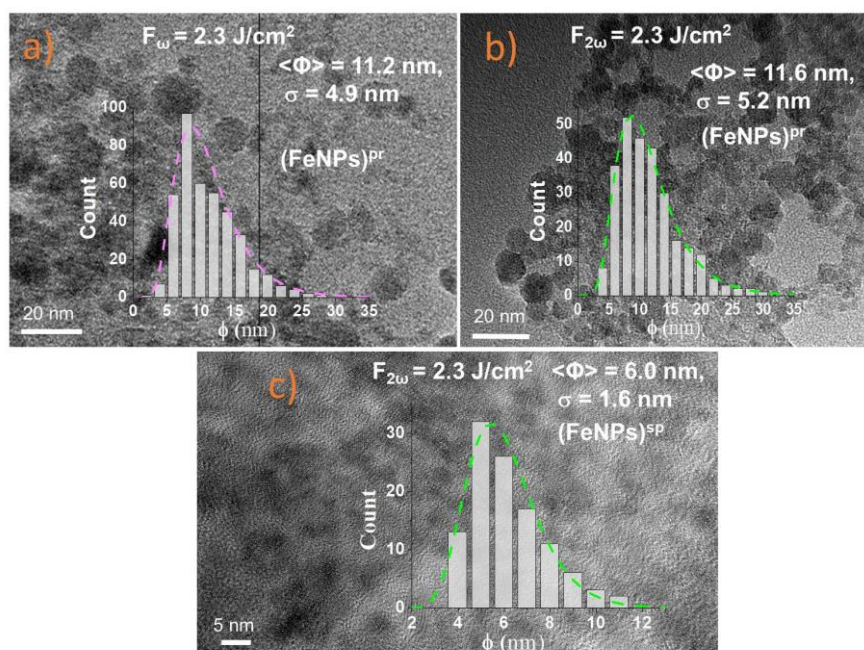


Figure 6.10 TEM images of the of : a) (FeNPs)^{pr} synthesized by $F_{\omega} = 2.3 \text{ J/cm}^2$; b) (FeNPs)^{pr} synthesized by $F_{2\omega} = 3.2 \text{ J/cm}^2$; c) (FeNPs)^{sp} synthesized by $F_{2\omega} = 3.2 \text{ J/cm}^2$. The inset in each figure shows the statistical size distribution with LogNormal fit, the average diameter (ϕ) and standard deviation (σ).

6.3.

Raman, FTIR, and XPS of iron oxide-based nanoparticles and carbon nanomaterial derived from Fe target

6.3.1.

Raman spectroscopy of Fe derived nanomaterial

The preparation of the samples for Raman measurement and the experimental conditions used for the characterization are explained in detail in Section 3.4.1. For the moment, Raman measurements were only performed in powder form, on the samples synthesized by simultaneous irradiation at both ω and 2ω frequency, by the collaboration with Prof. Gino Mariotto of the University of Verona. The measurements are shown in Figure 6.11.

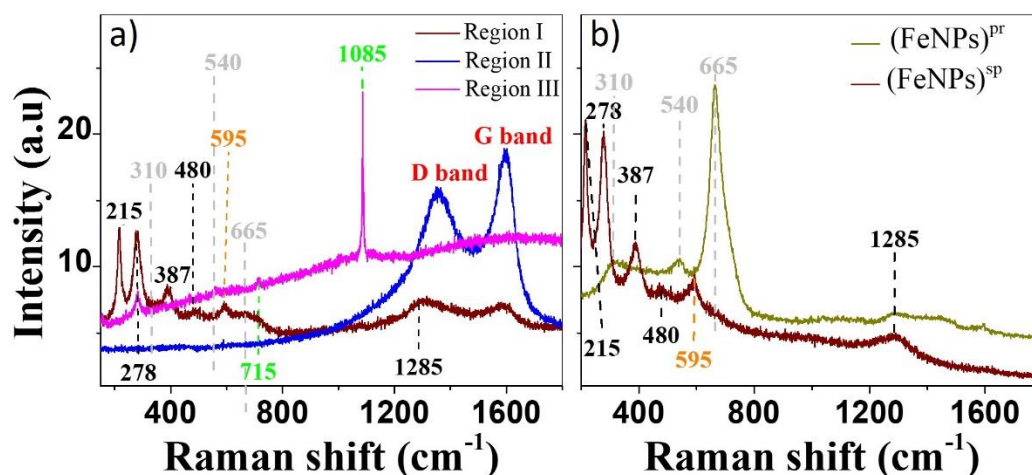


Figure 6.11 Typical Raman spectra of the colloidal dispersion of Fe derived nanomaterial a) before separation; b) after separation, on the corresponding (FeNPs)^{pr} and (FeNPs)^{sp}. The measurements of the panel a) are relative to three different regions of the samples, indicated as I, II, and III.

Herein, we identified four different phases of iron oxide: i) magnetite (Fe₃O₄), ii) hematite (Fe₂O₃), iii) wüstite (FeO), and iii) siderite (FeCO₃). The siderite is very rare in the sample, while hematite, wüstite, and magnetite are the most abundant oxides. With the exclusion of siderite which, to the best of our knowledge, has never been detected before of the present research, the other oxides are typically found as the product of the PLA of iron targets in pure water [83, 378].

To easily identify the Raman peaks of the different constituents, they are specified by different colors: gray for magnetite, red for the D and G bands of the CNM, green for siderite, black for hematite, and orange for wüstite.

Figure 6.11 (a) represents the Raman spectra of the fresh Fe derived nanomaterial before separation, on three different regions of the samples, denoted as I, II, and III. Figure 6.11 (b) shows instead the Raman spectra of both of (FeNPs)^{pr} and (FeNPs)^{sp} after separation.

Magnetite has a spinel structure belonging to space group O_h⁷, and according to group theory gives rise to five Raman modes: three T_{2g}, one E_g, and one A_{1g} [379–382]. Three of these modes are observed in the spectrum of Fe derived nanomaterial before separation and (FeNPs)^{pr} after separation: the strongest peak at about 665 cm⁻¹, identified as the A_{1g} mode, corresponds to the stretching vibrations of the

oxygen atoms along with the Fe-O bonds, while the weaker bands near to 540 cm^{-1} and 310 cm^{-1} are associated to one T_{1g} and to E_{2g} modes, respectively [383].

The peaks near 1085 cm^{-1} and 715 cm^{-1} are associated with siderite [384–386], and have been observed rarely, and uniquely in the samples before the separation shown Figure 6.11 a). At this stage, it is not clear the reason why siderite is not observed in the $(\text{FeNPs})^{\text{SP}}$ or the CNM, and we suppose that part of it, already in a very low concentration before the separation, may be lost during the different separation steps. The strong and sharp peak exactly at 1085 cm^{-1} represents the CO_3 band of siderite, associated with the symmetric stretching internal mode ν_1 . The peak located at 715 cm^{-1} is instead caused by in-plane bending internal mod ν_{4c} .

The peaks at 215 cm^{-1} , 278 cm^{-1} , 387 cm^{-1} , 480 cm^{-1} and 1285 cm^{-1} , are typical of hematite phase of iron oxide [84, 100, 381]. The bands at 215 cm^{-1} and 480 cm^{-1} correspond to A_{1g} mode [385], while the peaks at 282 cm^{-1} and 592 cm^{-1} are related to E_g mode of hematite[196]. Finally, the peak at 595 cm^{-1} is related to the wüstite [379, 387].

From the Raman analysis reported above, it seems that before the separation the colloidal dispersion is constituted by magnetite, hematite, siderite, wüstite, amorphous carbon-based material with clear D and G bands, and minimal traces of siderite. After the separation process (4 days of magnetization), $(\text{FeNPs})^{\text{Pr}}$ are principally constituted by magnetite, although a small signal associated with hematite may be observed. $(\text{FeNPs})^{\text{SP}}$ instead, have majority of hematite, and a small portion of wüstite.

6.3.2.

Magnetite to hematite conversion by laser irradiation in Raman spectroscopy

In Figure 6.12, the Raman spectra of $(\text{FeNPs})^{\text{Pr}}$ measured at different laser irradiation power is represented. It has been observed that $(\text{FeNPs})^{\text{Pr}}$, principally constituted by magnetite phase, are very sensitive to irradiation laser during the measurement of Raman spectra, and magnetite may be converted to relatively more

stable hematite nanoparticles [382], whenever the laser power is raised above than 10^{-2} kW/mm².

These results point to a photocatalytic activity of the semiconductor iron nanoparticles, probably inducing a reaction between the magnetite NPs, and the ambient CO₂ and H₂O molecules adsorbed on the nanostructured powders.

In order to draw a solid conclusion, further measurements are needed, for example performing Raman spectroscopy during the flow of a controlled CO₂ flux over the samples.

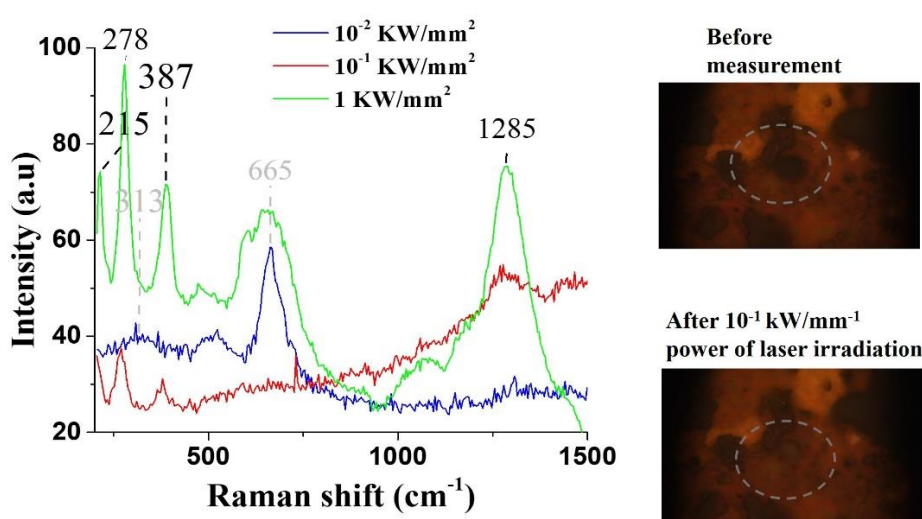


Figure 6.12 Raman spectra of (FeNPs)^{pr} synthesized by $F_{\omega, 2\omega} = 0.9$ J/cm², and excited by a laser irradiance of 10^{-2} kW/mm² (blue line), 10^{-1} kW/mm² (red line) and 1 kW/mm² (green line). The right side photos, show the measurement regions before and after the irradiation. The Raman spectra were excited at the wavelength of 638 nm.

6.3.3.

FTIR and XPS analysis on the Fe derived nanomaterial

Further surface characterization of the samples was obtained by both XPS and FTIR spectroscopies.

Figure 6.13 (a) shows the FTIR spectra of both fresh Fe derived nanomaterial, (FeNPs)^{sp} and CNM synthesized by green (2ω) laser pulses. We do not show the results relative to the sample obtained by dual-frequency ablation, since the results were completely equivalent. The two absorptions near 530 - 548 cm⁻¹ and 435 cm⁻¹

are attributed to the vibration of Fe-O in Fe_3O_4 and Fe_2O_3 [388–390], and are present in both the fresh Fe derived nanomaterial and $(\text{FeNPs})^{\text{SP}}$. The small peak at 874 cm^{-1} , may be associated to the carbonate in the FeCO_3 NPs, representing stretching vibrations of the D_{3h} symmetry [390], supporting the existence of siderite, coherently with the Raman spectra.

Figure 6.13 (b), is reported the comparison of the FTIR spectra of the CQDs/Au and the carbon nanomaterial (CNM) obtained by the iron target. The spectra are identical so that similar carbon structures (at least in terms of surface chemistry) are expected to be synthesized by both Au and Fe target. Hence, for the interpretation of the spectra, we send back the reader to Section 4.4.

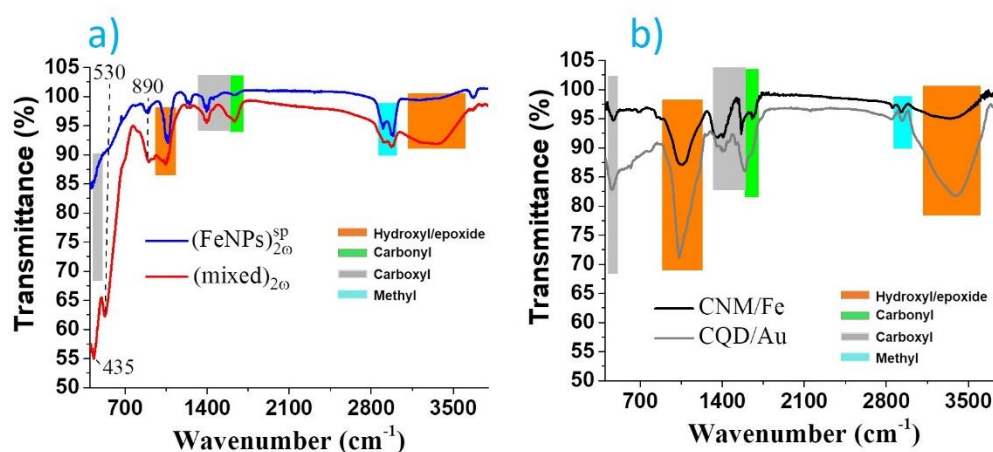


Figure 6.13 a) FTIR spectra of fresh Fe derived nanomaterial, $(\text{FeNPs})^{\text{SP}}$, and CNM synthesized by 2ω laser pulses. b) Comparison between the FTIR spectra of the CQDs/Au (gray) and the CNM obtained by PLA of iron (black).

A full energy survey XPS spectra of both $(\text{FeNPs})^{\text{PR}}$ and $(\text{FeNPs})^{\text{SP}}$ synthesized by dual-frequency laser pulses is shown in Figure 6.14, confirming that Fe and O are the principal constituents of the samples. In Figure 6.15 (a,b), are instead reported the XPS spectra in the Fe2p and O1s regions, respectively.

For both $(\text{FeNPs})^{\text{PR}}$ and $(\text{FeNPs})^{\text{SP}}$, two strong peaks of Fe $2p_{3/2}$ at 710.6 eV and Fe $2p_{1/2}$ at 724.4 eV have been observed [391], together with two satellite peaks at 717.7 eV and 732.6 eV [391]. In the O1s region, we detected the peaks of lattice oxygen (Fe-O, 529.9 eV) and surface hydroxyl (-OH, 531.9 eV) [391]. The

XPS spectra, in both Fe2p and O1s regions, may be associated to the presence of both hematite, magnetite, and Fe-O [391].

As expected, no significant differences have been observed between the (FeNPs)^{pr} and (FeNPs)^{sp} spectra, but a slightly higher concentration of surface hydroxyl (-OH, 531.9 eV) in (FeNPs)^{pr}.

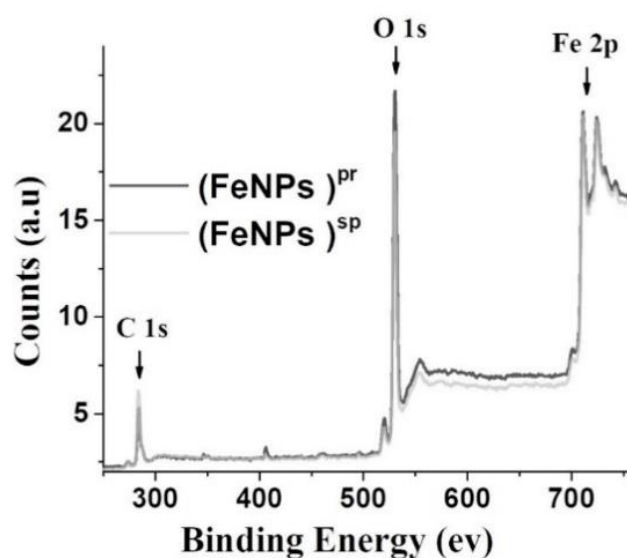


Figure 6.14 XPS survey spectra of (FeNPs)^{pr} and (FeNPs)^{sp} synthesized by dual frequency laser pulses ($\omega+2\omega$).

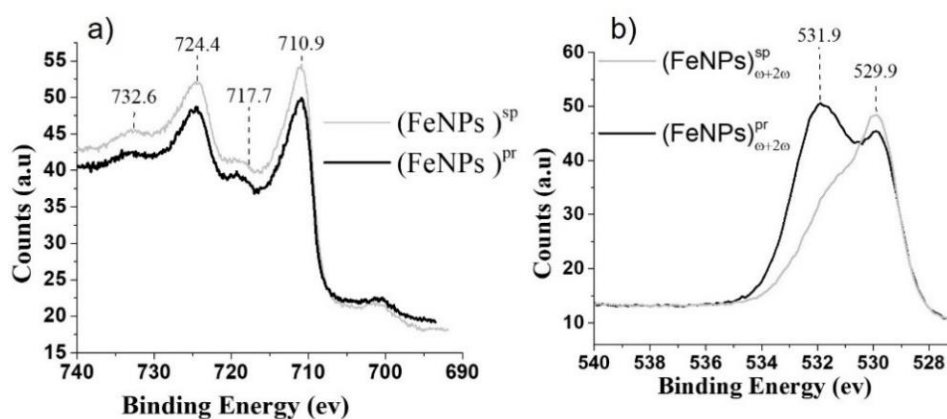


Figure 6.15 XPS spectrum in the a) Fe2p and b) O1s regions of both (FeNPs)^{pr} and (FeNPs)^{sp} synthesized by dual frequency laser pulses ($\omega+2\omega$).

6.4.

PL of the CQDs obtained by CO₂/C with Fe target

A clear PL emission has been observed in the transparent solution obtained from Fe derived nanomaterial after separation, even without the use of CO₂ carriers (NaOH) in the water.

Figure 6.16 a) shows the absorption band and PL of CNM synthesized by using simultaneously both green and infrared ($2\omega+\omega$) laser pulses and separated by the magnetization procedure reported in Figure 6.1. Concerning the absorption spectra, we observe the $\pi-\pi^*$ and $n-\pi^*$ transitions at 240 nm and 275 nm [351, 352], respectively, similarly to the case of the Au derived CQDs. What is peculiar, is a strong PL peak centered at 325 nm, without any emission in the blue region, which is detected only for the samples obtained by single-frequency pulses (ω or 2ω), as shown in Figure 6.16 b) and c), respectively. For these last samples (ω or 2ω), the final separation was obtained by magnetization followed by heating. The emission peak of CQDs/Fe synthesized by ω pulses is in the same position as in CQDs/Au (see Section 4.5.1), but the emission of the CQDs/Fe obtained by 2ω pulses is 25 nm blue-shifted, as shown in Figure 6.16 c).

One possible reason for the differences observed in the PL spectra might be the size of the CQDs, which were not analyzed by TEM in the case of Fe, because of the limited disposability of the proper infrastructure during the final part of the experimental work of the present thesis. A second possibility might be that the UV emission is effectively overlapped with a less intense PL in the blue region, preventing its final detection.

In order to exclude the possible influence of the heating step, applied only for the separation of the ω or 2ω samples, the measurements should be repeated, applying, for all the samples the same separation technique. Anyway, we put in evidence that in the case of the CQDs synthesized from the Au target, we observed no difference in the PL emission depending on the different frequency of the laser pulses used during PLA, or the separation techniques (including the heating process).

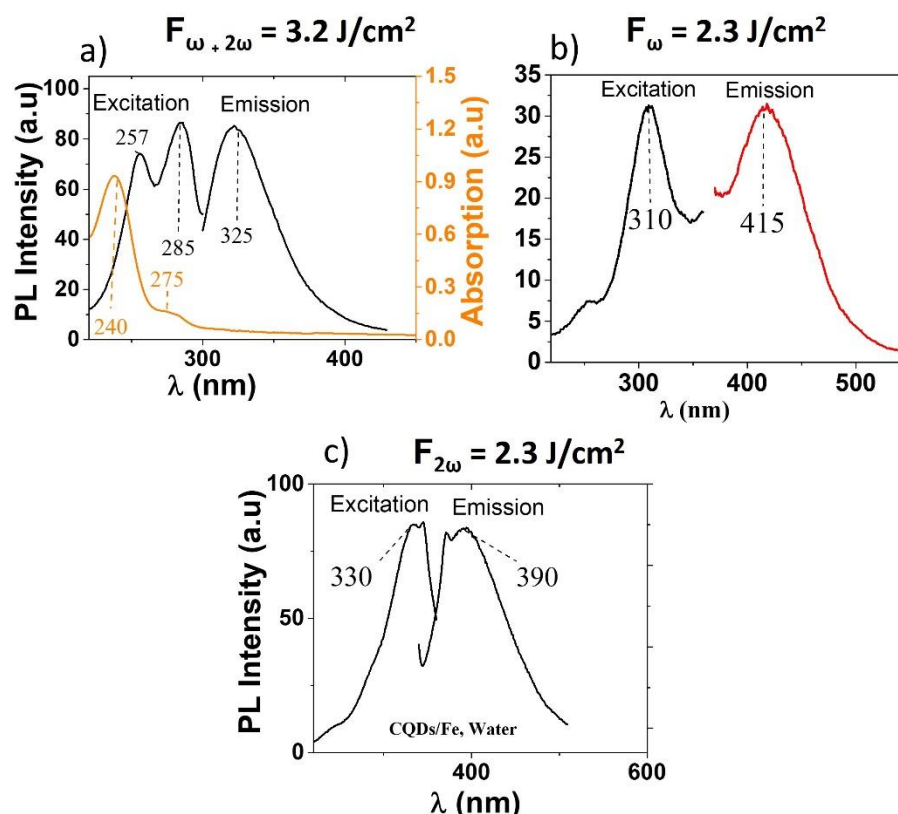


Figure 6.16 a) PL, excitation (black curves) and extinction (orange curve) spectra of the CQDs/Fe in the UV region. The CQDs were synthesized at $F_{\omega,2\omega} = 3.2 \text{ J/cm}^2$, and separated by magnetization. PL and excitation spectra of the CQDs/Fe, synthesized at laser pulse frequency ω b) or 2ω c), and separated by heating.

The physical or chemical origin of the strong UV luminescence, is hence controversial at the moment, and further measurements are needed in order get a better understanding. Here we point out again, that these special features are present only for the samples synthesized by simultaneous irradiation with pulses at both ω and 2ω frequency. As will be explained in the next Section 7, one possible key of interpretation is constituted by the synthesis of intermediate organic molecular material, which might reduce the nucleation time of the NPs, with a final reduction of their size [106].

6.5. Conclusion

Differently from all literature available at the moment on the ligand-free PLA of iron target in water, we observe the simultaneous synthesis of iron oxide NPs

together with carbon based material. The latter is identified after a proper separation of the metal oxide content, performed using a simple and low cost magnetization procedure. The PLA in water has been performed not only by irradiation of laser pulses at the fundamental (ω) or second harmonic frequency (2ω), but also by the simultaneous irradiation of ω and 2ω frequency laser pulses. In the latter case, unique results were obtained, both in terms of dimension of the resulting magnetic nanoparticles NPs and also in term of the PL spectra of the associated transparent carbon-based material. In fact, after the separation, the remaining liquid is transparent and characterized by absorption spectra similar to the one characteristic of the CQDs obtained from the Au target. The transparent water dispersion also presents photoluminescence, whose emission spectra can be roughly tuned from the UV (~ 325 nm) to the blue region (390 nm – 415 nm), depending on the laser parameters used during the PLA process. Due to the limited access to the experimental infrastructure imposed by the pandemic COVID-19 virus, it was not possible to perform TEM images of the CQDs and measure their quantum yield (QY). Their presence was hence confirmed at the moment by both PL and Raman spectroscopy. In the latter case, the Raman signal of the D and G bands of amorphous carbon was detected on the Fe derived nanomaterial before the separations process. Due to the small quantity of carbon nanomaterial synthesized by CO_2/C reduction, we were not able, at the moment, to obtain a significant Raman response from the carbon material obtained after the separation process. For this reason, it is in project the accumulation of a considerable amount of Fe derived nanomaterial (about 200 ml), which we consider sufficient to obtain a Raman response of the samples after the separation of the metal species. The physical origin of these structures, and a possible mechanism of the CO_2/C reduction induced by the PLA process, will be presented in the next Section 7.

The separation process we adopted, allows in general the separation of magnetic nanoparticles which respond with different efficiency to magnetization, which have been called as $(\text{FeNPs})^{\text{pr}}$ and $(\text{FeNPs})^{\text{sp}}$. The $(\text{FeNPs})^{\text{pr}}$ have a ‘fast’ response to the magnet used for the separation, precipitating completely after 4 days of magnetization, while the $(\text{FeNPs})^{\text{sp}}$ need a second magnetization step in order to be collected.

There is no difference in the dimension of the (FeNPs)^{PF} synthesized using laser pulses at the ω or 2ω frequencies, which have an average diameter of about 11 nm. Using the dual-frequency laser pulse irradiation (ω and 2ω simultaneously) we obtain instead smaller (FeNPs)^{PF}, with an average diameter of 4.5 nm.

Similar behavior is observed also for the (FeNPs)^{SP}. The latter, are obtained only when PLA is performed using 2ω pulses, or by the simultaneous irradiation with pulses at both ω and 2ω frequencies. TEM images show that the (FeNPs)^{SP}, when existing, are smaller than the (FeNPs)^{PF} counterparts. We obtain in fact average diameters of 6 nm when using 2ω pulses, while ultrasmall NPs with the average diameter of 1.8 nm are obtained by simultaneous irradiation with pulses at both frequencies.

As discussed along with the presentation of the experimental results, it is hard to try to make comparisons with the actual literature. In fact, to the best of our knowledge, it is the first time that PLA has been performed using the unique experimental conditions we propose (a small quantity of water, fixed target/pulse relative position, large ablation time).

The typical dimension of iron oxide NPs synthesized by PLA in pure water is between 10 nm and 20 nm [106], and a significant enhancement in the dimension of the NPs is observed when ω or 2ω frequency pulses are used, respectively [83]. To the best of our knowledge, the lowest value reported in the literature for the dimensions of iron oxide NPs synthesized by PLA in deionized water is around 5 nm and has been obtained using low energy pulses at the fundamental frequency (fluence is not reported) in a volume of 10 ml, with a total time of ablation of 180 minutes [392].

Due to the limited access to the experimental infrastructure in the last months of the research, the phases of the iron oxide NPs have been investigated by Raman spectroscopy only in the case of (FeNPs)^{PF} and (FeNPs)^{SP} synthesized by dual frequency laser pulses (ω and 2ω simultaneously). In the (FeNPs)^{PF}, we identified four different phases of iron oxide: i) magnetite (Fe_3O_4), ii) hematite (Fe_2O_3), iii) wüstite (FeO), and iii) siderite (FeCO_3). The siderite is very rare in the sample, while hematite, wüstite, and magnetite are the most abundant oxides. With the exclusion of siderite which, to the best of our knowledge, has never been detected

before of the present research, the other oxides are typically found as a product of the PLA of iron targets in pure water [83, 378]. The $(\text{FeNPs})^{\text{SP}}$ are instead principally constituted by the hematite phase. The Raman characterization of the $(\text{FeNPs})^{\text{PF}}$ and $(\text{FeNPs})^{\text{SP}}$ synthesized by single-frequency laser pulses (ω or 2ω) will be completed as soon as the infrastructure will be available.

Figure 6.17 report a scheme representing the different ‘phase’ regions of the PLA environment (similarly as in the theoretical Section 2), together with all the principal iron oxide and carbon-based materials observed during PLA of Fe targets.

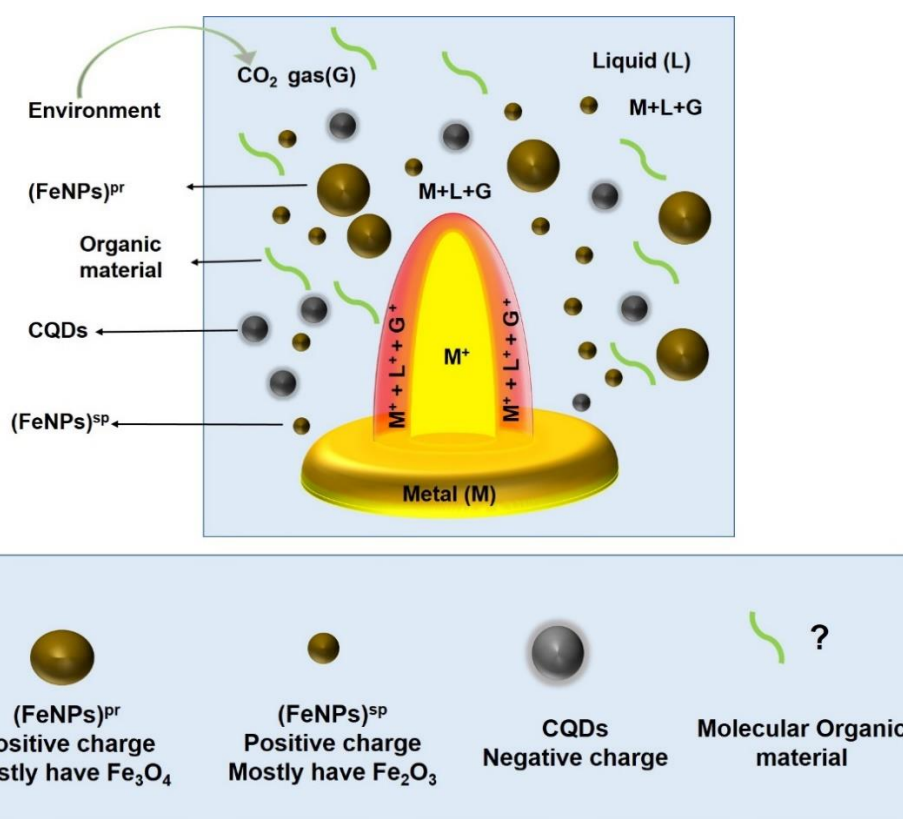


Figure 6.17 Schematic diagram representing the different ‘phase’ regions present in the PLA environment, together with all the materials synthesized during CO_2/C reduction by the use of Fe target. An interrogation point has been placed aside the symbol of the molecular organic material since its presence has still to be detected.

An interrogation point has been placed aside the symbol of the molecular organic material since its presence has still to be detected. As described in the *Conclusions Section*, the eventual presence of the molecular organic material will be investigated by the group of Prof. Stephan Barcowski (University of Duisburg-Essen), which

is an active collaborator in the presented research. The conceptual basis which sustains the hypothesis on the presence of the molecular organic material also in the case of PLA of Fe target will be clearer in the next chapter and are essentially based on the catalytic properties of the synthesized metal oxide nanoparticles. In fact, the catalytic activity of the (FeNPs)^{pr} has been observed during their Raman investigation in ambient conditions, at optical irradiance higher than 10^{-2} kW/mm², where the magnetite NPs readily transform their phases in hematite. It is based on the photocatalytic activity of the pre-formed NPs that we sustain the synthesis of molecular organic material during the PLA, which might be responsible for the small dimension of the nanoparticles we synthesized. In fact, the presence of some organic materials such as polyvinyl alcohol (PVA) [106], or N-(phosphonomethyl) iminodiacetic acid (PMIDA) [393], is responsible for the change of the nucleation time of the NPs, so that NPs with the dimension of the order of 5 nm, or even FeO_x clusters may be synthesized.

In this scenario, the simultaneous synthesis of the molecular organic material might explain the smaller dimension of the (FeNP)^{sp} synthesized by dual-frequency (ω and 2ω simultaneously) or single frequency 2ω laser pulses. In fact, the absorption of the metal oxide NPs is higher in the visible region than in the infrared and might enhance the production rate of the carbon-based materials obtained by the CO₂ reduction process. The same concept might be applied to explain the PL in the UV spectrum observed for the CQDs obtained by PLA of the Fe target by simultaneous ω and 2ω frequency pulses.

7 Our hypothesis on the CO₂/C reduction induced by PLA in water

7.1. Evidence of the catalytic activity of the NPs synthesized by PLA of transition metal target in the water

Three main direct experimental observations point to a catalytic activity of the NPs we synthesized by PLA of transition metal targets (Au, Ag, Fe) in water. The first is the magnetite to hematite photocatalytic conversion observed by laser irradiation with an irradiance higher than 10^{-2} kW/mm² in the Raman investigation of the Fe derived nanomaterial. The second, is the detection by SERS of the carbon monoxide (CO) adsorbed on the Au derived nanomaterial, and molecular organic material adsorbed on both the noble metals NPs (Au, Ag). The third is the final synthesis of solid carbon nanomaterial which has been observed, at the moment, in the form of CQDs and carbynoid nanocrystals supported by noble metal nanoparticles.

Synthesis of carbon nanomaterials by PLA in organic solvent without solid carbon target is not new. While carbynoid NWs supported by AuNPs have been recently synthesized by PLA of Au target in ethanol, the ablation in methanol, toluene, hexane or acetonitrile, gives rise to sp² carbon structures [394, 395]. Hence, the intermediate reduction of CO₂ to particular organic solvents seems to be a key factor for the synthesis of the carbon nanomaterial. In most of the investigation reported literature, it is not clear what is the precise mechanism leading to the condensation of the C_n ‘carbon units’, and the results are interpreted in terms of pyrolysis. Only in the research of *Pan et al.*[40], the formation of carbon sp hybridized nanomaterial in ethanol is explained by the formation of Au-H intermediate, followed by alcohol dehydrogenation with final formation of polyynes like C₂ units. Following the same building concept, in the light of the few experimental results reported in the literature, different small C_n units such as acetylene (C₂H₂), ethylene (C₂H₄), benzene (C₆H₆), hexane (C₆H₁₄) are expected to

be part of the list of possible precursors leading to condensation into sp^2 luminescent nanoparticles [394, 395].

In BECCS experiments conducted by electro-chemical cells, different spectroscopies, including SERS, may be coupled with traditional voltammetry to trace the final and intermediate products of the redox processes, both in liquid and gas phase [21, 35, 116]. SERS spectroscopy on both Ag and Au derived nanomaterial in form of nanoislands is a powerful tool for the detection of absorbed analysts [20, 39, 209, 396], and we underline again that the spectra reported in Figure 7.1 are characterized by the same molecular fingerprint for the two noble metals.

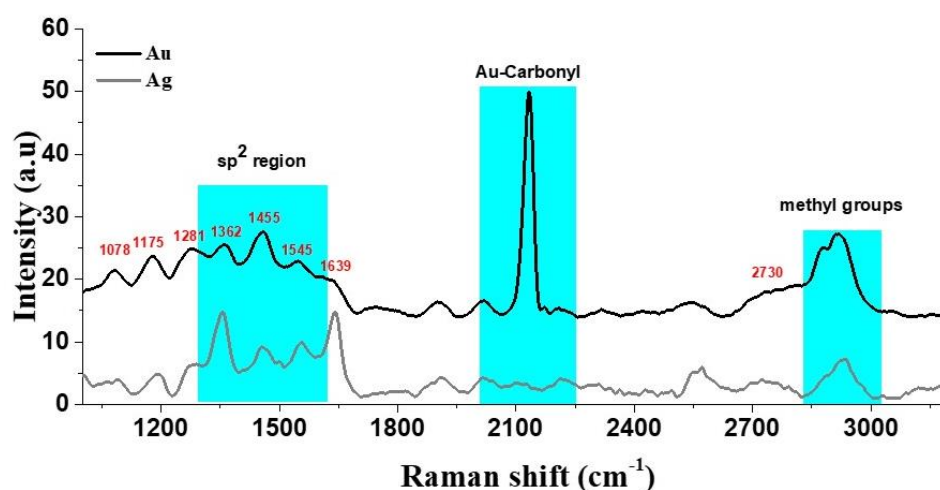


Figure 7.1 Details of the SERS spectra of the Au and Ag derived nanomaterial in powder form. All the Raman modes indicated in the figure are common to both the spectra. The measurements have been performed at the excitation wavelength of 638 nm, in low irradiation conditions (10^{-2} kW/mm²).

The SERS spectra above, are reported starting from the frequency of 1000 cm^{-1} , since the low-frequency modes are generally of difficult interpretation, being associated to the vibrations of the metal cores of the NPs complexed with oxygen species. In Table 7.1 we report the list of the molecular vibrations indicated in Figure 7.1 together with their corresponding Raman shift and interpretation. The frequencies of the Raman modes, coincide with the overlap of the multiple SERS spectra reported in [397], where AgNPs are used for the photochemical CO_2RR , where carbonate, bicarbonates, format and formic acid, are found as final possible stable products.

Table 7.1 Vibrational assignment of the molecular vibrations detected in the SERS spectra of Au and Ag based nanomaterial in powder form. The references for the frequency of the Raman modes on AgNPs are taken from [397]. The symbols used for the assignment of the Raman mode are: ν_s (symmetric stretching), ν_{as} (antisymmetric stretching), ω (wagging), and ρ (rocking).

Raman Mode Species	Raman shift (cm^{-1})
ν_s OCO / ν_s COH CO₃²⁻ / HCOOC	1078
ω CH HCOO⁻	1175
ρ OH HCOOC	1281
ρ CH HCOO⁻	1363
ν_s OCO HCOO⁻	1454
ν_{as} OCO CO₃²⁻	1541
ν_{as} OCO HCOO⁻	1639
ν CH, (ν_s OCO + ρ CH) HCOO⁻	2730, 2810

Despite the good matching between our experimental SERS spectra and the results reported in [397], we cannot exclude the formation of other carboxylic acids different from format (i.e lactate, acetic acid), and the results should be confirmed by a conclusive analytic investigation by liquid chromatography. The last, will be performed on the nanomaterials obtained by PLA of Au and Fe targets by the groups of Prof. Stephan Barcikowski and Prof. Torsten Schmidt from the University of Duisburg-Essen (Germany), through a new established collaboration.

Anyway, the actual results, offer us the possibility to speculate about the origin of the carbynoid nanostructures. Once at the surface of the noble MeNP, and with the increase of the CO₂ concentration as the pH increases, the formic acid molecules can interact and proceed with hydrogen and oxygen eliminations after which, according to Pan *et al.* [40], triple carbon-carbon bond can be formed.

Figure 7.2 shows the catalytic mechanism proposed by the group of Prof. Walter Azevedo from the *Department of Fundamental Chemistry* of UFPE. It

explains the possible formation of sp-hybridized material from for the polymerization reaction of formic acid initialized by the radical specie H , the latter produced by the cavitation process due to the laser ablation of the target. After initialization, the radical reaction proceeds by alternated carbon radical attack and hydrogen elimination. At the last carbon, there isn't other formic acids to react, and this carbon reacts again with the adjacent carbon and form alternated oxygen-oxygen bonds, similarly to Wittig-type reactions [398]. This process continues eliminating oxygen and forming carbene, with the final synthesis of noble metal-carbynoid NCs. The presented process may explain the formation of noble-metal/carbynoid nanocrystals, in the case the future liquid chromatography measurements do not detect the presence of ethanol in the colloidal dispersion after PLA.

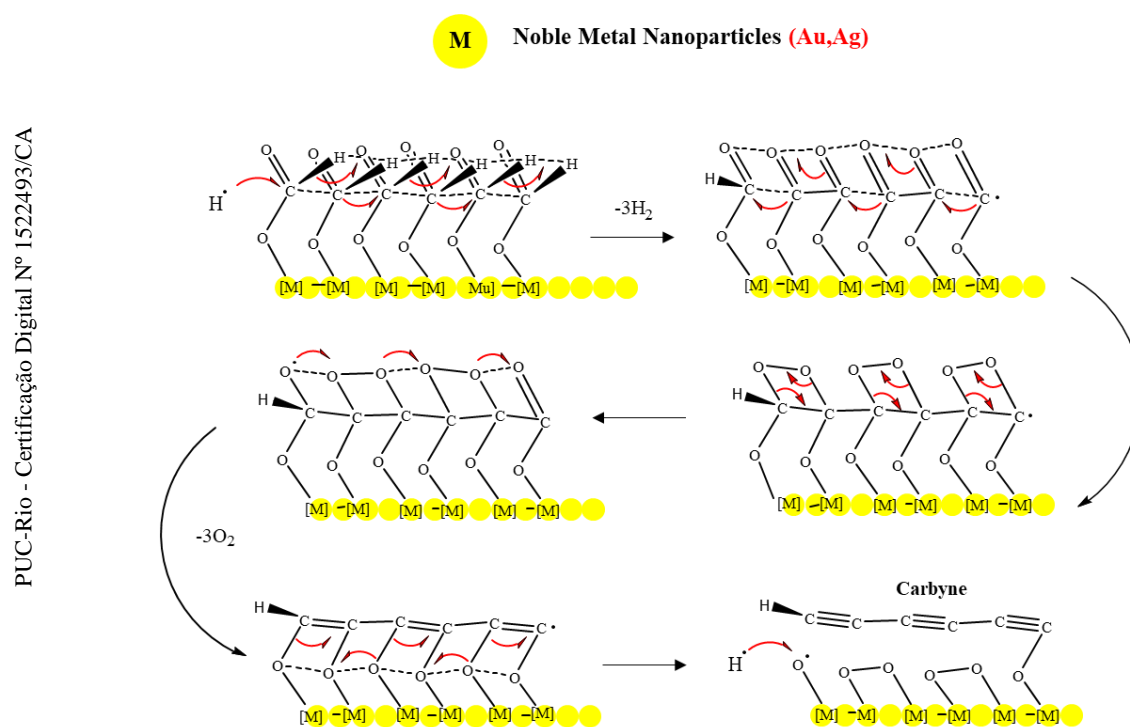


Figure 7.2 Radical polymerization mechanism of formic acid on the noble metal nanoparticle surface forming metal-carbynoid complexes.

From a general point of view, the reactant mixture constituted by the CO₂ and the strong H₂ and H• reducing agents produced by water decomposition during PLA of metal targets [32, 33, 181], represents an ideal environment for the synthesis of alcohol or hydrocarbons by redox processes [399–402]. Although the collective

plasma oscillations of the MeNPs drive different photocatalytic CO₂RR to hydrocarbons building units (C₂, C₃) and methanol [30, 71, 397], we rule out a key role of the LSPR excitation in the synthesis process of the carbon nanostructures. In fact, the LSPR band of Ag is not excited by the wavelength of 532 nm, control measurements by ablation of Au target using pulses at the wavelength of 1064 nm indicate that emissive carbon nanomaterial is still synthesized, and most of all Fe based NPs do not show any plasmonic resonance.

An interesting aspect, peculiar and common of MeNPs produced by PLA in water, is instead the coexistence of metal species in different oxidation states [32], with the possible formation of hybrid metal-oxide interfaces in the case of noble metals. Ag and Au are often used in noble-Me/MeO interfaces to obtain both water-splitting [95, 111] and CO₂RR by heterogeneous catalysis, with hydroformylation and production of different organic solvents depending on the H₂ content [403–405].

In our case, HRTEM images of both Au and Ag derived nanomaterial, reveal the presence of such hybrid interfaces. For Au, represented in Figure 7.3 (a) different NPs are characterized by the presence of Au and Au₂O₃ species. In Ag derived NPs, we found instead both Ag⁽⁰⁾, Ag⁺¹ and Ag⁺³ species inside the same nanoparticle. Figure 7.3 (b) report one specific example, where it is evident the presence of semiconducting Ag/Ag₂O interfaces. In the last, the presence of the metallic counterpart is essential to preserve the stability of the noble metal oxide [111], acting like electron pool to transfer the generated electrons to the reduced species after excitation of the band-gap. Normally, Ag₂O alone is in fact an unstable semiconductor oxide, with a band-gap of about 1.2 eV [111], while gold oxides (Au₂O, Au₂O₃) are poorly studied due to their intrinsic instability [406, 407], although ab-initio DFT calculus predict a direct-BG of about 0.82 eV for Au₂O [92].

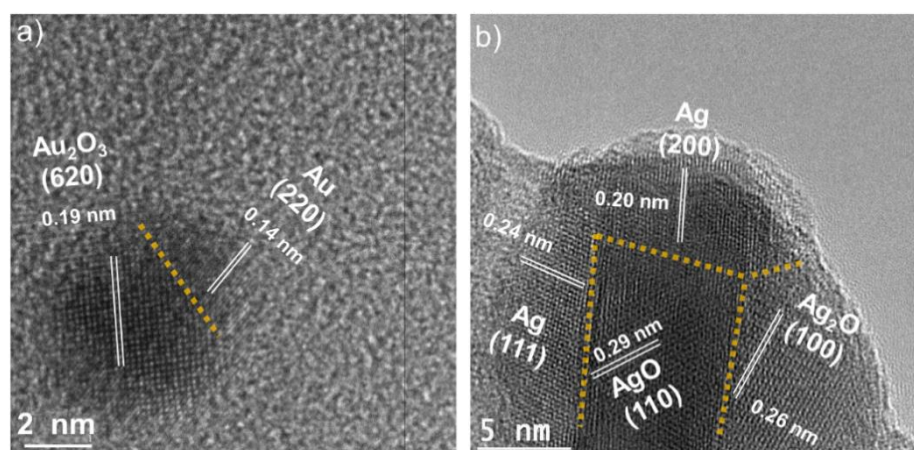


Figure 7.3 HRTEM images showing multiple oxidation states in the Au (a) and Ag (b) derived samples. The dotted orange lines are only used to help the interpretation of the figure. The interplanar distances of 0.19 nm and 0.14 nm observed in (a), are relative to the planes (620) and (220) of Au_2O_3 and Au, respectively [408–410]. In (b) are observed the interplanar distances of 0.20 nm, 0.24 nm, 0.27 nm and 0.29 nm, associated to the planes (200) and (111) of Ag [81, 411], (100) of Ag_2O [412], and (110) of AgO [81].

7.2.

Our hypothesis on PLA induced CO_2/C reduction in water

While the PLA process offers the possibility to activate redox processes by release of energy through Bremsstrahlung radiation [183], acoustic waves [32, 181], or direct absorption of the laser pulse, semiconducting transition MeO are most probably the platform on which CO_2RR is occurring. In this panorama, we propose a schematic model to explain the CO_2/C reduction occurring during PLA of transition metal targets, as represented in Figure 7.4.

Herein, we propose three different processes activated by the transition metal-oxide (TMeO) nanoreactors:

- (a) the one-step water splitting (WS);
- (b) the one-step CO_2 reduction reaction (CO_2RR);
- (c) the two-step CO_2RR

In one step WS [413] and CO_2RR [414] (Figure 7.4 a,b) electron (e^-) - hole (h^+) pairs are created after excitation of the band gap (BG) with promotion of the electrons from the valence band (VB) to the conduction band (CB). In both cases the oxygen evolution reaction (OER) leads to water oxidation by h^+ holes, while the hydrogen

ions are in competition between the hydrogen evolution reaction (HER) and the reduction of CO₂. Molecular oxygen (O₂) and hydrogen (H₂) are produced during the overall water splitting (OWS), characterized by an energy Gibbs variation of about 237 kJ/mol. CO₂RR may instead lead to the synthesis of different products, both in the gaseous phase, such as CO or CH₄, and liquid phase, such as carboxylic acids (R-COOH) [414]. While the products in the liquid phase may diffuse in the water environment or be adsorbed, or eventually chemically bound, on the surface of the TMeO nanoreactors, the gaseous species (CO₂, O₂, H₂, CO, CH₄) may be transported by the permanent microbubbles produced during PLA [32], which represents the reaction chamber where two-step CO₂RR may happen (Figure 7.4 (c)).

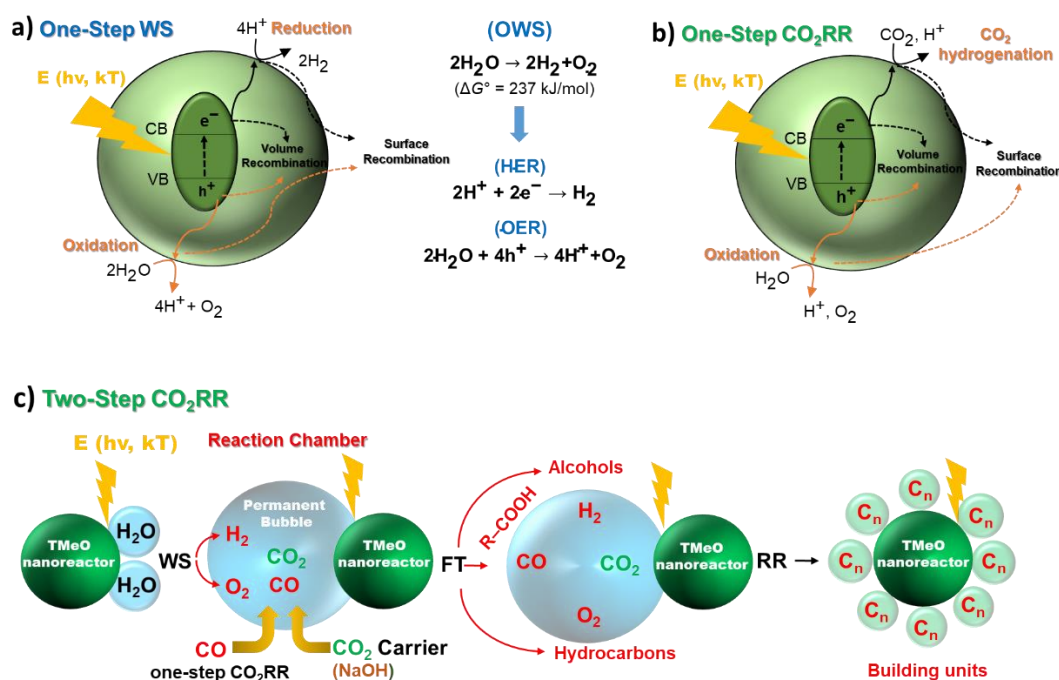
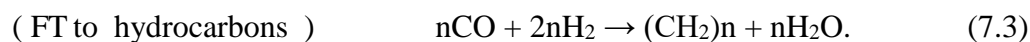
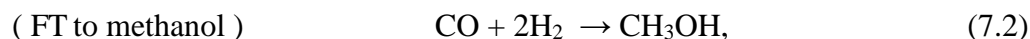
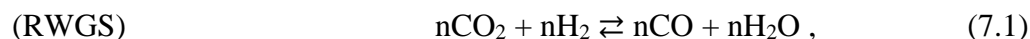


Figure 7.4 Scheme of the simultaneous physical-chemical processes involved in the CO₂/C reduction by PLA of TMe targets. a) One-step OWS. b) One-step CO₂RR. c) Two-step CO₂RR.

In this case, CO may be produced by both one-step CO₂RR and reverse water-gas shift (RWGS) reaction [415], and is further reduced to alcohols and hydrocarbons by Fischer-Tropsch (FT) [415, 416] CO₂ hydrogenation, after activation of the nanoreactors in contact with the permanent bubbles. For, example,

the RWGS and FT processes involved in the synthesis of methanol and hydrocarbons are expressed from the following reactions [415, 416]:



While the hydrocarbons may be transformed to CQDs by pulsed-laser pyrolysis [394], depending on the nature of the metal-oxide and the organic product (ethanol, methanol, carboxylic acids), the latter may be further catalytically reduced (RR) when in contact with the activated nanoreactors, leading to the formation of the $-\text{C}_n-$ building units, which finally may condensate in the form of solid carbon materials. It is worth noting that the mechanism we propose for the final formation of the carbon-based materials by PLA- CO_2/C , is a complex overlapping of one and two-step CO_2RR , and has been recently proposed as a cascade process to enhance the Faradaic efficiency in the synthesis of C_2 and C_3 products for industrial processes [417].

Following our model, the interaction of the laser-pulses with the persistent microbubbles (Figure 7.4) is fundamental to activate the reaction between the gases and the TMeO nanoreactors. To confirm this hypothesis, PLA on Au target was repeated at different laser pulse/target relative velocities, using the configuration with controllable mechanical base, as described in Figure 3.2b of Section 3. In Figure 7.5, we report the UV-Vis extinction spectra of the Au derived nanomaterial and the PL intensity of the corresponding CQDs, synthesized at $c_{\text{NaOH}} = 2.00 \text{ mM}$, and applying different relative velocities between the Au target and the laser pulse.

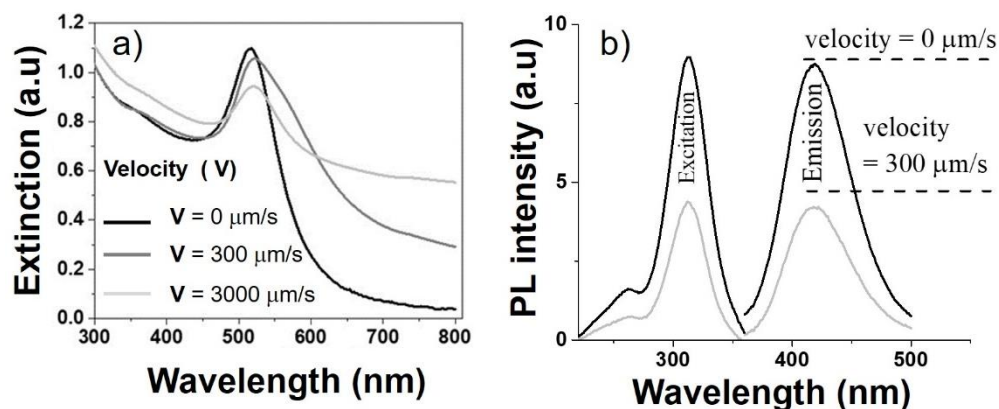


Figure 7.5 a) UV-Vis extinction spectra of the Au derived nanomaterial synthesized at $c_{\text{NaOH}} = 2.00 \text{ mM}$, and different relative velocity ($0 \mu\text{m/s}$, $300 \mu\text{m/s}$, $3000 \mu\text{m/s}$) between the Au target and the spot of the laser pulse. b) PL of the Au derived CQDs, depending on the relative velocity ($0 \mu\text{m/s}$, $300 \mu\text{m/s}$) between the Au target and the spot of the laser pulses during the PLA process.

As evident from the Figure 7.5(a), the colloidal dispersion becomes unstable increasing the velocity of the target, due to the poor rate of interaction of the laser pulse with the oxygen in the permanent bubbles, with broadening and red-shift of the LSPR spectra. The last observations suggest that the stability is reached when the laser pulse interacts steadily with the permanent bubbles, with subsequent oxidation of the MeNPs. The last result is quite new in literature, and put in evidence the fundamental role of OWS in the stability (i.e. oxidation) of gold nanoparticles. Coherently, also the production rate of the CQDs is decreased when the target is moving, according to the scheme proposed in Figure 7.5(b).

At the present stage, it is not clear what is the fundamental energy source activating the catalytic reactions in the semiconductors oxides, which most probably are triggered by the synergetic effect of Bremsstrahlung radiation [183], acoustic waves [32, 181], and the direct absorption of the laser pulse. In this sense, post-irradiation of the Au derived nanomaterial was performed in resonance with the LSPR band at the same optical fluence and ablation time used during the PLA process, putting the solution in equilibrium with a pure CO_2 environment at the pressure of 1 atm. The derived CQDs did not present any spectral changes, and only a slight decrease in the intensity of the corresponding PL spectra, if compared to samples derived from non-irradiated nanomaterial. This observation implies that

acoustic supersonic waves created during irradiation of metal NPs, or direct photon absorption (in resonance with the LSPR) cannot alone be responsible for the synthesis of the solid CQDs observed during PLA, at least at the optical fluence and concentration of NP used in the experiment [33]. The results suggest that the recombination of the C_n building units into solid carbonaceous material is not trivial, and can be accomplished only in the particular thermodynamic conditions created during PLA of the metal target [8].

7.3.

The consistency of the proposed model with the experimental results

The PLA-CO₂RR model described above, may have other implications further to the formation of solid carbon nanomaterials, starting from the control of the dimensions of the NPs. Exists a wide variety of surfactants acting as stabilizing agent in PLA of metals targets in water, such as sodium dodecyl sulfate (SDS) [331], fifth generation ethylenediamine-core poly(amidoamine) (PAMAM-G5) [141], polyvinylpyrrolidone [418], chitosan, ω -dithiol poly(N-isopropylacrylamide), poly(ethylene glycol), dextran [419], polyvinyl alcohol (PVA) [106], or N-(phosphonomethyl) iminodiacetic acid (PMIDA) [393]. In general, these solutes coordinate on the metal surfaces of the NPs, decrease the available nucleation time of the clusters and ions of the metal, and finally limit the growth of the NPs [6]. At the best of our knowledge, we report some of the smallest values concerning the dimension of transition metal NPs synthesized by ligand-free PLA in water by ns laser-pulses. When surfactants are not used, the typical sizes for noble metal NPs are of the order of 5-20 nm [8, 9, 418, 420, 421], and for iron oxide NPs they oscillates between 10 nm and 20 nm [422, 423]. In this scenario, we cannot exclude the possibility that the organic material created by CO₂RR, may coordinate on the surface of the transition metal oxide NPs, limiting their final size and coalescence.

This possibility is particularly fascinating for the case of the PLA performed by the use of dual frequency laser pulses. In such experiments, reported in Section 6, the component of the pulse at the fundamental frequency (ω) is performing the ablation, while the pulse at the second harmonic frequency (2ω) do not participate

to the production of NPs, but continuously irradiate the pre-formed NPs, probably enhancing the production of the organic materials. We remember here, that in such a particular experimental configuration, also the emission wavelength of the CQDs derived from Fe target is blue shifted in the UV region (≈ 320 nm), which might be associated to the reduced dimension of the carbon nanoparticles.

8 Conclusions and perspectives

8.1. Conclusions

As elucidated in the *Introduction Section*, the principle objective associated with this dissertation was the investigation on the origin of the different carbon based materials synthesized during PLA of transition metal targets in deionized water. This high challenging objective, was accompanied by peripheral objectives (or sub-objectives), some of which related to the use of all the transition metals, and others relative to the particular transition metal used during PLA.

Hence, we will divide the conclusions in three topics:

- experimental evidence of CO₂/C reduction induced by PLA of transition metal target in water;
- physical-chemical process associated to the observed CO₂/C reduction;
- control of the dimensions and optical properties of the synthesized nanomaterials;
- application of the synthesized nanomaterials.

After reporting the conclusions on each topic cited above, we will present the perspectives of the present investigation in different areas of research.

8.1.1. Experimental evidence of CO₂/C reduction induced by PLA of transition metal target in water

Differently from all literature available at the moment on the ligand-free PLA of metal target in water, we observe the simultaneous synthesis of metal-oxide based nanostructures together with carbon based material, both in nanostructured and molecular form.

We developed simple and low-cost separation techniques, without the addition of any chemical compound, which allowed the observation of different kind of carbon based materials. The latter, consist in organic molecules, luminescent carbon quantum dots (CQDs), and metal-carbon nanocomposites in the form of carbynoid sp hybridized nanocrystals coordinated and grown on noble metal nanoparticles. Of particular interest, is the observation of carbynoid nanowires supported by AuNPs (Cy@AuNWs). The crystal structure of the NWs is modified by the interaction with high energetic electrons, so that STEM and HRTEM investigation has been conducted at low electron acceleration voltage (80 keV). The corresponding morphology, dimensions and interplanar distances measured by HRTEM, are coherent with the results reported in the unique present in literature for analogues structures [40].

The nature of the CQDs derived from the noble metals has been studied by HRTEM, which revealed a graphitic structure. Also SERS spectroscopy on the powders of the Au and Ag derived nanomaterials revealed the presence of carbon nanostructures (D and G band), overlapped with a typical and identical (for Au and Ag) molecular fingerprint. We propose a possible interpretation of the SERS spectra associated to the organic molecular material, based on the presence of carboxylic acids adsorbed on the metal nanoparticles, and propose a scheme of radical polymerization of formic acid on the noble metal nanoparticle surface, which might be responsible of the formation of the metal-carbynoid complexes. At the moment, we did not detect the presence of metal-carbon NCs or carbon nanomaterial different from CQDs when the Fe target is ablated.

The different kind of carbon based nanostructures cited above, are not present in the colloidal solution with similar concentration. Most of the colloidal dispersion after the separation processes we applied, contains CQDs, and only a very small fraction is constituted by metal-carbynoid nanocomposites. The concentration of the latter is too small in order to have a proper spectroscopic identification in terms of extinction, Raman or PL spectroscopy, at least with the infrastructure disposable in Departments of Physics and Chemistry of PUC-Rio.

Together with the formation of solid carbon nanostructures, other experimental observations sustain the catalytic activity of the transition metal oxide NPs synthesized in the research, in particular:

the magnetite to hematite photocatalytic conversion observed by laser irradiation with an irradiance higher than 10^{-2} kW/mm² in the Raman investigation of the Fe derived nanomaterial;

the detection by SERS of the carbon monoxide (CO) adsorbed on the Au derived nanomaterial, and molecular organic material adsorbed on both the noble metals NPs (Au, Ag).

8.1.2.

Physical-chemical process associated to the observed CO₂/C reduction

In Section 7, we propose a scheme of the simultaneous physical-chemical processes involved in the CO₂/C reduction by PLA of TMe targets, consisting in one-step overall water splitting (OWS), one-step carbon dioxide reduction reaction (CO₂RR), and two-step CO₂RR. In this scheme, a fundamental role is attributed to the spatial overlap between the laser-pulses, the forming NPs, and the permanent bubbles transporting the gases produced during CO₂RR. This key role has been verified by the observation of the dependence of the stability of the Au derived nanomaterial and the production rate of the CQDs (associated to the intensity of the PL emission), on the relative velocity between the target and laser-pulse during the PLA process. The results indicate that the higher stability of the AuNPs, which mostly depends on their oxidation, and the higher CQDs production rate, is obtained for a fixed relative position between the target and the laser pulse.

The results, also explain the reason why the CO₂/C process has never been observed until now, although different decades of scientific research have been dedicated to the investigation of the PLA process in liquid. In fact, at the best of our knowledge, we used unique experimental parameters during the PLA, which have never been experimented with simultaneously by other groups: fixed laser pulse-target relative position, small quantity of liquid, and a great ablation time of the order of hours.

The high value of the ablation time, is probably responsible for the creation of metal/metal-oxide interfaces, or interfaces between different metal-oxides,

which might be responsible for the semiconducting nature of the synthesized nanoparticles, and their final catalytic properties.

8.1.3.

Control of the dimensions and optical properties of the synthesized nanomaterials

We report some of the smallest values of the dimension of transition metal NPs synthesized by ligand-free PLA in water by ns laser-pulses. When surfactants are not used, the typical sizes for noble metal NPs are of the order of 5-20 nm [8, 9, 40, 418, 420, 421], and for iron oxide NPs they oscillates between 10 nm and 20 nm [422, 423]. Smaller dimensions, similar to the ones we report, are obtained in literature only by the introduction of ligands in the water environment [106, 331, 393, 419, 422, 423].

Our results demonstrate the possibility to synthesize AuNPs, AgNPs, and iron oxide NPs with diameters as small as 1.8 nm, 4.0 nm and 1.8 nm, respectively. In the case of Fe derived nanomaterial, a magnetization process was used to separate the smallest iron-oxide nanoparticles, which are principally constituted of hematite, and synthesized by a unique experimental set-up, consisting in the simultaneous ablation with pulses containing both the fundamental (ω) and second-harmonic frequencies (2ω).

For Au and Fe metal targets, the results suggest that smaller NPs are obtained by the use of laser pulses at single 2ω frequency, in comparison with the results obtained by ω pulses. As explained above, for the Fe target, we also tested the simultaneous irradiation by dual frequency pulses. In the latter case, the ω frequency pulse was used for ablation, while the 2ω pulses were used for simultaneous irradiation ($F_{2\omega} = 0.9 \text{ J/cm}^2$), with a negligible contribution to the overall production rate.

The results show that the use of 2ω pulses, both in the case of single and dual frequency laser pulses, leads to NPs with smaller dimensions. The experimental observations may be interpreted based on the catalytic activity of the metal nanoparticles which, in the experimental condition reported above (2ω pulses or

dual frequency pulses), and following the PLA induced CO₂RR scheme proposed in the previous section, might produce a bigger quantity of molecular organic material during the ablation process, due to the higher optical absorption of the semiconductor NPs in the visible region, with a final higher rate of excitation. The molecular organic material may coordinate on the surface of the NPs, thus limiting their coalescence and growth, like it happens when surfactants are introduced in the PLA environment.

In all the experiments, NaOH (C_{NaOH}) was used to control the initial pH (prior to ablation) of the water environment and its initial total carbon TC₀, although in the case of Fe target, we were able to observe CO₂/C reduction also without the addition of the hydroxide.

In the case of Au and Ag target, the pH of the environment is responsible for the charge modulation and stability of the NPs. Varying the pH, we are also able to control both the dimension and the λ_{LSPR} of the noble metal NPs. In the case of Au derived nanomaterial, by parallel variation of both and the pulse fluence F , we can observe a maximum blue shift of about ~ 10 nm, which has never been observed in literature. One of the key points for the correct interpretation of the spectral blue-shift, is the detection of Au-carbonyl species in the SERS spectra of the dried powder of the nanoparticles. The presence of CO adsorbed on the AuNPs, which has a refractive index smaller than the water, may in fact be responsible for the observed blue-shift, together with the possible formation of the π -back bonding in metal-CO system, with the enhancement of the number of electrons participating to the localized plasma oscillations. An analog transfer of electrons may also happen from the shell of CAWs observed around some of the Au nanoparticles and their metallic core, contributing to the overall observed blue-shift.

In the case of AgNPs, two principal differences are observed in comparison with the case of Au: a bigger instability, attributed to the continuous oxidation of the AgNPs after the synthesis, and a progressive red-shift of λ_{LSPR} . Both are associated to the progressive oxidation of the surface of AgNPs, which are found to stabilize this process only after 2-3 weeks from the synthesis, with a final broadening and red-shift of the extinction spectra.

Due to the limited access to the experimental infrastructure in the last months of the research, the phases of the iron oxide NPs have been investigated (by Raman spectroscopy) only in the case of Fe derived nanomaterial synthesized by dual frequency laser pulses (ω and 2ω simultaneously). We identified four different phases of iron oxide: i) magnetite (Fe_3O_4), ii) hematite (Fe_2O_3), iii) wüstite (FeO), and iii) siderite (FeCO_3). The siderite is very rare in the sample, while hematite, wüstite, and magnetite are the most abundant oxides. With the exclusion of siderite which, to the best of our knowledge, has never been detected before of the present research, the other oxides are typically found as product of the PLA of iron targets in pure water. After the magnetic separation procedure, we were able to obtain two colloidal solution containing iron-oxide NPs with different size and different phase. Magnetite NPs with an average dimension of 4.6 nm, and ultrasmall hematite NPs with an average size down 2 nm. The average size of the bigger NPs was confirmed by a novel magnetic scanning microscope in collaboration with Prof. Jefferson F.D.F Araujo of the Department of Physics of PUC-Rio.

All the transition metal derived nanomaterials present, as the most populated carbon species, the photoluminescent CQDs. Both the chemical composition, size, and spectral properties of the CQDs seems to be not dependent on the frequency ω and fluence F of the laser pulse, or also on the total carbon value TC_0 , which only can modulate the intensity of the corresponding emission. Only in the case of Fe derived CQDs, the emission spectra can be roughly tuned from the UV (~ 325 nm) to the blue region (390 nm – 415 nm), depending on the laser parameters used during the PLA process. The UV emission is obtained by the ablation with dual-frequency pulses (ω and 2ω) and, following our scheme of the PLA induced CO_2RR , is probably associated with the synthesis of smaller carbon nanoparticles, due to the higher production rate of molecular organic materials, which should limit their size growth.

The solubility in water of the carbon NPs is assured by the presence of hydroxyl and carboxyl functional groups, as verified by FTIR and XPS spectroscopy, although also carbonyl and epoxy groups are present. Moreover, multi-wavelength emission TRPL measurements, suggest that the emission of our Au derived CQDs is mostly associated to surface states with two different lifetimes, without carbogenic contribution. The full width half maximum (FWHM) of the

emission is of the order of ~ 55 nm, quite smaller than the typical FWHM reported for other kinds of CQDs soluble in water emitting in the visible region, which is in the range between 80 nm and 110 nm.

Most interestingly, the QY was evaluated to be about 45%, which is, at the best of our knowledge, one order of magnitude higher than the typical values reported for luminescent carbon nanomaterials synthesized by both one or even two-step PLA processes.

Such a low FWHM and high QY may be associated to the peculiar source of carbon atoms in the liquid environment. In traditional PLA, the atoms constituting the core of the upcoming NPs are ejected from the solid carbon target in a multiphase form, such as vapors, liquid, solid pieces, which after condense together giving rise to a quite broad size distribution. In CO₂/C assisted synthesis, the building elements of the carbynoid NWs and CQDs are presumably C_n molecular units recombining in highly ordered structures.

8.1.4. Application of the synthesized nanomaterials

The Au derived nanomaterial obtained in the ultrasmall range, demonstrated the unique and intriguing property to enhance the angiogenesis process in endothelial cells, both by in vitro and in vivo tests, with huge potential in the field of regenerative medicine. At the light of the results reported in literature, the biological activity of the nanoparticles may also be linked to the production and release of carbon monoxide from the Au derived nanomaterial in the cell environment.

Similar to other works reported in literature, the Au derived nanomaterial may also be successfully applied for the plasmonic enhancement of the photodynamic activity of photosensitizers, like we demonstrated in the use of molecule Chlorin-e6, with an overproduction of oxygen of singlet, which might be applied for a lower administration of drugs in skin antitumor treatment.

8.2. Future work and perspectives

8.2.1. Future experimental work

Looking at the scheme we have proposed for the PLA induced CO₂/C reduction, shown in Figure 7.4 our most important purpose is now to run back the chain, that is understand what is the link between the particular organic intermediate product, and the final structure of the carbon nanomaterial derived from a specific metal target. The comprehension of this fundamental aspect, may allow in the future the control of the shape, dimension, hybridization and luminescence of the different functional carbon nanostructures. In particular, we propose the detection of different gases (H₂, H₂S, CO, NH₃, CH₄, C₂H₂, C₂H₄, C₆H₆) and carboxylic acids (HCOOH, CH₃COOH, CH₃CHOH, CH₂CHCOOH) which are supposed to be generated during the CO₂/C reduction induced by PLA. For this purpose, a new collaboration has been established between the *NanoLaserLab* of the Department of Physics of PUC-Rio and the groups of Prof. Stephan Barcikowski, Prof. Torsten Schmidt, and Prof. Sven Reichenberger of the Department of Chemistry of the University of Duisburg-Essen (Germany).

Also other analyses are needed in the immediate future in order to validate the interpretation of some of the presented experimental results.

Particularly important is the spectroscopic characterization of the Cy@AuNWs, which will be performed by Tip Enhanced Raman Spectroscopy (TERS) in the *InMetro* Institute of Rio de Janeiro. Although the graphitic nature of the CQDs has been revealed by HRTEM, it is also opportune to confirm this result by Raman spectroscopy, through the synthesis of a sufficient quantity of carbon nanoparticles.

Concerning the Fe derived nanomaterial, we are confident about the rapid possibility to obtain the Raman characterization of the different metal-oxides produced by PLA performed by laser pulses containing a single frequency (ω or 2ω). Also, the HRTEM characterization of the Fe derived CQDs with emission in the UV region will be a key investigation, in order to understand if the blue-shifted

emission (in comparison to all the other CQDS synthesized in this research) is associated with a smaller size.

The last fundamental parameter which needs to be measured to finalize the presented research is the CO₂/C absolute efficiency η . The latter, is the ratio between the value of the final total solid carbon TC_{solid} coming from the metal-carbynoid NCs and the CQDs, and the final total carbon (TC₀ + Δ TC) at the end of the PLA process ($\eta = \text{TC}_{\text{solid}} / \text{TC}_0 + \Delta\text{TC}$). While the denominator is well known from the tens of measurements performed along the research, due to a contamination problem during the dialysis process we were not able to measure the value of TC_{solid}. The contamination during the dialysis process, was in fact resolved only recently and allowed, for example, the correct characterization of the Au derived CQDs by FTIR and XPS spectroscopy. The dialyzed samples for the determination of η have been prepared and stored, and will be measured as soon as possible.

8.2.2. Perspectives

A consideration has to be done on the performance of the CO₂RR-PLA reactor in BEECS technology. Brazil emits on average about 100 kg of CO₂ to produce 1 MWh of energy [424], which gives an energetic value of 1 kWh for 100 g of CO₂. We can for the moment suppose that the C concentration of the samples after dialysis is lying in between the values of TC₀ (almost 100% conversion efficiency) and Δ TC. Looking at the results of Table 4.1, using $c_{\text{NaOH}} = 20.00$ mM, let's suppose to have a final TC after dialysis of 15 ppm.

The optical configuration used generally at the 2ω frequency during PLA, allow the synthesis of about 5 ml of colloidal solution in 1 hour, with the characteristics reported in Table 4.1. This corresponds to a mass of about 75 μ g of CO₂, corresponding to a BEECS added energetic value of $\sim 10^{-6}$ kW/h. To a first sight, this represents a negligible amount of energy, principally considering that the Q-Smart 850 laser system is operating with a maximum electrical power of about

10^3 VA. Anyway, the particular experimental conditions used in the synthesis have to be taken in consideration.

First of all, we used a very low value of energy and F of the laser pulses, with the aim to control the dimensions, stability and optical properties of the transition metal derived nanomaterials. But when such a fine tuning is not needed, PLA might be performed with our system with laser pulses 100 times more energetics of the ones typical used along the research, which can guarantee a first 2 order of magnitude higher production of nanomaterial. As second point, in the case the concentration of H_2 performs a major role in the synthesis of the carbon nanostructures, we can enhance the spatial overlap between the laser pulse and the permanent H_2 bubbles by out-focusing the beam, and using different metals such as aluminum (Al) or titan (Ti), may produce molecular hydrogen by water-splitting at really higher concentrations [425]. Also the repetition rate of the laser pulses has to be considered, since the use of high repetition rates (\approx kHz) might reduce the ablation times of orders of magnitude. Hence, we think that proper optical configuration and catalytic metal, may enhance the energetic value of PLA product of 3 orders of magnitude. Finally, a further increase in the production rate of carbon material may be definitively obtained by the control of the CO_2 concentration at the gas-liquid interface of the beaker were PLA is performed, using the experimental set-up shown in Figure 3.2b. The right balance between the CO_2 and NaOH concentration in the water solution, may allow the stability of the colloidal nanomaterial with values of TC_0 three order of magnitude higher, imaging a pure CO_2 gas atmosphere at the gas/liquid interface. Nevertheless, also the effect of CO_2 carriers different from NaOH has to be taken in consideration, amplifying the possibilities of a higher solid carbon production rate.

Considering all these aspects, we definitively think that the reported experimental results highlight the interesting possibility to draw an energetic ‘road-map’, with the aim to obtain CO_2RR -PLA based reactors for carbon nanoparticles production with an added energetic value in the range between 0,1 kWh and 1,0 kWh.

In conclusion, after decades of research, synthesis of nanomaterials by pulsed laser ablation in water is still considered to respond to most of the precepts of the ‘green chemistry’. One of the major points to sustain this inclusion, is the

conviction of the absence of secondary reactions products, commonly the main argument reported in literature to defend the minor cytotoxicity of the nanomaterials when compared to the chemically synthesized counterparts. The research developed during my PhD revolutionizes this point of view, showing that PLA of transition metal targets in water (Au, Ag, Fe) acts as an intrinsic photo-thermal catalytic cell, where CO₂RR runs simultaneously to the formation of metal nanoparticles. The reactions, lead to the formation of ‘invisible’ carbon based functional nanomaterials, unrevealed for decades due to the overlap of the spectral properties of the different metal and carbon species. The results shine a light on PLA in water as potential negative emission technology, with the unique property to convert CO₂ to solid functional nanomaterial.

Nevertheless, PLA of transition metal targets definitively represent a new platform also for investigation in fundamental physics, giving the possibility to advance in the exiting debate on the controversial existence of stable quase-1D carbynoid nanocrystals. Carbynoid material has taken much attention in fundamental physics since its discovery on the external surface of the Murchison meteorite, in late 1969, and is historically considered as the first ‘extraterrestrial’ material with traces of amino-acids [426], with no natural analogue carbon allotrope on the earth. Carbynoid systems only represent one specific example of the importance that carbon based materials have in the comprehension of astrochemical processes. Of particular interest will be the study of the CO₂RR using metals which are commonly found in the composition of meteorites, such as Fe, Ni, Si and Al [426]. PLA is in fact considered as the principal experimental technique to simulate the “space weathering”, which is the term used to refer to those processes, such as the bombardment by micrometeorites, solar wind ions, and cosmic rays, able to induce changes in the physical, chemical, mineralogical, and observational properties of the surface of asteroids, comets, and some planets and their satellites [427].

The possibility to control the size of the Au and Fe based nanomaterial down to the ultrasmall range ($r < 2$ nm), is instead particularly attractive in view of the potential applications in the emerging field of nanoparticle-based gene therapy. Moreover, in the light of the experimental results, it will be particularly interesting also to investigate the antibacterial and antiviral properties of the Ag derived

nanomaterial which we discovered to be characterized by photocatalytic semiconductor Ag/Ag₂O interfaces. Nevertheless, it is reported in the literature that carbon/Ag nanocomposites may significantly enhance the antibacterial and antiviral properties of the nanoparticles, which is particularly attractive after the recent discovery of the virus COVID-19 and the related social and economic problems [428].

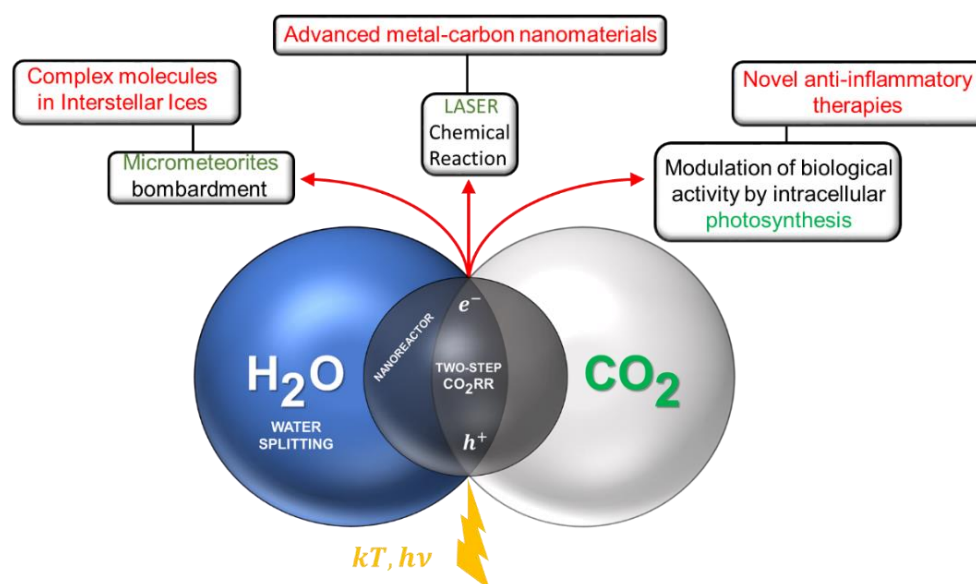


Figure 8.1 Diagram representing the main scientific areas where the discovery of the PLA induced CO_2/C reduction by metal-oxide semiconductors may open unexpected perspectives

As resumed in Figure 8.1, the present research may open unexpected perspectives in experimental biology and astrochemistry, and gives to the scientific community a new instrument for the bottom-up synthesis of advanced nanomaterial by CO_2/C laser-induced process.

9 Production

9.1.

List of publications

- T. Del Rosso, S. R. W.Louro, F. L. Deepak, E. C. Romani, Q. Zaman, **Tahir**, O. Pandoli, M. Cremona, F. L. Freire Junior, P. A. A. De Beule, T. De St. Pierre, R. Q.Aucelio, G. Mariotto, S. Gemini Piperni, A. R. Ribeiro, S. M. Landi, A.Magalhães, *Biocompatible Au@Carbynoid/Pluronic-F127 nanocomposites synthesized by pulsed laser ablation assisted CO₂ recycling*, **Applied Surface Science**, v. 441, p. 347-355, 2018.
- Jefferson.F.D.F.Araujo, **Tahir**, Soudabeh Aرسالani, Fernando L.Freire Jr, Gino Mariotto, Marco Cremona, Leonardo A.F.Mendoza, CleanioLuz-Lima Quaid Zaman, Tommaso Del Rosso, Oswaldo Baffa, Antonio C Bruno, *Novel scanning magnetic microscopy method for the characterization of magnetic nanoparticles*, **Journal of Magnetism and Magnetic Materials**, v. 499, p. 166300, 2020.
- Jefferson F. D. F. Araujo *,Andre L. A. Reis ,Angela A. P. Correa ,Elder Yokoyama ,Vanderlei C. Oliveira, Jr. ,Leonardo A. F. Mendoza ,Marcos A. C. Pacheco ,Cleanio Luz-Lima ,Amanda F. Santos ,Fredy G. Osorio G. ¹,Giancarlo E. Brito, Wagner W. R. Araujo, **Tahir**, Antonio C. Bruno , and Tommaso Del Rosso, *Scanning Magnetic Microscope Using a Gradiometric Configuration for Characterization of Rock Samples*, **Materials**, v. 12, n. 24, p. 4154, 2019.
- Daniele Fulvio*, Leonardo Fuks Maron, Yaima Cires Perez, **Tahir** and Tommaso Del Rosso, *Micrometeorite bombardment simulated by ns-pulsed laser ablation: morphological characterization of the impact craters*, accepted in **Icarus**.

- Quaid Zaman*, **Tahir**, A.R.J. Barreto, Jefferson F. D. F. Araujo, Luís D. Carlos, Albano N. Carneiro Neto, Marco Cremona, Zubair Ahmed, Andre Felipe Souza da Cruz, Jefferson S. Costa, Nadson Welkson Pereira de Souza, Karlo Q. da Costa, Victor Dmitriev, T. Del Rosso*, *Dielectric Loaded Waveguides as advanced platforms for diagnostic and application of transparent organic thin films*, submitted to **Langmuir**.
- Eloi B. de M. Junior, Fredy G. Osorio G., Frederico V. Gutierrez, Tommaso Del Rosso, **Tahir**, Leonardo A. F. Mendoza Cleanio Luz-Lima, Elder Yokoyama, Andre L. A. dos Reis, Geronimo Perez, Jesana de M. Silva, Antonio C. Bruno and Jefferson F. D. F Araujo, *Detecting surface-breaking flaws with a Hall effect gradiometric sensor*, accepted in **Measurements**, Pub Date : 2020-12-04.
- **Tahir**, Tommaso Del Rosso* *et. al.*, *CO₂/C reduction by pulsed laser ablation of transition metal target in water: opening new horizons in material science, experimental astrochemistry and nanomedicine (in preparation)*.

9.2.

Conferences

Preliminary experimental results have been presented in the following national and international scientific conferences:

- **Tahir**, M. Cremona, R.Q. Aucelio, C. A. Toloza, A. Laurenzana, F. Margheri, M. Del Rosso, G. Fibbi, F.L. Deepak, S. Landi, C.S. Casari, S. Peggiani, A. Facibeni and T. Del Rosso, *Novel insight on the potentialities of ligand-free pulsed laser ablation of a gold target in water: synthesis of biocompatible functional carbynoid nanostructures*, Cola 2019 (Maui Hawaii-USA), September **2019** (international, oral presentation).

- **Tahir**, Carlos Alberto Toloza, Alexandre Pinto Canellas, Marco Cremona, Fernando Lázaro Freire Júnior, Omar Pandoli, Sonia Renaux Wanderley Louro, Ricardo Queiroz Aucelio, Aline Magalhaes, Leonard Francis, Rafael C. Chavez and Tommaso Del Rosso, *Synthesis of functional Au@Carbynoid nanocomposites and Carbynoid luminescent nanoparticles during CO₂ recycling assisted by pulsed laser ablation of gold target in water*, Brazilian Physical Society Meeting XL ENFMC (Natal, R. N Brazil), September **2018** (national, poster).
- **Tahir**, Tommaso Del Rosso, Marco Cremona, Fernando Lázaro Freire Júnior, Omar Pandoli, Vinicius Mattoso, Sonia Renaux Wanderley Louro, Ricardo Queiroz Aucelio, Aline Magalhaes and Rafael C. Chavez, *Au@carbynoid/Pluronic-F127 nanocomposites drug-carriers synthesized by pulsed laser ablation in water*, Autumn Meeting of the Brazilian Physical Society (Foz do Iguaçu, Brazil), May **2018** (national, oral presentation).
- Amanda Farias dos Santos, Jefferson Ferraz D. F. Araujo, Antônio Carlos Bruno, Tommaso Del Rosso and **Tahir**, *Characterization of iron oxide nanoparticles using a scanning magnetic microscope*, Autumn Meeting of the Brazilian Physical Society (Foz do Iguaçu, Brazil), May **2018** (national, poster).

Appendix

A.1

Calculation of the dielectric function of small NPs

In the following we report the code, based on the MATLAB language, which we developed for the determination of the theoretical UV-Vis spectra associated to the experimental statistical distribution of the Au derived nanomaterial, based on the Mie theory.

```
clear all;
%clearvars;
```

Declaration of ranges, constants and *LogNormal* function

```
file_data = load('Au-Modified_J_C_n_k.txt');
exp_meas = load('ph12.txt');
%exp_meas = load('Figure-1.txt');
%exp_meas = load('PH-7-d = 3.8.txt');
file_liquid = 'N_H2O.txt';
lambda = 0.25:0.001:0.8; %wavelength domain (um)
d_0 = 1e4; %Cuvete length um
E = 1; %Maximum experimental value of extinction
spectrum
dp = 19.32; %Density of NP (g/cm^3)
lambda_max = 0.518e-6; %SPR resonance wavelength (um)
y0 = 0; %LogNorm constant
xc = 1.09;%3.217; %LogNorm constant
w_omega =0.296; %0.307; %LogNorm constant
```

```

A =58.14;%151;                                %LogNorm constant

%y1 = 014

%xc1 = 3.79;

%w_omega1= 0.2438;

%A1= 39.103;

n_fitted = @(r) y0 + (A./(sqrt(2*pi).* r.*1e3 .* w_omega)).*exp(-
(log(r.*1e3/xc).^2)/(2*(w_omega).^2)); % radius in um

%n_fitted= @(r)y1 + (A1./(sqrt(2*pi).* r.*1e3 .* w_omega1)).*exp(-
(log(r.*1e3/xc1).^2)/(2*(w_omega1).^2));

%n_fitted = @(r)y0 + (A./(sqrt(2*pi).* r.*1e3 .* w_omega)).*exp(-
(log(r.*1e3/xc).^2)/(2*(w_omega).^2))+ y1 + (A1./(sqrt(2*pi).* r.*1e3 .*
w_omega1)).*exp(-log(r.*1e3/xc1).^2)/(2*(w_omega1).^2));

radius_min = 1/1e3;%3/2/1e3;                  %Minimum radius um

radius_max = 30/1e3;%7.75/2/1e3;             %Maxium radius

radius_interval = 0.1/1e3;

radius_vec = (radius_min:radius_interval:radius_max); %radius in um
define os raios para os calculos da curva de extinçao total

n_int = integral(n_fitted, radius_min, radius_max); %Calculate
numerical integral

```

Dielectric function of bound electrons

```

Wavelength = file_data(:,1);                  % wavelength in nm

n_ref_index = file_data(:,2);                 % real part of refractive
index

k_ref_index = file_data(:,3);                 % Imaginary part of
refractive index

Wavelength_um = file_data(:,4);

e_real = n_ref_index.^2-k_ref_index.^2; % Real part of dielectric
function

e_Imag = 2.*n_ref_index.*k_ref_index; % Imaginary part of dielectric
function

e_bulk = e_real+1i.*e_Imag ;                  % Bulk dielectric constant

w_p = 1.3E16;                                 % Plasma frequency

Gama_bulk = 1.64E14;                          % Damping constant

```

```

c_s = 3E17; %Speed of light

w = 2.*pi.*c_s./Wavelength ; %Angular frequency

e_free = 1- w_p.^2./(w.^2+1i.*w.*Gama_bulk); % Dielectric constant of
free electrons

e_bound = e_bulk - e_free; % Dielectric constant of bound
electrons

e_bound_imag = imag(e_bound); %imaginary part of bound
electrons

v_f = 14.1E14; % Fermi velocity of electron

c = 1; % Proportinality constant

colors = 'rgbkcrbgkcrbgk';

figure;

hold on; box on; grid on;

for l = 1:length(radius_vec)

```

Particle properties

```

a = radius_vec(l);

Gamma_a = Gama_bulk + (c.*v_f ./ (a*1e3)); % Damping contant of small
particles%

wp_w = w_p.^2./(w.^2+Gamma_a.^2);

e_size_imag =e_bound_imag+(Gamma_a.*w_p.^2) ./ (w.*(w.^2+Gamma_a.^2));

n_size = sqrt(0.5.*(sqrt(e_real.^2+e_size_imag.^2)+ e_real));

k_size = sqrt(0.5.*(sqrt(e_real.^2+e_size_imag.^2)- e_real));

N_Au.wavelength = Wavelength_um;

N_Au.N = n_size - 1i*k_size;

N_Au.eps = N_Au.N.^2;

N_Au = INL_MD_Interpolate(N_Au,lambda);

N_liquid = INL_MD_Load(file_liquid);

N_liquid = INL_MD_Interpolate(N_liquid,lambda);

n = size(lambda,2);

for k = 1:n

```

```

        [a_n,b_n,x] =
INL_MS_SolidSphere(lambda(k),a,N_liquid.N(k),N_Au.N(k));

        n_norm(l) = n_fitted(a) / n_int;

        Q_ext_ss(k,l) = INL_MS_ExtinctionEfficiency(a_n,b_n,x);

        sigma_ext_pesad(k, l) = a ^ 2 * Q_ext_ss(k,l) * n_norm(l) *
radius_interval; %R^2*Q*n*dr

        end

end

```

Show the graphs

```

espec_ext = -sum(sigma_ext_pesad');

[peak, locs] = findpeaks(espec_ext);           %Find peaks
in results

N_particles = (2.303 * E / (d_0 * pi * peak(end))) * 1e12 %NP Density
per cm^3

n_mass = @(r) ( n_fitted(r) / n_int ) .* r.^3;

Concentration = (N_particles * 4/3 * pi * dp
*integral(n_mass,radius_min,radius_max)) * 1e-12 %Concentration in
(g/cm^3)

```

```
N_particles = 4.1710e+14
```

```
Concentration = 9.2939e-05
```

Plot results

```

title('Au nanoparticles');

xlabel('Wavelength (nm)')

ylabel('Extinsion (a.u.)')

xlim([300 800]);

%ylim([0 1.25]);

espec_ext= espec_ext / peak(end); %Normalize results by the last peak

plot(lambda*1000,espec_ext,'-b','LineWidth',3);

plot(exp_meas(:,1),exp_meas(:,2),'g','LineWidth',3);

hold off;

```

```
legend('Solid sphere logNorm','Experimental curve');
```

A.2 Dynamic Light Scattering (DLS) and ζ -potential

A nanoparticle analyzer model SZ-100 (Horiba, Japan) was used for the measurement of hydrodynamic size and surface potential (ζ -potential) of NPs in the colloidal dispersion.

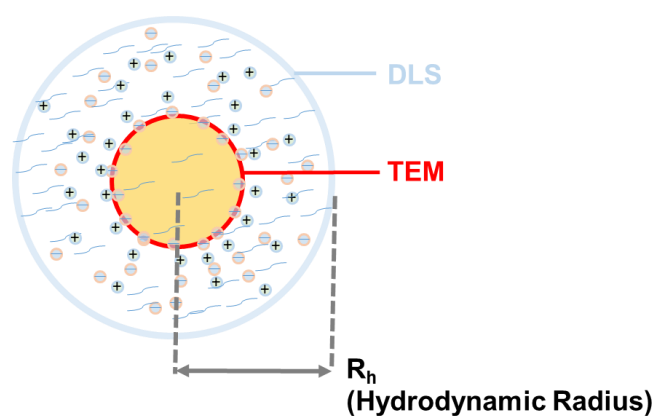


Figure S1 Cartoon sketch of hydrodynamic radius of NP.

As represented in Figure S1, and explained in Section 2.2.2, the hydrodynamic size is not the actual size of the metal core of the NPs, due to the Stern and diffusive layers. Hence, hydrodynamic size measured by DLS is always greater than the size of the NPs measured by TEM and/or Atomic Force Microscopy (AFM) [209].

Concerning the measurements of ζ -potential, the charged NPs moves under the action of an applied electric field, therefore the ratio between the NPs velocity and the external applied field, called electrophoretic mobility, is measured and used to calculate the ζ -potential using the Henry equation:

$$\mu_e = 2 \epsilon \zeta f(k. \alpha) / 3 \eta, \quad (S1)$$

where ε and η are the dielectric constant and the viscosity of the medium, respectively. $f(k, \alpha)$ is called the Henry function, in which α is the radius of the particle and k represent the thickness of the electrical double layer.

A.3 Transmission Electronic Microscopy

Transmission electronic microscopy (TEM) is a reliable and an effective technique in which the high energetic electron beam is transmitted through very thin specimen (sample) in order to study its structure. If the relativistic effect is neglected, then according to the de Broglie's Law the wavelength of the electron (λ_e) is inversely proportional to square root of accelerated electron's energy ($E^{1/2}$):

$$\lambda_e = \frac{1.2}{E_e^{1/2}} \quad . \quad (S2)$$

As we increase the energy of the accelerated electron, λ_e decreases and the resolution of TEM images is increasing. According to equation S2, if 100 keV energy electron beam are used, then λ_e will be 0.004 nm, which is much smaller than the atomic radius. However, the spherical and chromatic aberrations of magnetic lens decrease the resolution.

A TEM can be described by main three parts: illuminating system, the objective stage/lens, and image system, as shown in Figure 2. (a). The illumination system has the source of electrons, where electrons are extracted from the filament and focused by condenser lenses. The main purpose of the condenser lenses is to focus and deflect the electron beam in such a way to obtain a suitable illuminating condition, for example convergence angle and spot size. It is quite possible to adjust the condenser lens strength to acquire either convergence (e.g. as used in STEM, CBED) or parallel (e.g. as used in SAED, HRTEM) electron beam condition. In order to reduce the spherical aperture a condenser aperture is placed below the condenser lens. The sample holder is inserted just above the objective lens and, to align the sample with respect to electron beam, it can be rotated along one or two axis. The schematic diagram in Figure S2 (b) shows the electron beam ray path in the diffraction and image mode [429, 430].

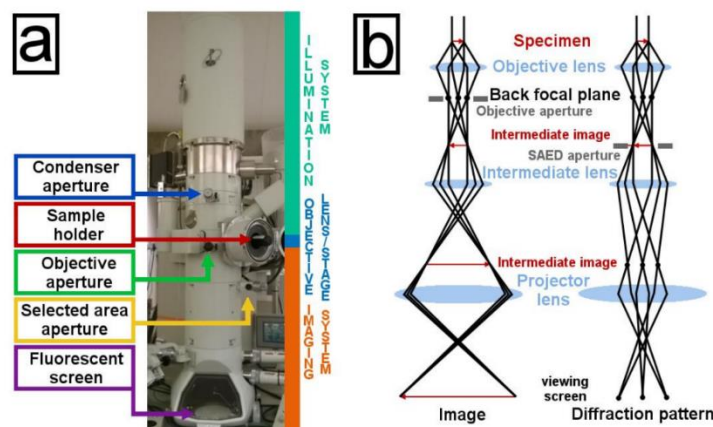


Figure S2 a) Picture with the main parts of the transmission electron microscope JEOL JEM-2100F. b) Schematic diagram of path of the electron ray in the two operating modes. The image mode is shown in the left, while the diffraction modes are shown in the right [429].

High Resolution Transmission Electronic microscopy: High Resolution Transmission Electronic microscopy (HRTEM) is used to obtain an image with information of the lattice fringes of a crystal. The contrast in TEM images mainly come from two types of contribution: amplitude contrast and phase contrast. The amplitude contrast is related to the variation of the thickness's crystal and /or atomic number across the crystal. The phase contrast is related to the phase change of the electron wave, in consequence lattice fringes of a thin crystal appears with high magnification and provide a high resolution image. The HRTEM uses both scattered and transmitted beam two create interference images of a crystal.

To have a complete characterization of the crystal structure of nanomaterials, generally HRTEM is followed by the study of the diffraction electron pattern, STEM and EDS.

STEM mode: Unlike the conventional TEM, in scanning transmission electron microscopy (STEM) the beam is focused to a fine spot of typical size 0.05 to 0.2 nm, and scanned on the sample in such a way that it is illuminated at each point with a beam parallel to optical axis. There is no contrast reversal in STEM as compared to HRTEM, which allows a direct interpretation of contrast. In STEM bright field (STEM BF), the detector capture those electrons scattered at lower

angle (such as diffract and direct beam), while in annular dark-field (ADF) the detector captures the electron scattered at higher angle, excluding the lower angle scattered electrons.

Energy Dispersion X-ray Spectroscopy (EDS): In energy dispersion X-ray spectroscopy (EDS or EDX), the characteristic X-ray are used to elementally or chemically analyze the sample. In this technique an energetic electron interacts with the sample in order to produce a characteristic x-ray which gives information about the sample composition.

10 Bibliography

- [1] P. P. Patil *et al.*, “Pulsed-laser – induced reactive quenching at liquid-solid interface: Aqueous oxidation of iron,” *Phys. Rev. Lett.*, vol. 58, no. 3, pp. 238–241, Jan. 1987.
- [2] F. Mafuné, J. Kohno, Y. Takeda, T. Kondow, and H. Sawabe, “Formation of Gold Nanoparticles by Laser Ablation in Aqueous Solution of Surfactant,” *J. Phys. Chem. B*, vol. 105, no. 22, pp. 5114–5120, Jun. 2001.
- [3] N. Mirghassemzadeh, M. Ghamkhari, and D. Dorrnian, “Dependence of Laser Ablation Produced Gold Nanoparticles Characteristics on the Fluence of Laser Pulse,” *Soft Nanosci. Lett.*, vol. 03, no. 04, pp. 101–106, 2013.
- [4] W. Norsyuhad, W. Shukri, N. Bidin, S. Affandi, and S. P. Bohari, “Synthesize of gold nanoparticles with 532 NM and 1064 NM pulse laser ablation,” *J. Teknol.*, vol. 78, no. 3, pp. 267–270, 2016.
- [5] G. Palazzo, G. Valenza, M. Dell’Aglia, and A. De Giacomo, “On the stability of gold nanoparticles synthesized by laser ablation in liquids,” *J. Colloid Interface Sci.*, vol. 489, pp. 47–56, Mar. 2017.
- [6] V. Amendola and M. Meneghetti, “What controls the composition and the structure of nanomaterials generated by laser ablation in liquid solution?,” *Phys. Chem. Chem. Phys.*, vol. 15, no. 9, pp. 3027–3046, 2013.
- [7] P. Singh *et al.*, “Green synthesis of gold and silver nanoparticles from *Cannabis sativa* (industrial hemp) and their capacity for biofilm inhibition,” *Int. J. Nanomedicine*, vol. Volume 13, pp. 3571–3591, Jun. 2018.
- [8] V. Amendola and M. Meneghetti, “Laser ablation synthesis in solution and size manipulation of noble metal nanoparticles,” *Phys. Chem. Chem. Phys.*, vol. 11, no. 20, p. 3805, 2009.
- [9] R. M. Tilaki, A. I. Zad, and S. M. Mahdavi, “The effect of liquid

- environment on size and aggregation of gold nanoparticles prepared by pulsed laser ablation,” *J. Nanoparticle Res.*, vol. 9, no. 5, pp. 853–860, Jun. 2007.
- [10] M. Sharif and D. Dorrnian, “Effect of NaCl Concentration on Silver Nanoparticles Produced by 1064 nm Laser Ablation in NaCl Solution,” *Mol. Cryst. Liq. Cryst.*, vol. 606, no. 1, pp. 36–46, Jan. 2015.
- [11] J. S. Anjali Devi, R. S. Aparna, R. R. Anjana, N. S. Vijila, J. Jayakrishna, and S. George, “Amplified luminescence quenching effect upon binding of nitrogen doped carbon nanodots to transition metal ions,” *Photochem. Photobiol. Sci.*, vol. 19, no. 2, pp. 207–216, May 2020.
- [12] G. YANG, “Laser ablation in liquids: Applications in the synthesis of nanocrystals,” *Prog. Mater. Sci.*, vol. 52, no. 4, pp. 648–698, May 2007.
- [13] T. X. Phuoc, “Complete Green Synthesis of Gold Nanoparticles using Laser Ablation in Deionized Water Containing Chitosan and Starch,” *J. Mater. Sci. Nanotechnol.*, vol. 1, no. 4, pp. 1–7, Dec. 2014.
- [14] D. Werner, S. Hashimoto, T. Tomita, S. Matsuo, and Y. Makita, “Examination of Silver Nanoparticle Fabrication by Pulsed-Laser Ablation of Flakes in Primary Alcohols,” *J. Phys. Chem. C*, vol. 112, no. 5, pp. 1321–1329, Feb. 2008.
- [15] V. Amendola, P. Riello, and M. Meneghetti, “Magnetic Nanoparticles of Iron Carbide, Iron Oxide, Iron@Iron Oxide, and Metal Iron Synthesized by Laser Ablation in Organic Solvents,” *J. Phys. Chem. C*, vol. 115, no. 12, pp. 5140–5146, Mar. 2011.
- [16] V. Amendola, G. A. Rizzi, S. Polizzi, and M. Meneghetti, “Synthesis of Gold Nanoparticles by Laser Ablation in Toluene: Quenching and Recovery of the Surface Plasmon Absorption,” *J. Phys. Chem. B*, vol. 109, no. 49, pp. 23125–23128, Dec. 2005.
- [17] A. Kanitz, J. S. Hoppius, M. del Mar Sanz, M. Maicas, A. Ostendorf, and E. L. Gurevich, “Synthesis of Magnetic Nanoparticles by Ultrashort Pulsed Laser Ablation of Iron in Different Liquids,” *ChemPhysChem*, vol. 18, no. 9, pp. 1155–1164, May 2017.

- [18] V. Amendola, S. Polizzi, and M. Meneghetti, “Free Silver Nanoparticles Synthesized by Laser Ablation in Organic Solvents and Their Easy Functionalization,” *Langmuir*, vol. 23, no. 12, pp. 6766–6770, Jun. 2007.
- [19] Tahir *et al.*, “CO₂/C reduction by pulsed laser ablation of noble metals targets: synthesis of sp-sp² carbon based nanostructures in water,” 2021.
- [20] T. Del Rosso *et al.*, “Biocompatible Au@Carbynoid/Pluronic-F127 nanocomposites synthesized by pulsed laser ablation assisted CO₂ recycling,” *Appl. Surf. Sci.*, vol. 441, pp. 347–355, May 2018.
- [21] H. Wang *et al.*, “Synergistic enhancement of electrocatalytic CO₂ reduction to C₂ oxygenates at nitrogen-doped nanodiamonds/Cu interface,” *Nat. Nanotechnol.*, vol. 15, no. 2, pp. 131–137, Feb. 2020.
- [22] C. Xie *et al.*, “Tandem Catalysis for CO₂ Hydrogenation to C₂–C₄ Hydrocarbons,” *Nano Lett.*, vol. 17, no. 6, pp. 3798–3802, Jun. 2017.
- [23] S. Kattel, P. J. Ramírez, J. G. Chen, J. A. Rodriguez, and P. Liu, “Active sites for CO₂ hydrogenation to methanol on Cu/ZnO catalysts,” *Science* (80-.), vol. 355, no. 6331, pp. 1296–1299, Mar. 2017.
- [24] C. Vogt *et al.*, “Unravelling structure sensitivity in CO₂ hydrogenation over nickel,” *Nat. Catal.*, vol. 1, no. 2, pp. 127–134, Feb. 2018.
- [25] G. Zeng *et al.*, “Enhanced Photocatalytic Reduction of CO₂ to CO through TiO₂ Passivation of InP in Ionic Liquids,” *Chem. - A Eur. J.*, vol. 21, no. 39, pp. 13502–13507, Sep. 2015.
- [26] H. Rao, L. C. Schmidt, J. Bonin, and M. Robert, “Visible-light-driven methane formation from CO₂ with a molecular iron catalyst,” *Nature*, vol. 548, no. 7665, pp. 74–77, Aug. 2017.
- [27] K. Niu *et al.*, “A spongy nickel-organic CO₂ reduction photocatalyst for nearly 100% selective CO production,” *Sci. Adv.*, vol. 3, no. 7, p. e1700921, Jul. 2017.
- [28] X. Zhang *et al.*, “Product selectivity in plasmonic photocatalysis for carbon dioxide hydrogenation,” *Nat. Commun.*, vol. 8, no. 1, p. 14542, Apr. 2017.

- [29] X. Zhang *et al.*, “Plasmon-Enhanced Catalysis: Distinguishing Thermal and Nonthermal Effects,” *Nano Lett.*, vol. 18, no. 3, pp. 1714–1723, Mar. 2018.
- [30] S. Yu and P. K. Jain, “Plasmonic photosynthesis of C1–C3 hydrocarbons from carbon dioxide assisted by an ionic liquid,” *Nat. Commun.*, vol. 10, no. 1, p. 2022, Dec. 2019.
- [31] W. Hou, W. H. Hung, P. Pavaskar, A. Goepfert, M. Aykol, and S. B. Cronin, “Photocatalytic Conversion of CO₂ to Hydrocarbon Fuels via Plasmon-Enhanced Absorption and Metallic Interband Transitions,” *ACS Catal.*, vol. 1, no. 8, pp. 929–936, Aug. 2011.
- [32] M.-R. Kalus *et al.*, “Determining the role of redox-active materials during laser-induced water decomposition,” *Phys. Chem. Chem. Phys.*, vol. 21, no. 34, pp. 18636–18651, 2019.
- [33] A. V. Simakin *et al.*, “The Effect of Gold Nanoparticle Concentration and Laser Fluence on the Laser-Induced Water Decomposition,” *J. Phys. Chem. B*, vol. 123, no. 8, pp. 1869–1880, Feb. 2019.
- [34] A. Chen and B.-L. Lin, “A Simple Framework for Quantifying Electrochemical CO₂ Fixation,” *Joule*, vol. 2, no. 4, pp. 594–606, Apr. 2018.
- [35] D. Esrafilzadeh *et al.*, “Room temperature CO₂ reduction to solid carbon species on liquid metals featuring atomically thin ceria interfaces,” *Nat. Commun.*, vol. 10, no. 1, p. 865, Dec. 2019.
- [36] T. N. Lin, K. H. Chih, C. T. Yuan, J. L. Shen, C. A. J. Lin, and W. R. Liu, “Laser-ablation production of graphene oxide nanostructures: from ribbons to quantum dots,” *Nanoscale*, vol. 7, no. 6, pp. 2708–2715, 2015.
- [37] S. H. Kang *et al.*, “Ultrafast Method for Selective Design of Graphene Quantum Dots with Highly Efficient Blue Emission,” *Sci. Rep.*, vol. 6, no. 1, p. 38423, Dec. 2016.
- [38] S. Corvera and O. Gealekman, “Adipose tissue angiogenesis: Impact on obesity and type-2 diabetes,” *Biochim. Biophys. Acta - Mol. Basis Dis.*, vol. 1842, no. 3, pp. 463–472, Mar. 2014.

- [39] T. Del Rosso *et al.*, “Synthesis of oxocarbon-encapsulated gold nanoparticles with blue-shifted localized surface plasmon resonance by pulsed laser ablation in water with CO₂ absorbers,” *Nanotechnology*, vol. 27, no. 25, p. 255602, Jun. 2016.
- [40] B. Pan, J. Xiao, J. Li, P. Liu, C. Wang, and G. Yang, “Carbyne with finite length: The one-dimensional sp carbon,” *Sci. Adv.*, vol. 1, no. 9, p. e1500857, Oct. 2015.
- [41] C. S. Casari, M. Tommasini, R. R. Tykwinski, and A. Milani, “Carbon-atom wires: 1-D systems with tunable properties,” *Nanoscale*, vol. 8, no. 8, pp. 4414–4435, 2016.
- [42] S. Sahu, B. Behera, T. K. Maiti, and S. Mohapatra, “Simple one-step synthesis of highly luminescent carbon dots from orange juice: application as excellent bio-imaging agents,” *Chem. Commun.*, vol. 48, no. 70, p. 8835, 2012.
- [43] X. Wang, Y. Feng, P. Dong, and J. Huang, “A Mini Review on Carbon Quantum Dots: Preparation, Properties, and Electrocatalytic Application,” *Front. Chem.*, vol. 7, p. 671, Oct. 2019.
- [44] S. L. Prabu, T. N. K. Suriyaprakash, and R. Thirumurugan, “Medicated Nanoparticle for Gene Delivery,” in *Advanced Technology for Delivering Therapeutics*, InTech, 2017.
- [45] R. Mendes, A. Fernandes, and P. Baptista, “Gold Nanoparticle Approach to the Selective Delivery of Gene Silencing in Cancer—The Case for Combined Delivery?,” *Genes (Basel)*, vol. 8, no. 3, p. 94, Mar. 2017.
- [46] X. Gao, C. Du, Z. Zhuang, and W. Chen, “Carbon quantum dot-based nanoprobes for metal ion detection,” *J. Mater. Chem. C*, vol. 4, no. 29, pp. 6927–6945, 2016.
- [47] S. Chu, Y. Cui, and N. Liu, “The path towards sustainable energy,” *Nat. Mater.*, vol. 16, no. 1, pp. 16–22, Jan. 2017.
- [48] V. Amendola, “Surface plasmon resonance of silver and gold nanoparticles in the proximity of graphene studied using the discrete dipole

- approximation method,” *Phys. Chem. Chem. Phys.*, vol. 18, no. 3, pp. 2230–2241, 2016.
- [49] A. Loiseau, V. Asila, G. Boitel-Aullen, M. Lam, M. Salmain, and S. Boujday, “Silver-Based Plasmonic Nanoparticles for and Their Use in Biosensing,” *Biosensors*, vol. 9, no. 2, p. 78, Jun. 2019.
- [50] A. Carrillo-Cazares, N. P. Jiménez-Mancilla, M. A. Luna-Gutiérrez, K. Isaac-Olivé, and M. A. Camacho-López, “Study of the Optical Properties of Functionalized Gold Nanoparticles in Different Tissues and Their Correlation with the Temperature Increase,” *J. Nanomater.*, vol. 2017, pp. 1–9, 2017.
- [51] R. B. Heimann, S. E. Evsyukov, and L. Kavan, Eds., *Carbyne and Carbynoid Structures*, vol. 21. Dordrecht: Springer Netherlands, 1999.
- [52] J. C. Vinci *et al.*, “Spectroscopic Characteristics of Carbon Dots (C-Dots) Derived from Carbon Fibers and Conversion to Sulfur-Bridged C-Dots Nanosheets,” *Appl. Spectrosc.*, vol. 69, no. 9, pp. 1082–1090, Sep. 2015.
- [53] J. Hodkiewicz and T. F. Scientific, “Characterizing Carbon Materials with Raman Spectroscopy,” *Prog. Mater. Sci.*, 2005.
- [54] S. Arrhenius, “XXXI. On the influence of carbonic acid in the air upon the temperature of the ground,” *London, Edinburgh, Dublin Philos. Mag. J. Sci.*, vol. 41, no. 251, pp. 237–276, Apr. 1896.
- [55] D. Hoad, “The 2015 Paris Climate Agreement: Outcomes and their impacts on small island states,” *Island Studies Journal*. 2016.
- [56] S. Fuss *et al.*, “Betting on negative emissions,” *Nat. Clim. Chang.*, vol. 4, no. 10, pp. 850–853, Oct. 2014.
- [57] Z. Zhang *et al.*, “Emerging hydrovoltaic technology,” *Nat. Nanotechnol.*, vol. 13, no. 12, pp. 1109–1119, Dec. 2018.
- [58] C. Fei Guo, T. Sun, F. Cao, Q. Liu, and Z. Ren, “Metallic nanostructures for light trapping in energy-harvesting devices,” *Light Sci. Appl.*, vol. 3, no. 4, pp. e161–e161, Apr. 2014.

- [59] X. Zhang *et al.*, “Highly selective and active CO₂ reduction electrocatalysts based on cobalt phthalocyanine/carbon nanotube hybrid structures,” *Nat. Commun.*, vol. 8, no. 1, p. 14675, Apr. 2017.
- [60] J. Li *et al.*, “Efficient electrocatalytic CO₂ reduction on a three-phase interface,” *Nat. Catal.*, vol. 1, no. 8, pp. 592–600, Aug. 2018.
- [61] N. Srekanth and K. L. Phani, “Selective reduction of CO₂ to formate through bicarbonate reduction on metal electrodes: new insights gained from SG/TC mode of SECM,” *Chem. Commun.*, vol. 50, no. 76, pp. 11143–11146, 2014.co2
- [62] N. Hoshi, M. Kato, and Y. Hori, “Electrochemical reduction of CO₂ on single crystal electrodes of silver Ag(111), Ag(100) and Ag(110),” *J. Electroanal. Chem.*, vol. 440, no. 1–2, pp. 283–286, Dec. 1997.
- [63] S. Zhao, R. Jin, and R. Jin, “Opportunities and Challenges in CO₂ Reduction by Gold- and Silver-Based Electrocatalysts: From Bulk Metals to Nanoparticles and Atomically Precise Nanoclusters,” *ACS Energy Lett.*, vol. 3, no. 2, pp. 452–462, Feb. 2018.
- [64] Y. Chen, C. W. Li, and M. W. Kanan, “Aqueous CO₂ Reduction at Very Low Overpotential on Oxide-Derived Au Nanoparticles,” *J. Am. Chem. Soc.*, vol. 134, no. 49, pp. 19969–19972, Dec. 2012.
- [65] M. Ma, B. J. Trzeźniewski, J. Xie, and W. A. Smith, “Selective and Efficient Reduction of Carbon Dioxide to Carbon Monoxide on Oxide-Derived Nanostructured Silver Electrocatalysts,” *Angew. Chemie Int. Ed.*, vol. 55, no. 33, pp. 9748–9752, Aug. 2016.
- [66] L. C. Buelens, V. V. Galvita, H. Poelman, C. Detavernier, and G. B. Marin, “Super-dry reforming of methane intensifies CO₂ utilization via Le Chateliers principle,” *Science (80-.)*, vol. 354, no. 6311, pp. 449–452, Oct. 2016.
- [67] L. Protasova and F. Snijkers, “Recent developments in oxygen carrier materials for hydrogen production via chemical looping processes,” *Fuel*, vol. 181, pp. 75–93, Oct. 2016.

- [68] J. Castelo-Quibén *et al.*, “Carbon - iron electro-catalysts for CO₂ reduction. The role of the iron particle size,” *J. CO₂ Util.*, vol. 24, pp. 240–249, Mar. 2018.
- [69] D. Kim, C. S. Kley, Y. Li, and P. Yang, “Copper nanoparticle ensembles for selective electroreduction of CO₂ to C₂–C₃ products,” *Proc. Natl. Acad. Sci.*, vol. 114, no. 40, pp. 10560–10565, Oct. 2017.
- [70] S. Link and M. A. El-Sayed, “Shape and size dependence of radiative, non-radiative and photothermal properties of gold nanocrystals,” *Int. Rev. Phys. Chem.*, vol. 19, no. 3, pp. 409–453, Jul. 2000.
- [71] S. Yu, A. J. Wilson, J. Heo, and P. K. Jain, “Plasmonic Control of Multi-Electron Transfer and C–C Coupling in Visible-Light-Driven CO₂ Reduction on Au Nanoparticles,” *Nano Lett.*, vol. 18, no. 4, pp. 2189–2194, Apr. 2018.
- [72] P. Christopher, H. Xin, and S. Linic, “Visible-light-enhanced catalytic oxidation reactions on plasmonic silver nanostructures,” *Nat. Chem.*, vol. 3, no. 6, pp. 467–472, Jun. 2011.
- [73] F. A. Bettelheim, W. H. Brown, M. K. Campbell, and S. O. Farrell, *Introduction to General, Organic, and Biochemistry(9th)*. 2010.
- [74] F. A. Cotton, G. Wilkinson, C. a. Murillo, and M. Bochmann, “Advanced Inorganic Chemistry, 6th Edition,” *Wiley-Interscience: New York*. 1999.
- [75] J. Meija *et al.*, “Atomic weights of the elements 2013 (IUPAC Technical Report),” *Pure Appl. Chem.*, vol. 88, no. 3, pp. 265–291, Mar. 2016.
- [76] M. Ilbert and V. Bonnefoy, “Insight into the evolution of the iron oxidation pathways,” *Biochim. Biophys. Acta - Bioenerg.*, vol. 1827, no. 2, pp. 161–175, Feb. 2013.
- [77] W. Sinha, M. G. Sommer, N. Deibel, F. Ehret, B. Sarkar, and S. Kar, “Silver corrole complexes: unusual oxidation states and near-IR-absorbing dyes,” *Chemistry*, 2014.
- [78] P. J. Sadler, “Gold—Progress in Chemistry, Biochemistry and Technology,” *Appl. Organomet. Chem.*, vol. 14, no. 3, pp. 171–171, Mar.

2000.

- [79] H. Muto, K. Yamada, K. Miyajima, and F. Mafuné, “Estimation of Surface Oxide on Surfactant-Free Gold Nanoparticles Laser-Ablated in Water,” *J. Phys. Chem. C*, vol. 111, no. 46, pp. 17221–17226, Nov. 2007.
- [80] J. P. Sylvestre *et al.*, “Surface chemistry of gold nanoparticles produced by laser ablation in aqueous media,” *J. Phys. Chem. B*, vol. 108, no. 43, pp. 16864–16869, 2004.
- [81] P. K. Baruah, A. Singh, L. Rangan, A. K. Sharma, and A. Khare, “Elucidation of size , structure , surface plasmon resonance , and photoluminescence of Ag nanoparticles synthesized by pulsed laser ablation in distilled water and its viability as SERS substrate,” *Appl. Phys. A*, vol. 126, no. 3, pp. 1–15, Mar. 2020.
- [82] V. Amendola *et al.*, “Magnetic iron oxide nanoparticles with tunable size and free surface obtained via a ‘green’ approach based on laser irradiation in water,” *J. Mater. Chem.*, vol. 21, no. 46, p. 18665, 2011.
- [83] E. Vahabzadeh and M. J. Torkamany, “Iron Oxide Nanocrystals Synthesis by Laser Ablation in Water: Effect of Laser Wavelength,” *J. Clust. Sci.*, vol. 25, no. 4, pp. 959–968, Jul. 2014.
- [84] T. Iwamoto and T. Ishigaki, “Fabrication of iron oxide nanoparticles using laser ablation in liquids,” in *Journal of Physics: Conference Series*, 2013.
- [85] T. J. Bergendahl, “The oxidation states of gold,” *J. Chem. Educ.*, vol. 52, no. 11, p. 731, Nov. 1975.
- [86] N. Saliba, D. . Parker, and B. . Koel, “Adsorption of oxygen on Au(111) by exposure to ozone,” *Surf. Sci.*, vol. 410, no. 2–3, pp. 270–282, Aug. 1998.
- [87] D. D. Eley and P. B. Moore, “Adsorption of oxygen on gold,” *Surf. Sci.*, vol. 76, no. 2, pp. L599–L602, Sep. 1978.
- [88] T. Dickinson, A. F. Povey, and P. M. A. Sherwood, “X-ray photoelectron spectroscopic studies of oxide films on platinum and gold electrodes,” *J. Chem. Soc. Faraday Trans. 1 Phys. Chem. Condens. Phases*, vol. 71, p. 298, 1975.

- [89] J. . Gottfried, N. Elghobashi, S. L. . Schroeder, and K. Christmann, "Oxidation of gold by oxygen-ion sputtering," *Surf. Sci.*, vol. 523, no. 1–2, pp. 89–102, Jan. 2003.
- [90] K. Juodkazis, "XPS studies on the gold oxide surface layer formation," *Electrochem. commun.*, vol. 2, no. 7, pp. 503–507, Jul. 2000.
- [91] E. Irissou, M.-C. Denis, M. Chaker, and D. Guay, "Gold oxide thin film grown by pulsed laser deposition in an O₂ atmosphere," *Thin Solid Films*, vol. 472, no. 1–2, pp. 49–57, Jan. 2005.
- [92] H. Shi, R. Asahi, and C. Stampfl, "Properties of the gold oxides Au₂O₃ and Au₂O : First-principles investigation," *Phys. Rev. B*, vol. 75, no. 20, p. 205125, May 2007.
- [93] J. J. Pireaux, M. Liehr, P. A. Thiry, J. P. Delrue, and R. Caudano, "Electron spectroscopic characterization of oxygen adsorption on gold surfaces. II. Production of gold oxide in oxygen DC reactive sputtering," *Surf. Sci.*, 1984.
- [94] L. K. Ono and B. R. Cuenya, "Formation and thermal stability of Au₂O₃ on gold nanoparticles: Size and support effects," *J. Phys. Chem. C*, 2008.
- [95] O. Diaz-Morales, F. Calle-Vallejo, C. de Munck, and M. T. M. Koper, "Electrochemical water splitting by gold: evidence for an oxide decomposition mechanism," *Chem. Sci.*, vol. 4, no. 6, p. 2334, 2013.
- [96] A. Ziashahabi, M. Prato, Z. Dang, R. Poursalehi, and N. Naseri, "The effect of silver oxidation on the photocatalytic activity of Ag/ZnO hybrid plasmonic/metal-oxide nanostructures under visible light and in the dark," *Sci. Rep.*, vol. 9, no. 1, p. 11839, Dec. 2019.
- [97] L. Vinet and A. Zhedanov, "A 'missing' family of classical orthogonal polynomials," *WILEY-VCH GmbH&Co. KGaA*, Nov. 2010.
- [98] L. Machala, J. Tuček, and R. Zbořil, "Polymorphous Transformations of Nanometric Iron(III) Oxide: A Review," *Chem. Mater.*, vol. 23, no. 14, pp. 3255–3272, Jul. 2011.
- [99] S. Babay, T. Mhiri, and M. Toumi, "Synthesis, structural and spectroscopic

- characterizations of maghemite γ -Fe₂O₃ prepared by one-step coprecipitation route,” *J. Mol. Struct.*, vol. 1085, pp. 286–293, Apr. 2015.
- [100] R. Zboril, M. Mashlan, and D. Petridis, “Iron(III) Oxides from Thermal Processes Synthesis, Structural and Magnetic Properties, Mössbauer Spectroscopy Characterization, and Applications †,” *Chem. Mater.*, vol. 14, no. 3, pp. 969–982, Mar. 2002.
- [101] H. Xu, X. Wang, and L. Zhang, “Selective preparation of nanorods and micro-octahedrons of Fe₂O₃ and their catalytic performances for thermal decomposition of ammonium perchlorate,” *Powder Technol.*, vol. 185, no. 2, pp. 176–180, Jul. 2008.
- [102] *Chemistry of the Elements*. 1997.
- [103] P. Majewski and B. Thierry, “Functionalized Magnetite Nanoparticles—Synthesis, Properties, and Bioapplications,” in *Particulate Systems in Nano- and Biotechnologies*, CRC Press, 2008, pp. 331–352.
- [104] A. K. Gupta and M. Gupta, “Synthesis and surface engineering of iron oxide nanoparticles for biomedical applications,” *Biomaterials*, vol. 26, no. 18, pp. 3995–4021, Jun. 2005.
- [105] B. S. Kariman, F. M. Aghamir, and H. R. Yousefi, “Synthesis of Au/Fe₃O₄ Magnetic Nanoparticles by Laser Ablation in Organic Solvents,” *J. Clust. Sci.*, vol. 26, no. 4, pp. 1373–1388, Jul. 2015.
- [106] E. Fazio, M. Santoro, G. Lentini, D. Franco, S. P. P. Guglielmino, and F. Neri, “Iron oxide nanoparticles prepared by laser ablation: Synthesis, structural properties and antimicrobial activity,” *Colloids Surfaces A Physicochem. Eng. Asp.*, vol. 490, pp. 98–103, Feb. 2016.
- [107] C. Xu and S. Sun, “New forms of superparamagnetic nanoparticles for biomedical applications,” *Advanced Drug Delivery Reviews*. 2013.
- [108] E. Fortin and F. L. Weichman, “Photoconductivity in Ag₂O,” *Phys. status solidi*, vol. 5, no. 3, pp. 515–519, 1964.
- [109] S. Giannakis *et al.*, “Iron oxide-mediated semiconductor photocatalysis vs. heterogeneous photo-Fenton treatment of viruses in wastewater. Impact of

- the oxide particle size.,” *J. Hazard. Mater.*, vol. 339, pp. 223–231, Oct. 2017.
- [110] Z. Lin, C. Du, B. Yan, and G. Yang, “Amorphous Fe₂O₃ for photocatalytic hydrogen evolution,” *Catal. Sci. Technol.*, vol. 9, no. 20, pp. 5582–5592, 2019.
- [111] X. Wang, S. Li, H. Yu, J. Yu, and S. Liu, “Ag₂O as a New Visible-Light Photocatalyst: Self-Stability and High Photocatalytic Activity,” *Chem. – A Eur. J.*, vol. 17, no. 28, pp. 7777–7780, Jul. 2011.
- [112] J. Roithová and D. Schröder, “Gas-Phase Models for Catalysis: Alkane Activation and Olefin Epoxidation by the Triatomic Cation Ag₂O⁺,” *J. Am. Chem. Soc.*, vol. 129, no. 49, pp. 15311–15318, Dec. 2007.
- [113] T. Ivanova, T. Homola, A. Bryukvin, and D. Cameron, “Catalytic Performance of Ag₂O and Ag Doped CeO₂ Prepared by Atomic Layer Deposition for Diesel Soot Oxidation,” *Coatings*, vol. 8, no. 7, p. 237, Jul. 2018.
- [114] Y. Zhang *et al.*, “Boosting the catalysis of gold by O₂ activation at Au-SiO₂ interface,” *Nat. Commun.*, vol. 11, no. 1, p. 558, Dec. 2020.
- [115] F. Pei *et al.*, “Electronic and Optical Properties of Noble Metal Oxides M₂SO (M = Cu, Ag and Au): First-principles Study,” *J. Korean Phys. Soc.*, vol. 55, no. 3(2), pp. 1243–1249, Sep. 2009.
- [116] D. Gao *et al.*, “Enhancing CO₂ Electroreduction with the Metal–Oxide Interface,” *J. Am. Chem. Soc.*, vol. 139, no. 16, pp. 5652–5655, Apr. 2017.
- [117] V. I. Klimov, J. A. McGuire, R. D. Schaller, and V. I. Rupasov, “Scaling of multiexciton lifetimes in semiconductor nanocrystals,” *Phys. Rev. B*, vol. 77, no. 19, p. 195324, May 2008.
- [118] G. M. Whitesides, “The ‘right’ size in nanobiotechnology,” *Nat. Biotechnol.*, vol. 21, no. 10, pp. 1161–1165, Oct. 2003.
- [119] P. Tartaj, M. a del P. Morales, S. Veintemillas-Verdaguer, T. González-Carretero, and C. J. Serna, “The preparation of magnetic nanoparticles for applications in biomedicine,” *J. Phys. D. Appl. Phys.*, vol. 36, no. 13, pp.

- R182–R197, Jul. 2003.
- [120] M. Quinten, *Optical Properties of Nanoparticle Systems*. Weinheim, Germany: Wiley-VCH Verlag GmbH & Co. KGaA, 2011.
- [121] I. Khan, K. Saeed, and I. Khan, “Nanoparticles: Properties, applications and toxicities,” *Arab. J. Chem.*, vol. 12, no. 7, pp. 908–931, Nov. 2019.
- [122] E. C. Dreaden, A. M. Alkilany, X. Huang, C. J. Murphy, and M. A. El-Sayed, “The golden age: gold nanoparticles for biomedicine,” *Chem. Soc. Rev.*, vol. 41, no. 7, pp. 2740–2779, Apr. 2012.
- [123] J. M. Caster, A. N. Patel, T. Zhang, and A. Wang, “Investigational nanomedicines in 2016: a review of nanotherapeutics currently undergoing clinical trials,” *Wiley Interdiscip. Rev. Nanomedicine Nanobiotechnology*, vol. 9, no. 1, p. e1416, Jan. 2017.
- [124] K. E. Fong and L.-Y. L. Yung, “Localized surface plasmon resonance: a unique property of plasmonic nanoparticles for nucleic acid detection,” *Nanoscale*, vol. 5, no. 24, p. 12043, 2013.
- [125] J. Jana, M. Ganguly, and T. Pal, “Enlightening surface plasmon resonance effect of metal nanoparticles for practical spectroscopic application,” *RSC Advances*. 2016.
- [126] J. Liu, M. Jalali, S. Mahshid, and S. Wachsmann-Hogiu, “Are plasmonic optical biosensors ready for use in point-of-need applications?,” *Analyst*. 2020.
- [127] M. Pavlin and V. B. Bregar, “Stability of nanoparticle suspensions in different biologically relevant media,” *Dig. J. Nanomater. Biostructures*, vol. 7, no. 4, 2012.
- [128] C. Rehbock, V. Merk, L. Gamrad, R. Streubel, and S. Barcikowski, “Size control of laser-fabricated surfactant-free gold nanoparticles with highly diluted electrolytes and their subsequent bioconjugation,” *Phys. Chem. Chem. Phys.*, vol. 15, no. 9, pp. 3057–3067, 2013.
- [129] Y. Lu, Y. Yin, Z.-Y. Li, and Y. Xia, “Synthesis and Self-Assembly of Au@SiO₂ Core–Shell Colloids,” *Nano Lett.*, vol. 2, no. 7, pp. 785–788,

Jul. 2002.

- [130] T. L. Moore *et al.*, “Nanoparticle colloidal stability in cell culture media and impact on cellular interactions,” *Chem. Soc. Rev.*, 2015.
- [131] J. Wolfram *et al.*, “Safety of Nanoparticles in Medicine,” *Curr. Drug Targets*, 2015.
- [132] J. V. Jokerst and S. S. Gambhir, “Molecular Imaging with Theranostic Nanoparticles,” *Acc. Chem. Res.*, vol. 44, no. 10, pp. 1050–1060, Oct. 2011.
- [133] J. Hainfeld and Huang, “Intravenous magnetic nanoparticle cancer hyperthermia,” *Int. J. Nanomedicine*, p. 2521, Jul. 2013.
- [134] G. Margheri *et al.*, “Tumor-tropic endothelial colony forming cells (ECFCs) loaded with near-infrared sensitive Au nanoparticles: A cellular stove approach to the photobleaching of melanoma,” *Oncotarget*, vol. 7, no. 26, Jun. 2016.
- [135] V. P. S. Jesus, L. Raniero, G. M. Lemes, T. T. Bhattacharjee, P. C. Caetano Júnior, and M. L. Castilho, “Nanoparticles of methylene blue enhance photodynamic therapy,” *Photodiagnosis Photodyn. Ther.*, vol. 23, pp. 212–217, Sep. 2018.
- [136] J. B. Vines, J.-H. Yoon, N.-E. Ryu, D.-J. Lim, and H. Park, “Gold Nanoparticles for Photothermal Cancer Therapy,” *Front. Chem.*, vol. 7, p. 120, Apr. 2019.
- [137] S. Huo *et al.*, “Ultrasmall Gold Nanoparticles as Carriers for Nucleus-Based Gene Therapy Due to Size-Dependent Nuclear Entry,” *ACS Nano*, vol. 8, no. 6, pp. 5852–5862, Jun. 2014.
- [138] J. Yoo *et al.*, “Electromagnetized gold nanoparticles mediate direct lineage reprogramming into induced dopamine neurons in vivo for Parkinson’s disease therapy,” *Nat. Nanotechnol.*, vol. 12, no. 10, pp. 1006–1014, Oct. 2017.
- [139] S. Barcikowski and G. Compagnini, “Advanced nanoparticle generation and excitation by lasers in liquids,” *Phys. Chem. Chem. Phys.*, vol. 15, no.

- 9, pp. 3022–3026, 2013.
- [140] F. Mafuné, J. Kohno, Y. Takeda, and T. Kondow, “Dissociation and Aggregation of Gold Nanoparticles under Laser Irradiation,” *J. Phys. Chem. B*, vol. 105, no. 38, pp. 9050–9056, Sep. 2001.
- [141] F. Giammanco, E. Giorgetti, P. Marsili, and A. Giusti, “Experimental and Theoretical Analysis of Photofragmentation of Au Nanoparticles by Picosecond Laser Radiation,” *J. Phys. Chem. C*, vol. 114, no. 8, pp. 3354–3363, Mar. 2010.
- [142] D. Zhang, B. Gökce, and S. Barcikowski, “Laser Synthesis and Processing of Colloids: Fundamentals and Applications,” *Chem. Rev.*, vol. 117, no. 5, pp. 3990–4103, Mar. 2017.
- [143] D. L. da Cunha, G. F. C. Pereira, J. F. Felix, J. Albino Aguiar, and W. M. de Azevedo, “Nanostructured hydrocerussite compound ($\text{Pb}_3(\text{CO}_3)_2(\text{OH})_2$) prepared by laser ablation technique in liquid environment,” *Mater. Res. Bull.*, vol. 49, pp. 172–175, Jan. 2014.
- [144] P. R. Willmott and J. R. Huber, “Pulsed laser vaporization and deposition,” *Rev. Mod. Phys.*, vol. 72, no. 1, pp. 315–328, Jan. 2000.
- [145] M. F. Becker *et al.*, “Metal nanoparticles generated by laser ablation,” *Nanostructured Mater.*, 1998.
- [146] R. M. Tilaki, A. I. Zad, and S. M. Mahdavi, “Size, composition and optical properties of copper nanoparticles prepared by laser ablation in liquids,” *Appl. Phys. A Mater. Sci. Process.*, 2007.
- [147] X. Liu, D. Du, and G. Mourou, “Laser ablation and micromachining with ultrashort laser pulses,” *IEEE J. Quantum Electron.*, vol. 33, no. 10, pp. 1706–1716, 1997.
- [148] R. Hibst and U. Keller, “Experimental studies of the application of the Er:YAG laser on dental hard substances: I. Measurement of the ablation rate,” *Lasers Surg. Med.*, vol. 9, no. 4, pp. 338–344, 1989.
- [149] S. H. Chung and E. Mazur, “Surgical applications of femtosecond lasers,” *J. Biophotonics*, vol. 2, no. 10, pp. 557–572, Oct. 2009.

- [150] M. Chakravarthi, R. Shilpakar, and K. . Shankar, “Carbon dioxide laser guidelines,” *J. Cutan. Aesthet. Surg.*, vol. 2, no. 2, p. 72, 2009.
- [151] S. Siano *et al.*, “Laser cleaning in conservation of stone, metal, and painted artifacts: state of the art and new insights on the use of the Nd:YAG lasers,” *Appl. Phys. A*, vol. 106, no. 2, pp. 419–446, Feb. 2012.
- [152] R. A. Ganeev *et al.*, “Pulsed laser deposition of metal films and nanoparticles in vacuum using subnanosecond laser pulses,” *Appl. Opt.*, vol. 46, no. 8, p. 1205, Mar. 2007.
- [153] J. Cheung and J. Horwitz, “Pulsed Laser Deposition History and Laser-Target Interactions,” *MRS Bull.*, vol. 17, no. 2, pp. 30–36, Feb. 1992.
- [154] T. Omi and K. Numano, “The Role of the CO₂ Laser and Fractional CO₂ Laser in Dermatology,” *LASER Ther.*, vol. 23, no. 1, pp. 49–60, 2014.
- [155] J. Ihlemann and B. Wolff-Rottke, “Excimer laser micro machining of inorganic dielectrics,” *Appl. Surf. Sci.*, vol. 106, pp. 282–286, Oct. 1996.
- [156] D. Perez and L. J. Lewis, “Molecular-dynamics study of ablation of solids under femtosecond laser pulses,” *Phys. Rev. B*, vol. 67, no. 18, p. 184102, May 2003.
- [157] B. Jaeggi, B. Neuenschwander, M. Schmid, M. Mural, J. Zuercher, and U. Hunziker, “Influence of the Pulse Duration in the ps-Regime on the Ablation Efficiency of Metals,” *Phys. Procedia*, vol. 12, pp. 164–171, 2011.
- [158] B. Zheng, G. Jiang, W. Wang, K. Wang, and X. Mei, “Ablation experiment and threshold calculation of titanium alloy irradiated by ultra-fast pulse laser,” *AIP Adv.*, vol. 4, no. 3, p. 031310, Mar. 2014.
- [159] A. Sikora, D. Grojo, and M. Sentis, “Wavelength scaling of silicon laser ablation in picosecond regime,” *J. Appl. Phys.*, vol. 122, no. 4, p. 045702, Jul. 2017.
- [160] A. Semerok *et al.*, “Experimental investigations of laser ablation efficiency of pure metals with femto, pico and nanosecond pulses,” *Appl. Surf. Sci.*, vol. 138–139, pp. 311–314, Jan. 1999.

- [161] M. Hashida, A. . Semerok, O. Gobert, G. Petite, Y. Izawa, and J. .- Wagner, “Ablation threshold dependence on pulse duration for copper,” *Appl. Surf. Sci.*, vol. 197–198, pp. 862–867, Sep. 2002.
- [162] A. V. Gusarov and I. Smurov, “Thermal model of nanosecond pulsed laser ablation: Analysis of energy and mass transfer,” *J. Appl. Phys.*, vol. 97, no. 1, p. 014307, Jan. 2005.
- [163] E. G. Gamaly, N. R. Madsen, M. Duering, A. V. Rode, V. Z. Kolev, and B. Luther-Davies, “Ablation of metals with picosecond laser pulses: Evidence of long-lived nonequilibrium conditions at the surface,” *Phys. Rev. B*, vol. 71, no. 17, p. 174405, May 2005.
- [164] J. Long *et al.*, “Early dynamics of cavitation bubbles generated during ns laser ablation of submerged targets,” *Opt. Express*, vol. 28, no. 10, p. 14300, May 2020.
- [165] J. Hohlfeld, S. S. Wellershoff, J. Güdde, U. Conrad, V. Jähnke, and E. Matthias, “Electron and lattice dynamics following optical excitation of metals,” *Chem. Phys.*, 2000.
- [166] G. L. Eesley, “Generation of nonequilibrium electron and lattice temperatures in copper by picosecond laser pulses,” *Phys. Rev. B*, 1986.
- [167] H. E. Elsayed-Ali, T. B. Norris, M. A. Pessot, and G. A. Mourou, “Time-resolved observation of electron-phonon relaxation in copper,” *Phys. Rev. Lett.*, vol. 58, no. 12, pp. 1212–1215, Mar. 1987.
- [168] S. Anisimov, B. Kapeliovich, and T. Perel’Man, “Electron emission from metal surfaces exposed to ultrashort laser pulses,” *Sov. J. Exp. Theor. Phys.*, 1974.
- [169] B. H. H. Christensen, K. Vestentoft, and P. Balling, “Short-pulse ablation rates and the two-temperature model,” *Appl. Surf. Sci.*, vol. 253, no. 15, pp. 6347–6352, May 2007.
- [170] L. Jiang and H.-L. Tsai, “Improved Two-Temperature Model and Its Application in Ultrashort Laser Heating of Metal Films,” *J. Heat Transfer*, vol. 127, no. 10, pp. 1167–1173, Oct. 2005.

- [171] E. G. Gamaly, A. V. Rode, V. T. Tikhonchuk, and B. Luther-Davies, “Electrostatic mechanism of ablation by femtosecond lasers,” *Appl. Surf. Sci.*, vol. 197–198, pp. 699–704, Sep. 2002.
- [172] N. M. Bulgakova, R. Stoian, A. Rosenfeld, I. V. Hertel, W. Marine, and E. E. B. Campbell, “A general continuum approach to describe fast electronic transport in pulsed laser irradiated materials: The problem of Coulomb explosion,” *Appl. Phys. A Mater. Sci. Process.*, 2005.
- [173] T. Sakka, S. Iwanaga, Y. H. Ogata, A. Matsunawa, and T. Takemoto, “Laser ablation at solid–liquid interfaces: An approach from optical emission spectra,” *J. Chem. Phys.*, vol. 112, no. 19, pp. 8645–8653, May 2000.
- [174] R. Fabbro, J. Fournier, P. Ballard, D. Devaux, and J. Virmont, “Physical study of laser-produced plasma in confined geometry,” *J. Appl. Phys.*, vol. 68, no. 2, pp. 775–784, Jul. 1990.
- [175] R. Cubeddu, D. Comelli, C. D’Andrea, P. Taroni, and G. Valentini, “Time-resolved fluorescence imaging in biology and medicine,” *Journal of Physics D: Applied Physics*. 2002.
- [176] A. De Giacomo *et al.*, “Laser Ablation of Graphite in Water in a Range of Pressure from 1 to 146 atm Using Single and Double Pulse Techniques for the Production of Carbon Nanostructures,” *J. Phys. Chem. C*, vol. 115, no. 12, pp. 5123–5130, Mar. 2011.
- [177] G. Compagnini, A. A. Scalisi, and O. Puglisi, “Production of gold nanoparticles by laser ablation in liquid alkanes,” *J. Appl. Phys.*, vol. 94, no. 12, p. 7874, 2003.
- [178] V. Amendola and M. Meneghetti, “Controlled size manipulation of free gold nanoparticles by laser irradiation and their facile bioconjugation,” *J. Mater. Chem.*, vol. 17, no. 44, p. 4705, 2007.
- [179] W. T. Nichols, T. Sasaki, and N. Koshizaki, “Laser ablation of a platinum target in water. II. Ablation rate and nanoparticle size distributions,” *J. Appl. Phys.*, vol. 100, no. 11, p. 114912, 2006.

- [180] M.-R. Kalus, V. Reimer, S. Barcikowski, and B. Gökce, “Discrimination of effects leading to gas formation during pulsed laser ablation in liquids,” *Appl. Surf. Sci.*, vol. 465, pp. 1096–1102, Jan. 2019.
- [181] M.-R. Kalus, N. Bärsch, R. Streubel, E. Gökce, S. Barcikowski, and B. Gökce, “How persistent microbubbles shield nanoparticle productivity in laser synthesis of colloids – quantification of their volume, dwell dynamics, and gas composition,” *Phys. Chem. Chem. Phys.*, vol. 19, no. 10, pp. 7112–7123, 2017.
- [182] E. V. Barmina, S. V. Gudkov, A. V. Simakin, and G. A. Shafeev, “Stable Products of Laser-Induced Breakdown of Aqueous Colloidal Solutions of Nanoparticles,” *J. Laser Micro/Nanoengineering*, vol. 12, no. 3, Dec. 2017.
- [183] A. De Giacomo *et al.*, “Cavitation dynamics of laser ablation of bulk and wire-shaped metals in water during nanoparticles production,” *Phys. Chem. Chem. Phys.*, vol. 15, no. 9, pp. 3083–3092, 2013.
- [184] I. Akhatov, O. Lindau, A. Topolnikov, R. Mettin, N. Vakhitova, and W. Lauterborn, “Collapse and rebound of a laser-induced cavitation bubble,” *Phys. Fluids*, vol. 13, no. 10, pp. 2805–2819, Oct. 2001.
- [185] M. C. Sportelli *et al.*, “Exceptionally stable silver nanoparticles synthesized by laser ablation in alcoholic organic solvent,” *Colloids Surfaces A Physicochem. Eng. Asp.*, 2018.
- [186] C. E. Marshall, “‘Theory of the stability of lyophobic colloids. The interaction of particles having an electric double layer.’ E. J. W. Verwey and J. T. G. Overbeek, with the collaboration of K. van Ness. Elsevier, New York-Amsterdam, 1948, 216 pp., \$4.50,” *J. Polym. Sci.*, vol. 4, no. 3, pp. 413–414, Jun. 1949.
- [187] H.-C. Schwarzer and W. Peukert, “Prediction of aggregation kinetics based on surface properties of nanoparticles,” *Chem. Eng. Sci.*, vol. 60, no. 1, pp. 11–25, Jan. 2005.
- [188] L. J. Morgan, “Polymeric stabilization of colloidal dispersions,” *Colloids and Surfaces*, vol. 15, pp. 356–357, Jan. 1985.

- [189] S. K. Tuteja, M. Kukkar, P. Kumar, A. K. Paul, and A. Deep, “Synthesis and Characterization of Silica-Coated Silver Nanoprobe for Paraoxon pesticide Detection,” *Bionanoscience*, vol. 4, no. 2, pp. 149–156, Jun. 2014.
- [190] N. Chopra, L. G. Bachas, and M. R. Knecht, “Fabrication and Biofunctionalization of Carbon-Encapsulated Au Nanoparticles,” *Chem. Mater.*, vol. 21, no. 7, pp. 1176–1178, Apr. 2009.
- [191] J. T. . Overbeek, “Recent developments in the understanding of colloid stability,” *J. Colloid Interface Sci.*, vol. 58, no. 2, pp. 408–422, Feb. 1977.
- [192] M. Ujihara and T. Imae, “Versatile one-pot synthesis of confeito-like Au nanoparticles and their surface-enhanced Raman scattering effect,” *Colloids Surfaces A Physicochem. Eng. Asp.*, vol. 436, pp. 380–385, Sep. 2013.
- [193] E. Giorgetti, P. Marsili, F. Giammanco, S. Trigari, C. Gellini, and M. Muniz-Miranda, “Ag nanoparticles obtained by pulsed laser ablation in water: surface properties and SERS activity,” *J. Raman Spectrosc.*, vol. 46, no. 5, pp. 462–469, May 2015.
- [194] M. Sportelli *et al.*, “The Pros and Cons of the Use of Laser Ablation Synthesis for the Production of Silver Nano-Antimicrobials,” *Antibiotics*, vol. 7, no. 3, p. 67, Jul. 2018.
- [195] F. Mafuné, J. Kohno, Y. Takeda, T. Kondow, and H. Sawabe, “Structure and Stability of Silver Nanoparticles in Aqueous Solution Produced by Laser Ablation,” *J. Phys. Chem. B*, vol. 104, no. 35, pp. 8333–8337, Sep. 2000.
- [196] S. Dadashi, R. Poursalehi, and H. Delavari, “Structural and Optical Properties of Pure Iron and Iron Oxide Nanoparticles Prepared via Pulsed Nd:YAG Laser Ablation in Liquid,” *Procedia Mater. Sci.*, vol. 11, pp. 722–726, 2015.
- [197] F. Piccapietra, L. Sigg, and R. Behra, “Colloidal stability of carbonate-coated silver nanoparticles in synthetic and natural freshwater,” *Environ. Sci. Technol.*, 2012.

- [198] B. Molleman and T. Hiemstra, “Time, pH, and size dependency of silver nanoparticle dissolution: the road to equilibrium,” *Environ. Sci. Nano*, vol. 4, no. 6, pp. 1314–1327, 2017.
- [199] B. Perito, E. Giorgetti, P. Marsili, and M. Muniz-Miranda, “Antibacterial activity of silver nanoparticles obtained by pulsed laser ablation in pure water and in chloride solution,” *Beilstein J. Nanotechnol.*, 2016.
- [200] M. Bobik, I. Korus, and L. Dudek, “The effect of magnetite nanoparticles synthesis conditions on their ability to separate heavy metal ions,” *Arch. Environ. Prot.*, vol. 43, no. 2, pp. 3–9, Jun. 2017.
- [201] STEFAN A. MAIER, *Plasmonics: Fundamentals and Applications*. New York: Springer, 2007.
- [202] H. Raether, *Surface Plasmons on Smooth and Rough Surfaces and on Gratings*. 1988.
- [203] S. L. Kleinman *et al.*, “Structure Enhancement Factor Relationships in Single Gold Nanoantennas by Surface-Enhanced Raman Excitation Spectroscopy,” *J. Am. Chem. Soc.*, vol. 135, no. 1, pp. 301–308, Jan. 2013.
- [204] L. Guo, J. A. Jackman, H.-H. Yang, P. Chen, N.-J. Cho, and D.-H. Kim, “Strategies for enhancing the sensitivity of plasmonic nanosensors,” *Nano Today*, vol. 10, no. 2, pp. 213–239, Apr. 2015.
- [205] Michael Quinten, “Optical Properties of Nanoparticle Systems: Mie and beyond - Quinten - Wiley Online Library,” *Wiley-VCH Verlag GmbH & Co. KGaA, Weinheim*, 2011. .
- [206] S. A. Maier, “Surface Plasmon Polaritons at Metal / Insulator Interfaces,” in *Plasmonics: Fundamentals and Applications*, New York, NY: Springer US, 2007, pp. 21–37.
- [207] V. Amendola and M. Meneghetti, “Size Evaluation of Gold Nanoparticles by UV–vis Spectroscopy,” *J. Phys. Chem. C*, vol. 113, no. 11, pp. 4277–4285, Mar. 2009.
- [208] G. Mie, “Beiträge zur Optik trüber Medien, speziell kolloidaler Metallösungen,” *Ann. Phys.*, vol. 330, no. 3, pp. 377–445, 1908.

- [209] Q. Zaman *et al.*, “Two-color surface plasmon resonance nanosizer for gold nanoparticles,” *Opt. Express*, vol. 27, no. 3, p. 3200, Feb. 2019.
- [210] L. B. Scaffardi, N. Pellegrini, O. de Sanctis, and J. O. Tocho, “Sizing gold nanoparticles by optical extinction spectroscopy,” *Nanotechnology*, vol. 16, no. 1, pp. 158–163, Jan. 2005.
- [211] G. Méjean *et al.*, “Towards a supercontinuum-based infrared lidar,” *Appl. Phys. B Lasers Opt.*, vol. 77, no. 2–3, pp. 357–359, Sep. 2003.
- [212] G. M. Jean, J. Kasparian, J. Yu, S. Frey, E. Salmon, and J.-P. Wolf, “Remote detection and identification of biological aerosols using a femtosecond terawatt lidar system,” *Appl. Phys. B Lasers Opt.*, vol. 78, no. 5, pp. 535–537, Mar. 2004.
- [213] A. C. Templeton, J. J. Pietron, R. W. Murray, and P. Mulvaney, “Solvent Refractive Index and Core Charge Influences on the Surface Plasmon Absorbance of Alkanethiolate Monolayer-Protected Gold Clusters,” *J. Phys. Chem. B*, vol. 104, no. 3, pp. 564–570, Jan. 2000.
- [214] A. Milani *et al.*, “Raman spectroscopy as a tool to investigate the structure and electronic properties of carbon-atom wires,” *Beilstein J. Nanotechnol.*, vol. 6, pp. 480–491, Feb. 2015.
- [215] L. E. Valenti and C. E. Giacomelli, “Stability of silver nanoparticles: agglomeration and oxidation in biological relevant conditions,” *J. Nanoparticle Res.*, vol. 19, no. 5, p. 156, May 2017.
- [216] N. W. P. de Souza, J. S. Costa, R. C. dos Santos, A. F. S. da Cruz, T. Del Rosso, and K. Q. da Costa, “Modal Analysis of Surface Plasmon Resonance Sensor Coupled to Periodic Array of Core-Shell Metallic Nanoparticles,” in *Resonance*, InTech, 2017.
- [217] C. S. S. R. Kumar, *Raman Spectroscopy for Nanomaterials Characterization*. Berlin, Heidelberg: Springer Berlin Heidelberg, 2012.
- [218] H. Guo, L. He, and B. Xing, “Applications of surface-enhanced Raman spectroscopy in the analysis of nanoparticles in the environment,” *Environ. Sci. Nano*, vol. 4, no. 11, pp. 2093–2107, 2017.

- [219] P. R. Griffiths and J. A. de Haseth, *Fourier Transform Infrared Spectrometry*. Hoboken, NJ, USA, NJ, USA: John Wiley & Sons, Inc., 2007.
- [220] J. R. Ferraro, K. Nakamoto, and C. W. Brown, *Introductory Raman Spectroscopy: Second Edition*. 2003.
- [221] R. Aroca, *Surface-Enhanced Vibrational Spectroscopy*. Chichester, UK: John Wiley & Sons, Ltd, 2006.
- [222] T. TAKENAKA, "Surface Enhanced Raman Scattering," *Rev. Laser Eng.*, vol. 9, no. 5, pp. 478–495, 1981.
- [223] M. Muniz-Miranda, F. Muniz-Miranda, and A. Pedone, "Spectroscopic and Computational Studies on Ligand-Capped Metal Nanoparticles and Clusters," in *Metal Nanoparticles and Clusters*, Cham: Springer International Publishing, 2018, pp. 55–87.
- [224] Pilot, Signorini, Durante, Orian, Bhamidipati, and Fabris, "A Review on Surface-Enhanced Raman Scattering," *Biosensors*, vol. 9, no. 2, p. 57, Apr. 2019.
- [225] H. Wei and H. Xu, "Hot spots in different metal nanostructures for plasmon-enhanced Raman spectroscopy," *Nanoscale*. 2013.
- [226] K. S. Pitzer, "The Nature of the Chemical Bond and the Structure of Molecules and Crystals: An Introduction to Modern Structural Chemistry.," *J. Am. Chem. Soc.*, vol. 82, no. 15, pp. 4121–4121, Aug. 1960.
- [227] P. A. Schultz and R. P. Messmer, "The nature of multiple bonds. 1. σ and π Bonds versus bent bonds, a computational survey," *J. Am. Chem. Soc.*, vol. 115, no. 23, pp. 10925–10937, Nov. 1993.
- [228] L. Pauling, "The nature of the chemical bond. Application of results obtained from the quantum mechanics and from a theory of paramagnetic susceptibility to the structure of molecules," *J. Am. Chem. Soc.*, vol. 53, no. 4, pp. 1367–1400, Apr. 1931.
- [229] V. N. Mochalin, O. Shenderova, D. Ho, and Y. Gogotsi, "The properties and applications of nanodiamonds," *Nat. Nanotechnol.*, vol. 7, no. 1, pp.

- 11–23, Jan. 2012.
- [230] A. K. Geim and K. S. Novoselov, “Rise of Graphene Nature Materials 2007 6 191,” *Nat. Mater.*, 2010.
- [231] M. Terrones, “Science and Technology of the Twenty-First Century: Synthesis, Properties, and Applications of Carbon Nanotubes,” *Annu. Rev. Mater. Res.*, vol. 33, no. 1, pp. 419–501, Aug. 2003.
- [232] M. Zeiger, N. Jäckel, V. N. Mochalin, and V. Presser, “Review: carbon onions for electrochemical energy storage,” *J. Mater. Chem. A*, vol. 4, no. 9, pp. 3172–3196, 2016.
- [233] L. B. Ebert, “Science of fullerenes and carbon nanotubes,” *Carbon N. Y.*, vol. 35, no. 3, pp. 437–438, 1997.
- [234] A. Cayuela, M. L. Soriano, C. Carrillo-Carrión, and M. Valcárcel, “Semiconductor and carbon-based fluorescent nanodots: the need for consistency,” *Chem. Commun.*, vol. 52, no. 7, pp. 1311–1326, 2016.
- [235] N. V. Tepliakov *et al.*, “ sp^2 – sp^3 -Hybridized Atomic Domains Determine Optical Features of Carbon Dots,” *ACS Nano*, vol. 13, no. 9, pp. 10737–10744, Sep. 2019.
- [236] C. S. Casari and A. Milani, “Carbyne: from the elusive allotrope to stable carbon atom wires,” *MRS Commun.*, vol. 8, no. 02, pp. 207–219, Jun. 2018.
- [237] W. A. Chalifoux and R. R. Tykwinski, “Synthesis of extended polyynes: Toward carbyne,” *Comptes Rendus Chim.*, vol. 12, no. 3–4, pp. 341–358, Mar. 2009.
- [238] L. D. Movsisyan, D. V. Kondratuk, M. Franz, A. L. Thompson, R. R. Tykwinski, and H. L. Anderson, “Synthesis of Polyynes Rotaxanes,” *Org. Lett.*, vol. 14, no. 13, pp. 3424–3426, Jul. 2012.
- [239] P. Cavaliere, “Mechanical Properties of Nanocrystalline Materials,” in *Handbook of Mechanical Nanostructuring*, Weinheim, Germany: Wiley-VCH Verlag GmbH & Co. KGaA, 2015, pp. 1–16.
- [240] S. Yang and M. Kertesz, “Linear C_n Clusters: Are They Acetylenic or

- Cumulenic?,” *J. Phys. Chem. A*, vol. 112, no. 1, pp. 146–151, Jan. 2008.
- [241] F. Innocenti, A. Milani, and C. Castiglioni, “Can Raman spectroscopy detect cumulenenic structures of linear carbon chains?,” *J. Raman Spectrosc.*, p. n/a-n/a, 2009.
- [242] Y. E. Park, S. K. Shin, and S. M. Park, “Power Dependence on Formation of Polyynes by Laser Ablation in Water,” *Bull. Korean Chem. Soc.*, vol. 34, no. 4, pp. 1039–1042, Apr. 2013.
- [243] Y. E. Park, S. K. Shin, and S. M. Park, “The physical effects on the formation of polyynes by laser ablation,” *Chem. Phys. Lett.*, vol. 568–569, pp. 112–116, May 2013.
- [244] A. Hirsch, “The era of carbon allotropes,” *Nat. Mater.*, vol. 9, no. 11, pp. 868–871, Nov. 2010.
- [245] S. Peggiani *et al.*, “Size-selected polyynes synthesised by submerged arc discharge in water,” *Chem. Phys. Lett.*, vol. 740, p. 137054, Feb. 2020.
- [246] D. R. Kohn, P. Gawel, Y. Xiong, K. E. Christensen, and H. L. Anderson, “Synthesis of Polyynes Using Dicobalt Masking Groups,” *J. Org. Chem.*, vol. 83, no. 4, pp. 2077–2086, Feb. 2018.
- [247] F. Cataldo, “Synthesis of polyynes (and ene-yne) segments by dechlorination reactions of chlorinated polyethylene wax and chlorinated docosane,” *J. Mater. Sci.*, vol. 35, no. 10, pp. 2413–2419, 2000.
- [248] L. Shi *et al.*, “Confined linear carbon chains as a route to bulk carbyne,” *Nat. Mater.*, vol. 15, no. 6, pp. 634–639, Jun. 2016.
- [249] A. Hu, Q.-B. Lu, W. W. Duley, and M. Rybachuk, “Spectroscopic characterization of carbon chains in nanostructured tetrahedral carbon films synthesized by femtosecond pulsed laser deposition,” *J. Chem. Phys.*, vol. 126, no. 15, p. 154705, Apr. 2007.
- [250] S. S. Jyothirmayee Aravind, V. Eswaraiah, and S. Ramaprabhu, “Facile synthesis of one dimensional graphene wrapped carbon nanotube composites by chemical vapour deposition,” *J. Mater. Chem.*, vol. 21, no. 39, p. 15179, 2011.

- [251] M. Inagaki and F. Kang, “Graphene derivatives: graphane, fluorographene, graphene oxide, graphyne and graphdiyne,” *J. Mater. Chem. A*, vol. 2, no. 33, pp. 13193–13206, 2014.
- [252] E. A. Belenkov and I. V. Shakhova, “Structure of carbinoid nanotubes and carbinofullerenes,” *Phys. Solid State*, vol. 53, no. 11, pp. 2385–2392, Nov. 2011.
- [253] B. Pan, J. Xiao, J. Li, P. Liu, C. Wang, and G. Yang, “Carbyne with finite length: The one-dimensional sp carbon,” *Sci. Adv.*, 2015.
- [254] A. C. Ferrari and J. Robertson, “Raman spectroscopy of amorphous, nanostructured, diamond-like carbon, and nanodiamond,” *Philos. Trans. R. Soc. London. Ser. A Math. Phys. Eng. Sci.*, vol. 362, no. 1824, pp. 2477–2512, Nov. 2004.
- [255] A. Lucotti *et al.*, “Raman and SERS investigation of isolated sp carbon chains,” *Chem. Phys. Lett.*, vol. 417, no. 1–3, pp. 78–82, Jan. 2006.
- [256] E. V. Efremov, F. Ariese, and C. Gooijer, “Achievements in resonance Raman spectroscopy,” *Anal. Chim. Acta*, vol. 606, no. 2, pp. 119–134, Jan. 2008.
- [257] N. Kumar, S. Mignuzzi, W. Su, and D. Roy, “Tip-enhanced Raman spectroscopy: principles and applications,” *EPJ Tech. Instrum.*, vol. 2, no. 1, p. 9, Dec. 2015.
- [258] E. Giorgetti *et al.*, “Förster resonance energy transfer (FRET) with a donor–acceptor system adsorbed on silver or gold nanoisland films,” *Phys. Chem. Chem. Phys.*, vol. 11, no. 42, p. 9798, 2009.
- [259] S. Ahirwar, S. Mallick, and D. Bahadur, “Electrochemical Method to Prepare Graphene Quantum Dots and Graphene Oxide Quantum Dots,” *ACS Omega*, 2017.
- [260] M. Reed, J. Randall, R. Aggarwal, R. Matyi, T. Moore, and A. Wetsel, “Observation of discrete electronic states in a zero-dimensional semiconductor nanostructure,” *Phys. Rev. Lett.*, vol. 60, no. 6, pp. 535–537,

- Feb. 1988.
- [261] A. P. Alivisatos, “Semiconductor clusters, nanocrystals, and quantum dots,” *Science* (80-.), 1996.
- [262] D. J. Griffiths and D. F. Schroeter, *Introduction to Quantum Mechanics*. Cambridge University Press, 2018.
- [263] C. Bartram, “Quantum Dot Physics- A Guide to Understanding QD Displays,” *Samsung Disp.*, 2018.
- [264] G. Su, C. Liu, Z. Deng, X. Zhao, and X. Zhou, “Size-dependent photoluminescence of PbS QDs embedded in silicate glasses,” *Opt. Mater. Express*, 2017.
- [265] X. Xu *et al.*, “Electrophoretic Analysis and Purification of Fluorescent Single-Walled Carbon Nanotube Fragments,” *J. Am. Chem. Soc.*, vol. 126, no. 40, pp. 12736–12737, Oct. 2004.
- [266] A. F. van Driel, G. Allan, C. Delerue, P. Lodahl, W. L. Vos, and D. Vanmaekelbergh, “Frequency-Dependent Spontaneous Emission Rate from CdSe and CdTe Nanocrystals: Influence of Dark States,” *Phys. Rev. Lett.*, vol. 95, no. 23, p. 236804, Dec. 2005.
- [267] C. Cheng, J. Li, and X. Cheng, “Photoluminescence lifetime and absorption spectrum of PbS nanocrystal quantum dots,” *J. Lumin.*, vol. 188, pp. 252–257, Aug. 2017.
- [268] K. Hola *et al.*, “Photoluminescence effects of graphitic core size and surface functional groups in carbon dots: COO⁻ induced red-shift emission,” *Carbon N. Y.*, vol. 70, no. 1, pp. 279–286, Apr. 2014.
- [269] P. Zhao and L. Zhu, “Dispersibility of carbon dots in aqueous and/or organic solvents,” *Chem. Commun.*, vol. 54, no. 43, pp. 5401–5406, 2018.
- [270] H. Liu *et al.*, “Synthesis of Luminescent Carbon Dots with Ultrahigh Quantum Yield and Inherent Folate Receptor-Positive Cancer Cell Targetability,” *Sci. Rep.*, vol. 8, no. 1, p. 1086, Dec. 2018.
- [271] R. Hardman, “A Toxicologic Review of Quantum Dots: Toxicity Depends

- on Physicochemical and Environmental Factors,” *Environ. Health Perspect.*, vol. 114, no. 2, pp. 165–172, Feb. 2006.
- [272] U. Resch-Genger and K. Rurack, “Determination of the photoluminescence quantum yield of dilute dye solutions (IUPAC Technical Report),” *Pure Appl. Chem.*, vol. 85, no. 10, pp. 2005–2013, Oct. 2013.
- [273] D. Li *et al.*, “Supra-(carbon nanodots) with a strong visible to near-infrared absorption band and efficient photothermal conversion,” *Light Sci. Appl.*, vol. 5, no. 7, pp. e16120–e16120, Jul. 2016.
- [274] X. T. Zheng, A. Ananthanarayanan, K. Q. Luo, and P. Chen, “Glowing graphene quantum dots and carbon dots: Properties, syntheses, and biological applications,” *Small*. 2015.
- [275] S. Zhu *et al.*, “Highly photoluminescent carbon dots for multicolor patterning, sensors, and bioimaging,” *Angew. Chemie - Int. Ed.*, 2013.
- [276] Y. Song, C. Zhu, J. Song, H. Li, D. Du, and Y. Lin, “Drug-Derived Bright and Color-Tunable N-Doped Carbon Dots for Cell Imaging and Sensitive Detection of Fe³⁺ in Living Cells,” *ACS Appl. Mater. Interfaces*, 2017.
- [277] H. Li *et al.*, “Microwave-assisted synthesis of N,P-doped carbon dots for fluorescent cell imaging,” *Microchim. Acta*, 2016.
- [278] Q. Y. Cai *et al.*, “A rapid fluorescence ‘switch-on’ assay for glutathione detection by using carbon dots-MnO₂ nanocomposites,” *Biosens. Bioelectron.*, 2015.
- [279] Y. Dong *et al.*, “Carbon-based dots co-doped with nitrogen and sulfur for high quantum yield and excitation-independent emission,” *Angew. Chemie - Int. Ed.*, 2013.
- [280] X. Huang, Y. Li, X. Zhong, A. E. Rider, and K. K. Ostrikov, “Fast Microplasma Synthesis of Blue Luminescent Carbon Quantum Dots at Ambient Conditions,” *Plasma Process. Polym.*, vol. 12, no. 1, pp. 59–65, Jan. 2015.
- [281] G. Gedda, C.-Y. Lee, Y.-C. Lin, and H. Wu, “Green synthesis of carbon dots from prawn shells for highly selective and sensitive detection of

- copper ions,” *Sensors Actuators B Chem.*, vol. 224, pp. 396–403, Mar. 2016.
- [282] M. Zhang *et al.*, “Facile synthesis of water-soluble, highly fluorescent graphene quantum dots as a robust biological label for stem cells,” *J. Mater. Chem.*, vol. 22, no. 15, p. 7461, 2012.
- [283] Z. L. Wu, M. X. Gao, T. T. Wang, X. Y. Wan, L. L. Zheng, and C. Z. Huang, “A general quantitative pH sensor developed with dicyandiamide N-doped high quantum yield graphene quantum dots,” *Nanoscale*, 2014.
- [284] D.-W. Deng, J.-S. Yu, and Y. Pan, “Water-soluble CdSe and CdSe/CdS nanocrystals: A greener synthetic route,” *J. Colloid Interface Sci.*, vol. 299, no. 1, pp. 225–232, Jul. 2006.
- [285] Z. Wang *et al.*, “53% Efficient Red Emissive Carbon Quantum Dots for High Color Rendering and Stable Warm White-Light-Emitting Diodes,” *Adv. Mater.*, vol. 29, no. 37, p. 1702910, Oct. 2017.
- [286] C. A. T. Toloza, S. Khan, R. L. D. Silva, E. C. Romani, F. L. Freire, and R. Q. Aucélio, “Different approaches for sensing captopril based on functionalized graphene quantum dots as photoluminescent probe,” *J. Lumin.*, vol. 179, pp. 83–92, Nov. 2016.
- [287] J. Zheng *et al.*, “An Efficient Synthesis and Photoelectric Properties of Green Carbon Quantum Dots with High Fluorescent Quantum Yield,” *Nanomaterials*, vol. 10, no. 1, p. 82, Jan. 2020.
- [288] M. L. Liu, B. Bin Chen, C. M. Li, and C. Z. Huang, “Carbon dots: synthesis, formation mechanism, fluorescence origin and sensing applications,” *Green Chem.*, vol. 21, no. 3, pp. 449–471, 2019.
- [289] F. Yuan *et al.*, “Engineering triangular carbon quantum dots with unprecedented narrow bandwidth emission for multicolored LEDs,” *Nat. Commun.*, vol. 9, no. 1, p. 2249, Dec. 2018.
- [290] X. Li, Z. Zhao, and C. Pan, “Electrochemical exfoliation of carbon dots with the narrowest full width at half maximum in their fluorescence spectra in the ultraviolet region using only water as electrolyte,” *Chem. Commun.*,

- vol. 52, no. 60, pp. 9406–9409, 2016.
- [291] Y.-P. Sun *et al.*, “Quantum-Sized Carbon Dots for Bright and Colorful Photoluminescence,” *J. Am. Chem. Soc.*, vol. 128, no. 24, pp. 7756–7757, Jun. 2006.
- [292] S. Kang *et al.*, “Graphene Oxide Quantum Dots Derived from Coal for Bioimaging: Facile and Green Approach,” *Sci. Rep.*, vol. 9, no. 1, p. 4101, Dec. 2019.
- [293] S. Hu, J. Liu, J. Yang, Y. Wang, and S. Cao, “Laser synthesis and size tailor of carbon quantum dots,” *J. Nanoparticle Res.*, vol. 13, no. 12, pp. 7247–7252, Dec. 2011.
- [294] H. Yu, X. Li, X. Zeng, and Y. Lu, “Preparation of carbon dots by non-focusing pulsed laser irradiation in toluene,” *Chem. Commun.*, 2016.
- [295] O. Raab, “Ueber die Wirkung fluorizierender Stoffe auf Infusorien,” *Z Biol*, vol. 47, p. 5, 1900.
- [296] C. S. Foote, “DEFINITION OF TYPE I and TYPE II PHOTSENSITIZED OXIDATION,” *Photochem. Photobiol.*, vol. 54, no. 5, pp. 659–659, Nov. 1991.
- [297] D. Fukumura and R. K. Jain, “Photodynamic therapy for cancer,” *Nat. Rev. Cancer*, vol. 3, no. 5, pp. 380–387, May 2003.
- [298] K. Plaetzer, B. Krammer, J. Berlanda, F. Berr, and T. Kiesslich, “Photophysics and photochemistry of photodynamic therapy: fundamental aspects,” *Lasers Med. Sci.*, vol. 24, no. 2, pp. 259–268, Mar. 2009.
- [299] F. H. Sakamoto, J. D. Lopes, and R. R. Anderson, “Photodynamic therapy for acne vulgaris: A critical review from basics to clinical practice,” *J. Am. Acad. Dermatol.*, vol. 63, no. 2, pp. 183–193, Aug. 2010.
- [300] N. Gamaleia *et al.*, “Photodynamic Activity of Nanogold-Doped Fotolon: Free Radicals Versus Singlet Oxygen,” *For. Immunopathol. Dis. Therap.*, vol. 2, no. 3, pp. 237–246, 2011.
- [301] N. F. Gamaleia and I. O. Shton, “Gold mining for PDT: Great expectations

- from tiny nanoparticles,” *Photodiagnosis Photodyn. Ther.*, 2015.
- [302] R. R. Avirah, D. T. Jayaram, N. Adarsh, and D. Ramaiah, “Squaraine dyes in PDT: from basic design to in vivo demonstration,” *Org. Biomol. Chem.*, vol. 10, no. 5, pp. 911–920, 2012.
- [303] T. Simon, S. C. Boca, and S. Astilean, “Pluronic-Nanogold hybrids: Synthesis and tagging with photosensitizing molecules,” *Colloids Surfaces B Biointerfaces*, 2012.
- [304] C. Liu and N. Zhang, “Nanoparticles in Gene Therapy,” 2011, pp. 509–562.
- [305] V. F. I. Van Tendeloo, C. Van Broeckhoven, and Z. N. Berneman, “Gene therapy: Principles and applications to hematopoietic cells,” *Leukemia*. 2001.
- [306] X. Gao, K.-S. Kim, and D. Liu, “Nonviral gene delivery: What we know and what is next,” *AAPS J.*, vol. 9, no. 1, pp. E92–E104, Mar. 2007.
- [307] C. M. Wiethoff and C. R. Middaugh, “Barriers to nonviral gene delivery,” *Journal of Pharmaceutical Sciences*. 2003.
- [308] Y. Tavan, S. H. Hosseini, and S. H. H. Y. Tavan, “novel rate of the reaction between NaOH with CO₂ at low temperature in spray dryer,” *Petroleum*, vol. 3, no. 1, pp. 51–55, Mar. 2017.
- [309] E. Solati, M. Mashayekh, and D. Dorrnian, “Effects of laser pulse wavelength and laser fluence on the characteristics of silver nanoparticle generated by laser ablation,” *Appl. Phys. A*, vol. 112, no. 3, pp. 689–694, Sep. 2013.
- [310] R. D. Niederriter, J. T. Gopinath, and M. E. Siemens, “Measurement of the M² beam propagation factor using a focus-tunable liquid lens,” *Appl. Opt.*, vol. 52, no. 8, p. 1591, Mar. 2013.
- [311] M. A. Al-Azawi and N. Bidin, “Gold nanoparticles synthesized by laser ablation in deionized water,” *Chinese J. Phys.*, vol. 53, no. 4, pp. 201–209, 2015., 2015.

- [312] H. Kogelnik, "On the Propagation of Gaussian Beams of Light Through Lenslike Media Including those with a Loss or Gain Variation," *Appl. Opt.*, vol. 4, no. 12, p. 1562, Dec. 1965.
- [313] M. Born *et al.*, *Principles of Optics*. Cambridge University Press, 1999.
- [314] D. Sangeeta and J. R. LaGraff, *Inorganic Materials Chemistry Desk Reference*. CRC Press, 2004.
- [315] R. V. Hoffman, *Organic Chemistry*. Hoboken, NJ, USA: John Wiley & Sons, Inc., 2004.
- [316] H. Baumann, S. C. Talmage, and C. J. Gobler, "Reduced early life growth and survival in a fish in direct response to increased carbon dioxide," *Nat. Clim. Chang.*, vol. 2, no. 1, pp. 38–41, Jan. 2012.
- [317] Shimadzu, "TOC-L Global Standard for TOC Analyzers," *Man. TOC*, 2018.
- [318] Y. Lu, J. Wang, H. Yuan, and D. Xiao, "Separation of carbon quantum dots on a C18 column by binary gradient elution via HPLC," *Anal. Methods*, vol. 6, no. 20, pp. 8124–8128, 2014.
- [319] M. M. Veiga, G. Angeloci-Santos, and J. A. Meech, "Review of barriers to reduce mercury use in artisanal gold mining," *Extr. Ind. Soc.*, vol. 1, no. 2, pp. 351–361, Nov. 2014.
- [320] F. Alzoubi, J. Al-Zoubi, M. Alqadi, H. A. Alshboul, and K. Aljarrah, "Synthesis and Characterization of Colloidal Gold Nanoparticles Controlled by the pH and Ionic Strength," *Chinese J. Phys.*, vol. 53, no. 5, pp. 100801-1-100801–9, 2015.
- [321] J. Araujo *et al.*, "Characterizing Complex Mineral Structures in Thin Sections of Geological Samples with a Scanning Hall Effect Microscope," *Sensors*, vol. 19, no. 7, p. 1636, Apr. 2019.
- [322] J. F. D. F. Araujo *et al.*, "Novel scanning magnetic microscopy method for the characterization of magnetic nanoparticles," *J. Magn. Magn. Mater.*, vol. 499, p. 166300, Apr. 2020.

- [323] J. F. D. F. Araujo *et al.*, “Scanning Magnetic Microscope Using a Gradiometric Configuration for Characterization of Rock Samples,” *Materials (Basel)*, vol. 12, no. 24, p. 4154, Dec. 2019.
- [324] N. G. Bastús, J. Comenge, V. V. Puentes, N. G. Bastús, J. Comenge, and V. V. Puentes, “Kinetically Controlled Seeded Growth Synthesis of Citrate-Stabilized Gold Nanoparticles of up to 200 nm: Size Focusing versus Ostwald Ripening,” *Langmuir*, vol. 27, no. 17, pp. 11098–11105, Sep. 2011.
- [325] F. Mafuné, J. Kohno, Y. Takeda, and T. Kondow, “Full Physical Preparation of Size-Selected Gold Nanoparticles in Solution: Laser Ablation and Laser-Induced Size Control,” *J. Phys. Chem. B*, vol. 106, no. 31, pp. 7575–7577, Aug. 2002.
- [326] A. Giusti, E. Giorgetti, S. Laza, P. Marsili, and F. Giammanco, “Multiphoton Fragmentation of PAMAM G5-Capped Gold Nanoparticles Induced by Picosecond Laser Irradiation at 532 nm,” *J. Phys. Chem. C*, vol. 111, no. 41, pp. 14984–14991, Oct. 2007.
- [327] N. V. V. Tarasenko, A. V. V. Butsen, E. A. A. Nevar, and N. A. A. Savastenko, “Synthesis of nanosized particles during laser ablation of gold in water,” *Appl. Surf. Sci.*, vol. 252, no. 13, pp. 4439–4444, Apr. 2006.
- [328] H. Muto, K. Miyajima, and F. Mafuné, “Mechanism of Laser-Induced Size Reduction of Gold Nanoparticles As Studied by Single and Double Laser Pulse Excitation,” *J. Phys. Chem. C*, vol. 112, no. 15, pp. 5810–5815, Apr. 2008.
- [329] M. A. Sobhan, M. J. Withford, and E. M. Goldys, “Enhanced Stability of Gold Colloids Produced by Femtosecond Laser Synthesis in Aqueous Solution of CTAB,” *Langmuir*, vol. 26, no. 5, pp. 3156–3159, Mar. 2010.
- [330] F. Mafuné, J. Kohno, Y. Takeda, and T. Kondow, “Growth of Gold Clusters into Nanoparticles in a Solution Following Laser-Induced Fragmentation,” *J. Phys. Chem. B*, vol. 106, no. 34, pp. 8555–8561, Aug. 2002.
- [331] F. Mafuné, J. Kohno, Y. Takeda, and T. Kondow, “Formation of Gold

- Nanonetworks and Small Gold Nanoparticles by Irradiation of Intense Pulsed Laser onto Gold Nanoparticles,” *J. Phys. Chem. B*, vol. 107, no. 46, pp. 12589–12596, Nov. 2003.
- [332] E. Giorgetti, F. Giammanco, P. Marsili, and A. Giusti, “Effect of Picosecond Postirradiation on Colloidal Suspensions of Differently Capped AuNPs,” *J. Phys. Chem. C*, vol. 115, no. 12, pp. 5011–5020, Mar. 2011.
- [333] G. Yincheng, N. Zhenqi, and L. Wenyi, “Comparison of removal efficiencies of carbon dioxide between aqueous ammonia and NaOH solution in a fine spray column,” *Energy Procedia*, vol. 4, pp. 512–518, 2011.
- [334] J. Antúnez-García, S. Mejía-Rosales, E. Pérez-Tijerina, J. M. Montejano-Carrizales, and M. José-Yacamán, “Coalescence and Collisions of Gold Nanoparticles,” *Materials (Basel)*, vol. 4, no. 2, pp. 368–379, Jan. 2011.
- [335] H. Wang, Y. Yang, T. Qu, Z. Kang, and D. Wang, “Cobalt, nitrogen-codoped carbon quantum dots as a synergistic catalyst for oxygen reduction reaction,” *Green Process. Synth.*, vol. 4, no. 4, Jan. 2015.
- [336] N. T. Ngoc Anh, P.-Y. Chang, and R.-A. Doong, “Sulfur-doped graphene quantum dot-based paper sensor for highly sensitive and selective detection of 4-nitrophenol in contaminated water and wastewater,” *RSC Adv.*, vol. 9, no. 46, pp. 26588–26597, 2019.
- [337] K. Linehan and H. Doyle, “Solution reduction synthesis of amine terminated carbon quantum dots,” *RSC Adv.*, vol. 4, no. 24, pp. 12094–12097, 2014.
- [338] J.-H. H. Zhang, A. Niu, J. Li, J.-W. W. Fu, Q. Xu, and D.-S. S. Pei, “In vivo characterization of hair and skin derived carbon quantum dots with high quantum yield as long-term bioprobes in zebrafish,” *Sci. Rep.*, vol. 6, no. 1, p. 37860, Dec. 2016.
- [339] A. Lucotti *et al.*, “sp Carbon chain interaction with silver nanoparticles probed by Surface Enhanced Raman Scattering,” *Chem. Phys. Lett.*, vol. 478, no. 1–3, pp. 45–50, Aug. 2009.

- [340] R. B. Heimann, J. Kleiman, and N. M. Salansky, “A unified structural approach to linear carbon polytypes,” *Nature*, vol. 306, no. 5939, pp. 164–167, Nov. 1983.
- [341] X. T. Feng, F. Zhang, Y. L. Wang, Y. Zhang, Y. Z. Yang, and X. G. Liu, “Luminescent carbon quantum dots with high quantum yield as a single white converter for white light emitting diodes,” *Appl. Phys. Lett.*, vol. 107, no. 21, p. 213102, Nov. 2015.
- [342] R. Souza da Costa, W. Ferreira da Cunha, N. Simenremis Pereira, and A. Marti Ceschin, “An Alternative Route to Obtain Carbon Quantum Dots from Photoluminescent Materials in Peat,” *Materials (Basel)*, vol. 11, no. 9, p. 1492, Aug. 2018.
- [343] V. Nguyen, L. Yan, J. Si, and X. Hou, “Femtosecond laser-induced size reduction of carbon nanodots in solution: Effect of laser fluence, spot size, and irradiation time,” *J. Appl. Phys.*, vol. 117, no. 8, p. 084304, Feb. 2015.
- [344] H. F. Shurvell, “Spectra- Structure Correlations in the Mid- and Far-Infrared,” in *Handbook of Vibrational Spectroscopy*, J. M. Chalmers, Ed. Chichester, UK: John Wiley & Sons, Ltd, 2006.
- [345] V. D. Ebajo, C. R. L. Santos, G. V. Alea, Y. A. Lin, and C.-H. Chen, “Regenerable Acidity of Graphene Oxide in Promoting Multicomponent Organic Synthesis,” *Sci. Rep.*, vol. 9, no. 1, p. 15579, Dec. 2019.
- [346] S. Stankovich, R. D. Piner, S. T. Nguyen, and R. S. Ruoff, “Synthesis and exfoliation of isocyanate-treated graphene oxide nanoplatelets,” *Carbon N. Y.*, vol. 44, no. 15, pp. 3342–3347, Dec. 2006.
- [347] Y. Si and E. T. Samulski, “Synthesis of Water Soluble Graphene,” *Nano Lett.*, vol. 8, no. 6, pp. 1679–1682, Jun. 2008.
- [348] R. Maiti, A. Midya, C. Narayana, and S. K. Ray, “Tunable optical properties of graphene oxide by tailoring the oxygen functionalities using infrared irradiation,” *Nanotechnology*, vol. 25, no. 49, p. 495704, Dec. 2014.
- [349] S. Xu, W. Yu, X. Yao, Q. Zhang, and Q. Fu, “Nanocellulose-assisted

- dispersion of graphene to fabricate poly(vinyl alcohol)/graphene nanocomposite for humidity sensing,” *Compos. Sci. Technol.*, vol. 131, pp. 67–76, Aug. 2016.
- [350] Y. V. Butenko *et al.*, “Photoemission study of onionlike carbons produced by annealing nanodiamonds,” *Phys. Rev. B*, vol. 71, no. 7, p. 075420, Feb. 2005.
- [351] V. A. Chhabra, R. Kaur, N. Kumar, A. Deep, C. Rajesh, and K.-H. H. Kim, “Synthesis and spectroscopic studies of functionalized graphene quantum dots with diverse fluorescence characteristics,” *RSC Adv.*, vol. 8, no. 21, pp. 11446–11454, 2018.
- [352] V. Kumar *et al.*, “Facile, rapid and upscaled synthesis of green luminescent functional graphene quantum dots for bioimaging,” *RSC Adv.*, vol. 4, no. 40, p. 21101, 2014.
- [353] B. De, B. Voit, and N. Karak, “Carbon dot reduced Cu₂O nanohybrid/hyperbranched epoxy nanocomposite: mechanical, thermal and photocatalytic activity,” *RSC Adv.*, vol. 4, no. 102, pp. 58453–58459, Oct. 2014.
- [354] G. E. LeCroy *et al.*, “Characteristic Excitation Wavelength Dependence of Fluorescence Emissions in Carbon ‘Quantum’ Dots,” *J. Phys. Chem. C*, vol. 121, no. 50, pp. 28180–28186, Dec. 2017.
- [355] Gaponenko SV, *Optical properties of semiconductor nanocrystals*, 1st ed. Cambridge: Cambridge University Press, 1998.
- [356] Z. Sun, X. Li, Y. Wu, C. Wei, and H. Zeng, “Origin of green luminescence in carbon quantum dots: specific emission bands originate from oxidized carbon groups,” *New J. Chem.*, vol. 42, no. 6, pp. 4603–4611, 2018.
- [357] D. Shen *et al.*, “Tuning the fluorescence performance of carbon dots with a reduction pathway,” *Nanoscale*, vol. 11, no. 13, pp. 5998–6003, 2019.
- [358] D. Reyes *et al.*, “Laser Ablated Carbon Nanodots for Light Emission,” *Nanoscale Res. Lett.*, vol. 11, no. 1, p. 424, Dec. 2016.
- [359] H. I. Abdel-Shafy and M. S. M. Mansour, “A review on polycyclic

- aromatic hydrocarbons: Source, environmental impact, effect on human health and remediation,” *Egypt. J. Pet.*, vol. 25, no. 1, pp. 107–123, Mar. 2016.
- [360] A. V Kabanov, E. V Batrakova, and V. Y. Alakhov, “Pluronic® block copolymers as novel polymer therapeutics for drug and gene delivery,” *J. Control. Release*, vol. 82, no. 2–3, pp. 189–212, Aug. 2002.
- [361] T. I. Abdullin, O. V. Bondar, Y. G. Shtyrin, M. Kahraman, and M. Culha, “Pluronic Block Copolymer-Mediated Interactions of Organic Compounds with Noble Metal Nanoparticles for SERS Analysis,” *Langmuir*, vol. 26, no. 7, pp. 5153–5159, Apr. 2010.
- [362] T. Simon, M. Potara, A. M. Gabudean, E. Licarete, M. Banciu, and S. Astilean, “Designing Theranostic Agents Based on Pluronic Stabilized Gold Nanoaggregates Loaded with Methylene Blue for Multimodal Cell Imaging and Enhanced Photodynamic Therapy,” *ACS Appl. Mater. Interfaces*, 2015.
- [363] I. Yoon, J. Z. Li, and Y. K. Shim, “Advance in photosensitizers and light delivery for photodynamic therapy,” *Clin. Endosc.*, 2013.
- [364] A. Laurenzana *et al.*, “Lipid rafts: integrated platforms for vascular organization offering therapeutic opportunities,” *Cell. Mol. Life Sci.*, vol. 72, no. 8, pp. 1537–1557, Apr. 2015.
- [365] L. Li, A. Hsu, and P. K. Moore, “Actions and interactions of nitric oxide, carbon monoxide and hydrogen sulphide in the cardiovascular system and in inflammation — a tale of three gases!,” *Pharmacol. Ther.*, vol. 123, no. 3, pp. 386–400, Sep. 2009.
- [366] B. Halliday, Tim; Davey, *Water and health in an overcrowded world*. Oxford: Oxford University Press, 2007.
- [367] E. M. Nolan and S. J. Lippard, “Tools and Tactics for the Optical Detection of Mercuric Ion,” *Chem. Rev.*, vol. 108, no. 9, pp. 3443–3480, Sep. 2008.
- [368] L. E. Kerper, N. Ballatori, and T. W. Clarkson, “Methylmercury transport across the blood-brain barrier by an amino acid carrier,” *Am. J. Physiol.*

- Integr. Comp. Physiol.*, vol. 262, no. 5, pp. R761–R765, May 1992.
- [369] Y. Wang, L. Zhang, R.-P. Liang, J.-M. Bai, and J.-D. Qiu, “Using Graphene Quantum Dots as Photoluminescent Probes for Protein Kinase Sensing,” *Anal. Chem.*, vol. 85, no. 19, pp. 9148–9155, Oct. 2013.
- [370] J. Homola, I. Koudela, and S. S. Yee, “Surface plasmon resonance sensors based on diffraction gratings and prism couplers: sensitivity comparison,” *Sensors Actuators B Chem.*, vol. 54, no. 1–2, pp. 16–24, Jan. 1999.
- [371] T. Tsuji, K. Iryo, N. Watanabe, and M. Tsuji, “Preparation of silver nanoparticles by laser ablation in solution: influence of laser wavelength on particle size,” *Appl. Surf. Sci.*, vol. 202, no. 1–2, pp. 80–85, Dec. 2002.
- [372] R. M. Tilaki, A. Irajizad, and S. M. Mahdavi, “Stability, size and optical properties of silver nanoparticles prepared by laser ablation in different carrier media,” *Appl. Phys. A*, vol. 84, no. 1–2, pp. 215–219, May 2006.
- [373] S. Lee and B.-H. Jun, “Silver Nanoparticles: Synthesis and Application for Nanomedicine,” *Int. J. Mol. Sci.*, vol. 20, no. 4, p. 865, Feb. 2019.
- [374] V. M. Renteria-Tapia and J. García-Macedo, “Influence of oxygen on the optical properties of silver nanoparticles,” *J. Nanosci. Nanotechnol.*, vol. 8, no. 12, pp. 6545–50, Dec. 2008.
- [375] S. Agnihotri, S. S. Mukherji, and S. S. Mukherji, “Size-controlled silver nanoparticles synthesized over the range 5–100 nm using the same protocol and their antibacterial efficacy,” *RSC Adv.*, vol. 4, no. 8, pp. 3974–3983, 2014.
- [376] A. Ali *et al.*, “Synthesis, characterization, applications, and challenges of iron oxide nanoparticles,” *Nanotechnol. Sci. Appl.*, vol. Volume 9, pp. 49–67, Aug. 2016.
- [377] B. Hu, H. Guo, P. Zhou, and Z.-L. Shi, “Characteristics of SARS-CoV-2 and COVID-19,” *Nat. Rev. Microbiol.*, pp. 1–14, Oct. 2020.
- [378] V. Amendola *et al.*, “Room-Temperature Laser Synthesis in Liquid of Oxide, Metal-Oxide Core-Shells, and Doped Oxide Nanoparticles,” *Chem. – A Eur. J.*, vol. 26, no. 42, pp. 9206–9242, Jul. 2020.

- [379] M. Hanesch, "Raman spectroscopy of iron oxides and (oxy)hydroxides at low laser power and possible applications in environmental magnetic studies," *Geophys. J. Int.*, vol. 177, no. 3, pp. 941–948, Jun. 2009.
- [380] M. A. Legodi, D. DEWAAL, and D. de Waal, "The preparation of magnetite, goethite, hematite and maghemite of pigment quality from mill scale iron waste," *Dye. Pigment.*, vol. 74, no. 1, pp. 161–168, 2007.
- [381] R. J. Thibeau, C. W. Brown, and R. H. Heidersbach, "Raman Spectra of Possible Corrosion Products of Iron," *Appl. Spectrosc.*, vol. 32, no. 6, pp. 532–535, Nov. 1978.
- [382] D. L. A. de Faria, S. Venâncio Silva, and M. T. de Oliveira, "Raman microspectroscopy of some iron oxides and oxyhydroxides," *J. Raman Spectrosc.*, vol. 28, no. 11, pp. 873–878, Nov. 1997.
- [383] O. N. Shebanova and P. Lazor, "Raman spectroscopic study of magnetite (FeFe₂O₄): a new assignment for the vibrational spectrum," *J. Solid State Chem.*, vol. 174, no. 2, pp. 424–430, Sep. 2003.
- [384] F. Rull, J. Martinez-Frias, A. Sansano, J. Medina, and H. G. M. Edwards, "Comparative micro-Raman study of the Nakhla and Vaca Muerta meteorites," *J. Raman Spectrosc.*, vol. 35, no. 6, pp. 497–503, Jun. 2004.
- [385] S. Das and M. J. Hendry, "Application of Raman spectroscopy to identify iron minerals commonly found in mine wastes," *Chem. Geol.*, vol. 290, no. 3–4, pp. 101–108, Nov. 2011.
- [386] W. Liang, L. Chen, L. Wang, Y. Yin, Z. Li, and H. Li, "High pressure synthesis of siderite (FeCO₃) and its thermal expansion coefficient," *High Temp. - High Press.*, vol. 47, no. 2, pp. 153–164, 2018.
- [387] W. Seifert, R. Thomas, and D. F. Rhede, "Origin of coexisting wustite, MgFe and REE phosphate minerals in graphite-bearing fluorapatite from the Rumburk granite," *Eur. J. Mineral.*, vol. 22, no. 4, pp. 495–507, Sep. 2010.
- [388] R. A. Bepari, P. Bharali, and B. K. Das, "Controlled synthesis of α - and γ -Fe₂O₃ nanoparticles via thermolysis of PVA gels and studies on α -Fe₂O₃

- catalyzed styrene epoxidation,” *J. Saudi Chem. Soc.*, vol. 21, pp. S170–S178, Jan. 2017.
- [389] A. G. Magdalena, I. M. B. Silva, R. F. C. Marques, A. R. F. Pipi, P. N. Lisboa-Filho, and M. Jafelicci, “EDTA-functionalized Fe₃O₄ nanoparticles,” *J. Phys. Chem. Solids*, vol. 113, pp. 5–10, Feb. 2018.
- [390] M. Y. Nassar, I. S. Ahmed, T. Y. Mohamed, and M. Khatab, “A controlled, template-free, and hydrothermal synthesis route to sphere-like α -Fe₂O₃ nanostructures for textile dye removal,” *RSC Adv.*, vol. 6, no. 24, pp. 20001–20013, 2016.
- [391] J.-C. J.-S. Wang *et al.*, “Synergistic photocatalysis of Cr(VI) reduction and 4-Chlorophenol degradation over hydroxylated α -Fe₂O₃ under visible light irradiation,” *J. Hazard. Mater.*, vol. 311, pp. 11–19, Jul. 2016.
- [392] G. Kurniawan and A. Khumaeni, “Synthesis of iron oxide nanoparticle using pulsed laser ablation method at low laser energy,” 2018, p. 020074.
- [393] G. Fracasso *et al.*, “Nanoaggregates of iron poly-oxo-clusters obtained by laser ablation in aqueous solution of phosphonates,” *J. Colloid Interface Sci.*, vol. 522, pp. 208–216, Jul. 2018.
- [394] I. Llamas-Jansa, C. Jäger, H. Mutschke, and T. Henning, “Far-ultraviolet to near-infrared optical properties of carbon nanoparticles produced by pulsed-laser pyrolysis of hydrocarbons and their relation with structural variations,” *Carbon N. Y.*, vol. 45, no. 7, pp. 1542–1557, Jun. 2007.
- [395] S. H. Lee, H. J. Jung, S. J. Lee, J. Theerthagiri, T. H. Kim, and M. Y. Choi, “Selective synthesis of Au and graphitic carbon-encapsulated Au (Au@GC) nanoparticles by pulsed laser ablation in solvents: Catalytic Au and acid-resistant Au@GC nanoparticles,” *Appl. Surf. Sci.*, vol. 506, p. 145006, Mar. 2020.
- [396] B. N. Khlebtsov, V. A. Khanadeev, E. V. Panfilova, D. N. Bratashov, and N. G. Khlebtsov, “Gold Nanoisland Films as Reproducible SERS Substrates for Highly Sensitive Detection of Fungicides,” *ACS Appl. Mater. Interfaces*, vol. 7, no. 12, pp. 6518–6529, Apr. 2015.

- [397] G. Kumari, X. Zhang, D. Devasia, J. Heo, and P. K. Jain, “Watching Visible Light-Driven CO₂ Reduction on a Plasmonic Nanoparticle Catalyst,” *ACS Nano*, vol. 12, no. 8, pp. 8330–8340, Aug. 2018.
- [398] L. F. van Staden, D. Gravestock, and D. J. Ager, “New developments in the Peterson olefination reaction,” *Chem. Soc. Rev.*, vol. 31, no. 3, pp. 195–200, May 2002.
- [399] J. Graciani *et al.*, “Highly active copper-ceria and copper-ceria-titania catalysts for methanol synthesis from CO₂,” *Science (80-.)*, vol. 345, no. 6196, pp. 546–550, Aug. 2014.
- [400] J. Klankermayer and W. Leitner, “Love at second sight for CO₂ and H₂ in organic synthesis,” *Science (80-.)*, vol. 350, no. 6261, pp. 629–630, Nov. 2015.
- [401] T. Kobayashi and H. Takahashi, “Novel CO₂ Electrochemical Reduction to Methanol for H₂ Storage,” *Energy & Fuels*, vol. 18, no. 1, pp. 285–286, Jan. 2004.
- [402] Y. El Fouih and C. Bouallou, “Recycling of Carbon Dioxide to Produce Ethanol,” *Energy Procedia*, vol. 37, pp. 6679–6686, 2013.
- [403] H. Mistry *et al.*, “Exceptional Size-Dependent Activity Enhancement in the Electroreduction of CO₂ over Au Nanoparticles,” *J. Am. Chem. Soc.*, vol. 136, no. 47, pp. 16473–16476, Nov. 2014.
- [404] S. A. Mavlyankariev, S. J. Ahlers, V. A. Kondratenko, D. Linke, and E. V. Kondratenko, “Effect of Support and Promoter on Activity and Selectivity of Gold Nanoparticles in Propanol Synthesis from CO₂, C₂H₄, and H₂,” *ACS Catal.*, vol. 6, no. 5, pp. 3317–3325, May 2016.
- [405] C. Zhao, A. Krall, H. Zhao, Q. Zhang, and Y. Li, “Ultrasonic spray pyrolysis synthesis of Ag/TiO₂ nanocomposite photocatalysts for simultaneous H₂ production and CO₂ reduction,” *Int. J. Hydrogen Energy*, vol. 37, no. 13, pp. 9967–9976, Jul. 2012.
- [406] V. Dolique, A.-L. Thomann, E. Millon, A. Petit, and P. Brault, “About the key factors driving the resistivity of AuOx thin films grown by reactive

- magnetron sputtering,” *Appl. Surf. Sci.*, vol. 295, pp. 194–197, Mar. 2014.
- [407] H. Tsai, E. Hu, K. Perng, M. Chen, J.-C. Wu, and Y.-S. Chang, “Instability of gold oxide Au₂O₃,” *Surf. Sci.*, vol. 537, no. 1–3, pp. L447–L450, Jul. 2003.
- [408] Y. Q. Wang, W. S. Liang, and C. Y. Geng, “Coalescence Behavior of Gold Nanoparticles,” *Nanoscale Res. Lett.*, vol. 4, no. 7, pp. 684–688, Jul. 2009.
- [409] J. Zhou *et al.*, “Fabrication of Gold Nanochains with Octreotide Acetate Template,” *J. Nanomater.*, vol. 2013, pp. 1–9, 2013.
- [410] R. Torres-Mendieta, D. Ventura-Espinosa, S. Sabater, J. Lancis, G. Mínguez-Vega, and J. A. Mata, “In situ decoration of graphene sheets with gold nanoparticles synthesized by pulsed laser ablation in liquids,” *Sci. Rep.*, vol. 6, no. 1, p. 30478, Sep. 2016.
- [411] S. S. Bayram, K. Lindfors, and A. S. Blum, “Tunable longitudinal modes in extended silver nanoparticle assemblies,” *Beilstein J. Nanotechnol.*, vol. 7, pp. 1219–1228, Aug. 2016.
- [412] E. Albitar, M. A. Valenzuela, S. Alfaro, G. Valverde-Aguilar, and F. M. Martínez-Pallares, “Photocatalytic deposition of Ag nanoparticles on TiO₂: Metal precursor effect on the structural and photoactivity properties,” *J. Saudi Chem. Soc.*, vol. 19, no. 5, pp. 563–573, Sep. 2015.
- [413] S. Chen, T. Takata, and K. Domen, “Particulate photocatalysts for overall water splitting,” *Nat. Rev. Mater.*, vol. 2, no. 10, p. 17050, Oct. 2017.
- [414] J. Wu, Y. Huang, W. Ye, and Y. Li, “CO₂ Reduction: From the Electrochemical to Photochemical Approach,” *Adv. Sci.*, vol. 4, no. 11, p. 1700194, Nov. 2017.
- [415] D. M. Drab *et al.*, “Hydrocarbon Synthesis from Carbon Dioxide and Hydrogen: A Two-Step Process,” *Energy & Fuels*, vol. 27, no. 11, pp. 6348–6354, Nov. 2013.
- [416] S. Roy, A. Cherevotan, and S. C. Peter, “Thermochemical CO₂ Hydrogenation to Single Carbon Products: Scientific and Technological Challenges,” *ACS Energy Lett.*, vol. 3, no. 8, pp. 1938–1966, Aug. 2018.

- [417] N. S. Romero Cuellar *et al.*, “Two-step electrochemical reduction of CO₂ towards multi-carbon products at high current densities,” *J. CO₂ Util.*, vol. 36, pp. 263–275, Feb. 2020.
- [418] T. Tsuji, D.-H. Thang, Y. Okazaki, M. Nakanishi, Y. Tsuboi, and M. Tsuji, “Preparation of silver nanoparticles by laser ablation in polyvinylpyrrolidone solutions,” *Appl. Surf. Sci.*, vol. 254, no. 16, pp. 5224–5230, Jun. 2008.
- [419] S. Besner, A. V. Kabashin, F. M. Winnik, and M. Meunier, “Synthesis of Size-Tunable Polymer-Protected Gold Nanoparticles by Femtosecond Laser-Based Ablation and Seed Growth,” *J. Phys. Chem. C*, vol. 113, no. 22, pp. 9526–9531, Jun. 2009.
- [420] A. F. M. Y. Haider, S. Sengupta, K. M. Abedin, and A. I. Talukder, “Fabrication of gold nanoparticles in water by laser ablation technique and their characterization,” *Appl. Phys. A*, vol. 105, no. 2, pp. 487–495, Nov. 2011.
- [421] E. Solati and D. Dorrnian, “Comparison Between Silver and Gold Nanoparticles Prepared by Pulsed Laser Ablation in Distilled Water,” *J. Clust. Sci.*, vol. 26, no. 3, pp. 727–742, May 2015.
- [422] L. Babes, B. Denizot, G. Tanguy, J. J. Le Jeune, and P. Jallet, “Synthesis of Iron Oxide Nanoparticles Used as MRI Contrast Agents: A Parametric Study,” *J. Colloid Interface Sci.*, vol. 212, no. 2, pp. 474–482, Apr. 1999.
- [423] P. Wagener, S. Barcikowski, N. Bärsch, and P. Gmbh, “Fabrication of nanoparticles and nanomaterials using laser ablation in liquids,” *Photonic Int.*, vol. 1, pp. 20–23, 2011.
- [424] “Brazilian Energy Balance 2018,” Rio de Janeiro, 2018.
- [425] M. Kitano, K. Tsujimaru, and M. Anpo, “Hydrogen Production Using Highly Active Titanium Oxide-based Photocatalysts,” *Top. Catal.*, vol. 49, no. 1–2, pp. 4–17, Jul. 2008.
- [426] K. KVENVOLDEN *et al.*, “Evidence for Extraterrestrial Amino-acids and Hydrocarbons in the Murchison Meteorite,” *Nature*, vol. 228, no. 5275, pp.

923–926, Dec. 1970.

- [427] Fulvio Daniele et al., “Micrometeorite bombardment simulated by ns-pulsed laser ablation: morphological characterization of the impact craters,” *Icarus.*, 2020.
- [428] M. Nicola *et al.*, “The socio-economic implications of the coronavirus pandemic (COVID-19): A review,” *International Journal of Surgery*. pp. 185–193, 2020.
- [429] Arnaud Mayence, “Design and characterization of nanoparticles and their assemblies,” Stockholm University, 2016.
- [430] D. B. Williams and C. B. Carter, *Transmission Electron Microscopy*. Boston, MA, MA: Springer US, 2009.